Mémoire d'Habilitation à Diriger des Recherches From microstructure to macroscopic properties: Some applications of the Hashin–Shtrikman principle

Sébastien Brisard

UNIVERSITÉ PARIS-EST

Mémoire d'Habilitation à Diriger des Recherches

From microstructure to macroscopic properties: Some applications of the Hashin–Shtrikman principle

Sébastien Brisard

Soutenue le 20 novembre 2017 devant le jury composé de :

Pierre Gilormini	*Président*
Samuel Forest	*Rapporteur*
Christian Hellmich	*Rapporteur*
Patrick Le Tallec	*Rapporteur*
Renald Brenner	*Examinateur*
Karam Sab	*Examinateur*

From microstructure to macroscopic properties: some applications of the Hashin–Shtrikman principle

Sébastien Brisard

July 2, 2018

Contents

List of Figures

Remerciements

Je souhaiterais remercier avant tout mon ami Yukio. Il ne le sait peut-être pas, mais c'est grâce à lui que je suis aujourd'hui un chercheur. En effet, c'est lui qui, en me racontant l'atmosphère exaltante du laboratoire d'économie dans lequel il préparait lui-même un doctorat à Chicago, m'a convaincu en 2006 de m'inscrire en thèse.

En ce qui concerne mes activités d'enseignement, ma gratitude va vers Philippe Bisch, Patrick de Buhan, Olivier Coussy, Luc Dormieux et Alain Ehrlacher. Je les considère comme les gardiens d'une certaine école française de mécanique. Ce ne sont pas des mandarins pour autant : ils n'hésitent pas à se remettre en question tous les ans pour tenir compte des évolutions des étudiants. J'aimerais pouvoir dire un jour que je m'inscris dans leur lignée.

Qui dit enseignement, dit étudiants. Je voudrais remercier tous mes étudiants : mes doctorants bien sûr, auxquels je suis sincèrement attaché, mais aussi tous les élèves ingénieurs qui ont suivi mes cours. Vous m'avez tous énormément apporté. Mes collègues savent à quel point je ressors euphorique d'un cours, et c'est grâce à vous.

Pour ce qui est de mon parcours de chercheur, quelques personnes m'ont apporté (et continuent à m'apporter) une aide très précieuse par leur bonne connaissance du monde de la recherche.

Olivier Coussy a guidé mes premiers pas dans le monde de la recherche. Lors de ma soutenance de thèse, j'avais déjà eu l'occasion de dire à quel point j'aurais aimé qu'il soit présent. C'est encore plus vrai aujourd'hui. Je pense que s'il était encore parmi nous, mon parcours de chercheur aurait été très différent, car il m'aurait sans doute encouragé à sortir de ma zone de confort. Pierre Levitz est devenu un ami très cher et je ne néglige jamais ses conseils, prodigués au cours de joyeux déjeuners pris en terrasse dans le Quartier Latin, en compagnie de son compère Laurent Michot. Bien que toujours très occupé, Michel Bornert me laisse toujours sa porte grande ouverte. J'ai beaucoup d'admiration pour sa culture scientifique très vaste, qui donne toujours une grande valeur à ses commentaires. Karam Sab et moi partageons de nombreuses thématiques scientifiques. Nous avons également l'occasion d'échanger sur le monde de la recherche en général. Sa phrase fétiche, « c'est ça qu'il faut faire », en dit long sur la clarté de son esprit !

Au laboratoire Navier, j'ai la chance d'avoir de nombreux collègues que je considère maintenant comme des amis. Vouloir les citer tous serait s'exposer au risque d'en oublier, aussi vais-je me contenter de citer mes voisins de bureau : Denis, Ghazi, Patrick, Gwendal, avec bien sûr une mention spéciale pour Camille : j'aurais difficilement pu trouver une voisine de bureau plus agréable. Merci également à Siavash pour avoir immortalisé avec talent ma soutenance.

Si le laboratoire Navier fonctionne aussi bien, c'est largement dû à nos assistantes qui sont des perles. Je voudrais en particulier remercier Marie-Françoise, qui contrairement à moi es-

pérait que mon épouse ne pourrait pas assister à ma soutenance. Elle aurait eu notre fille Clarisse pour elle toute seule ! Également, un grand merci à Rachida, Sabrina et Catherine, dont l'aide m'a été précieuse pour organiser cette soutenance (mais pas seulement).

Une petite pensée pour mes amis. Cela fait presque 20 ans que nous nous connaissons, et quelques uns d'entre vous étaient présents à ma soutenance. Vous ne savez pas à quel point cela me touche.

Je voudrais également remercier ma fille Clarisse, qui a une façon bien à elle de me faire comprendre lorsque mon travail empiète trop sur notre vie. Merci de m'aider à reprendre contact avec la réalité !

Pour finir, il m'est impossible d'exprimer ici toute la gratitude que j'éprouve pour mon épouse Pascale et son soutien indéfectible tant sur le plan professionnel que dans mes combats personnels. « Merci » est très en-dessous de ce que je te dois, mais il vient du fond de mon cœur.

Abstract/Résumé

Abstract

The present report is submitted in partial fulfilment of the French habilitation degree (*Habilitation à Diriger des Recherches*). Covering the period 2011–2017, it gives an overview of a selection of my research activities, conducted essentially at Laboratoire Navier[1].

Most of my research has been devoted to understanding how the macroscopic properties of random, heterogeneous materials relate to their microstructure. To investigate this question, I used almost systematically a variational approach based on the Hashin–Shtrikman principle, which results in a fairly consistent report. The reason for selecting such a tool lies in its high versatility; indeed, *any* trial field is admissible. This is extremely valuable for highly heterogeneous materials, where it can be difficult to propose e.g. admissible stress or strain fields.

The Hashin–Shtrikman principle is applied here in two different situations: *i.* in a statistical (theoretical) setting, and *ii.* in a numerical setting relying on Galerkin discretizations. In the former situation, the Hashin–Shtrikman principle leads to closed-form (or at least, semi-analytical) bounds or estimates of the effective properties. In the latter situation, the Hashin–Shtrikman principle allows to revisit a few existing *full-field* techniques. My contributions in both areas are discussed in two separate chapters.

For the sake of consistency of the present document, some of my research activities (relating to X-ray tomography and image analysis) have been purposely discarded. They are briefly discussed in the last chapter as a part of my prospective research project.

Résumé

Le présent mémoire est soumis pour l'obtention du diplôme d'Habilitation à Diriger des Recherches. Il couvre la période 2011–2017, et donne un aperçu de mes activités de recherches, conduites pour l'essentiel au Laboratoire Navier[1].

Mes recherches ont pour l'essentiel été consacrées à l'étude des relations entre microstructure et propriétés macroscopiques des matériaux hétérogènes aléatoires. Pour étudier ce problème, j'ai utilisé quasi-systématiquement une approche variationnelle basée sur le principe de Hashin–Shtrikman. Cette méthodologie unifiée conduit à une certaine cohérence de ce mémoire. La raison pour laquelle j'ai très tôt choisi cet outil est son extrême souplesse. En effet, tout champ test est admissible pour le principe de Hashin–Shtrikman. C'est un atout majeur

[1]Laboratoire Navier, UMR 8205, CNRS, ENPC, IFSTTAR, Université Paris-Est (Marne-la-Vallée, France)

pour les matériaux fortement hétérogènes, pour lesquels il peut être difficile de construire des champs statiquement ou cinématiquement admissibles.

Le principe de Hashin–Shtrikman est ici appliqué dans deux situations différentes : *i.* dans un cadre statistique (théorique), et *ii.* dans un cadre numérique s'appuyant sur des discrétisations de type Galerkin. Dans la première situation, le principe de Hashin–Shtrikman conduit à des bornes ou estimations analytiques ou au moins semi-analytiques des propriétés macroscopiques. Dans la deuxième situation, le principe de Hashin–Shtrikman permet de revisiter un certain nombre de techniques dites en champ complet. Mes contributions dans ces deux domaines sont discutées dans deux chapitres distincts.

Afin de garantir la cohérence du présent document, certains de mes travaux de recherche ont volontairement été mis de côté. Il s'agit en particulier de mes travaux relatifs à l'imagerie par tomographie aux rayons X et à l'analyse d'images. Ces thématiques de recherches sont discutées brièvement dans le dernier chapitre de cette thèse, où elles sont réintégrées à mon projet de recherche à venir.

Curriculum vitæ

Sébastien Brisard

Born in August 1978 in Toulouse, France

Laboratoire Navier (UMR 8205), CNRS, ENPC, IFSTTAR
Université Paris-Est, Marne-la-Vallée F-77455, France

+33 (0)1 64 15 37 51

sebastien.brisard@ifsttar.fr
http://navier.enpc.fr/BRISARD-Sebastien

IdHAL: sbrisard
ORCID: 0000-0002-1976-6263

Curriculum

November 2011 – now Research scientist at Laboratoire Navier[1]

September 2010 – October 2011 Research scientist at IFSTTAR (French Institute of Science and Technology for Transport, Development and Networks, Paris, France), MACS laboratory

September 2007 – August 2010 PhD at École des Ponts ParisTech, *Morphological analysis and numerical homogenization: application to cement paste*, under the supervision of Prof. Dormieux[1] and Dr. Levitz[2]

March 2007 – August 2007 Visiting scholar at UC Berkeley, *Characterization of the orientation of fibers by Digital Laminography in Ultra-High Performance, Fiber Reinforced Concrete*, under the supervision of Prof. Monteiro

September 2003 – February 2007 Bridge engineer at Sétra (French Highway Administration)

Teaching

September 2012 – now Assistant Professor at École des Ponts ParisTech: *Shells and Advanced Structures*, *Towards Structural Mechanics* (since 2016), *Introduction to the Dynamics and Stability of Mechanical Systems* (since 2016)

[1] Laboratoire Navier, UMR 8205, CNRS, ENPC, IFSTTAR, Université Paris-Est (Marne-la-Vallée, France)
[2] Laboratoire PHENIX (UMR8234), Sorbonne Universités, UPMC University, CNRS, Paris, France

September 2008 – September 2012 Assistant Professor at École des Ponts ParisTech: *Structural Analysis* and *Shells and Advanced Structures*

September 2003 – September 2008 Teaching Assistant at École des Ponts ParisTech: *Structural Analysis* and *Shells and Advanced Structures*

Education

September 2000 – August 2003 École des Ponts ParisTech (Marne-la-Vallée, France), Civil Engineering dpt.

September 1997 – August 1999 École Polytechnique (Palaiseau, France), Mechanics dpt. Final rank: 11/398.

Academic prizes

2017 Jean Mandel Prize Delivered by Laboratoire de Mécanique des Solides (École Polytechnique) and Centre des Matériaux (Mines ParisTech) – Tied with T. Morgeneyer

2012 PhD Award Delivered by Fondation de l'École des Ponts – Tied with N. Oppenchaim

Publications

[17] M. H. Khalili, J.-N. Roux, J.-M. Pereira, S. Brisard, and M. Bornert. "Numerical study of one-dimensional compression of granular materials. II. Elastic moduli, stresses, and microstructure". In: *Physical Review E* 95 (3 2017), p. 032908

[16] M. H. Khalili, J.-N. Roux, J.-M. Pereira, S. Brisard, and M. Bornert. "Numerical study of one-dimensional compression of granular materials. I. Stress-strain behavior, microstructure, and irreversibility". In: *Physical Review E* 95 (3 2017), p. 032907

[15] M. H. Khalili, S. Brisard, M. Bornert, P. Aimedieu, J.-M. Pereira, and J.-N. Roux. "Discrete Digital Projections Correlation: A Reconstruction-Free Method to Quantify Local Kinematics in Granular Media by X-ray Tomography". In: *Experimental Mechanics* (2017), pp. 1–12

[14] S. Brisard. "Towards improved Hashin–Shtrikman bounds on the effective moduli of random composites". In: *Mechanics & Industry* 18.2 (2017), p. 214

[13] S. Brisard. "Reconstructing displacements from the solution to the periodic Lippmann–Schwinger equation discretized on a uniform grid". In: *International Journal for Numerical Methods in Engineering* 109.4 (2017), pp. 459–486

[12] N. Mayercsik, S. Brisard, M. Vandamme, and K. Kurtis. “Using Fractal Geometry to Recover the 3D Air Void, Scale-Independent, Microstructure Information From 2D Sections of Mortars”. In: *Advances in Civil Engineering Materials* 5.2 (2016), pp. 1–21

[11] V.-P. Tran, J. Guilleminot, S. Brisard, and K. Sab. “Stochastic modeling of mesoscopic elasticity random field”. In: *Mechanics of Materials* 93 (2016), pp. 1–12

[10] S. Brisard, L. Dormieux, and K. Sab. “A variational form of the equivalent inclusion method for numerical homogenization”. In: *International Journal of Solids and Structures* 51.3-4 (2014), pp. 716–728

[9] F. Bignonnet, K. Sab, L. Dormieux, S. Brisard, and A. Bisson. “Macroscopically consistent non-local modeling of heterogeneous media”. In: *Computer Methods in Applied Mechanics and Engineering* 278.0 (2014), pp. 218–238

[8] S. Brisard, K. Sab, and L. Dormieux. “New boundary conditions for the computation of the apparent stiffness of statistical volume elements”. In: *Journal of the Mechanics and Physics of Solids* 61.12 (2013), pp. 2638–2658

[7] S. Brisard and P. Levitz. “Small-angle scattering of dense, polydisperse granular porous media: Computation free of size effects”. In: *Physical Review E* 87.1 (2013), p. 013305

[6] S. Brisard and L. Dormieux. “Combining Galerkin approximation techniques with the principle of Hashin and Shtrikman to derive a new FFT-based numerical method for the homogenization of composites”. In: *Computer Methods in Applied Mechanics and Engineering* 217-220.0 (2012), pp. 197–212

[5] S. Brisard, R. S. Chae, I. Bihannic, L. Michot, P. Guttmann, J. Thieme, G. Schneider, P. J. M. Monteiro, and P. Levitz. “Morphological quantification of hierarchical geomaterials by X-ray nano-CT bridges the gap from nano to micro length scales”. In: *American Mineralogist* 97.2 (2012), pp. 480–483

[4] S. Brisard, L. Dormieux, and D. Kondo. “Hashin–Shtrikman bounds on the shear modulus of a nanocomposite with spherical inclusions and interface effects”. In: *Computational Materials Science* 50.2 (2010), pp. 403–410

[3] S. Brisard and L. Dormieux. “FFT-based methods for the mechanics of composites: A general variational framework”. In: *Computational Materials Science* 49.3 (2010), pp. 663–671

[2] S. Brisard, L. Dormieux, and D. Kondo. “Hashin–Shtrikman bounds on the bulk modulus of a nanocomposite with spherical inclusions and interface effects”. In: *Computational Materials Science* 48.3 (2010), pp. 589–596

[1] O. Coussy and S. Brisard. “Prediction of drying shrinkage beyond the pore isodeformation”. In: *Journal of Mechanics of Materials and Structures* 4.2 (2009), pp. 263–279

Supervision of postdoctoral fellows

Michaël Bertin *Variance Reduction Techniques for the Homogenization of Random Materials*[3] (co-supervised with: C. Lebris and F. Legoll; March 2015 – February 2016).

Linlin Wang ANHYMA research project (hydromechanical couplings within the clay matrix of argilites), for which I am PI (co-supervised with: M. Vandamme; September 2013 – August 2014). This work was financially supported by Défi NEEDS MiPor.

Fatma Allouche *Methodologies and tools for the analysis of X-rays and electron tomography images; Application to nanostructured materials and geomaterials*[3] (co-supervised with: M. Bornert, N. Lenoir, E. Leroy, F. Dalmas; January 2013 – December 2013).

Supervision of PhD students

The french research system requires researchers to pass the so-called HDR (habilitation to supervise research) before they can formally advise PhD students. As a consequence, I am not the formal advisor of the students listed below, even if I am involved with their research work on a weekly basis.

Othmane Zerhouni *Solids with a microstructure: imaging, virtual multi-scale microstructures and 3D printing* (advisor: Dr. K. Danas; October 2016 – now)

Vinh Hoang Tan Le *Micromechanical modeling of cracking induced by hydromechanical stresses in heterogeneous porous materials by means of joint finite elements and inhomogeneity models with partial bonding of the interface*[3] (advisor: Dr. A. Pouya; October 2016 – now).

Mohamed Hassan Khalili *Combining micro CT and DEM to study the micromechanical origins of creep of granular materials*[3] (advisor: Dr. J.-N. Roux; October 2013 – November 2016).

Vinh Phuc Tran *Multiscale a priori probabilistic modelling of random heterogeneous materials*[3] (advisor: Prof. K. Sab; October 2013 – October 2016).

Yassine El Assami *Modelling time-dependent behaviour of concrete with the equivalent inclusion method* (advisor: Prof. L. Dormieux; February 2012 – May 2015)

Reviewing activities

I have been reviewing articles for the following journals: Applied Mathematics Research Express, Archive for Rational Mechanics and Analysis, Cement and Concrete Research, Computational Materials Science, Géotechnique Letters, International Journal for Numerical and

[3]This work has benefited from a French government grant managed by ANR within the frame of the national program Investments for the Future ANR-11-LABX-022-01.

Analytical Methods in Geomechanics, International Journal for Numerical Methods in Engineering, International Journal of Solids and Structures, Journal of Computational Physics, Journal of the Mechanics and Physics of Solids, Materials and Structures, Mechanics of Materials, Zeitschrift für Angewandte Mathematik und Mechanik.

I have also been reviewing project proposals for the following funding agencies: COFECUB (French Comity for the Academic Cooperation with Brazil), NWO (Netherlands Organization for Scientific Research).

Organization of seminars, conferences, and mini-symposia

Organizer of the monthly seminar of the *Multiscale* research team at Navier Laboratory:
http://navier.enpc.fr/Seminaire-d-equipe-Team-seminar

Co-organizer (with F. Willot) of the mini-symposium *Stochastics and Material Mechanics* at the *14th European Mechanics of Materials Conference*, Gothenburg, Sweden (August 27–29, 2014)

Co-organizer (with S. Meulenyzer) of the workshop on *Imaging of Construction Materials and Geomaterials* at École des Ponts ParisTech, Marne la Vallée, France (July 7–8, 2016)

Co-organizer (with J. Yvonnet) of the mini-symposium *Multiscale modeling of microstructures and their macroscopic properties* at the 2016 *EMI International conference*, Metz, France (October 25–27, 2016)

Member of the local organizing committee of the *6th Biot Conference on Poromechanics* at École des Ponts ParisTech, Marne la Vallée, France (July 9–13, 2017)

Member of the local organizing committee of the ECCOMAS thematic conference on *Computational Modeling of Complex Materials Across the Scales*, Paris, France (November 7–9, 2017)

Participation to boards – Other services to the community

Elected member of Navier's Laboratory Board

Elected member of the Teaching and Research Board at École des Ponts ParisTech

Strong involvement in a working group on pedagogy at École des Ponts

Maintainer of the `doubs` computing server:
http://navier.enpc.fr/Multi-scale-computing-resources

Involvement in open or collaborative projects

I maintain a blog dealing with scientific computing, micromechanics and imaging:
`http://sbrisard.github.io/`.

I am the main developer of the Janus project (FFT-based numerical homogenization):
`https://github.com/sbrisard/janus`.

I have been involved (as *committer*) in the Apache Commons-Math open source project:
`http://commons.apache.org/proper/commons-math/`.

Chapter 1

Introduction

The aim of this chapter is to give a brief overview of my professional and academic activities since my graduation as a civil engineer in 2002. Although not academic *per se*, my first professional experience as a bridge engineer had a decisive influence on my ensuing activities; besides, it allowed me to acquire an extremely valuable practical experience which I still find useful today. As such, it is presented in section 1.1. I then joined Laboratoire Navier, first as a PhD student (see section 1.2), then as a research scientist (see section 1.3). I have been fortunate enough to have the opportunity to teach at École des Ponts ParisTech immediatly after my graduation. Teaching is truly a vocation for me, and my teaching activities are briefly summarized in section 1.4. This chapter then closes with an outline of the remainder of this document in section 1.5, as well as a review of my publications, and how they relate to the different parts of the present report.

1.1 Bridge engineer at Sétra

I have been working at Sétra from 2003 to 2007. At that time, Sétra stood for "Service d'études techniques des routes et autoroutes"[1], and was providing technical support to the Ministry of Transportation as well as local authorities in matters pertaining to the design, maintenance and construction management of (large) bridges. I believe it was at that time somewhat comparable in scope (although certainly not in size) to the US Federal Highway Administration (FHWA). Sétra has since been merged into a larger entity, Cerema ("Centre d'études et d'expertise sur les risques, l'environnement, la mobilité et l'aménagement").

I acquired in this department a solid background in structural mechanics and bridge design. In particular, I was in charge of the preliminary design as well as validation of the contractor's final design of a large two-girder composite bridge near Avignon ("viaduc de franchissement aval de la Durance par la LEO" – Liaison Est-Ouest), see figure 1.1. This bridge had a wide, curved deck. It was the first large bridge in France to be designed according to the then fairly new "Eurocode 4" standard. This contributed a lot to strengthening my background in structural mechanics, in particular the post-critical behavior of steel plates.

I soon developed at Sétra a taste for methodological issues. For exemple, I developed an automated procedure for the finite element calculation of the influence surface of a bridge deck (see figure 1.2, left). Combining this calculation with a genetic algorithm to optimize

[1] Now: "Service d'études sur les transports, les routes et leurs aménagements"… how things change!

Figure 1.1: The "viaduc de franchissement aval de la Durance par la LEO à Avignon" (credits N. Janberg and Structurae).

the location of moving loads allowed me to produce charts for the design of standard two-girder composite bridges (see figure 1.2, right). These charts were published in the *Bulletin Ouvrages d'Art* (num. 54, march 2007)[2]. I have been recently informed by practising engineers that these charts are still used today (which I find a bit distressing!). Having access to a larger body of bibliographical resources, I later realized that the method I had proposed for computing influence surfaces had already been published fifteen years earlier [MW91], thus learning at my expense the importance of carrying out a thorough literature survey!

I also got involved in a research project on the fatigue of orthotropic bridges. Indeed, at that time, two large lift bridges were being designed and constructed in France (in Rouen and Bordeaux). In order to keep the overall weight of the deck to a minimum, the standard wearing course was replaced with a thin wearing course. What was overlooked at that time was the fact that a thick wearing course contributes significantly to the local bending stiffness of the bridge deck. As a consequence of reducing the thickness of the wearing course, the deck became extremely susceptible to fatigue.

I carried out a preliminary finite element study of this potential pathology. Then, I managed in 2006 the proposal for an ANR research project (*Génie Civil et Urbain (RGCU)*) called *OrthoPlus*, which was awarded a 576 k€ funding over 36 months. This project gathered both academic (Céréma, ENTPE, Ifsttar, …) and industrial (Arcadis ESG, Eiffage, …) partners. Unfortunately, I left Sétra before this project actually started.

1.2 PhD student at Laboratoire Navier

In 2006, my activities were increasingly theoretical, and I grew more and more isolated from my other colleagues at Sétra. It was only too natural for me to try and go back to academia. I should like to thank the late O. Coussy (then director of Institut Navier) and J.-C. Pauc (then director of Sétra) for supporting this undertaking. Following O. Coussy's advice, I registered

[2] http://www.setra.fr/html/boa/Data_Base_BOA/Collection_Numeros/boa_54.pdf, last retrieved 2017-06-07

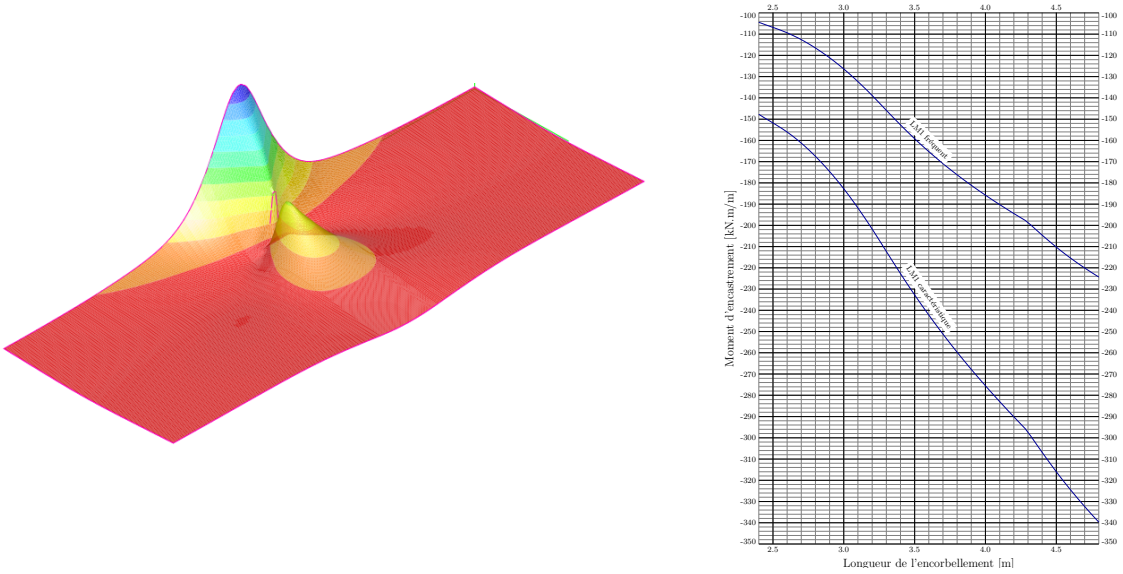

Figure 1.2: Finite element computation of the influence surface of the hogging moment of a two-girder composite bridge (left). Chart of this bending moment, for a class I traffic, as defined by Eurocode 1 (right).

for the Master of Science *Materials Science for Sustainable Construction* at École des Ponts ParisTech.

I conducted my research project under the supervision of Prof. P.J.M. Monteiro[3]. The aim was to use X-ray laminography (a 3D imaging device meant to be portable) for the analysis of the distribution of reinforcement in fiber reinforced concrete. This research project was for me an excellent opportunity to develop my skills in image analysis and 3D image reconstruction techniques. I later had the opportunity to again explore these topics(see section 1.3).

From 2007 to 2010, I prepared my PhD under the supervision of Prof. L. Dormieux[4] and P. Levitz[5]. The title of my dissertation is: *Morphological Analysis and Numerical Homogenization: Application to Cement Paste* [Bri11]. The original mix of micromechanical (L. Dormieux) and physical (P. Levitz) approaches was for me a permanent, exciting challenge that largely contributed to my work being awarded (together with N. Oppenchaim) the 2012 École des Ponts ParisTech Best Thesis Prize[6].

The main goal of this work was the characterization of the microstructure of C–S–H and the connections with its macroscopic properties. C–S–H (calcium silicate hydrate) is one the products of the hydration of cement pastes. It is widely agreed that it is responsible for the overall mechanical strength of hydrated cement pastes. Understanding the properties of C–S–H is therefore key to optimizing cement pastes (in order to e.g. reduce their extremely high CO_2 footprint).

[3]Department of Civil & Environmental Engineering, University of California, Berkeley
[4]Laboratoire Navier, UMR 8205, CNRS, ENPC, IFSTTAR, Université Paris-Est (Marne-la-Vallée, France)
[5]Laboratoire PHENIX (UMR8234), Sorbonne Universités, UPMC University, CNRS, Paris, France
[6]http://en.enpc.fr/les-prix-de-these-de-lecole-des-ponts-paristech, last retrieved 2017-06-13.

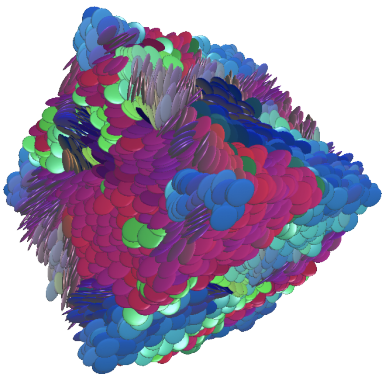

Figure 1.3: In a compact assembly of flat objects, strong orientational correlations are likely to develop. In the present case, 10 000 oblate spheroids were placed in a simulation box. The solid volume fraction is 60 %, and the aspect ratio of the spheroids is 1/8. Particles are colored according to their orientation: large, quasi-uniform color patches can be observed, which shows that particles tend to align themselves.

Back when I started my PhD, the microstructure of C–S–H remained widely mysterious. Various authors had proposed various morphologies, all of them relying on the notion of a basic building block: "globules" [All+87]; [Jen00]; [Jen08], "platelets" [GBN06], "needles" [Ric04]… This diverse zoology is largely due to the near impossibility of unbiased, direct observation of C–S–H at the relevant scale (a few tens of nanometers). Still, clarifying this microstructure is a real issue. Indeed, the porosity of C–S–H is relatively small (about 30 %). Anisotropic basic building blocks (such as platelets) must then induce strong local orientational correlations (as illustrated on figure 1.3). In turn, these correlations might induce noticeable effects on the macroscopic mechanical properties of C–S–H.

In this project, P. Levitz proposed a critical review of the above mentioned zoology relying on small-angle X-ray scattering (SAXS). Indeed, this experimental technique has various valuable assets: appropriate resolution, large scale samples (typically, $10\,\text{mm} \times 10\,\text{mm} \times 0,1\,\text{mm}$), no need to work under vacuum conditions, intrinsically three-dimensional information (no projection effects), … The major drawback being that SAXS is an *indirect* observation technique, that only provides the spectral density of the local electron density [DAB57]; [Por82]. It is therefore not possible to reconstruct the 3D local electron density, since only the modulus of its Fourier transform is known (the phase is missing).

Nevertheless, this technique is very interesting for cementitious materials. Indeed, it is well-known since the eighties [All+87] that cement pastes exhibit a characteristic SAXS pattern which is difficult to explain (see figure 1.4). Some authors consider that this pattern is the signature of a fractal microstructure [All+87]. However, it is difficult to reconcile this assumption with the relatively low porosity of C–S–H (fractals being generally open).

To tackle this issue, I adopted an inverse approach: is it possible to construct a (virtual) microstructure which reproduces the SAXS pattern of cement pastes? This led me to develop a numerical method for the computation of the SAXS pattern. The proposed method minimizes size-effects induced by truncation in the real space (the generated microstructures being relatively small from the perspective of SAXS). A first version of the method was proposed in my PhD thesis (see chapter 4 in reference [Bri11]). It was further improved in reference [BL13].

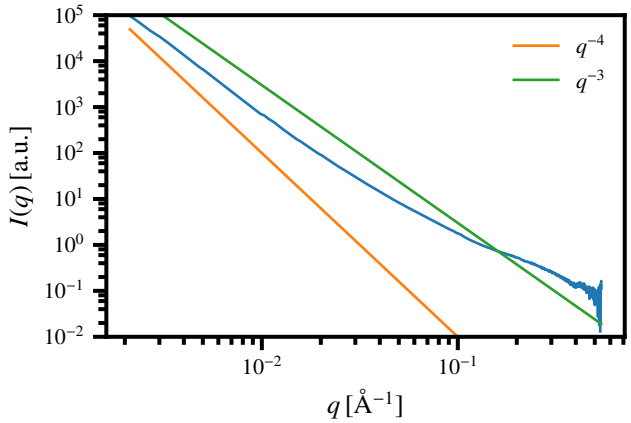

Figure 1.4: Small-angle X-ray scattering pattern of a CEM-I, 1.5 years old, hydrated cement paste ($w/c = 0.35$). The algebraic behavior as a fractional power of the scattering vector q has been reported by many teams. Its origin remains unclear.

Using this forward simulation tool, I was able to invalidate some microstructural hypotheses, showing that neither "globules", nor "platelets" could result in the typical SAXS pattern shown in figure 1.4.

During the course of my PhD, I also had the opportunity to carry out soft X-ray microscopy observations of C–S–H grains. This work was conducted in collaboration with Prof. P.J.M. Monteiro at the Bessy-II synchrotron in Berlin, Germany (beamline U41). Since the sample is mounted on a rotating stage in this microscope, it is in principle possible to carry out what should effectively be called *nanotomography*, thus providing three-dimensional insight into the microstructure of cement pastes at unprecedented scales (about 20 nm). However, reconstructing the 3D volume turned out to be a formidable task, that required to account for misalignment of the projections and the so-called "missing wedge" (since the sample cannot be fully rotated in this setup). Besides, the images produced by the soft X-ray microscope at Bessy-II/U41 are polluted by a number of artifacts, including: limited depth of field as well as non-uniform and non-stationary source. Although I was in the end able to produce a 3D reconstruction of the sample (see figure 1.5), the analysis of the microstructure that we were able to carry out was rather limited, due to these artifacts [Bri+12]. Still, this part of my PhD was extremely formative, as I had to implement state-of-the-art image analysis and reconstruction algorithms.

Meanwhile, I set out to investigate, under the supervision of Prof. L. Dormieux, the connections between microstructure and macroscopic properties. The –somewhat optimistic– goal was to try and come up with a mechanical model of C–S–H that would account for the microstructural characterization carried out with P. Levitz.

Of course, this goal turned out to be far too ambitious, and I was hardly able to bridge these two parts of my dissertation. However, the polarization techniques that I started to use then are still at the heart of my current research. Discussion of this topic is therefore deferred to the next section.

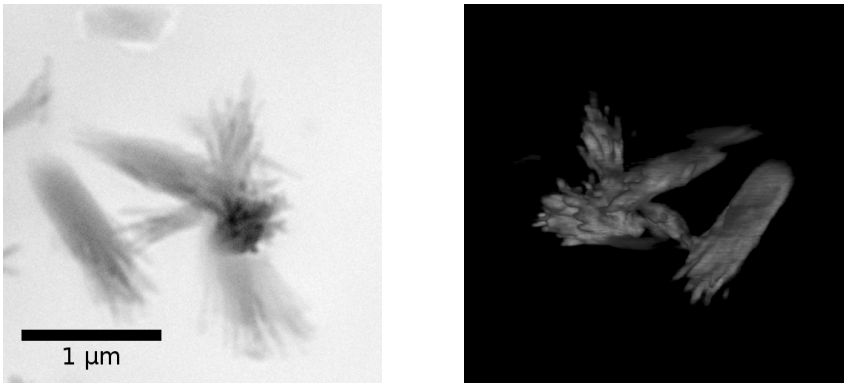

Figure 1.5: Soft X-ray microscopy transmission image of a hydrated cement paste (CEM-I, $w/c = 0.35$) (left). Three-dimensional reconstruction of the same grain (right). The lack of sharpness of the reconstructed volume is caused by the various artifacts inherent to the setup at Bessy-II/U41.

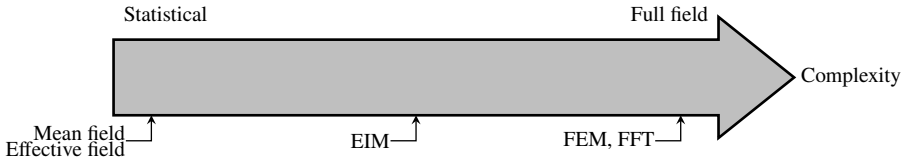

Figure 1.6: Homogenization methods can be laid out on a complexity scale: from the left-hand side to the right-hand side, the complexity increases.

1.3 Research scientist at Laboratoire Navier

I joined Ifsttar (*Institut français des sciences et technologies des transports, de l'aménagement et des réseaux*) immediately after the defense of my PhD. I worked for a year at the MACS department (*Mesures, Auscultation et Calcul Scientifique*). In fall 2011, a position opened at Laboratoire Navier and I had the good fortune to join the newly created *Multiscale* team.

Since then, my research has been focused on the homogenization of random, heterogeneous materials. More precisely, I explore the connections between microstructure and macroscopic properties. In theory, this problem can be considered as solved. Indeed, as will be discussed in chapter 2, solving the so-called *corrector problem* "suffices" to determine the macroscopic properties of a given microstructure. Unfortunately, solving this problem can be a formidable task, for which various methods have been devised. These methods can be laid out on an "complexity scale" (see figure 1.6). At the two ends of this complexity scale lie the two most famous families of homogenization techniques.

On the low-complexity side lie mean field/effective field methods, which are based on the solution to Eshelby's inhomogeneity problem [Esh57]. In this problem, a unique (ellipsoidal) inhomogeneity is embedded in an infinite matrix and subjected to a uniform strain at infinity. The resulting estimates of the macroscopic properties cannot really account for correlations, since the inhomogeneity is isolated in the underlying auxiliary problem. As a consequence, the microstructural information that these methods can account for quantitatively is rather limited. As an example, the total porosity of a porous medium is within the reach of these models, while the pore-size distribution is not [CB09]. Still, these methods should not be dismissed.

Indeed, they are extremely versatile, and can readily account for various kinds of material nonlinearities. Also, these methods are usually successful in reproducing global trends with respect to some material/microstructural properties.

At the other end of the complexity scale lie full field methods, where the corrector problem is solved numerically, either by means of standard (finite elements, boundary elements) or devoted numerical techniques. Provided that the various sources of errors are kept under control (these sources are briefly listed in section 4.3.3), full-field methods can be considered as "exact"; they are however rather cumbersome. For example, classical finite elements require a conforming mesh, which can be difficult to produce for highly heterogeneous microstructures. Extended finite element techniques (X-FEM) devoted to heterogeneous materials have been proposed in order to overcome this limitation [Tra+11]. Execution of the simulation is also generally a challenge, since a large number of degrees of freedom is generally involved; this usually calls for the implementation of high-performance computing (HPC) techniques. Rather than resorting to general-purpose numerical tools, which are sometimes ill-suited to the task, various authors have proposed devoted methods, specifically tailored to solving the corrector problem. Owing to their flexibility, so-called "FFT-based techniques" ought to be singled out. Initially proposed by Moulinec and Suquet [MS94] and Moulinec and Suquet [MS98], these methods have gained in popularity from the early 2010s: nowadays, many research groups accross the world are actively involved in the development and application of such techniques.

Quite surprisingly, the middle-range of the complexity scale is not well populated. Morphologically representative patterns [BSZ96] aim at improving Eshelby-based estimates through a finer description of the microstructure. However, it should be emphasized that the microstructure considered in these approaches is an idealization of the true microstructure. Again, the correlations are not introduced explicitly.

For very specific microstructures, it is possible to devise extremely efficient full-field methods that take advantage of the specific geometry. Only two examples of such problem specific methods will be cited here. As a first example, the equivalent inclusion method [MM75] really ought to be considered as an "approximate" full-field method, as it would be highly impractical to let the discretization parameter (the order of the interpolating polynomials) grow to large values (this will be discussed in chapter 4, section 4.3). As a second example, the recent work of Cancés and collaborators [Can+18] stand out as a remarkable combination of various efficient numerical techniques for assemblies of spherical inhomogeneities. A modified corrector problem is reformulated as a boundary integral equation [Can+15], which is discretized with spherical harmonics. Domain decomposition and multipole expansions then allow for an efficient implementation of the solver.

Numerical homogenization techniques have so far been classified by degree of complexity. Another interesting classification relies on the nature of the input of the method.

Full field methods (even approximate) require *realizations* of the microstructure as an input. Within the framework of random homogenization, it is necessary to solve the corrector problem for a large number of such realizations (statistical volume elements). Averaging the apparent properties of these statistical volume elements then delivers an estimate of the effective properties of the random heterogeneous material under consideration.

Conversely, we will call *statistical* those methods that deliver estimates of the macroscopic

properties from statistical descriptors of the microstructure. From this perspective, mean field/effective field methods, Hashin–Shtrikman bounds, higher order bounds [BM66]; [McC70]; [Mil81]; [Mil82]; [MP82] and exact series expansions[Tor97] can all be seen as statistical.

Even if they generally deliver estimates rather than approximations with controlled numerical error, I personally tend to favor statistical approaches over full-field methods. I do think that the former offer a deeper insight into the connections between microstructure and macroscopic properties. Indeed, it is fairly easy within this framework to vary some microstructural parameters and observe the results on the macroscopic properties. Full-field methods, on the other hand, result in an extremely rich output, but they also require a rich input, to the extent that it is sometimes difficult to filter out this massive quantity of data. Identifying what details of the microstructure had the most significant impact on the macroscopic properties is not a trivial task within the framework of full-field methods. However, for many applications, full-field simulations are in fact the only option, and both classes of methods should really be seen as serving different purposes.

I think it is clear from the above discussion why the development of improved statistical methods has always been the focus of my research. My goal is the derivation of statistical estimates of the macroscopic properties that would account for a more detailed statistical description of the microstructure than standard, Eshelby-based methods, while remaining less costly than full-field methods. I also do not want to introduce any idealization of the microstructure. To do so, I soon selected the Hashin–Shtrikman principle [HS62b] as the appropriate, systematic framework, for two main reasons.

First, this variational principle is extremely flexible, since *any* trial stress-polarization is admissible[7]. This is at odds with the more classical minimum potential and complementary energy principles, for which admissibility conditions are sometimes difficult to fulfill with the rather simple trial fields that are required by theoretical derivations.

Second, the estimates resulting from this principle can be worked out without any idealization/simplification of the microstructure. The *exact* geometry is taken into account (see for example reference [Wil77]), while the quality of the approximation is controlled by the richness of the trial stress-polarization. Under some mild additional assumptions, this allows the derivation of rigorous bounds on the true effective properties.

The celebrated Hashin–Shtrikman bounds [HS62a] on the effective elastic moduli of isotropic heterogeneous materials are a classical example of how the variational Hashin–Shtrikman principle can be applied to derive bounds/estimates on the macroscopic properties. These bounds result from selecting the most simple (phase-wise constant) trial stress-polarization. Somewhat naively, I imagined that I only had to apply the same principle with more complex (enriched) trial stress-polarizations to improve on these estimates/bounds. However, selecting a "good" trial stress-polarization turned out to be rather difficult. In other words, the classical Hashin–Shtrikman bounds are extremely robust (difficult to improve upon).

Fairly recently, I have devised a general framework to account for a local description of the microstructure within the framework of the Hashin–Shtrikman principle (see chapter 3,

[7] The stress-polarization will be defined more precisely in chapter 2, section 2.3. Suffice it to say for the time being that the trial field that is involved in the variational principle of Hashin and Shtrikman is a second-rank, symmetric tensor field that is called "stress-polarization".

section 3.2), with fairly good prospects.

My quest for improved bounds on the macroscopic properties has been rather frustrating so far. Meanwhile, I soon realized that the Hashin–Shtrikman principle could also be used in a numerical setting, for the derivation of numerical methods. Quite surprisingly, this research topic (although not the one I favored initially) turned out to be the area where I have been most productive.

Although extremely simple, the idea was rather original, as I believe I was the first to apply Galerkin-like discretizations to the variational form of the Lippmann–Schwinger equation (which is equivalent to the Hashin–Shtrikman principle, as will be discussed in chapter 2, section 2.3). Using an appropriate discretization of the trial stress-polarization delivers an estimate of the true stress-polarization at equilibrium. I have explored two possible discretization schemes: voxel-wise constant stress-polarizations, and stress-polarizations that are polynomial over each inhomogeneity.

The former choice allowed me to revisit FFT-based techniques initially introduced by Moulinec and Suquet [MS94] and Moulinec and Suquet [MS98], as discussed in chapter 4, section 4.2. A significant part of my research has been devoted to this topic. I was able to propose a formulation that results in rigorous bounds on the apparent properties. I also clarified the distinction between discretization of the underlying continuous integral equation, and solution to the discrete problem. Introducing this separation of concerns allowed me to prove that FFT-based techniques actually converge to the desired solution upon refining the grid, and to replace the fixed-point iterations initially proposed by Moulinec and Suquet with more efficient Krylov-subspace iterative linear solvers. In order to reduce Gibbs-like spurious oscillations in the numerical solution, I also introduced so-called filtered discrete Green operators. My recent work in this area is devoted to the development of a posteriori error estimators for FFT-based homogenization techniques.

The latter choice led to a variational form of the classical equivalent inclusion method, initially proposed by Moschovidis and Mura [MM75]. In that case, the variational setting is clearly superior to the classical approach based on collocation, as will be discussed in chapter 4, section 4.3. As a by-product of this work, I was also able to propose a rigorous mathematical justification of the approximation of the Green operator for strains introduced heuristically by Willis [Wil77] (see chapter 3, section 3.1).

***

To close this section on my research activities, I would like to mention topics related to image analysis and 3D imaging techniques. As already mentioned in section 1.2, these topics represented a significant part of my PhD work. Since the defense of my PhD however, I have only marginally contributed to this field, which will therefore not be presented in detail in this report. However, I do want to dedicate a more significant share of my (post-Habilitation) research time to these topics (as will be discussed in chapter 5).

Regarding 3D imaging, first. I recently took an active part in the PhD work of M.H. Khalili, who developed the so-called *discrete digital projection correlation* method (D-DPC). This method allows the identification of the rigid body motion of each individual grain in a granular material. The main asset of the proposed technique is the fact that a limited number of radio-

graphs of the current configuration suffice to compute estimate these motions. This allows for rapid acquisition (even in a laboratory setting). The price to pay is a relatively high computational cost, requiring the use of HPC techniques. M.H. Khalili was able to prove that the method had the potential to deliver accurate results. I would like to pursue this work towards more realistic experimental conditions (involving a large number of grains).

During the course of the PhD work of M.H. Khalili, we also questioned some of the fundamental asumptions that standard reconstruction techniques rely upon. We were able to show that these simplifying asumptions could have a significant impact on the accuracy of the reconstruction. I would like to explore these issues more thoroughly.

Regarding image analysis, now. With P. Levitz, we proposed a technique allowing to estimate the small-angle scattering spectrum of a material from a transmission image (radiograph). This technique is very simple and requires minimal preparation of the image (thus inducing only a limited loss of information). It allows to compare two seemingly very different imaging techniques[8] that operate at complementary resolutions. However, this technique is not devoid of artefacts, that we would like to investigate theoretically. Meanwhile, I have recently been involved in a joint work with C.A. Davy[9], P. Levitz[10] and L. Michot[10] for the application of this technique to cementitious materials.

To conclude this brief section on image analysis, I should like to mention that I was the main organizer in july 2016 of a workshop on *Imaging of Construction Materials and Geomaterials*, which gathered about 90 participants at École des Ponts ParisTech. Following this workshop, I have been asked by the editor in chief of *Cement and Concrete Research* to coordinate a review paper on X-ray tomography of cementitious materials, for which I will be more specifically in charge of writing the theoretical sections.

1.4 Teacher at École des Ponts ParisTech

My teaching activities are extremely dear to me. I like preparing courses and classes, thinking of the "best" way to introduce complex notions, writing lecture notes, interacting with students… and feeling that maybe they learned something from me!

I was fortunate enough to be in a position to teach immediatly after my graduation from École des Ponts ParisTech in 2003. I should like to take the opportunity to thank Prof. P. Bisch[11], with whom I have been working for so many years, as well as Prof. A. Ehrlacher[12]. At that time, both placed their trust in a young engineer with no teaching experience whatsoever!

Owing to my initial professional activities, most courses I took part to are related to structural mechanics: *Structural Mechanics*, *Shells & Advanced Structures*, *Towards Structural Mechanics*, *Introduction to the Dynamics and Stability of Mechanical Systems*, …, all at the

[8] It should be recalled that transmission imaging operates in the real space, while small angle scattering operates in the Fourier space.

[9] Laboratoire de Mécanique de Lille (LML, FRE CNRS 3723), L2MGC EA 4114, Université de Cergy-Pontoise, Centrale Lille, Villeneuve d'Ascq, France

[10] See footnote 5 in the present chapter.

[11] EGIS Industries

[12] Head of the Department of Mechanical Engineering and Materials Science at École des Ponts ParisTech

MEng level. After I received my PhD degree, I also got involved in two courses on *Imaging of Random Heterogeneous Materials* (at the MSc level). In these courses, I was in charge of the following topics: statistical tools for the description of random heterogeneous media, numerical scale bridging, image analysis, small-angle scattering of X-rays.

Of course, it is impossible to sum up in a few lines all the personal lessons I learned from these multiple teaching experiences. I will therefore focus on my longest experience within the course *Shells & Advanced Structures*, as it might have an influence on my future research activities as well.

The course on *Shells & Advanced Structures* mainly addresses the theory of plates and shells, although some other advanced notions such as beams with high curvature or Vlasov's theory of torsion might also be touched upon. I have been involved in this course (which is taught by Prof. P. Bisch) since 2003. I am in charge of half of the 12 sessions of 2.5 hours (both lectures and tutorials). Owing to its reputation of being difficult, the students that enrol for this optional course are usually highly motivated, which results in an extremely agreeable atmosphere. However, I must own that some students are dispirited by the mathematical difficulties induced by the use of curvilinear coordinates.

My long-term involvement in this course has naturally resulted in a very rich experience, which allows me to better anticipate the questions of the students, and select the problem-solving techniques that I find most accessible. To cite but one exemple, I never invoke during tutorial sessions the general equilibrium equations of shells in curvilinear coordinates. Rather, I derive these equations from the principle of virtual work for each new problem specifically. Such approach indeed allows to account at a very early stage for the simplifications that might be induced by the geometry of the shell under consideration (cylinder, sphere, …).

Meanwhile, it is only too natural that I developed my own vision of how a course on the theory of plates and shells might be taught. For example, I would favor an *intrinsic* formulation. Indeed, the students are usually still struggling with covariant and contravariant indices at the end of the 12 sessions, while they are much more comfortable with intrinsic notations (to which they were introduced during the course on *Continuum Mechanics* at École des Ponts ParisTech). As another example, rather than the classical displacement-based approach, I would introduce the various theories through a stress-based approach. Indeed, the former leads to the concurrent invocation of plane stress *and* plane strain hypotheses (both being of course mutually exclusive!), while the latter does not result in such contradictions.

Besides the pedagogical aspects, I have also benefited from this experience at the theoretical level. Indeed, I have investigated for my own sake such difficult issues as boundary layers and the boundary conditions for the Kirchhoff–Love model or the formulation of plate and shell finite elements. I have a fairly up-to-date knowledge of the theoretical literature on (homogeneous) plates and shells, to the extent that I am now considering investigating these topics at research level (see chapter 5) and get recognition from the academic world. I have recently been asked by K. Sab[13] to be the coauthor of three chapters on the classical theories of plates in the *Encyclopædia of Mechanics* to be published by Springer; this certainly constitutes a first step towards this goal.

[13] See footnote 4 in the present chapter.

1.5 Outline of this report

For the sake of conciseness and coherence, this document is focused on the various applications I have proposed of the Lippmann–Schwinger equation and Hashin–Shtrikman principle to capture the connection between microstructure and macroscopic properties. The structure of this document is briefly overviewed below; for each section, my relevant publications are also listed. Although the topics discussed in this document represent the major part of my post-PhD research work, such selection means that some other works have also been purposefuly left out (see references [BL13]; [Bri+12]; [Kha+17a]; [Kha+17b]; [Kha+17c]; [May+16]). Some of these topics will however be briefly discussed in chapter 5.

Chapter 2 sets up the general framework for this report. It gives a brief overview of homogenization and classical polarization techniques (namely, the Lippmann–Schwinger equation and the Hashin–Shtrikman principle). This chapter is not intended as a treatise on these topics. It is rather used to define the essential tools and notations that are to be used throughout this document. Being essentially reference material, this chapter is not directly connected to any of my publications.

Chapter 3 then discusses applications of the Hashin–Shtrikman principle in a (semi-) analytical setting. This chapter describes a few applications that fall into the category of statistical methods as defined in section 1.3 of the present chapter. It opens with the classical Hashin–Shtrikman bounds (see section 3.1) the derivation of which is recalled so as to serve as a basis for the derivation of improved bounds. More importantly, section 3.1 discusses the approximation of the fourth-rank Green operator of a bounded domain, for which I proposed a mathematical justification in reference [BSD13]. The (hopeless?) quest for improved bounds is discussed in section 3.2, which presents a possible approach that was initiated in reference [Bri17b]. The chapter then closes with three applications for which I was indeed able to propose Hashin–Shtrikman like bounds on the macroscopic properties, namely nanocomposites (see section 3.3 and references [BDK10a]; [BDK10b]), eigenstressed materials (see section 3.4 and references [BG17]; [BG18]) and stress-gradient materials (see section 3.5 and references [Tra+18a]; [Tra+18b]).

Chapter 4 is the numerical counterpart of the previous chapter. It discusses two strategies for the Galerkin discretization of the Lippmann–Schwinger equation (see section 4.1). The first strategy relies on a discretization of the trial stress-polarization over a uniform, cartesian grid in a periodic setting (see section 4.2, references [BD10]; [BD12]; [Bri17a] and some use-cases in references [BD14]; [Tra+16]). It results in a variational form of the celebrated FFT-based methods introduced by Moulinec and Suquet. The second strategy uses (for simple matrix–inclusions microstructures) trial stress-polarizations that are polynomial over each inclusion (see section 4.3 and references [BDS13]; [BDS14]). This approach leads to a variational form of the equivalent inclusion method of Moschovidis and Mura.

Finally, chapter 5 offers a general conclusion and some perspectives to the work presented in this report. It also outlines the research topics I would like to investigate and that define my vision of my research work for the next few years.

Chapter 2

General framework

This chapter introduces the general framework that is to apply throughout this report. Rather than a self-contained reference work on heterogeneous materials, it should be understood as a brief list of known definitions and essential mathematical results that will be invoked in chapters 3 and 4. Section 2.1 gives a short and practical overview of homogenization within the framework of linear elasticity. Then, section 2.2 introduces the fourth-rank Green operator for various types of boundary conditions. This operator is the essential tool underlying polarization techniques, which are described in section 2.3 and will be extensively used in the subsequent chapters.

2.1 A brief overview of homogenization

The present section defines some concepts that are essential to the homogenization of linearly elastic, random heterogeneous materials. A mathematical description of the microstructure of such materials is proposed in section 2.1.1. Sections 2.1.2 and 2.1.4 then address the determination of the apparent and effective properties of statistical and representative volume elements.

2.1.1 Mathematical description of the microstructure of heterogeneous materials

We consider a heterogeneous material that occupies the geometrical domain $\Omega \subset \mathbb{R}^d$ ($d = 2, 3$). For any local quantity $\mathcal{Q}$, $\langle \mathcal{Q} \rangle$ denotes its volume average over Ω

$$\langle \mathcal{Q} \rangle = \frac{1}{|\Omega|} \int_{\mathbf{x} \in \Omega} \mathcal{Q}(\mathbf{x}) \, \mathrm{d}V_{\mathbf{x}}. \tag{2.1}$$

Most of this report is devoted to linear elasticity; $\mathbf{C}(\mathbf{x})$ denotes the local stiffness tensor at $\mathbf{x} \in \Omega$. The linear elastic stress-strain relationship then reads for $\mathbf{x} \in \Omega$: $\boldsymbol{\sigma}(\mathbf{x}) = \mathbf{C}(\mathbf{x}) : \boldsymbol{\varepsilon}(\mathbf{x})$, where $\boldsymbol{\sigma}$ (resp. $\boldsymbol{\varepsilon}$) denotes the stress (resp. strain) field.

So-called *N-phase materials* are a specific class of heterogeneous materials. They are defined by the regions $\Omega_1, \ldots, \Omega_N \subset \Omega$ occupied by phases $1, \ldots, N$, or, equivalently, by the indicator functions $\chi_1, \ldots, \chi_N$ of these phases.

Unless otherwise stated, Greek indices always refer to phases, and sums over Greek indices always run over the whole range $1, \ldots, N$. Obviously, the $\chi_1, \ldots, \chi_N$ satisfy the partition of

unity property ($\sum_\alpha \chi_\alpha = 1$). For any local quantity $\mathcal{Q}$, $\langle \mathcal{Q} \rangle_\alpha$ denotes its volume average over phase $\alpha = 1, \dots, N$

$$\langle \mathcal{Q} \rangle_\alpha = \frac{1}{|\Omega_\alpha|} \int_{\mathbf{x} \in \Omega_\alpha} \mathcal{Q}(\mathbf{x}) \, \mathrm{d}V_\mathbf{x}, \tag{2.2}$$

and we obviously have $\langle \mathcal{Q} \rangle = \sum_\alpha f_\alpha \langle \mathcal{Q} \rangle_\alpha$, where $f_\alpha = |\Omega_\alpha|/|\Omega|$ denotes the volume fraction of phase $\alpha = 1, \dots, N$.

Within the framework of linear elasticity, $\mathbf{C}_\alpha$ denotes the elastic stiffness of phase $\alpha = 1, \dots, N$, so that for a N-phase material, $\mathbf{C} = \sum_\alpha \chi_\alpha \mathbf{C}_\alpha$. The local stress-strain relationship now reads, for $\mathbf{x} \in \Omega_\alpha$: $\boldsymbol{\sigma}(\mathbf{x}) = \mathbf{C}_\alpha : \boldsymbol{\varepsilon}(\mathbf{x})$.

2.1.2 Apparent and effective properties – Statistical and representative volume elements

For statistically homogeneous and ergodic microstructures, it is well-known that the effective properties are retrieved from the solution to a boundary value problem posed on a *infinite* domain. This is of course highly impractical. Instead, we first compute the *apparent* stiffness $\mathbf{C}^{\mathrm{app}}(\Omega)$ (to be defined below) of a finite volume element Ω, and estimate the *effective* stiffness as the limit of the apparent stiffness for large volume elements Ω

$$\mathbf{C}^{\mathrm{eff}} = \lim_{|\Omega| \to +\infty} \mathbf{C}^{\mathrm{app}}(\Omega), \tag{2.3}$$

provided that appropriate boundary conditions are applied to $\partial\Omega$. In practice, due to the randomness of the microstructure, $\mathbf{C}^{\mathrm{app}}(\Omega)$ is a random variable that depends not only on the geometry of the domain $\Omega \subset \mathbb{R}^d$, but also on the realization of the microstructure under consideration. It is then customary to take the ensemble average in equation (2.3)

$$\mathbf{C}^{\mathrm{eff}} = \lim_{|\Omega| \to +\infty} \mathbb{E}[\mathbf{C}^{\mathrm{app}}(\Omega)]. \tag{2.4}$$

In turn, this ensemble average is evaluated empirically in a standard Monte-Carlo setting. To emphasize the random nature of the apparent stiffness, the domain Ω will be called, following Ostoja-Starzewski [Ost06], a *Statistical Volume Element* (SVE). The SVE is considered as a *Representative Volume Element* (RVE) when the fluctuations of its apparent stiffness are below a user-defined threshold. In that case, the apparent stiffness of the RVE (only one realization) delivers an accurate estimate of the effective stiffness.

We are now in a position to define the apparent stiffness of the SVE Ω as the linear operator that maps the average strain $\langle \boldsymbol{\varepsilon} \rangle$ to the average stress $\langle \boldsymbol{\sigma} \rangle$

$$\langle \boldsymbol{\sigma} \rangle = \mathbf{C}^{\mathrm{app}}(\Omega) : \langle \boldsymbol{\varepsilon} \rangle, \tag{2.5}$$

where $\boldsymbol{\varepsilon}$ and $\boldsymbol{\sigma}$ are the local strains and stresses that solve the so-called *corrector problem*

$$\mathbf{div}\, \boldsymbol{\sigma} = \mathbf{0}, \quad \boldsymbol{\sigma} = \mathbf{C} : \boldsymbol{\varepsilon}, \quad \boldsymbol{\varepsilon} = \boldsymbol{\epsilon}[\mathbf{u}], \tag{2.6}$$

where $\epsilon[\mathbf{u}]$ denotes the symmetric part of the gradient of the displacement $\mathbf{u}$.

The above field equations (in Ω) are complemented with appropriate boundary conditions (on $\partial\Omega$), to be discussed below. It should first be observed that for homogenization purposes, the exact displacement $\mathbf{u}$ from which the strain $\boldsymbol{\varepsilon}$ derives does not matter (provided that it exists!). This is emphasized by introducing the spaces of compatible ($\mathscr{E}$) and divergence-free ($\mathscr{S}$), second-rank, symmetric, tensor fields

$$\boldsymbol{\varepsilon} \in \mathscr{E}(\Omega) \iff \boldsymbol{\varepsilon} = \epsilon[\mathbf{u}] \text{ for some } \mathbf{u} \quad \text{and} \quad \boldsymbol{\sigma} \in \mathscr{S}(\Omega) \iff \mathbf{div}\,\boldsymbol{\sigma} = \mathbf{0}, \tag{2.7}$$

where the above differential operators should be understood in the sense of generalized functions. Equations (2.6) may then be rewritten as follows

$$\text{Find } \boldsymbol{\varepsilon} \in \mathscr{E}(\Omega) \text{ and } \boldsymbol{\sigma} \in \mathscr{S}(\Omega) \text{ such that } \boldsymbol{\sigma} = \mathbf{C} : \boldsymbol{\varepsilon}, \tag{2.8}$$

or, equivalently

$$\text{Find } \boldsymbol{\varepsilon} \in \mathscr{E}(\Omega) \text{ such that } \mathbf{C} : \boldsymbol{\varepsilon} \in \mathscr{S}(\Omega). \tag{2.9}$$

For problem (2.9) to be well-posed, $\boldsymbol{\varepsilon}$ and/or $\boldsymbol{\sigma}$ should in fact be seeked in subspaces of $\mathscr{E}(\Omega)$ and $\mathscr{S}(\Omega)$, respectively. This is discussed in section 2.1.3 below, where the classical Dirichlet, Neumann and periodic boundary conditions are introduced.

Remark 2.1. *Equation (2.5) should really be understood as a series of $d(d+1)/2$ calculations (with linearly independent prescribed macroscopic strains or stresses).*

Remark 2.2. *For the sake of clarity, functional spaces will not be specified in the remainder of this work. It should however be understood that elements of $\mathscr{E}(\Omega)$ and $\mathscr{S}(\Omega)$ are at least component-wise square integrable. In physical terms, this means that only finite energy strains and stresses will be considered.*

It will be useful to introduce the space $\mathscr{T}_2(\Omega)$ of symmetric, second-rank tensors with square integrable components. Then, $\mathscr{E}(\Omega) \subset \mathscr{T}_2(\Omega)$ and $\mathscr{S}(\Omega) \subset \mathscr{T}_2(\Omega)$.

2.1.3 Computation of apparent properties: boundary conditions

In this section, various classical boundary conditions that must complement the field equations (2.6) are listed. For a finite-size SVE Ω, each of these boundary conditions defines a different apparent stiffness $\mathbf{C}^{\text{app}}(\Omega)$. Consistency of these definitions (as $|\Omega| \to +\infty$) is discussed in section 2.1.4.

Essential (Dirichlet) boundary conditions We introduce the subspace $\mathscr{E}^{\text{ess}}(\Omega) \subset \mathscr{E}(\Omega)$ of compatible strain fields with essential (Dirichlet) boundary conditions

$$\boldsymbol{\varepsilon} \in \mathscr{E}^{\text{ess}}(\Omega) \iff \boldsymbol{\varepsilon} = \epsilon[\mathbf{u}] \text{ for some } \mathbf{u} \text{ such that } \mathbf{u}|_{\partial\Omega} = \mathbf{0}, \tag{2.10}$$

and it is observed that $\langle \boldsymbol{\varepsilon} \rangle = \mathbf{0}$ for all $\boldsymbol{\varepsilon} \in \mathscr{E}^{\text{ess}}(\Omega)$. The apparent stiffness $\mathbf{C}^{\text{ess}}(\Omega)$ is then defined from the solution to the following problem

$$\text{Find } \boldsymbol{\varepsilon} \in \overline{\boldsymbol{\varepsilon}} + \mathscr{E}^{\text{ess}}(\Omega) \text{ such that } \mathbf{C} : \boldsymbol{\varepsilon} \in \mathscr{S}(\Omega), \tag{2.11}$$

where $\overline{\boldsymbol{\varepsilon}}$ is a constant (prescribed) strain, which coincides with the macroscopic strain: $\langle \boldsymbol{\varepsilon} \rangle = \overline{\boldsymbol{\varepsilon}}$. The macroscopic stress is then computed a posteriori as the volume average $\langle \boldsymbol{\sigma} \rangle$, from which the apparent stiffness is deduced: $\langle \boldsymbol{\sigma} \rangle = \mathbf{C}^{\text{ess}}(\Omega) : \overline{\boldsymbol{\varepsilon}}$.

It should be noted that the Dirichlet boundary conditions thus defined are also known as *Kinematic Uniform Boundary Conditions* (KUBC), see for example reference [Kan+03].

Natural (Neumann) boundary conditions We now introduce the following subspace $\mathcal{S}^{\text{nat}}(\Omega) \subset \mathcal{S}(\Omega)$ of divergence-free stress fields with natural (Neumann) boundary conditions

$$\boldsymbol{\sigma} \in \mathcal{S}^{\text{nat}}(\Omega) \iff \boldsymbol{\sigma} \in \mathcal{S}(\Omega) \quad \text{and} \quad \boldsymbol{\sigma} \cdot \mathbf{n} = \mathbf{0} \text{ on } \partial\Omega, \tag{2.12}$$

where $\mathbf{n}$ denotes the outer normal to $\partial\Omega$. It should be noted that $\langle \boldsymbol{\sigma} \rangle = \mathbf{0}$ for all $\boldsymbol{\sigma} \in \mathcal{S}^{\text{nat}}(\Omega)$. The solution to the following problem defines the apparent compliance $\mathbf{S}^{\text{nat}}(\Omega)$

$$\text{Find } \boldsymbol{\sigma} \in \overline{\boldsymbol{\sigma}} + \mathcal{S}^{\text{nat}}(\Omega) \text{ such that } \mathbf{C}^{-1} : \boldsymbol{\sigma} \in \mathcal{E}(\Omega), \tag{2.13}$$

where $\overline{\boldsymbol{\sigma}}$ is a prescribed stress, which coincides with the macroscopic stress: $\langle \boldsymbol{\sigma} \rangle = \overline{\boldsymbol{\sigma}}$. The apparent compliance $\mathbf{S}^{\text{nat}}(\Omega)$ maps the prescribed stress to the macroscopic strain $\langle \boldsymbol{\varepsilon} \rangle$ (which is computed a posteriori): $\langle \boldsymbol{\varepsilon} \rangle = \mathbf{S}^{\text{nat}}(\Omega) : \overline{\boldsymbol{\sigma}}$. The apparent stiffness is then obtained through inversion: $\mathbf{C}^{\text{nat}}(\Omega) = [\mathbf{S}^{\text{nat}}(\Omega)]^{-1}$.

It is again observed that the Neumann boundary conditions thus defined are also known as *Static Uniform Boundary Conditions* (SUBC), see for example reference [Kan+03].

Periodic Boundary Conditions The SVE Ω is a rectangular prism $\Omega = (0, L_1) \times \ldots \times (0, L_d)$; we define the subspaces $\mathcal{E}^{\text{per}}(\Omega)$ and $\mathcal{S}^{\text{per}}(\Omega)$ of Ω-periodic, compatible and divergence-free strain and stress fields

$$\boldsymbol{\varepsilon} \in \mathcal{E}^{\text{per}}(\Omega) \iff \boldsymbol{\varepsilon} = \boldsymbol{\epsilon}[\mathbf{u}] \text{ for some } \Omega\text{-periodic } \mathbf{u}, \tag{2.14}$$

$$\boldsymbol{\sigma} \in \mathcal{S}^{\text{per}}(\Omega) \iff \boldsymbol{\sigma} \in \mathcal{S}(\Omega) \quad \text{and} \quad \boldsymbol{\sigma} \cdot \mathbf{e}_i \text{ is } \Omega\text{-periodic for } i = 1, \ldots, d. \tag{2.15}$$

It should ne noted that the second condition in (2.15) is usually written "$\boldsymbol{\sigma} \cdot \mathbf{n}$ is skew-periodic". I find this terminology confusing, as the outer normal (thus the traction) is not uniquely defined (its direction depends on whether the cell standing on the "left" or "right" of the edge is considered). It is further observed that $\langle \boldsymbol{\varepsilon} \rangle = \mathbf{0}$ for all $\boldsymbol{\varepsilon} \in \mathcal{E}^{\text{per}}(\Omega)$. The corrector problem with periodic boundary conditions reads

$$\text{Find } \boldsymbol{\varepsilon} \in \overline{\boldsymbol{\varepsilon}} + \mathcal{E}^{\text{per}}(\Omega) \text{ such that } \mathbf{C} : \boldsymbol{\varepsilon} \in \mathcal{S}^{\text{per}}(\Omega), \tag{2.16}$$

where $\overline{\boldsymbol{\varepsilon}}$ is a prescribed strain, which coincides with the macroscopic strain: $\langle \boldsymbol{\varepsilon} \rangle = \overline{\boldsymbol{\varepsilon}}$. Similarly to the apparent stiffness for essential boundary conditions, the apparent stiffness $\mathbf{C}^{\text{per}}(\Omega)$ is then found from the following identity: $\langle \boldsymbol{\sigma} \rangle = \mathbf{C}^{\text{per}}(\Omega) : \overline{\boldsymbol{\varepsilon}}$.

2.1.4 Discussion of the various boundary conditions

It can be shown that the boundary conditions stated in section 2.1.2 all comply with the Hill–Mandel lemma. In other words, $\langle \boldsymbol{\sigma} : \boldsymbol{\varepsilon} \rangle = \langle \boldsymbol{\sigma} \rangle : \langle \boldsymbol{\varepsilon} \rangle$, provided that either of the following conditions is fullfilled

1. $\boldsymbol{\varepsilon} \in \overline{\boldsymbol{\varepsilon}} + \mathscr{E}^{\text{ess}}(\Omega)$ and $\boldsymbol{\sigma} \in \mathscr{S}(\Omega)$,
2. $\boldsymbol{\varepsilon} \in \mathscr{E}(\Omega)$ and $\boldsymbol{\sigma} \in \overline{\boldsymbol{\sigma}} + \mathscr{S}^{\text{nat}}(\Omega)$,
3. $\boldsymbol{\varepsilon} \in \overline{\boldsymbol{\varepsilon}} + \mathscr{E}^{\text{per}}(\Omega)$ and $\boldsymbol{\sigma} \in \mathscr{S}^{\text{per}}(\Omega)$,

where $\overline{\boldsymbol{\varepsilon}}$ and $\overline{\boldsymbol{\sigma}}$ are constant, second-rank, symmetric tensors. The Hill–Mandel lemma in turn has two important consequences. First, it shows that all three apparent stiffnesses $\mathbf{C}^{\text{ess}}(\Omega)$, $\mathbf{C}^{\text{nat}}(\Omega)$ and $\mathbf{C}^{\text{per}}(\Omega)$ are *symmetric*, fourth-rank tensors. Second, it is an essential ingredient to prove that $\mathbf{C}^{\text{ess}}(\Omega)$, $\mathbf{C}^{\text{nat}}(\Omega)$ and $\mathbf{C}^{\text{per}}(\Omega)$ converge to the effective stiffness $\mathbf{C}^{\text{eff}}$ as the size of the SVE Ω grows to infinity (under the assumption of ergodicity, see reference [Sab92]). To close this section, it should be observed that

$$\mathbf{C}^{\text{nat}}(\Omega) \leq \mathbf{C}^{\text{eff}} \leq \mathbf{C}^{\text{ess}}(\Omega), \tag{2.17}$$

for all SVE Ω [Hue90], where the above inequalities should be understood in the sense of quadratic forms. The apparent stiffness associated to periodic boundary conditions does not provide a bound on the effective stiffness, although it has been observed that $\mathbf{C}^{\text{per}}(\Omega)$ converges faster to $\mathbf{C}^{\text{eff}}$ than $\mathbf{C}^{\text{ess}}(\Omega)$ and $\mathbf{C}^{\text{nat}}(\Omega)$ [Kan+03].

***

It will be shown in section 2.3 that the boundary-value problems that define the various apparent stiffnesses can be reformulated as an integral equation (the Lippmann–Schwinger equation). Its kernel is the fourth-rank Green operator, that we now proceed to define.

2.2 The fourth-rank Green operator

For reasons that will become clearer in section 2.3.1, it is convenient to consider the following problem in Ω

$$\mathbf{div}\, \boldsymbol{\sigma} = \mathbf{0}, \quad \boldsymbol{\sigma} = \mathbf{C}_0 : \boldsymbol{\varepsilon} + \boldsymbol{\varpi}, \quad \boldsymbol{\varepsilon} = \boldsymbol{\epsilon}[\mathbf{u}], \tag{2.18}$$

where $\mathbf{C}_0$ denotes the elastic stiffness of a homogeneous material, and $\boldsymbol{\varpi}$ is a spatially varying eigenstress. The above problem is formulated on the same geometrical domain Ω as problem (2.6) that defines the apparent stiffness of the SVE. It is not well-posed, since the boundary conditions have not yet been specified.

Although the microstructure is considerably simpler than for problem (2.6) (it is homogeneous!), problem (2.18) remains complex owing to the fact that the eigenstress is not uniform. However, it should be observed that this problem is linear; as such, the output (in particular, the strain $\boldsymbol{\varepsilon}$) depends linearly on the sole loading parameter $\boldsymbol{\varpi}$. Following Korringa [Kor73],

Kröner [Krö74], and Zeller and Dederichs [ZD73], we therefore introduce the linear operator $\boldsymbol{\Gamma}_0$ that maps the eigenstress onto the opposite of the strain: $\boldsymbol{\varepsilon} = -\boldsymbol{\Gamma}_0[\boldsymbol{\varpi}]$, the sign being purely conventional. $\boldsymbol{\Gamma}_0$ thus defined is the so-called fourth-rank Green operator for strains. Depending on the boundary conditions that complement problem (2.18), various such operators can be defined.

2.2.1 The fourth-rank Green operator for essential boundary conditions

Complementing problem (2.18) with the boundary condition $\mathbf{u}|_{\partial\Omega} = \mathbf{0}$ defines the Green operator $\boldsymbol{\Gamma}_0^{\text{ess}}$ for essential (Dirichlet) boundary conditions. In other words, $\boldsymbol{\varepsilon} = -\boldsymbol{\Gamma}_0^{\text{ess}}[\boldsymbol{\varpi}]$ is the unique solution to the problem

$$\text{Find } \boldsymbol{\varepsilon} \in \mathscr{E}^{\text{ess}}(\Omega) \text{ such that } \mathbf{C}_0 : \boldsymbol{\varepsilon} + \boldsymbol{\varpi} \in \mathscr{S}(\Omega). \tag{2.19}$$

2.2.2 The fourth-rank Green operator for periodic boundary conditions

It should be observed that the above definition of $\boldsymbol{\Gamma}_0^{\text{ess}}$ is purely formal, since a closed-form expression of this operator is in general not known. However, if the Dirichlet boundary conditions are replaced with periodic boundary conditions, then the resulting Green operator has an explicit expansion in Fourier space. More precisely, assuming that the domain Ω is a rectangular prism $\Omega = (0, L_1) \times \ldots \times (0, L_d)$, $\boldsymbol{\varepsilon} = -\boldsymbol{\Gamma}_0^{\text{per}}[\boldsymbol{\varpi}]$ is the unique solution to the problem

$$\text{Find } \boldsymbol{\varepsilon} \in \mathscr{E}^{\text{per}}(\Omega) \text{ such that } \mathbf{C}_0 : \boldsymbol{\varepsilon} + \boldsymbol{\varpi} \in \mathscr{S}^{\text{per}}(\Omega). \tag{2.20}$$

In the above problem, all mechanical fields can be expanded as Fourier series [Suq90]. In particular

$$\boldsymbol{\varepsilon}(\mathbf{x}) = -\boldsymbol{\Gamma}_0^{\text{per}}[\boldsymbol{\varpi}](\mathbf{x}) = -\sum_{\mathbf{k}\in\mathbb{Z}^d} \exp\Big[2\mathrm{i}\pi\Big(\frac{k_1 x_1}{L_1} + \cdots + \frac{k_d x_d}{L_d}\Big)\Big]\tilde{\boldsymbol{\Gamma}}_0^{\text{per}}(\mathbf{k}) : \tilde{\boldsymbol{\varpi}}_{\mathbf{k}}, \tag{2.21}$$

where $\tilde{\boldsymbol{\varpi}}_{\mathbf{k}}$ is the $\mathbf{k}$-th Fourier coefficient of the periodic eigenstress $\boldsymbol{\varpi}$

$$\tilde{\boldsymbol{\varpi}}_{\mathbf{k}} = \frac{1}{L_1 \ldots L_d} \int_{\mathbf{x}\in\Omega} \exp\Big[-2\mathrm{i}\pi\Big(\frac{k_1 x_1}{L_1} + \cdots + \frac{k_d x_d}{L_d}\Big)\Big]\boldsymbol{\varpi}(\mathbf{x})\,\mathrm{d}V_{\mathbf{x}}. \tag{2.22}$$

For isotropic reference materials, a closed-form expression of the Fourier coefficients $\tilde{\boldsymbol{\Gamma}}_0^{\text{per}}(\mathbf{k})$ of $\boldsymbol{\Gamma}_0^{\text{per}}$ is provided in appendix A, section A.1.

2.2.3 The fourth-rank Green operator of the whole space

The fourth-rank Green operator for strains $\boldsymbol{\Gamma}_0^{\infty}$ of the whole space is generally introduced as an approximation (for large domains Ω) of the Green operator $\boldsymbol{\Gamma}_0^{\text{ess}}$ of bounded domains with essential boundary conditions [PW95]; [Wil77]. This approximation will be further discussed

in chapter 3 (see in particular section 3.1). $\boldsymbol{\Gamma}_0^\infty$ is defined as the linear operator that maps $\boldsymbol{\varpi}$ to the unique solution $\boldsymbol{\varepsilon} = -\boldsymbol{\Gamma}_0^\infty[\boldsymbol{\varpi}]$ to the following problem

$$\text{Find } \boldsymbol{\varepsilon} \in \mathscr{E}(\mathbb{R}^d) \text{ such that } \mathbf{C}_0 : \boldsymbol{\varepsilon} + \boldsymbol{\varpi} \in \mathscr{S}(\mathbb{R}^d), \tag{2.23}$$

where it is observed that the finite-energy solution is indeed unique (see section 3.1.4). For isotropic materials, the resulting Green operator is classically decomposed into a singular part $\mathbf{P}_0$ and a translation invariant regular part $\boldsymbol{\Gamma}_0^\infty(\mathbf{r})$ [Bur07]; [KL08]; [Tor02]

$$\boldsymbol{\Gamma}_0^\infty[\boldsymbol{\varpi}](\mathbf{x}) = \mathbf{P}_0 : \boldsymbol{\varpi}(\mathbf{x}) + \lim_{\delta\to 0} \int_{\substack{\mathbf{y}\in\mathbb{R}^d \\ \|\mathbf{y}-\mathbf{x}\|\geq\delta}} \boldsymbol{\Gamma}_0^\infty(\mathbf{x}-\mathbf{y}) : \boldsymbol{\varpi}(\mathbf{y})\, \mathrm{d}V_{\mathbf{y}}, \tag{2.24}$$

where $\mathbf{P}_0$ denotes the Hill tensor of the d-dimensional sphere. Closed-form expressions of $\mathbf{P}_0$ and $\boldsymbol{\Gamma}_0^\infty(\mathbf{r})$ are provided in appendix A, section A.2.

2.2.4 Properties of the fourth-rank Green operators

Regardless of the geometry of Ω, the Green operator for strains $\boldsymbol{\Gamma}_0$ has a number of well-known properties, that are briefly recalled below. First, it is a self-adjoint linear operator; in other words

$$\langle \boldsymbol{\varpi}_1 : \boldsymbol{\Gamma}_0[\boldsymbol{\varpi}_2] \rangle = \langle \boldsymbol{\Gamma}_0[\boldsymbol{\varpi}_1] : \boldsymbol{\varpi}_2 \rangle, \tag{2.25}$$

for all eigenstresses $\boldsymbol{\varpi}_1$ and $\boldsymbol{\varpi}_2$ (as a result of Hill–Mandel's lemma). Then, for all $\boldsymbol{\varpi}$

$$\langle \boldsymbol{\Gamma}_0[\boldsymbol{\varpi}] \rangle = \mathbf{0} \quad \text{and} \quad \boldsymbol{\Gamma}_0[\mathbf{C}_0 : \boldsymbol{\Gamma}_0[\boldsymbol{\varpi}]] = \boldsymbol{\Gamma}_0[\boldsymbol{\varpi}], \tag{2.26}$$

the proof of equation $(2.26)_2$ can be found in reference [Wil01] (see also reference [MMS01] in the periodic case). Finally, for any *uniform* eigenstress $\boldsymbol{\varpi} = \text{const}$.

$$\boldsymbol{\Gamma}_0[\boldsymbol{\varpi}] = \mathbf{0}, \tag{2.27}$$

since $\mathbf{u} = \mathbf{0}$ is solution of problem (2.18) in that case.

***

We are now ready to introduce the Lippmann–Schwinger equation and its variational formulation as the Hashin–Shtrikman principle. These two tools constitute the foundations of the developments that will be presented in the subsequent chapters.

2.3 Polarization techniques for linear elasticity

2.3.1 The Lippmann–Schwinger equation

It is readily observed that the corrector problem with essential boundary conditions (2.11) is equivalent to

$$\text{Find } \boldsymbol{\varepsilon} \in \overline{\boldsymbol{\varepsilon}} + \mathscr{E}^{\text{ess}}(\Omega) \text{ and } \boldsymbol{\tau} \in \mathscr{T}_2(\Omega) \text{ such that } \begin{cases} \mathbf{C}_0 : \boldsymbol{\varepsilon} + \boldsymbol{\tau} \in \mathscr{S}(\Omega), \\ \boldsymbol{\tau} = (\mathbf{C} - \mathbf{C}_0) : \boldsymbol{\varepsilon}, \end{cases} \tag{2.28}$$

where a new unknown, the so-called *stress-polarization* $\boldsymbol{\tau}$ (second-rank, symmetric tensor with square-integrable components) has been introduced. Equation $(2.28)_1$ shows that the stress-polarization plays the role of an eigenstress. However, this eigenstress is not free, since it is related to the actual strain $\boldsymbol{\varepsilon}$ through equation $(2.29)_2$. We therefore will purposely use different notations for eigenstresses ($\boldsymbol{\varpi}$) and stress-polarizations ($\boldsymbol{\tau}$). The Green operator $\boldsymbol{\Gamma}_0^{\text{ess}}$ can be used to express the solution to equation $(2.28)_1$, leading to the equivalent formulation

$$\text{Find } \boldsymbol{\varepsilon}, \boldsymbol{\tau} \in \mathcal{T}_2(\Omega) \text{ such that } \boldsymbol{\varepsilon} = \overline{\boldsymbol{\varepsilon}} - \boldsymbol{\Gamma}_0^{\text{ess}}[\boldsymbol{\tau}] \quad \text{and} \quad \boldsymbol{\tau} = (\mathbf{C} - \mathbf{C}_0) : \boldsymbol{\varepsilon}. \tag{2.29}$$

It should be observed that equation (2.29) automatically implies that $\boldsymbol{\varepsilon} \in \overline{\boldsymbol{\varepsilon}} + \mathcal{E}^{\text{ess}}(\Omega)$. The unknown strain $\boldsymbol{\varepsilon}$ is therefore seeked in the most general space $\mathcal{T}_2(\Omega)$ in problem (2.29). Eliminating the stress-polarization $\boldsymbol{\tau}$ leads to

$$\boldsymbol{\varepsilon} + \boldsymbol{\Gamma}_0^{\text{ess}}[(\mathbf{C} - \mathbf{C}_0) : \boldsymbol{\varepsilon}] = \overline{\boldsymbol{\varepsilon}}, \tag{2.30}$$

with unknown $\boldsymbol{\varepsilon}$. Equation (2.30) is known as the Lippmann–Schwinger equation [Kor73]; [Krö74]; [ZD73]. In the present work, the following version of the Lippmann–Schwinger equation will be preferred

$$(\mathbf{C} - \mathbf{C}_0)^{-1} : \boldsymbol{\tau} + \boldsymbol{\Gamma}_0^{\text{ess}}[\boldsymbol{\tau}] = \overline{\boldsymbol{\varepsilon}}, \tag{2.31}$$

where the strain $\boldsymbol{\varepsilon}$ has been eliminated in problem (2.29). It is again emphasized that in equation (2.31), no requirements apply to $\boldsymbol{\tau}$ [contrary to $\boldsymbol{\varepsilon}$ in problem (2.11)]. Taking the volume average of equation $(2.29)_2$, it is found that the apparent stiffness $\mathbf{C}^{\text{ess}}(\Omega)$ is retrieved from the solution to equation (2.31) as follows

$$\left[\mathbf{C}^{\text{ess}}(\Omega) - \mathbf{C}_0\right] : \overline{\boldsymbol{\varepsilon}} = \langle \boldsymbol{\tau} \rangle. \tag{2.32}$$

Turning now to periodic boundary conditions, it can be similarly shown that the corrector problem with periodic boundary conditions (2.16) is equivalent to the following periodic Lippmann–Schwinger equation

$$(\mathbf{C} - \mathbf{C}_0)^{-1} : \boldsymbol{\tau} + \boldsymbol{\Gamma}_0^{\text{per}}[\boldsymbol{\tau}] = \overline{\boldsymbol{\varepsilon}}, \tag{2.33}$$

and we again have in that case

$$\left[\mathbf{C}^{\text{per}}(\Omega) - \mathbf{C}_0\right] : \overline{\boldsymbol{\varepsilon}} = \langle \boldsymbol{\tau} \rangle. \tag{2.34}$$

2.3.2 The Hashin–Shtrikman principle

The variational principle of Hashin and Shtrikman [HS62b] was initially introduced for kinematic uniform boundary conditions. However, its statement for periodic boundary conditions is identical [MK88]. We therefore adopt generic notations in the present section whereby $\boldsymbol{\Gamma}_0$ stands for $\boldsymbol{\Gamma}_0^{\text{ess}}$ (resp. $\boldsymbol{\Gamma}_0^{\text{per}}$) and $\mathbf{C}^{\text{app}}(\Omega)$ stands for $\mathbf{C}^{\text{ess}}(\Omega)$ [resp. $\mathbf{C}^{\text{per}}(\Omega)$] for kinematic uniform boundary conditions (resp. periodic boundary conditions). In both cases, the Lippmann–Schwinger equation reads [see equations (2.31) and (2.33)]

$$(\mathbf{C} - \mathbf{C}_0)^{-1} : \boldsymbol{\tau} + \boldsymbol{\Gamma}_0[\boldsymbol{\tau}] = \overline{\boldsymbol{\varepsilon}}, \tag{2.35}$$

the solution of which will be denoted $\boldsymbol{\tau}^\star$ in the present section. The following functional (which will be called the *Hashin–Shtrikman functional* in the remainder of this work) is defined for any stress-polarization $\boldsymbol{\tau}$ (viewed as a trial function)

$$\mathrm{HS}(\boldsymbol{\tau};\overline{\boldsymbol{\varepsilon}}) = \tfrac{1}{2}\overline{\boldsymbol{\varepsilon}} : \mathbf{C}_0 : \overline{\boldsymbol{\varepsilon}} + \overline{\boldsymbol{\varepsilon}} : \langle\boldsymbol{\tau}\rangle - \tfrac{1}{2}\langle\boldsymbol{\tau} : (\mathbf{C}-\mathbf{C}_0)^{-1} : \boldsymbol{\tau}\rangle - \tfrac{1}{2}\langle\boldsymbol{\tau} : \boldsymbol{\Gamma}_0[\boldsymbol{\tau}]\rangle. \tag{2.36}$$

For $\boldsymbol{\Gamma}_0 = \boldsymbol{\Gamma}_0^{\mathrm{ess}}$ (resp. $\boldsymbol{\Gamma}_0 = \boldsymbol{\Gamma}_0^{\mathrm{per}}$), the above equation defines $\mathrm{HS}^{\mathrm{ess}}$ (resp. $\mathrm{HS}^{\mathrm{per}}$). Regardless of the reference medium $\mathbf{C}_0$ and the boundary conditions, the Hashin–Shtrikman functional HS is stationary at the solution $\boldsymbol{\tau}^\star$ of the Lippmann–Schwinger equation (2.35). Besides, its value at $\boldsymbol{\tau}^\star$ is known

$$\mathrm{HS}(\boldsymbol{\tau}^\star;\overline{\boldsymbol{\varepsilon}}) = \tfrac{1}{2}\overline{\boldsymbol{\varepsilon}} : \mathbf{C}^{\mathrm{app}}(\Omega) : \overline{\boldsymbol{\varepsilon}}. \tag{2.37}$$

When the stiffness $\mathbf{C}_0$ of the reference medium is arbitrary, the *nature* (minimum, maximum or saddle point) of the critical point of HS cannot be stated. However, the above variational principle turns into an extremum principle if the reference medium is stiffer (resp. softer) than any phase of the composite. More precisely, if $\mathbf{C}(\mathbf{x}) \geq \mathbf{C}_0$ (resp. $\mathbf{C}(\mathbf{x}) \leq \mathbf{C}_0$) at any point $\mathbf{x} \in \Omega$, then $\boldsymbol{\tau}^\star$ is the unique maximizer (resp. minimizer) of HS

$$\mathbf{C}_0 \overset{\geq}{\leq} \mathbf{C} \quad \Rightarrow \quad \mathrm{HS}(\boldsymbol{\tau};\overline{\boldsymbol{\varepsilon}}) \overset{\geq}{\leq} \tfrac{1}{2}\overline{\boldsymbol{\varepsilon}} : \mathbf{C}^{\mathrm{app}}(\Omega) : \overline{\boldsymbol{\varepsilon}} \text{ for all } \boldsymbol{\tau} \in \mathscr{T}_2(\Omega), \tag{2.38}$$

where $\mathbf{C} \geq \mathbf{C}_0$ (resp. $\mathbf{C} \leq \mathbf{C}_0$) is a shorthand for "$\mathbf{C}(\mathbf{x}) - \mathbf{C}_0$ is positive (resp. negative) indefinite at any point $\mathbf{x} \in \Omega$".

The above bounds on the macroscopic energy can readily be turned into bounds on the apparent stiffness. To do so, we select trial stress-polarizations that depend linearly on the macroscopic strain $\overline{\boldsymbol{\varepsilon}}$ through some (fourth-rank) localization tensor $\mathbf{T}$ [$\boldsymbol{\tau}(\mathbf{x}) = \mathbf{T}(\mathbf{x}) : \overline{\boldsymbol{\varepsilon}}$ for all $\mathbf{x} \in \Omega$]. The Hashin–Shtrikman functional then becomes a quadratic form of the macroscopic strain $\overline{\boldsymbol{\varepsilon}}$, which can be recast as

$$\mathrm{HS}(\mathbf{T} : \overline{\boldsymbol{\varepsilon}};\overline{\boldsymbol{\varepsilon}}) = \tfrac{1}{2}\overline{\boldsymbol{\varepsilon}} : \mathbf{C}^{\mathrm{HS}} : \overline{\boldsymbol{\varepsilon}}, \tag{2.39}$$

and equation (2.38) translates into

$$\mathbf{C}_0 \overset{\geq}{\leq} \mathbf{C} \quad \Rightarrow \quad \mathbf{C}^{\mathrm{HS}} \overset{\geq}{\leq} \mathbf{C}^{\mathrm{app}}(\Omega). \tag{2.40}$$

The Hashin–Shtrikman principle is a powerful tool, which can provide bounds on the macroscopic elastic energy for *any* choice of the stress-polarization $\boldsymbol{\tau}$. Of course, tight bounds require complex stress-polarization fields, but even very simple choices can result in bounds that improve significantly upon the classical Voigt and Reuss bounds. For example, the celebrated bounds of [HS62a] are obtained with phase-wise constant stress-polarization fields. These bounds are universal: they apply to *any statically isotropic* composite (regardless of the details of its microstructure). This asset can also be seen as a weakness, as will be discussed in section 3.2.

Remark 2.3. *In the Lippmann–Schwinger equations* (2.31) *and* (2.33) *as well as in the definition* (2.36) *of the Hashin–Shtrikman functional, the term involving* $(\mathbf{C} - \mathbf{C}_0)$ *is singular in these regions of the domain* Ω *where* $\mathbf{C} = \mathbf{C}_0$*. In these regions, the stress-polarization* $\boldsymbol{\tau}$ *must be set to* $\mathbf{0}$*. More generally, the stress-polarization must be orthogonal to the null-space of the linear operator* $\mathbf{C} - \mathbf{C}_0$*.*

Accounting for this special case would unnecessarily complicate the discussions that follow (see for example [BD12]). Therefore, from now on, it will be assumed that $\mathbf{C} - \mathbf{C}_0$ *is invertible at any point of the domain* Ω*.*

Chapter 3

Bounds on the effective properties

In section 1.3 of chapter 1, we introduced *statistical* homogenization methods, that strive to relate the macroscopic properties of heterogeneous materials to some statistical descriptors of their microstructure. The present chapter gathers a few applications of the Hashin–Shtrikman principle that could accordingly be thought of as *statistical*.

It opens in section 3.1 with the classical bounds of Hashin–Shtrikman, which are revisited in the light of our paper [BSD13]. A general methodology is proposed for the derivation of bounds of the Hashin–Shtrikman type, that is then consistently applied throughout this chapter. Observing that the trial stress-polarizations used to derive the classical Hashin–Shtrikman bounds are quite poor, section 3.2 investigates possible enrichments, with the hope to produce sharper bounds. It is shown that the Hashin–Shtrikman bounds are remarkably robust. However, it is also argued in this section that the new enrichment procedure recently proposed in reference [Bri17b] offers exciting perspectives. The chapter closes with various, unrelated, successful applications of the Hashin–Shtrikman principle within the framework of statistical approaches: nanocomposites (see section 3.3 and references [BDK10a]; [BDK10b]), eigen-stressed materials (see section 3.4 and references [BG17]; [BG18]) and stress-gradient materials (see section 3.5 and references [Tra+18a]; [Tra+18b]; [Tra16]).

In the present chapter, χ denotes the indicator function of the SVE $\Omega \subset \mathbb{R}^d$: $\chi(\mathbf{x}) \in \{0, 1\}$, $\chi(\mathbf{x}) = 1 \iff \mathbf{x} \in \Omega$. The bounded domain Ω will frequently be embedded in a homogeneous reference material that occupies the whole space $\Omega \subset \mathbb{R}^d$. We will therefore often consider local quantities $\mathcal{Q}$ that are defined *over the whole space*. Despite that, $\langle \mathcal{Q} \rangle$ will always refer to its volume average over the domain Ω [consistently with equation (2.1)].

3.1 Classical bounds – The "modified" Green operator

It has already been mentioned in section 2.2 that the definition of the fourth-rank Green operator for essential boundary conditions $\mathbf{\Gamma}_0^{\text{ess}}$ is formal. Indeed, a closed-form expression of this operator is in general not known. As such, the Hashin–Shtrikman principle is arguably useless. However, it is customary, for "large" domains Ω to approximate $\mathbf{\Gamma}_0^{\text{ess}}$ with the Green operator $\mathbf{\Gamma}_0^{\infty}$ of the whole space $\mathbb{R}^d$ as follows

$$\mathbf{\Gamma}_0^{\text{ess}}[\boldsymbol{\tau}] \approx \mathbf{\Gamma}_0^{\infty}[\boldsymbol{\tau} - \chi\langle\boldsymbol{\tau}\rangle], \tag{3.1}$$

where $\boldsymbol{\tau} \in \mathcal{T}_2(\Omega)$. It should be observed that $\boldsymbol{\tau}$ is defined in Ω (since it is to be applied to Γ_0^{ess}); for equation (3.1) to be meaningful, $\boldsymbol{\tau}$ is extended to the whole space $\mathbb{R}^d$ with $\boldsymbol{\tau}(\mathbf{x}) = \mathbf{0}$

for $\mathbf{x} \notin \Omega$. Therefore, $\boldsymbol{\tau} - \chi\langle\boldsymbol{\tau}\rangle$ is also defined over the whole space and supported in Ω. It is also noted that applying in equation (3.1) $\boldsymbol{\Gamma}_0^\infty$ to the fluctuations of the stress-polarization, rather than the stress-polarization itself is necessary in order to preserve property (2.27) of the exact Green operator Γ_0^{ess}.

Approximation (3.1) is usually attributed to Willis [Wil77], but can be traced back to Brown [Bro55] who (within the framework of conductivity) introduced a similar correction in order to analyze the thermodynamic limit of conditionally convergent integrals (see also reference [Tor97]). Although it has successfully been invoked on multiple occasions [PW95], the meaning of this approximation is rather unclear, and it must be emphasized that it was justified by Willis on the basis of heuristic arguments only. How should equation (3.1) be understood? Surely not point-wise, as it must fail near the boundary of Ω (regardless of how large Ω is). I have long been puzzled by this point, until I stumbled upon an indirect, rigorous justification of the use of the right-hand side of equation (3.1) as a new, modified Green operator. In this approach, which is briefly summarized in the present section, approximation (3.1) is no longer invoked (and it indeed does *not* hold). More details, including proofs, can be found in reference [BSD13].

3.1.1 The modified Lippmann–Schwinger equation

For the sake of clarity, the Lippmann–Schwinger equation (2.31) introduced in section 2.3.1 is reproduced below

$$(\mathbf{C} - \mathbf{C}_0)^{-1} : \boldsymbol{\tau} + \boldsymbol{\Gamma}_0^{\text{ess}}[\boldsymbol{\tau}] = \overline{\boldsymbol{\varepsilon}}, \tag{3.2}$$

where $\overline{\boldsymbol{\varepsilon}}$ denotes the (prescribed) macroscopic strain. Following Willis [Wil77], this equation is conveniently replaced with the following, more tractable integral equation

$$(\mathbf{C} - \mathbf{C}_0)^{-1} : \boldsymbol{\tau} + \boldsymbol{\Gamma}_0^{\infty}[\boldsymbol{\tau} - \chi\langle\boldsymbol{\tau}\rangle] = \overline{\boldsymbol{\varepsilon}}, \tag{3.3}$$

and the solution to equation (3.3) is deemed to provide a good approximation of the solution to equation (3.2) for "large" domains Ω. Clearly, such a statement would be quite hard to prove mathematically. I therefore took a different route in [BSD13]. In this work, rather than considering equation (3.3) as an approximation to equation (3.2), I considered this equation in its own right, with no reference to the initial problem with essential boundary conditions.

Equation (3.3) will henceforth be referred to as the *modified Lippmann–Schwinger equation*. For the time being, $\overline{\boldsymbol{\varepsilon}}$ in this equation is considered as a mere loading parameter, with no connection with the macroscopic strain. Let $\boldsymbol{\tau} \in \mathscr{T}_2(\Omega)$ denote the unique solution to equation (3.3) (assessment of the existence and uniqueness of this solution is deferred to section 3.1.4). It is first observed that $\boldsymbol{\tau}$ defines a compatible strain field $\boldsymbol{\varepsilon} \in \mathscr{E}(\Omega)$

$$\boldsymbol{\varepsilon} = (\mathbf{C} - \mathbf{C}_0)^{-1} : \boldsymbol{\tau} = \overline{\boldsymbol{\varepsilon}} - \boldsymbol{\Gamma}_0^{\infty}[\boldsymbol{\tau} - \chi\langle\boldsymbol{\tau}\rangle]. \tag{3.4}$$

That $\boldsymbol{\varepsilon}$ is geometrically compatible over $\mathbb{R}^d$ (hence, over Ω) readily results from the definition of the Green operator of the whole space (see section 2.2.3). Furthermore, $\mathbf{C}_0 : \boldsymbol{\varepsilon} + \boldsymbol{\tau} - \chi\langle\boldsymbol{\tau}\rangle$

is divergence-free over $\mathbb{R}^d$. Therefore, $\mathbf{C}_0 : \boldsymbol{\varepsilon} + \boldsymbol{\tau}$ is divergence-free over Ω, and we define the following stress field

$$\boldsymbol{\sigma} = \mathbf{C}_0 : \boldsymbol{\varepsilon} + \boldsymbol{\tau}. \tag{3.5}$$

It should be emphasized that $\boldsymbol{\sigma}$ is not divergence-free over the whole space $\mathbb{R}^d$, since the traction $\boldsymbol{\sigma} \cdot \mathbf{n}$ is discontinuous at the boundary $\partial\Omega$. Combining equations (3.4) and (3.5), it is readily found that $\boldsymbol{\sigma} = \mathbf{C} : \boldsymbol{\varepsilon}$ in Ω. To summarize, the solution $\boldsymbol{\tau}$ to the modified Lippmann–Schwinger equation (3.3) allowed us to construct, for a prescribed strain $\overline{\boldsymbol{\varepsilon}}$, a geometrically compatible strain $\boldsymbol{\varepsilon} \in \mathscr{E}(\Omega)$ and a divergence-free stress $\boldsymbol{\sigma} \in \mathscr{S}(\Omega)$ that are related through the local constitutive equation of the *heterogeneous* material. This suggests that a *new* apparent stiffness [which would differ from $\mathbf{C}^{\mathrm{ess}}(\Omega)$, $\mathbf{C}^{\mathrm{nat}}(\Omega)$ or $\mathbf{C}^{\mathrm{per}}(\Omega)$ defined in section 2.1.2] may be defined, based on $\boldsymbol{\sigma}$ and $\boldsymbol{\varepsilon}$ thus constructed. More precisely, observing that equations (3.3), (3.4) and (3.5) are *linear*, it is possible to introduce the strain- and stress- localization tensors $\mathbf{A}^{\mathrm{mix}}$ and $\mathbf{B}^{\mathrm{mix}}$ and the apparent stiffness $\mathbf{C}^{\mathrm{mix}}(\mathbf{C}_0, \Omega)$ defined as

$$\langle \boldsymbol{\varepsilon} \rangle = \mathbf{A}^{\mathrm{mix}} : \overline{\boldsymbol{\varepsilon}}, \quad \langle \boldsymbol{\sigma} \rangle = \mathbf{B}^{\mathrm{mix}} : \overline{\boldsymbol{\varepsilon}} \quad \text{and} \quad \mathbf{C}^{\mathrm{mix}}(\mathbf{C}_0, \Omega) = \mathbf{B}^{\mathrm{mix}} : \left(\mathbf{A}^{\mathrm{mix}}\right)^{-1}, \tag{3.6}$$

the above definitions ensuring that equation (2.5) holds for $\mathbf{C}^{\mathrm{mix}}(\mathbf{C}_0, \Omega)$. Besides, equation (3.5) trivially results in

$$\left[\mathbf{C}^{\mathrm{mix}}(\mathbf{C}_0, \Omega) - \mathbf{C}_0\right] : \langle \boldsymbol{\varepsilon} \rangle = \langle \boldsymbol{\tau} \rangle. \tag{3.7}$$

In equations (3.6) and (3.7), the subscript "mix" stands for *mixed boundary conditions*, because the modified Lippmann–Schwinger equation (3.3) is equivalent to a problem of elastic equilibrium where both static (on the boundary $\partial\Omega$ of the SVE) and kinematic (at infinity) boundary conditions (see section 3.1.2) are applied. However, such terminology is rather poor, as many alternative mixed boundary conditions can be proposed. Being unambiguous in the present work, this terminology will however be preserved.

It is observed that the newly introduced apparent stiffness depends not only on the shape of the SVE Ω, but also on the stiffness $\mathbf{C}_0$ of the reference material. The above definition immediatly raises an essential question: is the apparent stiffness $\mathbf{C}^{\mathrm{mix}}(\mathbf{C}_0, \Omega)$ consistent? By consistency, we mean here that $\mathbf{C}^{\mathrm{mix}}(\mathbf{C}_0, \Omega)$ should converge to the effective stiffness $\mathbf{C}^{\mathrm{eff}}$ as the size of the SVE Ω tends to infinity (see section 2.1.4). This question will be addressed in section 3.1.2, the remainder of this section being devoted to understanding the meaning of the loading parameter $\overline{\boldsymbol{\varepsilon}}$.

To do so, a remarkable mathematical property of the Green operator $\boldsymbol{\Gamma}_0^{\infty}$ will be used (see theorem 2 in reference [BSD13]). Assuming that Ω is *ellipsoidal*, and that $\boldsymbol{\varpi} \in \mathscr{T}_2(\mathbb{R}^d)$ is supported in Ω, then

$$\langle \boldsymbol{\Gamma}_0^{\infty}[\boldsymbol{\varpi}] \rangle = \mathbf{P}_0(\Omega) : \langle \boldsymbol{\varpi} \rangle, \tag{3.8}$$

where $\mathbf{P}_0(\Omega)$ denotes the Hill tensor of ellipsoid Ω with respect to the reference material $\mathbf{C}_0$. Two comments should be made regarding equation (3.8). First, if $\boldsymbol{\varpi}$ is *constant* within Ω,

then it coincides with the celebrated result of Eshelby [Esh57]. Second, an earlier proof of this equation can be found in reference [RH91][1].

Combining equations (3.4) and (3.8), it is readily found that $\langle \boldsymbol{\varepsilon} \rangle = \overline{\boldsymbol{\varepsilon}}$ for the strain defined through equation (3.4) from the solution $\boldsymbol{\tau}$ to the modified Lippmann–Schwinger equation (3.3). In other words, the loading parameter $\overline{\boldsymbol{\varepsilon}}$ coincides with the macroscopic strain, which is prescribed in this approach. In turn, this simplifies the computation of the apparent stiffness $\mathbf{C}^{\mathrm{mix}}(\mathbf{C}_0, \Omega)$ [initially defined by equation (3.6)] as the linear operator that maps the prescribed macroscopic strain onto the macroscopic stress

$$\langle \boldsymbol{\sigma} \rangle = \mathbf{C}^{\mathrm{mix}}(\mathbf{C}_0, \Omega) : \overline{\boldsymbol{\varepsilon}} = \mathbf{C}^{\mathrm{mix}}(\mathbf{C}_0, \Omega) : \langle \boldsymbol{\varepsilon} \rangle. \tag{3.9}$$

Together with the symmetry of the Green operator $\boldsymbol{\Gamma}_0^{\infty}$ (see lemma 1 in reference [BSD13]), this further leads to the symmetry of the apparent stiffness $\mathbf{C}^{\mathrm{mix}}(\mathbf{C}_0, \Omega)$, which was not obvious from equations (3.6). Also, equation (3.7) reads

$$\left[\mathbf{C}^{\mathrm{mix}}(\mathbf{C}_0, \Omega) - \mathbf{C}_0\right] : \overline{\boldsymbol{\varepsilon}} = \langle \boldsymbol{\tau} \rangle. \tag{3.10}$$

Unless otherwise stated, it will always be assumed in the remainder of section 3.1 that Ω is ellipsoidal. Therefore, equations (3.8), (3.9) and (3.10) hold.

3.1.2 The underlying corrector problem

In the previous section 3.1.1, the new apparent stiffness $\mathbf{C}^{\mathrm{mix}}(\mathbf{C}_0, \Omega)$ was introduced by means of the solution $\boldsymbol{\tau}$ to the modified Lippmann–Schwinger equation (3.3), the local strain $\boldsymbol{\varepsilon}$ and stress $\boldsymbol{\sigma}$ being reconstructed a posteriori from $\boldsymbol{\tau}$ [see equations (3.4) and (3.5)].

While working on the paper [BSD13], it was observed by K. Sab that this new apparent stiffness could be given a mechanical interpretation, provided that Ω is ellipsoidal. Indeed, the local strain and stress fields solve the following problem

$$\text{Find } \mathbf{t} \in \mathcal{T}_2,\ \boldsymbol{\varepsilon} \in \overline{\boldsymbol{\varepsilon}} + \mathcal{C}(\mathbb{R}^d) \text{ and } \boldsymbol{\sigma} \in \chi \mathbf{t} + \mathcal{S}(\mathbb{R}^d) \text{ such that } \begin{cases} \boldsymbol{\sigma} = \mathbf{C} : \boldsymbol{\varepsilon} & (\Omega), \\ \boldsymbol{\sigma} = \mathbf{C}_0 : \boldsymbol{\varepsilon} & (\mathbb{R}^d \setminus \Omega), \\ \langle \boldsymbol{\varepsilon} \rangle = \overline{\boldsymbol{\varepsilon}}, \end{cases} \tag{3.11}$$

where $\mathbf{t}$ is an unknown constant, symmetric, second-rank tensor that is selected in order to further ensure that $\langle \boldsymbol{\varepsilon} \rangle = \overline{\boldsymbol{\varepsilon}}$.

It should be observed that problem (3.11) is formulated over the whole space $\mathbb{R}^d$; its well-posedness must therefore be assessed carefully, and the mathematical developments that were required to this effect will be briefly exposed in section 3.1.4 (in particular, $\boldsymbol{\varepsilon} - \overline{\boldsymbol{\varepsilon}}$ and $\boldsymbol{\sigma} - \chi \mathbf{t}$ are square integrable over the whole space). Also, although the strain and stress tensors $\boldsymbol{\varepsilon}$ and $\boldsymbol{\sigma}$ are defined over the full space $\mathbb{R}^d$, only their values within the SVE Ω are really relevant. In particular, it is recalled that quantities such as $\langle \boldsymbol{\varepsilon} \rangle$ are to be understood as volume averages over the SVE Ω.

[1] It should however be noted that the proof of these authors relies on Fubini's theorem. Owing to the singularities of the Green operator, the applicability of this theorem seems questionable.

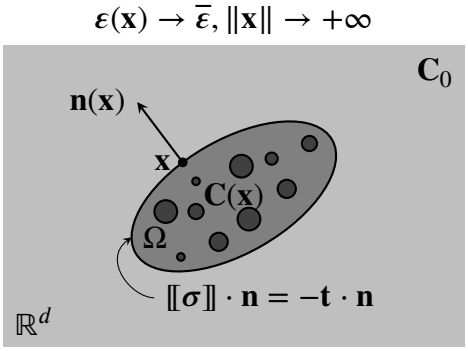

Figure 3.1: Illustration of the mixed boundary conditions introduced in section 3.1.2. The SVE Ω is embedded in the unbounded reference material $\mathbf{C}_0$. A uniform strain $\overline{\boldsymbol{\varepsilon}}$ is imposed at infinity, and the uniform traction $\mathbf{t}$ that is applied at the boundary $\partial\Omega$ is selected so as to ensure that the prescribed strain at infinity coincides with the average strain within the SVE, $\overline{\boldsymbol{\varepsilon}} = \langle \boldsymbol{\varepsilon} \rangle$. (Reproduced from reference [BSD13])

Problem (3.11) should be understood as follows (see also figure 3.1): the heterogeneous, ellipsoidal SVE Ω is embedded in the unbounded reference material, which is subjected to a uniform strain $\overline{\boldsymbol{\varepsilon}}$ at infinity. Surface loads are also applied to the boundary $\partial\Omega$. Their density is given by the expression $[\![\boldsymbol{\sigma}]\!] \cdot \mathbf{n} = -\mathbf{t} \cdot \mathbf{n}$, where $\mathbf{t}$ is an unknown, constant tensor chosen a posteriori in order to ensure that the macroscopic strain $\langle \boldsymbol{\varepsilon} \rangle$ coincides with the strain at infinity $\overline{\boldsymbol{\varepsilon}}$. It is emphasized that in problem (3.11), $\overline{\boldsymbol{\varepsilon}}$ is the sole loading parameter, since $\mathbf{t}$ is not a free parameter. It is remarkable that this additional unknown does not appear in the formulation as the integral equation (3.3) [it can readily be shown that in fact, $\mathbf{t} = \langle \boldsymbol{\tau} \rangle$].

In practice, problem (3.11) can be solved through two sub-problems. In the first sub-problem, only the uniform strain at infinity is applied

$$\text{Find } \boldsymbol{\varepsilon} \in \overline{\boldsymbol{\varepsilon}} + \mathscr{E}(\mathbb{R}^d) \text{ and } \boldsymbol{\sigma} \in \mathscr{S}(\mathbb{R}^d) \text{ such that } \begin{cases} \boldsymbol{\sigma} = \mathbf{C} : \boldsymbol{\varepsilon} & (\Omega), \\ \boldsymbol{\sigma} = \mathbf{C}_0 : \boldsymbol{\varepsilon} & (\mathbb{R}^d \setminus \Omega) \end{cases} \tag{3.12}$$

and its solution depends linearly on the loading parameter $\overline{\boldsymbol{\varepsilon}}$: $\langle \boldsymbol{\varepsilon} \rangle = \mathbf{A}_1 : \overline{\boldsymbol{\varepsilon}}$ and $\langle \boldsymbol{\sigma} \rangle = \mathbf{B}_1 : \overline{\boldsymbol{\varepsilon}}$. In the second sub-problem, only the (given) surface load is applied at the boundary of the SVE Ω

$$\text{Find } \boldsymbol{\varepsilon} \in \mathscr{E}(\mathbb{R}^d) \text{ and } \boldsymbol{\sigma} \in \chi\mathbf{t} + \mathscr{S}(\mathbb{R}^d) \text{ such that } \begin{cases} \boldsymbol{\sigma} = \mathbf{C} : \boldsymbol{\varepsilon} & (\Omega), \\ \boldsymbol{\sigma} = \mathbf{C}_0 : \boldsymbol{\varepsilon} & (\mathbb{R}^d \setminus \Omega), \end{cases} \tag{3.13}$$

and we now have for this sub-problem $\langle \boldsymbol{\varepsilon} \rangle = \mathbf{A}_2 : \mathbf{t}$ and $\langle \boldsymbol{\sigma} \rangle = \mathbf{B}_2 : \mathbf{t}$. When both $\overline{\boldsymbol{\varepsilon}}$ and $\mathbf{t}$ are applied, we have $\langle \boldsymbol{\varepsilon} \rangle = \mathbf{A}_1 : \overline{\boldsymbol{\varepsilon}} + \mathbf{A}_2 : \mathbf{t}$. Enforcing that $\langle \boldsymbol{\varepsilon} \rangle = \overline{\boldsymbol{\varepsilon}}$ leads to

$$\mathbf{t} = \mathbf{A}_2^{-1} : (\mathbf{I} - \mathbf{A}_1) : \overline{\boldsymbol{\varepsilon}} \quad \text{and} \quad \langle \boldsymbol{\sigma} \rangle = \left[\mathbf{B}_1 + \mathbf{B}_2 : \mathbf{A}_2^{-1} : (\mathbf{I} - \mathbf{A}_1) \right] : \overline{\boldsymbol{\varepsilon}}, \tag{3.14}$$

where the quantity within the square brackets is the seeked apparent stiffness $\mathbf{C}^{\text{mix}}(\mathbf{C}_0, \Omega)$.

Reformulation of the modified Lippmann–Schwinger equation (3.3) as the mechanical problem (3.11) then allowed us to derive the associated principles of minimum potential and com-

plementary energy (see theorems 8 and 9 in reference [BSD13]). In turn, the following important property of the apparent stiffness resulted from these principles

$$\mathbf{C}^{\mathrm{nat}}(\Omega) \leq \mathbf{C}^{\mathrm{mix}}(\mathbf{C}_0, \Omega) \leq \mathbf{C}^{\mathrm{ess}}(\Omega), \tag{3.15}$$

and in fact

- $\mathbf{C}^{\mathrm{mix}}(\mathbf{C}_0, \Omega) \to \mathbf{C}^{\mathrm{ess}}(\Omega)$ for "rigid" reference materials ("$\mathbf{C}_0 \to +\infty$"),
- $\mathbf{C}^{\mathrm{mix}}(\mathbf{C}_0, \Omega) \to \mathbf{C}^{\mathrm{nat}}(\Omega)$ for "soft" reference materials ("$\mathbf{C}_0 \to 0$"),

both results being stated less loosely in reference [BSD13] (see theorems 10 and 11). Clearly, $\mathbf{C}^{\mathrm{mix}}(\mathbf{C}_0, \Omega)$ can therefore not be considered as an approximation of $\mathbf{C}^{\mathrm{ess}}(\Omega)$. However, under the assumption of statistical homogeneity and ergodicity, it is known that $\mathbf{C}^{\mathrm{nat}}(\Omega), \mathbf{C}^{\mathrm{ess}}(\Omega) \to \mathbf{C}^{\mathrm{eff}}$ for large SVEs [Sab92]. Therefore, equation (3.15) proves that the newly defined apparent stiffness is consistent, in the sense that $\mathbf{C}^{\mathrm{mix}}(\mathbf{C}_0, \Omega) \to \mathbf{C}^{\mathrm{eff}}$ for large SVEs.

3.1.3 The modified Hashin–Shtrikman principle

Probably the most important result related to the modified Lippmann–Schwinger equation (3.3) and the related apparent stiffness $\mathbf{C}^{\mathrm{mix}}(\mathbf{C}_0, \Omega)$ is the fact that it is possible to state a variational principle similar to that of Hashin and Shtrikman [HS62b]. More precisely, we introduce the following functional (see reference [BSD13], theorem 12)

$$\mathrm{HS}^{\mathrm{mix}}(\boldsymbol{\tau}; \overline{\boldsymbol{\varepsilon}}) = \tfrac{1}{2}\overline{\boldsymbol{\varepsilon}} : \mathbf{C}_0 : \overline{\boldsymbol{\varepsilon}} + \overline{\boldsymbol{\varepsilon}} : \langle \boldsymbol{\tau} \rangle - \tfrac{1}{2}\langle \boldsymbol{\tau} : (\mathbf{C} - \mathbf{C}_0)^{-1} : \boldsymbol{\tau} \rangle - \tfrac{1}{2}\langle \boldsymbol{\tau} : \boldsymbol{\Gamma}_0^{\infty}[\boldsymbol{\tau} - \chi\langle \boldsymbol{\tau} \rangle] \rangle, \tag{3.16}$$

for any test function $\boldsymbol{\tau}$ supported in Ω. It can then be shown that $\mathrm{HS}^{\mathrm{mix}}$ enjoys the same properties as the similar functionals defined for essential or periodic boundary conditions (see section 2.3.2). More precisely, $\mathrm{HS}^{\mathrm{mix}}$ is stationary at the solution $\boldsymbol{\tau}^\star$ to the modified Lippmann–Schwinger equation (3.3). Besides, at this critical point

$$\mathrm{HS}^{\mathrm{mix}}(\boldsymbol{\tau}^\star; \overline{\boldsymbol{\varepsilon}}) = \tfrac{1}{2}\overline{\boldsymbol{\varepsilon}} : \mathbf{C}^{\mathrm{mix}}(\mathbf{C}_0, \Omega) : \overline{\boldsymbol{\varepsilon}}. \tag{3.17}$$

For reference materials that are softer or stiffer than all phases in the composite, the above stationarity condition turns into an extremum condition

$$\mathbf{C}_0 \overset{\geq}{\leq} \mathbf{C} \quad \Rightarrow \quad \mathrm{HS}^{\mathrm{mix}}(\boldsymbol{\tau}; \overline{\boldsymbol{\varepsilon}}) \overset{\geq}{\leq} \tfrac{1}{2}\overline{\boldsymbol{\varepsilon}} : \mathbf{C}^{\mathrm{mix}}(\mathbf{C}_0, \Omega) : \overline{\boldsymbol{\varepsilon}}$$
$$\text{for all } \boldsymbol{\tau} \in \mathscr{T}_2(\mathbb{R}^d) \text{ supported in } \Omega. \tag{3.18}$$

For a finite-size SVE Ω, the above stated modified Hashin–Shtrikman principle allows to produce bounds on the apparent stiffness $\mathbf{C}^{\mathrm{mix}}(\mathbf{C}_0, \Omega)$. Then, letting the size of Ω grow to infinity will result in rigorous bounds on the effective properties of the heterogeneous material (see section 3.1.5).

It should be observed that the functional $\mathrm{HS}^{\mathrm{mix}}$ defined by equation (3.16) is superior to $\mathrm{HS}^{\mathrm{ess}}$ defined by equation (2.36) in that it involves a unique Green operator (regardless of the shape and size of the ellipsoidal SVE Ω), namely $\boldsymbol{\Gamma}_0^{\infty}$ which is known in closed-form.

3.1.4 On the solution to elasticity problems in the whole space

In the present section, we briefly sketch some of the results that were needed for the mathematical analysis of problem (2.23) that defines the Green operator $\boldsymbol{\Gamma}_0^\infty$, the modified Lippmann–Schwinger equation (3.3) and the equivalent problem (3.11).

It is first emphasized that the analysis presented in [BSD13] was eased considerably by the observation that local displacements are of little use in a homogenization perspective that essentially requires local strains and stresses. For each elasticity problem that was formulated on the whole space $\mathbb{R}^d$, we therefore did not require the uniqueness of the displacement and were not concerned by its regularity.

This observation led us to prefer the space of compatible strains over the space of kinematically admissible displacements. It is recalled that in section 2.1.2, we introduced the spaces of second-rank, symmetric tensor fields $\mathcal{T}_2(\mathbb{R}^d)$ with square-integrable components, the space of compatible strain fields $\mathcal{E}(\mathbb{R}^d) \subset \mathcal{T}_2(\mathbb{R}^d)$ and the space of divergence-free stress fields $\mathcal{S}(\mathbb{R}^d) \subset \mathcal{T}_2(\mathbb{R}^d)$. In reference [BSD13] (see theorem 4), we first proved that these spaces are in direct orthogonal sum

$$\mathcal{T}_2(\mathbb{R}^d) = \mathcal{E}(\mathbb{R}^d) \overset{\perp}{\oplus} \mathcal{S}(\mathbb{R}^d) \quad \text{for the scalar product} \quad \langle \boldsymbol{\sigma}, \boldsymbol{\varepsilon} \rangle = \int_{\mathbf{x}\in\mathbb{R}^d} \boldsymbol{\sigma}(\mathbf{x}) : \boldsymbol{\varepsilon}(\mathbf{x}) \, \mathrm{d}V_{\mathbf{x}}, \tag{3.19}$$

see also reference [Mil02] for a similar result in a periodic setting. Introducing a variational setting, we then went on to prove the well-posedness of problem (2.23), which resulted in a rigorous definition of $\boldsymbol{\Gamma}_0^\infty : \mathcal{T}_2(\mathbb{R}^d) \to \mathcal{E}(\mathbb{R}^d)$ (see theorems 6 and 7 in reference [BSD13]). A similar analysis also allowed us to prove that the modified Lippmann–Schwinger equation (3.3) is well-posed in $\mathcal{T}_2(\mathbb{R}^d)$. All other results listed in sections 3.1.1, 3.1.2 and 3.1.3 were then obtained.

To close this section, it should be observed that well-posedness of problem (2.23) is a somewhat classical result among mathematicians[2] (to the point that we were not able to point at a specific reference). The traditional route would be to consider the following regularized problem

$$\text{Find } \mathbf{u} \in [\mathrm{H}^1(\mathbb{R}^d)]^d \text{ such that } \eta\mathbf{u} - \mathbf{div}\big(\mathbf{C}_0 : \boldsymbol{\epsilon}[\mathbf{u}] + \boldsymbol{\varpi}\big) = \mathbf{0}, \tag{3.20}$$

where $\eta \geq 0$. When $\eta = 0$, the initial problem (2.23) is recovered. When $\eta > 0$, coercivity is readily proved for the above problem, which is therefore well-posed; $\mathbf{u}_\eta$ denotes its unique solution. It can be shown that, as $\eta \to 0$, $\eta\mathbf{u}_\eta$ converges strongly to 0 in $[\mathrm{L}^2(\mathbb{R}^d)]^d$ (up to a sub-sequence), while $\boldsymbol{\epsilon}[\mathbf{u}_\eta]$ converges weakly (up to a sub-sequence) to $\boldsymbol{\varepsilon}_0$ in $\mathcal{T}_2(\mathbb{R}^d)$, such that $\mathbf{div}(\mathbf{C}_0 : \boldsymbol{\varepsilon}_0 + \boldsymbol{\varpi}) = \mathbf{0}$.

It is then shown that there exists $\mathbf{u}_0 \in [\mathrm{L}^2_{\mathrm{loc}}(\mathbb{R}^d)]^d$ such that $\boldsymbol{\varepsilon}_0 = \boldsymbol{\epsilon}[\mathbf{u}_0]$, which completes the proof. It is observed that, besides the regularity of the strain field, this approach also provides the regularity of the displacement field, which was not required (and indeed, overlooked) in our approach.

[2] F. Legoll, private communication, oct. 3rd, 2016.

3.1.5 The classical Hashin–Shtrikman bounds revisited

We are now in a position to revisit the classical Hashin–Shtrikman bounds [HS62a]; [Wil77], the derivation of which is outlined below. Including this derivation in the present work serves two purposes. First, it underlines the fact that using the modified Hashin–Shtrikman principle introduced in section 3.1.3 avoids the need for ad-hoc approximations of the Green operator for strains. Second, it introduces the more elaborate derivations that will be presented in the remainder of this chapter.

We now assume that a reference material with elastic stiffness $\mathbf{C}_0$ has been chosen, such that $\mathbf{C}_0 \geq \mathbf{C}$ at any point of the heterogeneous material[3]. Then, from the principle (3.18),

$$\tfrac{1}{2}\overline{\boldsymbol{\varepsilon}} : \mathbf{C}^{\mathrm{mix}}(\mathbf{C}_0, \Omega) : \overline{\boldsymbol{\varepsilon}} \leq \mathrm{HS}^{\mathrm{mix}}(\boldsymbol{\tau}; \overline{\boldsymbol{\varepsilon}}), \tag{3.21}$$

for all $\boldsymbol{\tau} \in \mathcal{T}_2(\mathbb{R}^d)$, supported in Ω. Following Hashin and Shtrikman, the above inequality is tested with a phase-wise constant stress-polarization field.

At this point, it should be emphasized that the Hashin–Shtrikman bounds should be derived within the probabilistic setting of random homogenization. This means that equation (3.21) is really written for one SVE Ω, that is one realization of the random material, occupying the ellipsoidal domain Ω. This realization is produced from an *infinite* realization, discarding all materials that fall outside the domain Ω.

Assuming that the stress-polarization $\boldsymbol{\tau}$ is properly defined as a weakly homogeneous, ergodic random field (over *the whole space* $\mathbb{R}^d$), inequality (3.21) then holds realization-by-realization for the truncated stress-polarization field $\chi\boldsymbol{\tau}$ (which is indeed supported in Ω). Ensemble averaging both sides, we get for infinitely large domains Ω

$$\tfrac{1}{2}\overline{\boldsymbol{\varepsilon}} : \mathbf{C}^{\mathrm{eff}} : \overline{\boldsymbol{\varepsilon}} \leq \lim_{|\Omega|\to+\infty} \mathbb{E}\big[\mathrm{HS}(\chi\boldsymbol{\tau}; \overline{\boldsymbol{\varepsilon}})\big], \tag{3.22}$$

where the "mix" superscript has been omitted, as mixed boudary conditions will be assumed from now on unless otherwise stated. Under mild assumptions, it can be shown that

$$\begin{aligned}\lim_{|\Omega|\to+\infty} \mathbb{E}\big[\mathrm{HS}(\chi\boldsymbol{\tau}; \overline{\boldsymbol{\varepsilon}})\big] = {} & \tfrac{1}{2}\overline{\boldsymbol{\varepsilon}} : \mathbf{C}_0 : \overline{\boldsymbol{\varepsilon}} + \overline{\boldsymbol{\varepsilon}} : \mathbb{E}\boldsymbol{\tau} \\ & - \tfrac{1}{2}\sum_{\alpha} (\mathbf{C}_\alpha - \mathbf{C}_0)^{-1} :: \mathbb{E}\big[\chi_\alpha(\mathbf{0})\, \boldsymbol{\tau}(\mathbf{0}) \otimes \boldsymbol{\tau}(\mathbf{0})\big] \\ & - \tfrac{1}{2}\mathbf{P}_0 :: \mathbf{R}_{\tau\tau}(\mathbf{0}) - \tfrac{1}{2}\lim_{\delta\to 0} \int_{\substack{\mathbf{r}\in\mathbb{R}^d \\ \|\mathbf{r}\|\geq\delta}} \boldsymbol{\Gamma}_0^{\infty}(\mathbf{r}) :: \mathbf{R}_{\tau\tau}(\mathbf{r})\, \mathrm{d}V_{\mathbf{r}},\end{aligned} \tag{3.23}$$

see appendix B for a detailed proof. In the above equation, $\mathbf{R}_{\tau\tau}$ denotes the autocovariance of the trial stress-polarization random field: $\mathbf{R}_{\tau\tau}(\mathbf{r}) = \mathbb{E}\big[\boldsymbol{\tau}(\mathbf{0}) \otimes \boldsymbol{\tau}(\mathbf{r})\big] - \mathbb{E}\boldsymbol{\tau} \otimes \mathbb{E}\boldsymbol{\tau}$.

To sum up, in order to produce an upper-bound on the effective stiffness, we need to chose the statistically homogeneous random field $\boldsymbol{\tau}$ (trial stress-polarization) and evaluate the right-hand side of inequality (3.22) using equation (3.23).

[3] Conversely, if $\mathbf{C}_0 \leq \mathbf{C}$ at any point of the heterogeneous material, inequality (3.21) should be reversed.

To do so, it is recalled that χ_α denotes the indicator function of phase $\alpha = 1, \dots, N$. We observe that $\chi, \chi_1, \dots, \chi_N$ are all defined over the whole space $\mathbb{R}^d$ and that χ is *deterministic* while $\chi_1, \dots, \chi_N$ are *random fields*. With these observations at hand, we select the following phase-wise constant trial stress-polarization

$$\boldsymbol{\tau}(\mathbf{x}) = \sum_\alpha \chi_\alpha(\mathbf{x})\, \boldsymbol{\tau}_\alpha, \tag{3.24}$$

for all $\mathbf{x} \in \mathbb{R}^d$, where $\boldsymbol{\tau}_1, \dots, \boldsymbol{\tau}_N$ are *deterministic*, second-rank, symmetric tensors[4]. Their actual values will be found later through optimization of the modified Hashin–Shtrikman functional HS. It should be noted that the trial stress-polarization field thus constructed is obviously statistically homogeneous and ergodic, since it is a linear combination of the statistically homogeneous and ergodic random fields $\chi_1, \dots, \chi_N$.Therefore, equation (3.23) holds and we have

$$\mathbb{E}\boldsymbol{\tau} = \sum_\alpha f_\alpha \boldsymbol{\tau}_\alpha, \quad \mathbb{E}\big[\chi_\alpha(\mathbf{0})\, \boldsymbol{\tau}(\mathbf{0}) \otimes \boldsymbol{\tau}(\mathbf{0})\big] = \sum_\alpha f_\alpha \boldsymbol{\tau}_\alpha \otimes \boldsymbol{\tau}_\alpha$$
$$\text{and} \quad \mathbf{R}_{\tau\tau}(\mathbf{r}) = \sum_{\alpha,\beta} \big[S_{\alpha\beta}(\mathbf{r}) - f_\alpha f_\beta\big]\, \boldsymbol{\tau}_\alpha \otimes \boldsymbol{\tau}_\beta, \tag{3.25}$$

where $S_{\alpha\beta}(\mathbf{r}) = \mathbb{E}[\chi_\alpha(\mathbf{0})\chi_\beta(\mathbf{r})]$ denotes the two-point probability function of phases α and β. Gathering equations (3.23) and (3.25), we finally find that

$$\tfrac{1}{2}\overline{\boldsymbol{\varepsilon}} : \mathbf{C}^{\text{eff}} : \overline{\boldsymbol{\varepsilon}} \le \lim_{|\Omega|\to+\infty} \mathbb{E}\big[\mathrm{HS}(\chi\boldsymbol{\tau}; \overline{\boldsymbol{\varepsilon}})\big] = \tfrac{1}{2}\overline{\boldsymbol{\varepsilon}} : \mathbf{C}_0 : \overline{\boldsymbol{\varepsilon}} + \sum_\alpha f_\alpha \boldsymbol{\tau}_\alpha : \overline{\boldsymbol{\varepsilon}}$$
$$- \tfrac{1}{2}\sum_\alpha f_\alpha \boldsymbol{\tau}_\alpha : (\mathbf{C}_\alpha - \mathbf{C}_0)^{-1} : \boldsymbol{\tau}_\alpha - \tfrac{1}{2}\sum_{\alpha,\beta} \boldsymbol{\tau}_\alpha : \mathbf{P}_{\alpha\beta} : \boldsymbol{\tau}_\beta, \tag{3.26}$$

where

$$\mathbf{P}_{\alpha\beta} = \big[S_{\alpha\beta}(\mathbf{0}) - f_\alpha f_\beta\big]\, \mathbf{P}_0 + \lim_{\delta\to 0} \int_{\substack{\mathbf{r}\in\mathbb{R}^d \\ \|\mathbf{r}\|\ge\delta}} \big[S_{\alpha\beta}(\mathbf{r}) - f_\alpha f_\beta\big] \boldsymbol{\Gamma}_0^\infty(\mathbf{r})\, \mathrm{d}V_{\mathbf{r}}. \tag{3.27}$$

The above bound on the macroscopic strain energy is then optimized with respect to the free parameters $\boldsymbol{\tau}_1, \dots, \boldsymbol{\tau}_N$, leading to the stationarity conditions

$$f_\alpha(\mathbf{C}_\alpha - \mathbf{C}_0)^{-1} : \boldsymbol{\tau}_\alpha + \sum_\beta \mathbf{P}_{\alpha\beta} : \boldsymbol{\tau}_\beta = f_\alpha \overline{\boldsymbol{\varepsilon}}, \tag{3.28}$$

and finally to the optimal bound

$$\tfrac{1}{2}\overline{\boldsymbol{\varepsilon}} : \mathbf{C}^{\text{eff}} : \overline{\boldsymbol{\varepsilon}} \le \tfrac{1}{2}\overline{\boldsymbol{\varepsilon}} : \mathbf{C}_0 : \overline{\boldsymbol{\varepsilon}} + \tfrac{1}{2}\sum_\alpha f_\alpha \boldsymbol{\tau}_\alpha : \overline{\boldsymbol{\varepsilon}}. \tag{3.29}$$

[4]It is recalled that, unless otherwise stated, sums over Greek indices run from 1 to N: $\sum_\alpha \cdots = \sum_{\alpha=1}^N \cdots$

When all two-point probability functions $S_{\alpha\beta}(\mathbf{r})$ depend on the norm of the lag vector $\mathbf{r}$ only (the microstructure is then said to be statistically isotropic in the weak sense), a closed-form expression of the above bound can be derived [Wil77]. Indeed, in that case

$$\mathbf{P}_{\alpha\beta} = f_\alpha(\delta_{\alpha\beta} - f_\beta)\,\mathbf{P}_0, \tag{3.30}$$

where $\mathbf{P}_0$ denotes Hill's tensor of a spherical inclusion embedded in the reference material $\mathbf{C}_0$. Then

$$\mathbf{C}^{\text{eff}} \leq \mathbf{C}^{\text{HS}} = \sum_\alpha f_\alpha \mathbf{C}_\alpha : \mathbf{A}_\alpha^{\text{HS}}, \tag{3.31}$$

with

$$\mathbf{A}_\alpha^{\text{HS}} = \mathbf{A}_\alpha^\infty : \left(\textstyle\sum_\beta f_\beta \mathbf{A}_\beta^\infty\right)^{-1} \quad \text{and} \quad \mathbf{A}_\alpha^\infty = \left[\mathbf{I} + \mathbf{P}_0 : (\mathbf{C}_\alpha - \mathbf{C}_0)\right]^{-1}, \tag{3.32}$$

which denote the Hashin–Shtrikman and dilute estimates of the strain localization tensor of phase $\alpha = 1, \ldots, N$, respectively. This completes the derivation of the classical bounds of Hashin and Shtrikman [HS62a] for weakly isotropic heterogeneous materials. Keeping this derivation in mind will help understand the developments presented in the remainder of this chapter.

Before we proceed, it should be observed that the above developments have successfully been extended to so-called *ellipsoidal* distributions in reference [Wil77] and more famously – for particulate microstructures– in reference [PW95]. However, the physical meaning of these distribution remains rather mysterious. In particular, it is not clear whether such microstructures are realizable, except in the trivial case where *all* two-point probability functions $S_{\alpha\beta}$ depend on the same quantity $\sqrt{\mathbf{r}\cdot\mathbf{Q}\cdot\mathbf{r}}$ ($\mathbf{Q}$: second-rank, symmetric, positive definite tensor).

***

In the previous section, we have introduced a new apparent stiffness $\mathbf{C}^{\text{mix}}(\mathbf{C}_0, \Omega)$ that better lends itself to estimation through an integral equation of the Lippmann–Schwinger type than the usual apparent stiffness $\mathbf{C}^{\text{ess}}(\Omega)$ associated with essential boundary conditions. Contrary to what was suggested in the literature, $\mathbf{C}^{\text{mix}}(\mathbf{C}_0, \Omega)$ should not be considered as approximating $\mathbf{C}^{\text{ess}}(\Omega)$ – and in fact, there is no need to. This new apparent stiffness is consistent in the sense of homogenization: for infinitely large SVEs, the effective stiffness is indeed recovered. The modified Hashin–Shtrikman functional – already used in e.g. [PW95]; [Wil77] – delivers rigorous bounds on $\mathbf{C}^{\text{mix}}(\mathbf{C}_0, \Omega)$, hence on the effective stiffness $\mathbf{C}^{\text{eff}}$.

These results can of course be used for the determination of Hashin–Shtrikman like bounds on the effective properties (as will be illustrated in the remainder of this chapter). In the next chapter, it will further be shown that the modified Lippmann–Schwinger equation and Hashin–Shtrikman principle are essential ingredients leading to a variational form of the equivalent inclusion method (see section 4.3).

3.2 The (hopeless?) quest for improved bounds

The celebrated bounds of Hashin and Shtrikman [HS62a] are *universal* in the sense that they hold for *any* (weakly isotropic) composite. Although this universality is usually seen as a

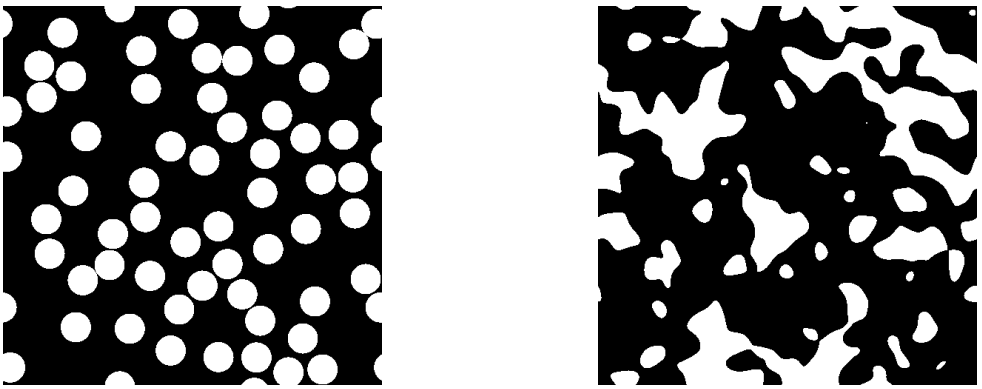

Figure 3.2: Hashin–Shtrikman bounds cannot discriminate between the above two isotropic microstructures, although they *look* different. The microstructure on the left-hand side represents a 2D assembly of monodisperse hard disks, generated by a standard Monte–Carlo method [AT87]. The microstructure on the right-hand side (courtesy O. Zerhouni) was generated through thresholding of a Gaussian random field [Lev98]; [RT95]. In both cases, the volume fraction of the "white" phase is $f_{\text{white}} = 30\,\%$.

strength, I tend to see it as a call for improved bounds. Indeed, the classical bounds incorporate only a very limited set of statistical descriptors of the microstructure (namely, the volume fractions of all phases[5]). As such, the Hashin–Shtrikman bounds cannot discriminate between the two (isotropic, but very different) microstructures depicted in figure 3.2.

The Hashin–Shtrikman bounds are optimal second-order bounds in the sense that they are exact up to second-order in the difference between the elastic properties of the various phases of the composite. Based on different variational principles and/or trial fields, higher-order bounds have been derived – see section 21.2 in reference [Tor02] for a thorough review. Beran and Molyneux [BM66] and McCoy [McC70] derived third-order bounds that were further simplified by Milton [Mil81]; [Mil82]. Fourth-order bounds were also derived by Milton and Phan-Thien [MP82]. Evaluation of these bounds is of increasing complexity. Indeed, higher-order microstructural information is included in these bounds through complex quantities that are difficult to measure experimentally (or compute numerically on a virtual microstructure) and have no intuitive physical meaning. For example, the third-order bounds of isotropic, two-phase materials require the following microstructural parameters

$$\zeta_1 = \frac{9}{2f_1f_2}I_2, \quad \eta_1 = \frac{5\zeta_1}{21} + \frac{150}{7f_1f_2}I_4, \tag{3.33}$$

with

$$I_k = \lim_{\delta\to 0} \int_{\substack{r,s\geq\delta \\ -1\leq u\leq 1}} P_k(u)\left[S_{111}(r,s,t) - \frac{S_{11}(r)S_{11}(s)}{f_1}\right] \mathrm{d}u \frac{\mathrm{d}r}{r}\frac{\mathrm{d}s}{s}. \tag{3.34}$$

In the above integral, P_k denotes the k-th order Legendre polynomial, S_{11} (resp. S_{111}) the two-point (resp. three-point) probability function. It is observed that due to isotropy, the two-point probability function depends on the norm of the lag vector only, while the three-point

[5] And possibly aspect ratios and distribution of orientations for ellipsoidal distributions, not discussed here.

probability function depends on the sides r, s, t of the triangle formed by the three points and u denotes the cosine of the angle between the sides r and s of the triangle ($t = \sqrt{r^2 + s^2 - 2rsu}$).

It should be emphasized that none of the above higher-order bounds have been obtained by means of the Hashin–Shtrikman principle, while fairly simple (simplistic) trial fields [see equation (3.24)] are used in combination with this principle to derive the second-order bounds. I therefore found it natural to seek improved bounds by means of the Hashin–Shtrikman principle and *enriched* trial (stress-polarization) fields. This however proved to be a formidable quest for which I have not yet succeeded.

In the remainder of this section, two attempts at producing "good" enriched trial fields for statistically isotropic microstructures are discussed. Section 3.2.1 describes a naive attempt at accounting for the particle-size distribution in a particulate composite. Then, sections 3.2.2 and 3.2.3 present a generic approach for the production of trial stress-polarization fields that make use of enhanced descriptors of the microstructure. Both attempts failed in the sense that the classical bounds of Hashin and Shtrikman [HS62a] were retrieved (enriching the trial fields did not improve the bounds). I do believe however that these failed attempts show the route to an approach that might not fail; as such, these negative results deserve to be presented in this report.

Before we proceed, the terminology used in the present section will be clarified. It is recalled that the classical, phase-wise constant stress-polarization trial field (3.24) considered in reference [HS62b] reads: $\boldsymbol{\tau} = \sum_\alpha \chi_\alpha \boldsymbol{\tau}_\alpha$. In this expression, the microstructure is accounted for by means of the indicator functions $\chi_1, \ldots, \chi_N$. Any such function that returns a local information on the geometry of the microstructure will be called a *probe*. A probe should be understood as a random field defined over the microstructure. The bound on the effective elastic moduli that results from the optimization of the Hashin–Shtrikman functional with respect to these trial stress-polarizations depends on the volume fractions $f_1, \ldots, f_N$, which are expectations of the $\chi_1, \ldots, \chi_N$. In what follows, expectations that are built with probes of the microstructure will be called *statistical descriptors*.

3.2.1 Failing to account for the particle-size distribution

In this section, we test a naive enrichment of the phase-wise constant trial field defined by equation (3.24). As a motivating example, we consider a two-phase composite with a bidisperse distribution of spherical inclusions. Of course, the equations of classical linear elasticity define no internal length and the effective properties should only be affected by the ratio of the radii of the inclusions. Our goal is to quantify this particle-size distribution effect.

The most natural enrichment of the trial stress-polarization (3.24) is probably the following three-term expression

$$\boldsymbol{\tau}(\mathbf{x}) = \chi_{\mathrm{m}}(\mathbf{x})\boldsymbol{\tau}_{\mathrm{m}} + \chi_1(\mathbf{x})\boldsymbol{\tau}_1 + \chi_2(\mathbf{x})\boldsymbol{\tau}_2, \tag{3.35}$$

where three phases have been introduced to estimate the effective properties of the two-phase composite *i.* the matrix: phase "m" (volume fraction f_{m}, stiffness $\mathbf{C}_{\mathrm{m}}$), *ii.* the large inclusions: phase "1" (radius a_1, volume fraction f_1, stiffness $\mathbf{C}_{\mathrm{i}}$) and *iii.* the small inclusions: phase "2" (radius a_2, volume fraction f_2, stiffness $\mathbf{C}_{\mathrm{i}}$). The total volume fraction of inclusions is of course $f_{\mathrm{i}} = f_1 + f_2$.

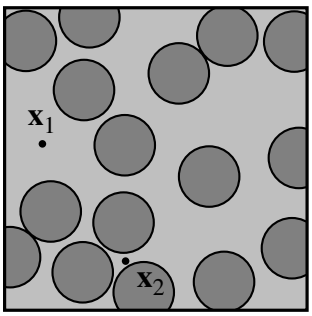

Figure 3.3: Classical Hashin–Shtrikman trial stress-polarizations are blind to the surroundings of the observation point. The value of the trial stress-polarization is the same for both points $\mathbf{x}_1$ and $\mathbf{x}_2$, despite the fact that $\mathbf{x}_1$ is surrounded by phase 1 (light gray), while $\mathbf{x}_2$ lies near the boundary with phase 2 (dark gray).

Optimizing the Hashin–Shtrikman functional HS with respect to these trial fields again leads to the linear system (3.28). It can then readily be verified that $\boldsymbol{\tau}_1 = \boldsymbol{\tau}_2$, and the classical Hashin–Shtrikman bounds are retrieved. In other words, this approach does not separate large and small pores.

This negative result was not fully expected. Indeed, the two-point probability functions $S_{\alpha\beta}$ *are* affected by the particle-size distribution. However, despite what equation (3.27) defining the P-tensors suggests, the full details of the two-point probability functions are not captured by $\mathbf{P}_{\alpha\beta}$. Indeed, assuming weak isotropy, equation (3.30) applies and the reminiscence of the particle-size distribution is lost at this point.

3.2.2 Considering alternative probes of the microstructure

The work described in this section has been published in reference [Bri17b]. It is motivated by two observations.

First, the phase-wise constant trial stress-polarization defined by equation (3.24) is insensitive to the neighborhood of the observation point, since $\boldsymbol{\tau}(\mathbf{x})$ depends on the phase at $\mathbf{x}$ only. Therefore the trial stress-polarization at points $\mathbf{x}_1$ and $\mathbf{x}_2$ will be identical in figure 3.3 despite the fact that $\mathbf{x}_1$ is surrounded by phase 1, while $\mathbf{x}_2$ lies near the boundary with phase 2.

Second, it is recalled that our initial goal was to produce bounds on the effective properties that incorporate advanced statistical descriptors of the microstructure. What these statistical descriptors should be is however an open question. Since the classical bounds of Hashin and Shtrikman [HS62a] depend on the volume fractions only (one-point probability functions), it is natural to try and incorporate the two-, three-, …n-point probability functions. However, these statistical descriptors are probably not the best suited to the task, as illustrated by the exact series expansion of the effective moduli derived by Torquato [Tor97]. In this work, it is shown that for isotropic materials, the two-point probability functions appear only in combination with higher-order probability functions. Therefore, any attempt at improving the Hashin–Shtrikman bounds with one- and two- point probability functions only will fail. Since higher-order probability functions are difficult to measure (even on virtual microstructures), another hierarchy of statistical descriptors should be considered.

To sum up, the classical trial stress-polarization (3.24) is based on probes (the indicator

functions χ_α) that ignore the neighborhood of the observation point and lead to statistical descriptors (the two-point probability functions $S_{\alpha\beta}$) that if considered alone are not relevant to homogenization within the framework of linear elasticity.

These observations led us to replace the point-wise information delivered by the indicator functions χ_α with probes of the microstructure that account (in an aggregated way) for the geometry of a *neighborhood* surrounding the observation point. The local volume fractions are simple probes that fall into this category and were shown through effective-field approaches to influence significantly the effective elastic properties [WBH99].

The local volume fractions are defined with respect to a specified, sliding window $\mathscr{W} \subset \mathbb{R}^d$ centered at the origin ($\mathbf{0} \in \mathscr{W}$). For $\alpha = 1, \dots, N$, the local volume fraction $f_\alpha^{\mathrm{loc}}(\mathbf{x}; \mathscr{W})$ is then defined as the volume fraction of phase α in the window $\mathscr{W}$ centered at $\mathbf{x}$

$$f_\alpha^{\mathrm{loc}}(\mathbf{x}; \mathscr{W}) = \frac{1}{|\mathscr{W}|} \int_{\mathbf{y} \in \mathbf{x} + \mathscr{W}} \chi_\alpha(\mathbf{y}) \, \mathrm{d}V_{\mathbf{y}}. \tag{3.36}$$

Contrary to the global volume fraction f_α, which is deterministic, the local volume fraction f_α^{loc} is a random variable that depends on the size (and shape) of the sliding window $\mathscr{W}$. For infinitely small windows, f_α^{loc} can only take the values 0 or 1 (since $f_\alpha^{\mathrm{loc}} \sim \chi_\alpha$ in that case); for infinitely large windows, it takes the constant value f_α (global volume fraction). For finite-size sliding windows, it is randomly distributed between 0 and 1. The ensemble average of f_α^{loc} is obviously f_α; the asymptotic behavior of its variance is summarized below [Kan+03]

$$\lim_{|\mathscr{W}| \to 0} \operatorname{var} f_\alpha^{\mathrm{loc}} = f_\alpha(1 - f_\alpha) \quad \text{and} \quad \lim_{|\mathscr{W}| \to +\infty} |\mathscr{W}| \operatorname{var} f_\alpha^{\mathrm{loc}} = \int_{\mathbf{r} \in \mathbb{R}^3} S_{\alpha\alpha}(\mathbf{r}) \, \mathrm{d}V_{\mathbf{r}}. \tag{3.37}$$

It is observed that the f_α^{loc} are not independent, as $f_1^{\mathrm{loc}} + \cdots + f_N^{\mathrm{loc}} = 1$. Therefore, all enriched trial fields that will be proposed in the remainder of this section will depend on $f_1^{\mathrm{loc}}, \dots, f_{N-1}^{\mathrm{loc}}$ only. A possible form for $\boldsymbol{\tau}$ would then be

$$\boldsymbol{\tau}(\mathbf{x}) = \tilde{\boldsymbol{\tau}}\big[f_1^{\mathrm{loc}}(\mathbf{x}; \mathscr{W}), \dots, f_{N-1}^{\mathrm{loc}}(\mathbf{x}; \mathscr{W})\big], \tag{3.38}$$

where the *deterministic* mapping $(\phi_1, \dots, \phi_{N-1}) \mapsto \tilde{\boldsymbol{\tau}}(\phi_1, \dots, \phi_{N-1})$ is to be specified. The above trial stress-polarization does account for the neighborhood of the observation point $\mathbf{x}$. However, it does not depend on the phase at $\mathbf{x}$, which is an unrealistic assumption. Equation (3.38) is therefore altered as follows

$$\boldsymbol{\tau}(\mathbf{x}) = \sum_\alpha \chi_\alpha(\mathbf{x}) \, \tilde{\boldsymbol{\tau}}_\alpha\big[f_1^{\mathrm{loc}}(\mathbf{x}; \mathscr{W}), \dots, f_{N-1}^{\mathrm{loc}}(\mathbf{x}; \mathscr{W})\big], \tag{3.39}$$

that now require N *deterministic* mappings $(\phi_1, \dots, \phi_{N-1}) \mapsto \tilde{\boldsymbol{\tau}}_\alpha(\phi_1, \dots, \phi_N)$ for $\alpha = 1, \dots, N$. Plugging expression (3.39) into equation (3.23) and optimizing the resulting bound (3.22) with respect to the unknown mappings $\tilde{\boldsymbol{\tau}}_1, \dots, \tilde{\boldsymbol{\tau}}_N$ should in theory deliver: *i.* the optimal $\tilde{\boldsymbol{\tau}}_\alpha$ and *ii.* a bound on the effective properties that account for the local volume fractions. This general approach is probably intractable, and I chose *a priori* in reference [Bri17b] mappings that are polynomial in the local volume fractions

$$\boldsymbol{\tau}(\mathbf{x}) = \sum_{\alpha=1}^{N} \sum_{p=0}^{M} \chi_\alpha(\mathbf{x}) \big[f_1^{\mathrm{loc}}(\mathbf{x}; \mathscr{W})\big]^p \boldsymbol{\tau}_{\alpha p}, \tag{3.40}$$

where M denotes the order of the polynomials, and $\boldsymbol{\tau}_{\alpha p}$ are deterministic, second-rank, symmetric tensors. It should be noted that the above expression is indeed an enrichment of the initial expression (3.24) (which corresponds to the $p = 0$ terms).

The resulting bounds are expected to depend on the size of the sliding window $\mathscr{W}$. For infinitely small or infinitely large windows, the trial stress-polarization (3.40) is phase-wise constant, and the classical Hashin–Shtrikman bounds are recovered. In all other cases, the finite size of the sliding window $\mathscr{W}$ introduces a length-scale to which the characteristic length-scale(s) of the microstructure could be compared. Therefore, the resulting bounds might be expected to be sensitive to (relative) sizes, thus to particle-size distributions.

Similarly to section 3.1.5, to estimate the bounds resulting from the particular choice (3.40) of the trial stress-polarization field, we must now evaluate the quantity $\lim_{|\Omega|\to+\infty} \mathbb{E}\big[\mathrm{HS}(\chi\boldsymbol{\tau};\overline{\boldsymbol{\varepsilon}})\big]$.

3.2.3 Evaluation of the Hashin–Shtrikman functional

In the present section, we consider the following slight generalization of the enriched trial stress-polarization (3.40)

$$\boldsymbol{\tau}(\mathbf{x}) = \sum_{\alpha=1}^{N}\sum_{p=0}^{M} \chi_\alpha(\mathbf{x})\psi_p(\mathbf{x})\boldsymbol{\tau}_{\alpha p}, \tag{3.41}$$

where $\psi_0, \dots, \psi_M$ are M general probes of the microstructure. Unless otherwise stated, sums over Greek indices ($\alpha, \beta, \dots$) run from 1 to N, while sums over Latin indices ($p, q, \dots$) run from 0 to M; this convention applies to the present section 3.2.3 as well as the next section 3.2.4. We assume that $\psi_0 = 1$, in order to ensure that the above expression is indeed an enrichment of the classical (phase-wise constant) trial stress-polarization field (3.24). Furthermore, the above trial stress-polarization field must be weakly statistically homogeneous (see assumption B.1 in appendix B). It is therefore required that $\mathbb{E}\big[\chi_\alpha(\mathbf{x})\psi_p(\mathbf{x})\big]$ and $\mathbb{E}\big[\chi_\alpha(\mathbf{x})\psi_p(\mathbf{x})\chi_\beta(\mathbf{x}+\mathbf{r})\psi_q(\mathbf{x}+\mathbf{r})\big]$ be translation-invariant (with respect to $\mathbf{x}$), and we introduce the following statistical descriptors of the microstructure

$$\Psi_{\alpha p} = \mathbb{E}\big[\chi_\alpha(\mathbf{0})\psi_p(\mathbf{0})\big] \quad \text{and} \quad \Psi_{\alpha p\beta q}(\mathbf{r}) = \mathbb{E}\big[\chi_\alpha(\mathbf{0})\chi_\beta(\mathbf{r})\psi_p(\mathbf{0})\psi_q(\mathbf{r})\big]. \tag{3.42}$$

It is recalled that the quantity $\lim_{|\Omega|\to+\infty} \mathbb{E}\big[\mathrm{HS}(\chi\boldsymbol{\tau};\overline{\boldsymbol{\varepsilon}})\big]$ is given by equation (3.23). Each term of this expression was evaluated separately in reference [Bri17b]. Substituting

$$\mathbb{E}\boldsymbol{\tau} = \sum_{\alpha,p} \Psi_{\alpha p}\boldsymbol{\tau}_{\alpha p} \quad \text{and} \quad \mathbf{R}_{\tau\tau}(\mathbf{r}) = \sum_{\alpha,\beta,p,q} \Psi_{\alpha p\beta q}(\mathbf{r})\boldsymbol{\tau}_{\alpha p} \otimes \boldsymbol{\tau}_{\beta q}, \tag{3.43}$$

into equation (3.23) leads to the following upper-bound on the effective elastic energy of the heterogeneous material (assuming that the reference material is stiffer than all phases in the composite, $\mathbf{C}_0 \geq \mathbf{C}_\alpha$, $\alpha = 1, \dots, N$)

$$\begin{aligned}\tfrac{1}{2}\overline{\boldsymbol{\varepsilon}} : \mathbf{C}^{\mathrm{eff}} : \overline{\boldsymbol{\varepsilon}} \leq \tfrac{1}{2}\overline{\boldsymbol{\varepsilon}} : \mathbf{C}_0 : \overline{\boldsymbol{\varepsilon}} + \sum_{\alpha,p} \Psi_{\alpha p}\boldsymbol{\tau}_{\alpha p} : \overline{\boldsymbol{\varepsilon}} - \tfrac{1}{2}\sum_{\alpha,p,q} \Psi_{\alpha p\alpha q}(\mathbf{0})\,\boldsymbol{\tau}_{\alpha p} : (\mathbf{C}_\alpha - \mathbf{C}_0)^{-1} : \boldsymbol{\tau}_{\alpha q} \\ - \tfrac{1}{2}\sum_{\alpha,\beta,p,q} \boldsymbol{\tau}_{\alpha p} : \mathbf{P}_{\alpha p\beta q} : \boldsymbol{\tau}_{\beta q},\end{aligned} \tag{3.44}$$

where

$$\mathbf{P}_{\alpha p\beta q} = \left[\Psi_{\alpha p\beta q}(\mathbf{0}) - \Psi_{\alpha p}\Psi_{\beta q}\right]\mathbf{P}_0 + \lim_{\delta\to 0}\int_{\substack{\mathbf{r}\in\mathbb{R}^d\\ \|\mathbf{r}\|\geq\delta}}\left[\Psi_{\alpha p\beta q}(\mathbf{r}) - \Psi_{\alpha p}\Psi_{\beta q}\right]\boldsymbol{\Gamma}_0^{\infty}(\mathbf{r})\,\mathrm{d}V_{\mathbf{r}}. \quad (3.45)$$

The bound given by equation (3.44) is optimal if the $\boldsymbol{\tau}_{\alpha p}$ solve the following linear system

$$\sum_q \Psi_{\alpha p\alpha q}(\mathbf{0})\,(\mathbf{C}_\alpha - \mathbf{C}_0)^{-1} : \boldsymbol{\tau}_{\alpha q} + \sum_{\beta,q}\mathbf{P}_{\alpha p\beta q} : \boldsymbol{\tau}_{\beta q} = \Psi_{\alpha p} : \overline{\boldsymbol{\varepsilon}}, \quad (3.46)$$

and we have in this case

$$\tfrac{1}{2}\overline{\boldsymbol{\varepsilon}} : \mathbf{C}^{\mathrm{eff}} : \overline{\boldsymbol{\varepsilon}} \leq \tfrac{1}{2}\overline{\boldsymbol{\varepsilon}} : \mathbf{C}_0 : \overline{\boldsymbol{\varepsilon}} + \tfrac{1}{2}\sum_{\alpha,p}\Psi_{\alpha p}\boldsymbol{\tau}_{\alpha p} : \overline{\boldsymbol{\varepsilon}}. \quad (3.47)$$

In general, the system (3.46) must be solved numerically. Then, the bound (3.47) can be evaluated. This bound is expected to improve on the classical Hashin–Shtrikman bound, as discussed in section 3.2.4 below.

3.2.4 Towards improved bounds on the effective moduli?

It is natural, to assess the quality of the bound (3.47), to first assume that the descriptors $\psi_1, \ldots, \psi_M$ of the microstructure are weakly isotropic in the sense that the two-point correlations $\Psi_{\alpha p\beta q}(\mathbf{r})$ defined by equation $(3.42)_2$ depend solely on the norm r of the lag vector $\mathbf{r}$: $\psi_{\alpha p\beta q}(\mathbf{r}) = \psi_{\alpha p\beta q}(r)$.

The local volume fractions defined in section 3.2.2 can be cited as an example of isotropic probing of the microstructure when the sliding window $\mathscr{W}$ is spherical. In other words, the following statistical descriptors of the microstructure

$$\langle \chi_\alpha(\mathbf{0})\left[f_\beta^{\mathrm{loc}}(\mathbf{0};\mathscr{W})\right]^p \chi_\gamma(\mathbf{r})\left[f_\delta^{\mathrm{loc}}(\mathbf{r};\mathscr{W})\right]^q\rangle \quad (3.48)$$

are isotropic, provided that $\mathscr{W}$ is spherical.

For isotropic probes, expressions (3.46) and (3.47) simplify considerably, since the second term in equation (3.45) vanishes

$$\mathbf{P}_{\alpha p\beta q} = \left[\Psi_{\alpha p\beta q}(\mathbf{0}) - \Psi_{\alpha p}\psi_{\beta q}\right]\mathbf{P}_0. \quad (3.49)$$

In the linear system (3.46), it is then convenient to isolate the $\boldsymbol{\tau}_{\beta q}$ with $q = 0$. Observing that $\Psi_{\alpha 0} = f_\alpha$ and $\Psi_{\alpha p\beta 0}(\mathbf{0}) = \delta_{\alpha\beta}\Psi_{\alpha p}$, and plugging equation (3.49) into equation (3.46) then leads to the linear system

$$\begin{aligned}\Psi_{\alpha p}\left[(\mathbf{C}_\alpha - \mathbf{C}_0)^{-1} + \mathbf{P}_0\right] : \boldsymbol{\tau}_{\alpha 0} - \Psi_{\alpha p}\sum_{\beta=1}^{N} f_\beta\mathbf{P}_0 : \boldsymbol{\tau}_{\beta 0}\\ + \sum_{q=1}^{M}\Psi_{\alpha p\alpha q}(\mathbf{0})\,(\mathbf{C}_\alpha - \mathbf{C}_0)^{-1} : \boldsymbol{\tau}_{\alpha q} + \sum_{\beta=1}^{N}\sum_{q=1}^{M}\mathbf{P}_{\alpha p\beta q} : \boldsymbol{\tau}_{\beta q} = \Psi_{\alpha p}\overline{\boldsymbol{\varepsilon}}. \quad (3.50)\end{aligned}$$

Comparing the above equation with equation (3.28), it is found that the solution is such that $\boldsymbol{\tau}_{1,0}, \dots, \boldsymbol{\tau}_{N,0}$ coincides with the classical Hashin–Shtrikman polarizations, and that $\boldsymbol{\tau}_{\alpha p} = \mathbf{0}$ for $\alpha = 1, \dots, N$ and $p = 1, \dots, M$. In other words, the optimal enriched trial stress-polarization (3.41) coincides with the classical Hashin–Shtrikman trial stress-polarization and does not result in an improved bound on the macroscopic elastic energy!

Isotropy is again the culprit. In the classical approach of Hashin and Shtrikman (see section 3.1.5), the two-point probability function vanishes for isotropic microstructures. In the present, extended approach, the enriched part of the trial stress-polarization vanishes for isotropic probes $\psi_1, \dots, \psi_M$.

There is nothing to be done with the fact that the microstructure is isotropic. What can be acted upon is the probes: we must make sure not to probe the microstructure isotropically. Going back to the local volume fractions, isotropy of the probes is broken as soon as the window $\mathscr{W}$ is no longer spherical.

This suggests to implement the method presented here with the local volume fractions as probes, and a non-spherical window $\mathscr{W}$. However, with only one such window, the resulting bound is expected to be anisotropic (even for isotropic microstructures). To restore the isotropy of the bounds, the window $\mathscr{W}$ should therefore be rotated in all directions. I intend to investigate this extension of the work presented here, with the hope that improved bounds on the effective stiffness can be obtained.

***

In the previous section, we discussed some attempts at enriching the trial stress-polarizations in order to produce bounds on the effective properties that are sharper than the classical Hashin–Shtrikman bounds. While these attempts have not yet been successful, the remainder of this chapter is devoted to various applications of the Hashin–Shtrikman principle (with simple trial stress-polarizations) that do deliver useful bounds or estimates.

3.3 Nanocomposites

This section describes the derivation of Hashin–Shtrikman bounds on the effective moduli of nanocomposites with spherical inclusions. This work was initially published in [BDK10a]; [BDK10b]. Quoting from the *Aims and scope* section of the *Nanocomposite* journal[6], nanocomposites can be defined as follows

> "Nanocomposites are multiphase or hybrid materials which when combined together, display markedly different properties from the bulk components. Nanocomposites differ from conventional composite materials due to the nanoscale dimensions of the filler phase and the exceptionally high surface to volume ratio of this phase. As a result they often possess unique mechanical, thermal, electrical, optical or catalytic properties which are controlled by factors such as local chemistry, mobility, morphology, or crystallinity.

[6] http://www.tandfonline.com/action/journalInformation?show=aimsScope&journalCode=ynan20, last retrieved 2016-12-14

> In addition, nanocomposites often offer a combination of several properties, making them even more attractive as multifunctional materials for the future, with potential applications in aerospace, healthcare, energy materials, sensors and other systems."

Depending on the material forming the matrix, nanocomposites are often classified as polymer-matrix composites [Arm15]; [ASI16] and ceramic-matrix composites [Pal15]. Nanofillers can have various shapes, ranging from elongated (e.g. carbon nanotubes [Bha16]; [Mit+15]) to plate-like (e.g. clay platelets [Aze+13]) and nearly equi-axed nanoparticles (e.g. nanospheres [SDS09]).

From the mechanical standpoint, nanomaterials are known to exhibit size-effects: the volume fraction being fixed, the overall properties (stiffness, toughness) of the composite generally improve when the size of the nanofillers is decreased [Chi+05]; [CJS06]; [FP03]; [Rey+01]. Surface stresses that develop at the matrix-inclusion interface [MA04] might explain this size effect. Indeed, the generalized Young–Laplace [GM75]; [GM78] that governs the equilibrium of these solid-solid interfaces is size-dependent since it involves the local curvature of the interface.

Predictive models of the effective elastic properties of nanocomposites therefore require homogenization techniques that account for these size-effects. The general micromechanical framework was set by Duan, Wang, Huang, and Karihaloo [Dua+05], who also derived Mori–Tanaka and self-consistent estimates for nanocomposites with spherical inclusions. Le Quang and He [LH07] then extended these results to transverse isotropic materials. In reference [LH08], the same authors also proposed extensions to nanocomposites of the Voigt and Reuss bounds. In their concluding remarks, they noted that

> "The next step toward developing a more involved variational approach will be the extension of the well-known Hashin–Shtrikman variational principles to inhomogeneous materials with linear spring-layer and coherent imperfect interfaces. This extension is certainly of great importance but seems to be very difficult for the moment."

In references [BDK10a]; [BDK10b], I found that this extension was in fact quite feasible. For reasons that will be exposed in section 3.3.4, only lower bounds on the elastic moduli could be derived. At that time, I found it quite remarkable that the new bounds should coincide with the Mori–Tanaka estimates of Duan, Wang, Huang, and Karihaloo [Dua+05].

In the present section, the main steps of the derivation of these bounds are outlined (the reader is referred to references [BDK10a]; [BDK10b] for more details). The model of elastic interface of Gurtin and Murdoch [GM75] is first introduced in section 3.3.1. For this model to fit in the Hashin–Shtrikman variational framework, this interface is then temporarily replaced in section 3.3.2 with an interphase of small, but finite thickness. How to derive explicit lower-bounds on the bulk and shear moduli of the effective material with interphases is then discussed in sections 3.3.3, 3.3.4 and 3.3.5; letting the thickness of the interphase go to zero finally provides the seeked bounds on the effective properties of the nanocomposite. Section 3.3.6 goes back to the remarkable coincidence of Mori–Tanaka estimates and Hashin–Shtrikman bounds; it is shown *a posteriori* that this is a rather general result.

3.3.1 The interface model of Gurtin and Murdoch

Near the interface between two phases, the environment of atoms is very different from that of the bulk phases, which results in an excess of strain energy near the interface. In turn, surface energy gives rise to surface stresses through the celebrated Shuttleworth [Shu50] equation. This is fairly well known for liquid-liquid interfaces (see for example chapter 6 in reference [Cou10]), where the so-called surface tension is constant.

Surface stresses also develop at any solid-solid interface [MA04]. However, their macroscopic effects are really noticeable for higly curved interfaces only (nanocomposites): surface stresses can therefore safely be neglected in general.

It should be observed at this point that the connection between surface energy, surface tension and surface stress is still highly debated [HJ13]; [Mak14]. This debate, which relies on subtle thermodynamical considerations, is outside the scope of the present work. Also, attention must be paid to the framework (Lagrangian vs. Eulerian) that is adopted for the description of the deformation/creation of interfaces [Cou10]. This can however be overlooked within the framework of small deformation and displacement.

The surface stress is a second-rank, symmetric tensor of the plane tangent to the interface that will be denoted $\boldsymbol{\sigma}_\mathrm{s}$ in what follows. When interface effects occur, the bulk equilibrium equations are unchanged. However, the surface stress induces a jump of the traction vector $\boldsymbol{\sigma}\cdot\mathbf{n}$ ($\boldsymbol{\sigma}$: bulk stress; $\mathbf{n}$: normal to the interface); both are related through the generalized Young–Laplace equation [GM75]

$$\partial_\alpha\boldsymbol{\sigma}_\mathrm{s}\cdot\mathbf{a}^\alpha+[\![\boldsymbol{\sigma}]\!]\cdot\mathbf{n}=\mathbf{0}, \tag{3.51}$$

where (ξ^1,ξ^2) denotes a parameterization of the interface, ∂_α denotes the partial derivative with respect to ξ^α ($\alpha=1,2$) and $(\mathbf{a}^1,\mathbf{a}^2)$ denotes the natural (contravariant) basis.

To complement the generalized Young–Laplace equation, a "constitutive equation" must also be provided for the interface. Within the framework of linear elasticity, the following simple surface stress-surface strain relationship is adopted [GM75]: $\boldsymbol{\sigma}_\mathrm{s}=\mathbf{L}_\mathrm{s}:\boldsymbol{\varepsilon}_\mathrm{s}$, where $\boldsymbol{\varepsilon}_\mathrm{s}$ denotes the classical membrane strain of shell theory. When the two phases are perfectly bound, the displacement is continuous accross the interface, and $\boldsymbol{\varepsilon}_\mathrm{s}=\mathbf{a}\cdot\boldsymbol{\varepsilon}\cdot\mathbf{a}$, where $\mathbf{a}=\mathbf{I}-\mathbf{n}\otimes\mathbf{n}$ denotes the metric tensor of the interface and $\boldsymbol{\varepsilon}$ denotes as usual the bulk strain. The constitutive relation thus introduced is associated to the two adjacent phases. If both bulk phases are isotropic, it is natural to assume the following isotropic representation of the surface stiffness tensor $\mathbf{L}_\mathrm{s}$

$$\mathbf{L}_\mathrm{s}=\left[\lambda_\mathrm{s}a_{\alpha\beta}a_{\gamma\delta}+\mu_\mathrm{s}(a_{\alpha\gamma}a_{\beta\delta}+a_{\alpha\delta}a_{\beta\gamma})\right]\mathbf{a}^\alpha\otimes\mathbf{a}^\beta\otimes\mathbf{a}^\gamma\otimes\mathbf{a}^\delta, \tag{3.52}$$

where λ_s and μ_s are the Lamé constants of the interface. Since $\mathbf{L}_\mathrm{s}$ is a tensor of the tangent plane, the constitutive relation can be written in terms of the bulk strain

$$\boldsymbol{\sigma}_\mathrm{s}=\mathbf{L}_\mathrm{s}:\boldsymbol{\varepsilon}. \tag{3.53}$$

3.3.2 The equivalent interphase

Following Hashin [Has02] the solid-solid *interfaces* were replaced in references [BDK10a]; [BDK10b] with *interphases* of small, but finite thickness. The Hashin–Shtrikman principle

then applies verbatim,which led to a derivation of thickness-dependent bounds on the effective elastic moduli of nanocomposites. Then, letting the thickness of the interphase go to zero, bounds on the effective properties of the composite with interfaces were obtained.

In reference [BDK10a], it was shown that taking $\frac{a}{h}\mathbf{C}_\mathrm{s}$ (a: radius of the spherical inhomogeneity; h: thickness of the interphase) for the bulk elastic stiffness of the interphase ensures the consistency of this approach, with

$$\mathbf{C}_\mathrm{s} = \frac{4\mu_\mathrm{s}}{a}\frac{\lambda_\mathrm{s}+\mu_\mathrm{s}}{2\mu_\mathrm{s}-\lambda_\mathrm{s}}\mathbf{J} + 2\frac{\mu_\mathrm{s}}{a}\mathbf{K}. \tag{3.54}$$

In other words, with this choice, the solution to the elastic equilibrium of a composite with interphases tends to that of the same composite with interfaces as the thickness of the interphases goes to 0.

3.3.3 Homogenization of nanocomposites

Determination of the effective properties of nanocomposites proceeds similarly to classical composites [CD02]; [Dua+05]. The corrector problem (2.6) introduced in section 2.1 must now be complemented with the generalized Young–Laplace equation (3.51) and the constitutive equation (3.53). Owing to the continuity of the displacement, it is natural to adopt essential boundary conditions. Indeed, how to define natural boundary conditions when the boundary of the SVE includes solid-solid interfaces remains unclear. It should be observed that the macroscopic stress $\langle\boldsymbol{\sigma}\rangle$ now includes surface stresses

$$\langle\boldsymbol{\sigma}\rangle = \frac{1}{|\Omega|}\int_\Omega \boldsymbol{\sigma}\,\mathrm{d}V + \frac{1}{|\Omega|}\int_\Sigma \boldsymbol{\sigma}_\mathrm{s}\,\mathrm{d}S, \tag{3.55}$$

where Σ denotes the union of all interfaces.

To close this section, it is observed that if equivalent interphases are used in place of interfaces, it is sufficient to solve the standard corrector problem (2.6).

3.3.4 Bounds on the effective properties of nanocomposites

The derivation presented in references [BDK10a]; [BDK10b] is restricted to simple composites with monodisperse, spherical inclusions (radius: a) embedded in a homogeneous matrix. Assuming isotropic, linear elasticity, $\mathbf{C}_\mathrm{m}$ (resp. $\mathbf{C}_\mathrm{i}$, $\mathbf{L}_\mathrm{s}$) denotes the stiffness of the matrix (resp. inclusions, interfaces). As argued in section 3.3.2, the interfaces are replaced with interphases of finite thickness h and stiffness $\frac{a}{h}\mathbf{C}_\mathrm{s}$.

We are now left with the problem of bounding the effective properties of an assembly of composite spheres (inclusion+interphase). In order to apply the Hashin–Shtrikman principle, we must select a reference material and define a suitable trial stress-polarization.

Selection of the reference material is the result of two observations. First, the stiffness of the interphase scales as h^{-1}: it becomes infinitely large as $h \to 0$ and it is not possible to find a reference material that is stiffer than all phases. Second, it is generally true that $\mathbf{C}_\mathrm{i} \geq \mathbf{C}_\mathrm{m}$ (inclusions act as reinforcement in nanocomposites). The stiffness of the matrix is therefore

selected as reference material ($\mathbf{C}_0 = \mathbf{C}_\mathrm{m}$), which will result in a lower bound on the effective properties of the nanocomposite.

Owing to our choice of the reference material, it is sufficient to define the trial stress-polarization in the inclusions and interphases (it must be null in the matrix). It is natural to first consider phase-wise constant trial stress-polarizations. Since the microstructure is isotropic, equations (3.31) and (3.32) apply. It is then readily found that for vanishing thickness of the interphase, the lower-bound on the effective stiffness that is obtained is the classical Hashin–Shtrikman bound on two-phase composites with *perfect* interfaces. In other words, the interface stiffness is not accounted for. In order to improve on these bounds, it is necessary to consider more complex trial stress-polarizations.

3.3.5 Bounds based on morphologically representative patterns

The selected trial stress-polarizations selected in references [BDK10a]; [BDK10b] are not uniform, but are identical within each composite sphere (spherical inclusion + finite-thickness interphase)

$$\boldsymbol{\tau}(\mathbf{x}) = \sum_{i=1}^{+\infty} \boldsymbol{\tau}_\mathrm{p}(\mathbf{x} - \mathbf{x}^i), \tag{3.56}$$

where $\mathbf{x}^1, \mathbf{x}^2, \ldots$ denote the centers of the spherical inclusions[7] and $\boldsymbol{\tau}_\mathrm{p}(\mathbf{r})$ is a deterministic field (the randomness of $\boldsymbol{\tau}$ comes from the location of the inclusions only). Since the matrix is not polarized, $\boldsymbol{\tau}_\mathrm{p}(\mathbf{r})$ must be null for $\|\mathbf{r}\| \geq a + h$. Of course, the case of phase-wise constant stress-polarizations explored in section 3.3.4 corresponds to

$$\boldsymbol{\tau}_\mathrm{p}(\mathbf{r}) = \boldsymbol{\tau}_\mathrm{i} \text{ for } \|\mathbf{r}\| \leq a \quad \text{and} \quad \boldsymbol{\tau}_\mathrm{p}(\mathbf{r}) = \boldsymbol{\tau}_\mathrm{s} \text{ for } a \leq \|\mathbf{r}\| \leq a + h, \tag{3.57}$$

where $\boldsymbol{\tau}_\mathrm{i}$ and $\boldsymbol{\tau}_\mathrm{s}$ are constant, second-rank, symmetric tensors.

In order to derive bounds on the effective properties, we must again evaluate the quantity $\lim_{|\Omega|\to+\infty} \mathbb{E}\big[\mathrm{HS}(\chi\boldsymbol{\tau}; \bar{\boldsymbol{\varepsilon}})\big]$. Again, evaluation of the term involving the Green operator for strains is problematic. Unfortunately, the results presented in appendix B are of no use in the present case, since the trial stress-polarization (3.56) is defined by means of the inclusion centers, rather than the indicator function of each phases. Therefore, the statistical descriptor that is expected to arise is the radial distribution function, rather than the two-point probability function.

The present case is best handled within the framework of morphologically representative patterns introduced by Bornert, Stolz, and Zaoui [BSZ96]. Here, the pattern (p subscript) is the association of one inclusion and its interphase; the volume fraction f_p of the patterns is

$$f_\mathrm{p} = \left(1 + \frac{h}{a}\right)^3 f, \tag{3.58}$$

[7] It should be noted that, according to the framework presented in section 3.1.5, the trial stress-polarization is defined over an unbounded realization of the composite. Therefore, the number of inclusions is indeed infinite.

and their local stiffness $\mathbf{C}_{\mathrm{p}}(\mathbf{r})$ is defined as follows

$$\mathbf{C}_{\mathrm{p}}(\mathbf{r}) = \mathbf{C}_{\mathrm{i}} \text{ for } \|\mathbf{r}\| \leq a \quad \text{and} \quad \mathbf{C}_{\mathrm{p}}(\mathbf{r}) = \frac{a}{h}\mathbf{C}_{\mathrm{s}} \text{ for } a \leq \|\mathbf{r}\| \leq a + h. \tag{3.59}$$

Bornert and coauthors evaluated the thermodynamic limit of the Hashin–Shtrikman functional for trial stress-polarizations based on morphologically representative, ellipsoidal patterns that are distributed ellipsoidally. Assuming here that the spherical inclusions are distributed isotropically, the results presented in reference [BSZ96] apply. In particular,

$$\begin{aligned}\lim_{|\Omega|\to+\infty} \mathbb{E}\big[\mathrm{HS}(\chi\boldsymbol{\tau};\overline{\boldsymbol{\varepsilon}})\big] = {}& \tfrac{1}{2}\overline{\boldsymbol{\varepsilon}} : \mathbf{C}_{\mathrm{m}} : \overline{\boldsymbol{\varepsilon}} + f_{\mathrm{p}}\langle\boldsymbol{\tau}_{\mathrm{p}}\rangle_{\mathrm{p}} : \overline{\boldsymbol{\varepsilon}} - \tfrac{1}{2}f_{\mathrm{p}}\langle\boldsymbol{\tau}_{\mathrm{p}} : (\mathbf{C}_{\mathrm{p}} - \mathbf{C}_{\mathrm{m}})^{-1} : \boldsymbol{\tau}_{\mathrm{p}}\rangle_{\mathrm{p}} \\ & - \tfrac{1}{2}f_{\mathrm{p}}\langle\boldsymbol{\tau}_{\mathrm{p}} : \boldsymbol{\Gamma}_{\mathrm{m}}^{\infty}[\boldsymbol{\tau}_{\mathrm{p}}]\rangle_{\mathrm{p}} + \tfrac{1}{2}f_{\mathrm{p}}^{2}\langle\boldsymbol{\tau}_{\mathrm{p}}\rangle_{\mathrm{p}} : \mathbf{P}_{\mathrm{m}} : \langle\boldsymbol{\tau}_{\mathrm{p}}\rangle_{\mathrm{p}},\end{aligned} \tag{3.60}$$

where $\boldsymbol{\Gamma}_{\mathrm{m}}^{\infty}$ and $\mathbf{P}_{\mathrm{m}}$ denote the fourth-rank Green operator of the matrix and Hill tensor of a spherical inclusion embedded in the matrix. Furthermore, for any quantity $\mathcal{Q}$, $\langle\mathcal{Q}\rangle_{\mathrm{p}}$ denotes the volume average over the pattern

$$\langle\mathcal{Q}\rangle_{\mathrm{p}} = \left[\frac{4\pi}{3}(a+h)^{3}\right]^{-1} \int_{\|\mathbf{r}\|\leq a+h} \mathcal{Q}(\mathbf{r})\,\mathrm{d}V_{\mathbf{r}}. \tag{3.61}$$

In references [BDK10a]; [BDK10b], I chose for $\boldsymbol{\tau}_{\mathrm{p}}$ the stress-polarization that arises from the solution to a generalized form of Eshelby's inhomogeneity problem, where one pattern is embedded in an infinite matrix. At that time, I did not realize that this was in fact the optimal choice, although this result was stated in reference [BSZ96].

Plugging this particular form of $\boldsymbol{\tau}_{\mathrm{p}}$ into equation (3.60), evaluating each term in turn, and taking the limit as $h \to 0$, led in reference [BDK10a] to the following lower bound on the effective bulk modulus κ^{eff} of the nanocomposite

$$\kappa^{\mathrm{eff}} \geq \kappa_{\mathrm{m}} + \frac{f(\kappa_{\mathrm{m}} + \frac{4}{3}\mu_{\mathrm{m}})(\kappa_{\mathrm{p}} - \kappa_{\mathrm{m}})}{f\kappa_{\mathrm{m}} + \frac{4}{3}\mu_{\mathrm{m}} + (1-f)\kappa_{\mathrm{p}}}, \quad \text{with} \quad \kappa_{\mathrm{p}} = \kappa_{\mathrm{i}} + \frac{4}{3a}(\lambda_{\mathrm{s}} + \mu_{\mathrm{s}}), \tag{3.62}$$

where κ_{m} and μ_{m} (resp. κ_{i} and μ_{i}) denote the bulk and shear moduli of the matrix (resp. the inclusions).

Similarly, a lower bound on the effective modulus of the nanocomposite was derived in reference [BDK10b]; the reader is referred to this paper for its closed-form expression, which is too long to be reported here.

An important finding of these two papers was the fact that the bounds derived from the Hashin–Shtrikman principle were identical to the Mori–Tanaka estimates derived for nanocomposites by Duan, Wang, Huang, and Karihaloo [Dua+05]. At that time, I made this observation (which was not unexpected) at the end of a quite lengthy derivation, without realizing how general it was. A more careful reading of paper by Bornert, Stolz, and Zaoui [BSZ96] would actually have spared me most of the calculations presented in these papers! This is addressed in the next section.

3.3.6 Hashin–Shtrikman bounds and Mori–Tanaka estimates

In the previous section, it was shown that Mori–Tanaka estimates of the effective properties of nanocomposites are in fact bounds in the Hashin–Shtrikman sense. This result was obtained after lengthy calculations in references [BDK10a]; [BDK10b]. In the present section, it is recalled that this result is in fact general. Most of the proof can be found in reference [BSZ96], although the conclusion is not fully stated in terms of Mori–Tanaka estimates.

We again follow an approach based on morphologically representative patterns, allowing now for multiple patterns: N denotes the total number of patterns. Greek lower indices referring to patterns, $\Omega_\alpha \subset \mathbb{R}^d$ is the domain occupied by the reference α-pattern (centered at the origin) and $\mathbf{C}_\alpha(\mathbf{r})$ is the local stiffness of the α-pattern ($\mathbf{r} \in \Omega_\alpha$). In the microstructure under consideration, the α-patterns are centered at $\mathbf{x}_\alpha^1, \mathbf{x}_\alpha^2, \ldots$.

In order to relate Hashin–Shtrikman bounds to Mori–Tanaka estimates, the matrix (index "m") must be selected as reference material. It is assumed here that the matrix is stiffer than all other phases in the composite, so that an upper-bound on the effective stiffness will be derived. The trial stress-polarization must then be null outside the patterns and, following Bornert, Stolz, and Zaoui [BSZ96], we chose the trial stress-polarization

$$\boldsymbol{\tau}(\mathbf{x}) = \sum_{\alpha=1}^{N} \sum_{i=1}^{+\infty} \boldsymbol{\tau}_\alpha(\mathbf{x} - \mathbf{x}_\alpha^i), \tag{3.63}$$

where $\boldsymbol{\tau}_1, \ldots \boldsymbol{\tau}_N$ are unknown local stress-polarization fields that are supported in $\Omega_1, \ldots, \Omega_N$, respectively. Under the assumption that all patterns have the same spherical shape, and that their centers are distributed isotropically, Bornert, Stolz, and Zaoui [BSZ96] obtain the following expression

$$\begin{aligned}\lim_{|\Omega|\to+\infty} \mathbb{E}\big[\mathrm{HS}(\chi\boldsymbol{\tau};\overline{\boldsymbol{\varepsilon}})\big] = {} & \tfrac{1}{2}\overline{\boldsymbol{\varepsilon}} : \mathbf{C}_\mathrm{m} : \overline{\boldsymbol{\varepsilon}} + \sum_\alpha f_\alpha \langle \boldsymbol{\tau}_\alpha \rangle_\alpha : \overline{\boldsymbol{\varepsilon}} \\ & - \tfrac{1}{2} \sum_\alpha f_\alpha \langle \boldsymbol{\tau}_\alpha : (\mathbf{C}_\alpha - \mathbf{C}_\mathrm{m})^{-1} : \boldsymbol{\tau}_\alpha \rangle_\alpha \\ & - \tfrac{1}{2} \sum_\alpha f_\alpha \langle \boldsymbol{\tau}_\alpha : \boldsymbol{\Gamma}_\mathrm{m}^\infty[\boldsymbol{\tau}_\alpha] \rangle_\alpha \\ & + \tfrac{1}{2} \sum_{\alpha,\beta} f_\alpha f_\beta \langle \boldsymbol{\tau}_\alpha \rangle_\alpha : \mathbf{P}_\mathrm{m} : \langle \boldsymbol{\tau}_\beta \rangle_\beta, \end{aligned} \tag{3.64}$$

where f_α denotes the fraction of the volume occupied by all α-patterns. Similarly to the previous section, $\langle \mathcal{Q} \rangle_\alpha$ is the volume average of the quantity $\mathcal{Q}$ over the reference (spherical) domain Ω_α. It should be noted that in reference [BSZ96], equation (3.64) is extended to ellipsoidal patterns that are distributed ellipsoidally. For the sake of simplicity, only the isotropic case is considered here. The local trial stress-polarizations $\boldsymbol{\tau}_1, \ldots \boldsymbol{\tau}_N$ are optimal if [BSZ96]

$$(\mathbf{C}_\alpha - \mathbf{C}_\mathrm{m})^{-1} : \boldsymbol{\tau}_\alpha + \boldsymbol{\Gamma}_\mathrm{m}^\infty[\boldsymbol{\tau}_\alpha] = \overline{\boldsymbol{\varepsilon}} + \mathbf{P}_\mathrm{m} : \sum_\beta f_\beta \langle \boldsymbol{\tau}_\beta \rangle_\beta = \boldsymbol{\varepsilon}_\mathrm{m}, \tag{3.65}$$

and the optimal bound on the macroscopic strain energy reads

$$\tfrac{1}{2}\overline{\boldsymbol{\varepsilon}} : \mathbf{C}^\mathrm{eff} : \overline{\boldsymbol{\varepsilon}} \leq \tfrac{1}{2}\overline{\boldsymbol{\varepsilon}} : \mathbf{C}_\mathrm{m} : \overline{\boldsymbol{\varepsilon}} + \sum_\alpha f_\alpha \langle \boldsymbol{\tau}_\alpha \rangle_\alpha : \overline{\boldsymbol{\varepsilon}}. \tag{3.66}$$

The optimality condition (3.65) is an equation of Lippmann–Schwinger type: $\boldsymbol{\tau}_\alpha$ is therefore the (inhomogeneous) stress-polarization induced in the reference α-pattern embedded in the unbounded reference material, and subjected to the uniform strain $\boldsymbol{\varepsilon}_\mathrm{m}$ at infinity. The corresponding strain $\boldsymbol{\varepsilon}_\alpha = (\mathbf{C}_\alpha - \mathbf{C}_\mathrm{m})^{-1} : \boldsymbol{\tau}_\alpha$ can be considered as an estimate of the local strain within α-patterns. Similarly, $\boldsymbol{\varepsilon}_\mathrm{m}$ defined by equation (3.65) can be considered as an estimate of the strain within the matrix. At this point, this strain is unknown. Quoting Bornert, Stolz, and Zaoui [BSZ96], $\boldsymbol{\varepsilon}_\mathrm{m}$ ought to be chosen according to the condition: "[the strain at infinity] is only determined by the condition that [the macroscopic strain] equals the average trial strain field", which is recognized as the closure condition for the derivation of Mori–Tanaka estimates. We provide below a proof (that was missing in reference [BSZ96]) of this statement.

Observing that $\boldsymbol{\tau}_\alpha$ is supported in a spherical (thus, ellipsoidal) domain, the generalized Eshelby theorem (3.8) applies to the average of equation (3.65) over the α-pattern

$$\langle \boldsymbol{\varepsilon}_\alpha \rangle_\alpha = \boldsymbol{\varepsilon}_\mathrm{m} - \langle \boldsymbol{\Gamma}_\mathrm{m}^\infty[\boldsymbol{\tau}_\alpha] \rangle_\alpha = \boldsymbol{\varepsilon}_\mathrm{m} - \mathbf{P}_\mathrm{m} : \langle \boldsymbol{\tau}_\alpha \rangle_\alpha = \overline{\boldsymbol{\varepsilon}} + \mathbf{P}_\mathrm{m} : \sum_\beta f_\beta \langle \boldsymbol{\tau}_\beta \rangle_\beta - \mathbf{P}_\mathrm{m} : \langle \boldsymbol{\tau}_\alpha \rangle_\alpha, \quad (3.67)$$

and

$$\sum_\alpha f_\alpha \langle \boldsymbol{\varepsilon}_\alpha \rangle_\alpha + \Big(1 - \sum_\alpha f_\alpha\Big) \boldsymbol{\varepsilon}_\mathrm{m} = \overline{\boldsymbol{\varepsilon}}, \quad (3.68)$$

which completes the proof. We are now in a position to show that the resulting bound (3.66) coincides with the Mori–Tanaka estimate. We first define the (inhomogeneous) dilute strain localization tensor $\mathbf{A}_\alpha^\infty$, which maps the strain in the matrix $\boldsymbol{\varepsilon}_\mathrm{m}$ to the local strain in the α-pattern. Equation (3.68) then leads to $\boldsymbol{\varepsilon}_\mathrm{m} = \mathbf{A}_\mathrm{m}^\mathrm{HS} : \overline{\boldsymbol{\varepsilon}}$ and $\boldsymbol{\varepsilon}_\alpha = \mathbf{A}_\alpha^\mathrm{HS} : \overline{\boldsymbol{\varepsilon}}$, with

$$\mathbf{A}_\mathrm{m}^\mathrm{HS} = \big(f_\mathrm{m}\mathbf{I} + \textstyle\sum_\alpha f_\alpha \langle \mathbf{A}_\alpha^\infty \rangle_\alpha\big)^{-1} \quad \text{and} \quad \mathbf{A}_\alpha^\mathrm{HS} = \mathbf{A}_\alpha^\infty : \mathbf{A}_\mathrm{m}^\mathrm{HS} \quad (3.69)$$

and, upon substitution in equation (3.66),

$$\mathbf{C}^\mathrm{eff} \leq \mathbf{C}^\mathrm{HS} = f_\mathrm{m}\mathbf{C}_\mathrm{m} : \mathbf{A}_\mathrm{m}^\mathrm{HS} + \sum_\alpha f_\alpha \mathbf{C}_\alpha : \mathbf{A}_\alpha^\mathrm{HS}, \quad (3.70)$$

which coincides with the Mori–Tanaka estimate of the effective stiffness.

To sum up, for isotropic microstructures which can be described by spherical morphologically representative patterns, Mori–Tanaka estimates of the effective stiffness are bounds in the Hashin–Shtrikman sense, provided that the matrix is stiffer or softer than all other phases.

3.3.7 Closing remarks

To close this section on the effective properties of nanocomposites, it is observed that introducing an interface model of the Gurtin–Murdoch type indeed results in size-effects. More precisely, decreasing the size of the inclusions while keeping their volume fraction constant tends to stiffen the composite [see for example equation (3.62)]. This was to be expected, since the radius of curvature of the interface defines a characteristic length scale (contrary to classical elasticity that defines no such length scale).

Simple substitution of the interface model with an equivalent (thin) interphase model allowed us to derive rigorous bounds on the effective elastic properties. However, our analysis also raised some questions regarding the Gurtin–Murdoch model itself. These questions all pertain to the fact that the stiffness $\mathbf{L}_\mathrm{s}$ [defined by equation (3.52)] is not a material property, since the interface is immaterial.

Of course, $\mathbf{L}_\mathrm{s}$ is expected to depend on the nature of the two materials it separates. However, there is no reason to think that $\mathbf{L}_\mathrm{s}$ should *not* depend on other parameters, such as the geometry of the interface itself. In other words, λ_s and μ_s in equation (3.52) might be functions of the radius a of the inclusions. Presently, this issue can probably be addressed by molecular simulations only.

A second issue relates to the positivity of $\mathbf{L}_\mathrm{s}$. Thermodynamic stability of conventional elastic continua classically requires the (3D) elastic stiffness to be positive definite. Such line of reasoning does not apply to elastic interfaces. Indeed, the interface being immaterial, it is not possible to isolate a small interface element and state the stability of its equilibrium. It can therefore not be excluded that $\mathbf{L}_\mathrm{s}$ be indefinite, and atomistic simulations indeed suggest that this might be the case [She05].

From the perspective of the Hashin–Shtrikman approach presented here, the positivity of the equivalent 3D stiffness $\mathbf{C}_\mathrm{s}$ defined in section 3.3.2 *must* be ensured, which induces restrictions on the elastic constants λ_s and μ_s, namely: $\mu_\mathrm{s} > 0$ and $0 < \lambda_\mathrm{s} + \mu_\mathrm{s} < 3\mu_\mathrm{s}$ [see equation (3.54)]. If these inequalities are not satisfied by the nanocomposite at hand, then the bounds derived in this section are not valid. These conditions are motivated by purely mathematical considerations. Their physical implications (if any) ought to be explored.

3.4 The case of eigenstressed materials

The present section describes some recent work initiated in 2015 by discussions with S. Ghabezloo[8], who uncovered inconsistencies in the derivation of Mori–Tanaka estimates of the poroelastic properties proposed by Ulm, Constantinides, and Heukamp [UCH04]. At that time, I was well aware of the limitations of the Mori–Tanaka scheme (even in the classical, elastic case), and set out to derive Hashin–Shtrikman estimates of these properties in order to overcome these limitations. Considering the pore pressure as a special case of eigenstress [DKU06], I started working on variational estimates of the macroscopic properties of eigenstressed materials.

Using the Hashin–Shtrikman principle to derive estimates of these properties was already proposed by Bornert, Masson, Ponte Castañeda, and Zaoui [Bor+01]. I took the derivation one step further, and was able to prove that the resulting variational estimates enjoyed the same properties as their exact counterparts.

This work has been partly published in a conference paper [BG17], while the journal paper corresponding to the whole study is currently in preparation [BG18]. The present section is organized as follows. Section 3.4.1 defines the eigenstrain influence tensors that govern the macroscopic behavior of eigenstressed materials; the properties of these effective coefficients are listed; their Mori–Tanaka estimates are then discussed. Section 3.4.2 then extends the

[8] Laboratoire Navier, UMR 8205, CNRS, ENPC, IFSTTAR, Université Paris-Est (Marne-la-Vallée, France)

Hashin–Shtrikman principle to eigenstressed materials. Then, it is shown in section 3.4.3 how this principle can be used to derive variational estimates of the eigenstrain influence tensors; properties of these estimates are analyzed. Possible extensions of the proposed method are discussed in section 3.4.4.

3.4.1 Effective properties of eigenstressed materials

Section 3.4 is devoted to the homogenization of eigenstressed, N-phase materials. We consider a SVE Ω of such a material and adopt the notation defined in section 2.1.1. The local stress-strain relationship now reads, for $\mathbf{x} \in \Omega_\alpha$: $\boldsymbol{\sigma}(\mathbf{x}) = \mathbf{C}_\alpha : \boldsymbol{\varepsilon}(\mathbf{x}) + \boldsymbol{\varpi}_\alpha$, where $\boldsymbol{\varpi}_\alpha$ denotes the (constant) eigenstress in phase $\alpha = 1, \dots, N$. The effective behavior of such materials is governed by the following macroscopic equations [DB92]

$$\langle \boldsymbol{\varepsilon} \rangle_\alpha = \mathbf{A}_\alpha : \mathbf{E} - \sum_\beta \mathbf{D}_{\alpha\beta} : \mathbf{C}_\beta^{-1} : \boldsymbol{\varpi}_\beta \quad \text{and} \quad \langle \boldsymbol{\sigma} \rangle = \mathbf{C}^{\text{eff}} : \langle \boldsymbol{\varepsilon} \rangle + \boldsymbol{\varpi}^{\text{eff}}, \tag{3.71}$$

where it is recalled that $\langle \boldsymbol{\varepsilon} \rangle_\alpha$ denotes the average strain over phase α [see equation (2.2)]. $\mathbf{A}_1, \dots \mathbf{A}_N$ are the well-known strain-localization tensors, and

$$\mathbf{C}^{\text{eff}} = \sum_\alpha f_\alpha \mathbf{C}_\alpha : \mathbf{A}_\alpha \quad \text{and} \quad \boldsymbol{\varpi}^{\text{eff}} = \sum_\alpha f_\alpha \mathbf{A}_\alpha^{\mathsf{T}} : \boldsymbol{\varpi}_\alpha, \tag{3.72}$$

are the effective stiffness and eigenstress, respectively. The fourth-rank tensors $\mathbf{D}_{\alpha\beta}$ are the eigenstrain influence tensors introduced by Dvorak and Benveniste [DB92]. They enjoy the following properties

$$\sum_\beta \mathbf{D}_{\alpha\beta} = \mathbf{I} - \mathbf{A}_\alpha, \quad \sum_\beta \mathbf{D}_{\alpha\beta} : \mathbf{C}_\beta^{-1} = \mathbf{0}, \quad \sum_\alpha f_\alpha \mathbf{D}_{\alpha\beta} = \mathbf{0}, \tag{3.73a}$$

$$f_\alpha \mathbf{D}_{\alpha\beta} : \mathbf{C}_\beta^{-1} = f_\beta \big(\mathbf{D}_{\beta\alpha} : \mathbf{C}_\alpha^{-1} \big)^{\mathsf{T}}. \tag{3.73b}$$

The apparent properties of the eigenstressed, heterogeneous material are classically obtained from the application of equations (3.71) and (3.72) to the solution of the following corrector problem on the SVE Ω [which replaces problem (2.6)]

$$\mathbf{div}\, \boldsymbol{\sigma} = \mathbf{0}, \quad \boldsymbol{\sigma} = \mathbf{C} : \boldsymbol{\varepsilon} + \boldsymbol{\varpi}, \quad \boldsymbol{\varepsilon} = \epsilon[\mathbf{u}], \tag{3.74}$$

together with appropriate boundary conditions. In equation $(3.74)_2$, $\boldsymbol{\varpi}$ denotes the eigenstress field [$\boldsymbol{\varpi}(\mathbf{x}) = \boldsymbol{\varpi}_\alpha$ for $\mathbf{x} \in \Omega_\alpha$]. Using again the spaces $\mathscr{E}(\Omega)$, $\mathscr{E}^{\text{ess}}(\Omega)$, $\mathscr{E}^{\text{per}}(\Omega)$, $\mathscr{S}(\Omega)$, $\mathscr{S}^{\text{nat}}(\Omega)$ and $\mathscr{S}^{\text{per}}(\Omega)$ introduced in section 2.1.2, the new corrector problem is stated below for all classical boundary conditions.

Essential (Dirichlet) boundary conditions

$$\text{Find } \boldsymbol{\varepsilon} \in \overline{\boldsymbol{\varepsilon}} + \mathscr{E}^{\text{ess}}(\Omega) \text{ such that } \mathbf{C} : \boldsymbol{\varepsilon} + \boldsymbol{\varpi} \in \mathscr{S}(\Omega), \tag{3.75}$$

Natural (Neumann) boundary conditions

$$\text{Find } \boldsymbol{\sigma} \in \overline{\boldsymbol{\sigma}} + \mathcal{S}^{\text{nat}}(\Omega) \text{ such that } \mathbf{C}^{-1} : (\boldsymbol{\sigma} - \boldsymbol{\varpi}) \in \mathcal{E}(\Omega), \tag{3.76}$$

Periodic boundary conditions

$$\text{Find } \boldsymbol{\varepsilon} \in \overline{\boldsymbol{\varepsilon}} + \mathcal{E}^{\text{per}}(\Omega) \text{ such that } \mathbf{C} : \boldsymbol{\varepsilon} + \boldsymbol{\varpi} \in \mathcal{S}^{\text{per}}(\Omega) \tag{3.77}$$

Mixed boundary conditions (extending to eigenstressed materials the boundary conditions introduced in section 3.1.2 for eigenstress-free elasticity)

$$\text{Find } \mathbf{t} \in \mathcal{T}_2, \boldsymbol{\varepsilon} \in \overline{\boldsymbol{\varepsilon}} + \mathcal{E}(\mathbb{R}^d) \text{ and } \boldsymbol{\sigma} \in \chi \mathbf{t} + \mathcal{S}(\mathbb{R}^d) \text{ such that } \begin{cases} \boldsymbol{\sigma} = \mathbf{C} : \boldsymbol{\varepsilon} + \boldsymbol{\varpi} & (\Omega), \\ \boldsymbol{\sigma} = \mathbf{C}_0 : \boldsymbol{\varepsilon} & (\mathbb{R}^d \setminus \Omega), \\ \langle \boldsymbol{\varepsilon} \rangle = \overline{\boldsymbol{\varepsilon}}, \end{cases} \tag{3.78}$$

and the Lippmann–Schwinger equation associated with problem (3.78) reads

$$(\mathbf{C} - \mathbf{C}_0)^{-1} : \boldsymbol{\tau} + \boldsymbol{\Gamma}_0^{\infty}[\boldsymbol{\tau} + \boldsymbol{\varpi} - \chi \langle \boldsymbol{\tau} + \boldsymbol{\varpi} \rangle] = \overline{\boldsymbol{\varepsilon}}. \tag{3.79}$$

However, solving any of the above local problems is often quite difficult, and estimates of the $\mathbf{A}_\alpha$ and $\mathbf{D}_{\alpha\beta}$ are of great practical value.

Revisiting the work of Mori and Tanaka [MT73], Benveniste [Ben87] proposed estimates of the strain localization tensors. His approach was then extended by Dvorak and Benveniste [DB92] to the eigenstrain influence tensors. The estimates of Dvorak and Benveniste were however restricted to materials with aligned inclusions of identical (ellipsoidal) shape. This limitation was later overcome by Pichler and Hellmich [PH10], who derived closed-form expressions of the estimates of the eigenstrain influence tensors for any distribution of ellipsoidal inclusions.

It is well-known that the Mori–Tanaka approach might deliver estimates of the effective stiffness that are not symmetric. Such unphysical estimates might occur in the case of non-aligned inclusions and/or inclusions of different shapes [BDC91]; [Fer91]; [SP01]. Pichler and Hellmich [PH10] have shown that in those cases where the classical Mori–Tanaka estimate of the effective stiffness *is* symmetric, their estimates of the eigenstrain influence tensors are consistent with properties (3.73). Conversely, if the Mori–Tanaka estimate of the effective stiffness is *not* symmetric, the Pichler–Hellmich estimates of the eigenstrain influence tensors are not physically acceptable.

Our aim is to propose alternative estimates of these tensors, which are always acceptable. Our estimates are derived from the variational framework introduced by Hashin and Shtrikman [HS62b] and later extended to eigenstressed materials by Bornert, Masson, Ponte Castañeda, and Zaoui [Bor+01]. Our main contribution is to show that these estimates always verify identities (3.73). Such robustness comes with a price, though. Indeed, it requires additional information on how the phases are distributed [namely, the P-tensors defined by equation (3.27)].

3.4.2 The Hashin–Shtrikman principle for eigenstressed materials

The variational Hashin–Shtrikman principle(s) stated in sections 2.3.2 and 3.1.3 can readily be extended to eigenstressed materials (see in particular [Bor+01] for "classical" boundary conditions). In the present section, only the so-called modified Hashin–Shtrikman principle of section 3.1.3 is stated. Expression (3.16) of the Hashin–Shtrikman functional is modified as follows

$$\begin{aligned}\mathrm{HS}^{\mathrm{mix}}(\boldsymbol{\tau};\overline{\boldsymbol{\varepsilon}},\boldsymbol{\varpi}_1,\dots,\boldsymbol{\varpi}_N) = {}& \tfrac{1}{2}\overline{\boldsymbol{\varepsilon}} : \mathbf{C}_0 : \overline{\boldsymbol{\varepsilon}} + \overline{\boldsymbol{\varepsilon}} : \langle \boldsymbol{\tau}+\boldsymbol{\varpi}\rangle - \tfrac{1}{2}\langle \boldsymbol{\tau} : (\mathbf{C}-\mathbf{C}_0)^{-1} : \boldsymbol{\tau}\rangle \\ & - \tfrac{1}{2}\langle (\boldsymbol{\tau}+\boldsymbol{\varpi}) : \boldsymbol{\Gamma}_0^{\infty}[\boldsymbol{\tau}+\boldsymbol{\varpi}-\chi\langle\boldsymbol{\tau}+\boldsymbol{\varpi}\rangle]\rangle. \end{aligned} \tag{3.80}$$

Again, this functional is stationary at the solution $\boldsymbol{\tau}$ to the modified Lippmann–Schwinger equation (3.79). Furthermore, for reference materials that are softer (resp. stiffer) than all phases in the composite, HS is minimal at this point and inequality (3.18) can be extended to the present eigenstressed case. Then, using the same probabilistic setting as in section 3.1.5, we find for all homogeneous and ergodic trial stress-polarization random field $\boldsymbol{\tau}$ with square integrable autocovariance

$$\begin{aligned}\mathbf{C}_0 \overset{\geq}{\leq} \mathbf{C} \quad \Rightarrow \quad \lim_{|\Omega|\to+\infty} \mathbb{E}\big[\mathrm{HS}(\chi\boldsymbol{\tau};\overline{\boldsymbol{\varepsilon}},\boldsymbol{\varpi}_1,\dots,\boldsymbol{\varpi}_N)\big] \overset{\geq}{\leq} {}& \tfrac{1}{2}\overline{\boldsymbol{\varepsilon}} : \mathbf{C}^{\mathrm{eff}} : \overline{\boldsymbol{\varepsilon}} \\ & + \sum_{\alpha} f_\alpha \boldsymbol{\varpi}_\alpha : \mathbf{A}_\alpha : \overline{\boldsymbol{\varepsilon}} - \tfrac{1}{2}\sum_{\alpha,\beta} f_\alpha \boldsymbol{\varpi}_\alpha : \mathbf{D}_{\alpha\beta} : \mathbf{C}_\beta^{-1} : \boldsymbol{\varpi}_\beta, \end{aligned} \tag{3.81}$$

where the right-hand side of the above inequality is the effective elastic energy of the eigenstressed composite.

3.4.3 Variational estimates of the eigenstrain influence tensors

It results from the previous section that finding the critical point of HS over the *whole* space of stress-polarizations delivers the *exact* values of the effective stiffness $\mathbf{C}^{\mathrm{eff}}$, strain localization tensors $\mathbf{A}_\alpha$ and eigenstrain influence tensors $\mathbf{D}_{\alpha\beta}$. Likewise, finding the critical point of HS over a *subspace* of stress-polarizations delivers *estimates*.

We again adopt the classical Hashin–Shtrikman phase-wise constant trial stress-polarization defined by equation (3.24). Then, the arguments developed in section 3.1.5 and appendix B carry over to the eigenstressed case, and it can readily be shown that

$$\begin{aligned}\lim_{|\Omega|\to+\infty} \mathbb{E}\big[\mathrm{HS}(\boldsymbol{\tau};\overline{\boldsymbol{\varepsilon}},\boldsymbol{\varpi}_1,\dots,\boldsymbol{\varpi}_N)\big] = {}& \tfrac{1}{2}\overline{\boldsymbol{\varepsilon}} : \mathbf{C}_0 : \overline{\boldsymbol{\varepsilon}} + \sum_{\alpha} f_\alpha \overline{\boldsymbol{\varepsilon}} : (\boldsymbol{\tau}_\alpha + \boldsymbol{\varpi}_\alpha) \\ & - \tfrac{1}{2}\sum_{\alpha} f_\alpha \boldsymbol{\tau}_\alpha : (\mathbf{C}_\alpha - \mathbf{C}_0)^{-1} : \boldsymbol{\tau}_\alpha - \tfrac{1}{2}\sum_{\alpha,\beta} (\boldsymbol{\tau}_\alpha + \boldsymbol{\varpi}_\alpha) : \mathbf{P}_{\alpha\beta} : (\boldsymbol{\tau}_\beta + \boldsymbol{\varpi}_\beta). \end{aligned} \tag{3.82}$$

If the reference material is stiffer or softer than all phases of the composite, the above expression delivers a *bound* on the effective elastic energy of the eigenstressed material; this bound can then be optimized with respect to the unknown stress-polarizations $\boldsymbol{\tau}_1,\dots,\boldsymbol{\tau}_N$.

If the reference fails to satisfy these requirements, the critical value of expression (3.82) delivers an *estimate* of the effective elastic energy. The stationarity conditions read

$$f_\alpha(\mathbf{C}_\alpha - \mathbf{C}_0)^{-1} : \boldsymbol{\tau}_\alpha + \sum_\beta \mathbf{P}_{\alpha\beta} : \big(\boldsymbol{\tau}_\beta + \boldsymbol{\varpi}_\beta\big) = f_\alpha \overline{\boldsymbol{\varepsilon}}, \tag{3.83}$$

which degenerate as expected into the linear system (3.28) in the eigenstress-free case. The linear system (3.83) can in general not be solved for the trial stress-polarizations $\boldsymbol{\tau}_1, \dots, \boldsymbol{\tau}_N$ analytically. However, owing to linearity, it is formally possible to express the solution as follows [BG18]

$$(\mathbf{C}_\alpha - \mathbf{C}_0)^{-1} : \boldsymbol{\tau}_\alpha = \mathbf{A}_\alpha^{\mathrm{HS}} : \overline{\boldsymbol{\varepsilon}} - \sum_\beta \mathbf{D}_{\alpha\beta}^{\mathrm{HS}} : \mathbf{C}_\beta^{-1} : \boldsymbol{\varpi}_\beta, \tag{3.84}$$

where the tensors $\mathbf{A}_\alpha^{\mathrm{HS}}$ and $\mathbf{D}_{\alpha\beta}^{\mathrm{HS}}$ are found (numerically) from the inversion of equation (3.83). Plugging equation (3.84) into equation (3.82) and introducing

$$\mathbf{C}^{\mathrm{HS}} = \sum_\alpha f_\alpha \mathbf{C}_\alpha : \mathbf{A}_\alpha^{\mathrm{HS}}, \tag{3.85}$$

it is found that

$$\begin{aligned}\lim_{|\Omega|\to+\infty} \mathbb{E}\big[\mathrm{HS}(\boldsymbol{\tau}; \overline{\boldsymbol{\varepsilon}}, \boldsymbol{\varpi}_1, \dots, \boldsymbol{\varpi}_N)\big] = \tfrac{1}{2}\overline{\boldsymbol{\varepsilon}} : \mathbf{C}^{\mathrm{HS}} : \overline{\boldsymbol{\varepsilon}} + \sum_\alpha f_\alpha \boldsymbol{\varpi}_\alpha : \mathbf{A}_\alpha^{\mathrm{HS}} : \overline{\boldsymbol{\varepsilon}} \\ - \tfrac{1}{2}\sum_{\alpha,\beta} f_\alpha \boldsymbol{\varpi}_\alpha : \mathbf{D}_{\alpha\beta}^{\mathrm{HS}} : \mathbf{C}_\beta^{-1} : \boldsymbol{\varpi}_\beta.\end{aligned} \tag{3.86}$$

Gathering equations (3.81) and (3.86) finally shows that $\mathbf{C}^{\mathrm{HS}}$, $\mathbf{A}_\alpha^{\mathrm{HS}}$ and $\mathbf{D}_{\alpha\beta}^{\mathrm{HS}}$ ought to be considered as variational estimates of the effective stiffness $\mathbf{C}^{\mathrm{eff}}$, the strain localization tensors $\mathbf{A}_\alpha$ and the eigenstrain influence tensors $\mathbf{D}_{\alpha\beta}$, respectively. For ellipsoidal distributions, these estimates coincide with the Pichler–Hellmich estimates [PH10] (aligned inclusions of identical shape). Outside this particular case, they generally differ from these estimates, as the following discussion will show.

Careful analysis of the linear system (2.28) in fact shows that the variational estimates $\mathbf{A}_\alpha^{\mathrm{HS}}$ and $\mathbf{D}_{\alpha\beta}^{\mathrm{HS}}$ enjoy the same properties (3.73) as their exact counterparts [BG18]. As a consequence, the variational estimate of the effective stiffness is always symmetric, unlike the Mori–Tanaka (or Pichler–Hellmich) estimate. This suffices to prove that the proposed variational estimates of the eigenstrain influence tensors differ in general from their Pichler–Hellmich estimates. While the latter might take unphysical values (when the Mori–Tanaka estimate of the effective stiffness is not symmetric), the former are always consistent with identities (3.73). The proposed variational estimates are therefore appealing alternatives to the Pichler–Hellmich estimates in cases where the latter do not satisfy identities (3.73).

3.4.4 Closing remarks

In this section, we have proposed an alternative to the Pichler–Hellmich [PH10] estimates of the eigenstrain influence tensors. Our variational estimates are derived from the Hashin–Shtrikman principle, extended to eigenstressed materials. Unlike the Pichler–Hellmich estimates, the variational estimates are in general not explicit; they can however be retrieved from

the solution to a small linear system which is inverted numerically. It is proved that, unlike Pichler–Hellmich estimates, the variational estimates of the strain concentration tensors and eigenstrain influence tensors are always (regardless of the microstructure at hand) physically acceptable [in the sense that they satisfy identities (3.73)].

This robustness comes with a price, though: compared with the Pichler–Hellmich method, the present method requires additional microstructural parameters [the so-called P-tensors defined by equation (3.27)] that are related to two-point probability functions of the underlying random microstructure. Evaluation of these P-tensors therefore requires a fine statistical analysis of the microstructure, which can be costly.

There are numerous applications of the framework outlined above, ranging from thermoelasticity (eigenstrains induced by temperature changes), poroelasticity (pore pressures are eigenstresses) to plasticity (plastic strains are eigenstrains [MVH17]).

The reader might question the originality of the work presented in the present section 3.4. Indeed, the derivation of variational estimates of the effective properties of eigenstressed materials was already outlined by Bornert, Masson, Ponte Castañeda, and Zaoui [Bor+01], among others. However, the resulting estimates were not confronted to properties (3.73): our main (non-trivial) contribution was to show that the variational estimates are indeed consistent with these properties.

It should be observed that, for suitable reference materials, the variational approach delivers bounds on the effective elastic energy of the eigenstressed material. In turn, these bounds result in inequalities that must be satisfied by the effective properties. For the effective moduli, these inequalities are straightforward bounds. For the eigenstrain influence tensors, they are much more intricate but still deliver valuable information that ought to be taken into account.

From this perspective, we analyzed the Biot coefficients of unsaturated, poroelastic materials [BG17]. This preliminary investigation allowed us to give a variational interpretation of the so-called pore isodeformation assumption [CB09]. I intend to carry out a deeper investigation on these issues. In particular, I would like to understand under which conditions the Bishop parameter χ introduced in [CB09] is lower than the saturation in liquid S_{L}.

To close this section, it should be noted that the method outlined in section 3.2.4 for the derivation of improved bounds on the effective moduli readily extends to eigenstressed materials and we intend to combine both approaches to derive improved estimates of the eigenstrain influence tensors.

3.5 Stress-gradient materials

This section is devoted to the doctoral work of Tran [Tra16] (advisor: K. Sab[9]; co-supervisor: J. Guilleminot[10]). It builds on the recent development of the stress-gradient model by Forest and Sab [FS12] (see also reference [SLF16] for a mathematical justification).

[9] See footnote 8 in the present chapter.

[10] Université Paris-Est, Laboratoire Modélisation et Simulation Multi Échelle (MSME UMR 8208 CNRS), Marne-la-Vallée, France

This model can be seen as complementary to the celebrated strain-gradient model of Mindlin [Min64]. Both belong to the wide class of generalized continua (see chapter 5 in reference [Tra16] for a more thorough review). The goal of both models is to introduce one or more material internal length(s), of which classical elasticity is devoid.

Prior references [FS12]; [SLF16] ensuring that the stress-gradient model rests on firm theoretical grounds, we applied in the work of Tran [Tra16] this theory to the homogenization of stress-gradient composites as classical continua[11]. We first introduced a simplified elastic, linear, isotropic, material model (involving only one material internal length, rather than three in the general case). We then proposed a general framework for the homogenization of stress-gradient materials (extended Hill–Mandel principle, boundary conditions for the corrector problem, etc.). We then derived the solution to Eshelby's spherical inhomogeneity problem, which allowed us to derive Mori–Tanaka estimates of the effective properties of stress-gradient materials. Finally, we extended the Hashin–Shtrikman principle to stress-gradient materials and proposed rigorous bounds on the effective properties of stress-gradient materials. Unlike classical continua, the resulting bounds depend explicitly on the correlation length even for isotropic microstructures.

The present section is organized as follows. Section 3.5.1 gives a brief overview of the stress-gradient model introduced in references [FS12]; [SLF16]. It also presents the simplified elastic, linear, isotropic material model proposed by Tran [Tra16], to be used subsequently. Section 3.5.2 introduces the theoretical framework for the homogenization of stress-gradient materials and presents Mori–Tanaka estimates of the effective stiffness. Finally, Hashin–Shtrikman bounds are discussed in section 3.5.3.

Remark 3.1 (On higher-rank tensors)**.** *In the present section, we deal with tensors with rank ranging from first to sixth. We will define minor symmetries for these tensors as follows*

$$T_{ij} = T_{ji}, \quad T_{ijk} = T_{jik}, \quad T_{ijkl} = T_{jikl} = T_{ijlk}, \quad T_{ijklmn} = T_{jiklmn} = T_{ijkmln}, \tag{3.87}$$

all tensors considered having implicitly the minor symmetries[12]*. In turn, major symmetry of fourth- and sixth-rank tensors is defined with respect to the double- and triple-dot products, respectively (*$\mathbf{T} : \mathbf{T}' = T_{ij}T'_{ij}$, $\mathbf{T} \therefore \mathbf{T}' = T_{ijk}T'_{ijk}$*)*

$$T_{ijkl} = T_{klij} \quad \textit{and} \quad T_{ijklmn} = T_{lmnijk}. \tag{3.88}$$

In most situations, the rank of the tensors can be inferred from the context: therefore, the same typeface (namely, ***bold face****) is used for all these entities. Where confusion might occur, the rank of the tensor will be subscripted. Thus,*

$$\mathbf{I}_2 = \delta_{ij}\mathbf{e}_i \otimes \mathbf{e}_j \quad \textit{and} \quad \mathbf{I}_4 = \frac{1}{2}\left(\delta_{ik}\delta_{jl} + \delta_{il}\delta_{jk}\right)\mathbf{e}_i \otimes \mathbf{e}_j \otimes \mathbf{e}_k \otimes \mathbf{e}_l \tag{3.89}$$

[11] In the present section, elastic materials for which the strain energy (resp. complementary strain energy) density depends on the strain (resp. stress) only will be referred to as "classical", as opposed to "generalized" continua. In the strain-gradient literature classical continua are often referred to as "Cauchy" continua. This terminology is improper for stress-gradient continua, since the internal state of stress is still defined by the Cauchy stress tensor, which is itself governed by the classical equilibrium equation.

[12] Minor symmetries cannot be defined unambiguously for fifth-rank tensors (see section 3.5.3).

denote the second- and fourth- rank identity tensors, respectively.

Finally, the trace of a second-rank tensor $\mathbf{T}$ *is usually defined as the scalar* $\operatorname{tr}\mathbf{T} = T_{ii} = \mathbf{T} : \mathbf{I}_2$. *Similarly, we will define the trace of a third-rank tensor* $\mathbf{T}$ *as the vector* $T_{ijj}\mathbf{e}_i = \mathbf{T} : \mathbf{I}_2$, *so that the divergence of the stress tensor* $\boldsymbol{\sigma}$ *is the trace of its gradient* $\mathbf{grad}\,\boldsymbol{\sigma}$.

3.5.1 The stress-gradient model

In the celebrated strain-gradient model of Mindlin [Min64], the strain-energy density w depends on the strain $\boldsymbol{\epsilon}$ and its first gradient $\mathbf{grad}\,\boldsymbol{\epsilon}$. Likewise, in the stress-gradient model of Forest and Sab [FS12], the complementary strain energy density w^* depends on the stress $\boldsymbol{\sigma}$ and its first gradient $\mathbf{grad}\,\boldsymbol{\sigma}$. More precisely, the complementary strain energy of the stress-gradient body Ω is given by the following expression

$$W^*(\boldsymbol{\sigma}) = \int_{\mathbf{x}\in\Omega} w^*\big(\mathbf{x}, \boldsymbol{\sigma}(\mathbf{x}), \mathbf{grad}\,\boldsymbol{\sigma}(\mathbf{x})\big)\,\mathrm{d}V_{\mathbf{x}}, \tag{3.90}$$

where the complementary strain energy density w^* depends explicitly on the observation point $\mathbf{x} \in \Omega$ to account for material heterogeneities.

The local equations that define the elastic equilibrium of a *clamped*[13] stress-gradient body are then found from the minimization of the complementary strain energy W^* under the constraint that the local stress $\boldsymbol{\sigma}$ be in equilibrium with the body forces $\mathbf{b}$ ($\mathbf{div}\,\boldsymbol{\sigma} + \mathbf{b} = \mathbf{0}$).

Before we proceed to this optimization, it should first be observed that $\mathbf{div}\,\boldsymbol{\sigma}$ is the trace of $\mathbf{grad}\,\boldsymbol{\sigma}$; it is therefore natural to decompose the stress-gradient $\mathbf{grad}\,\boldsymbol{\sigma}$ as the orthogonal sum of a trace-free part $\mathbf{R}$ and its complement that is fully defined by the body forces $\mathbf{b}$

$$\mathbf{grad}\,\boldsymbol{\sigma} = \mathbf{R} - \frac{2}{d+1}\mathbf{I}_4 \cdot \mathbf{b}, \quad \text{where} \quad \mathbf{R} : \mathbf{I}_2 = \mathbf{0} \quad \text{and} \quad \mathbf{R} \therefore \mathbf{I}_4 \cdot \mathbf{b} = 0. \tag{3.91}$$

The trace-free part $\mathbf{R}$ of the stress-gradient $\mathbf{grad}\,\boldsymbol{\sigma}$ is the orthogonal projection of $\mathbf{grad}\,\boldsymbol{\sigma}$ onto the space of third-rank, trace-free tensors, and we write $\mathbf{R} = \mathbf{K}_6 \therefore \mathbf{grad}\,\boldsymbol{\sigma}$, where the sixth-rank orthogonal projector $\mathbf{K}_6$ is defined in e.g. section 6.1.1 of reference [Tra16]. Following Forest and Sab [FS12], we then assume that the complementary strain energy density depends on the stress and the trace-free part of its gradient

$$W^*(\boldsymbol{\sigma}) = \int_{\Omega} w^*(\boldsymbol{\sigma}, \mathbf{R})\,\mathrm{d}V, \tag{3.92}$$

where the explicit dependency on the observation point has been omitted. Optimization of this functional then leads to the following boundary value problem

$$\mathbf{div}\,\boldsymbol{\sigma} + \mathbf{b} = \mathbf{0} \qquad \mathbf{R} = \mathbf{K}_6 \therefore \mathbf{grad}\,\boldsymbol{\sigma} \qquad (\Omega) \tag{3.93a}$$

$$\mathbf{e} = \partial_{\boldsymbol{\sigma}} w^* \qquad \boldsymbol{\phi} = \partial_{\mathbf{R}} w^* \qquad (\Omega) \tag{3.93b}$$

$$\mathbf{e} = \boldsymbol{\epsilon}[\mathbf{u}] + \mathbf{div}\,\boldsymbol{\phi} \qquad (\Omega) \tag{3.93c}$$

$$\mathbf{sym}(\mathbf{u} \otimes \mathbf{n}) + \boldsymbol{\phi} \cdot \mathbf{n} = \mathbf{0} \qquad (\partial\Omega) \tag{3.93d}$$

[13] At this stage, we are not really in a position to define a clamped stress-gradient body, since its generalized degrees of freedom have not been defined yet. However, since no natural boundary conditions are prescribed, we *know* that minimizing W^* will indeed lead to a clamped body.

which effectively defines the elastic equilibrium of a *clamped* stress-gradient body (**n**: outer normal to $\partial\Omega$). Equations (3.93a) are the generalized equilibrium equations, equations (3.93b) are the generalized constitutive laws and equation (3.93c) is the compatibility condition. It should be observed that we are now in a position to define the meaning of clamping for stress-gradient materials [through boundary condition (3.93d)].

The vector field $\mathbf{u}$ and the third-rank tensor field $\boldsymbol{\phi}$ are the generalized degrees of freedom of stress-gradient materials. Since $\boldsymbol{\phi}$ is energy-conjugate to the trace-free variable $\mathbf{R}$, it is likewise trace-free ($\boldsymbol{\phi} : \mathbf{I}_2 = \mathbf{0}$). While $\mathbf{u}$ can be interpreted as a displacement, the physical meaning of $\boldsymbol{\phi}$ remains unclear. It should be noted that the strain measure $\mathbf{e}$ that is the energy-conjugate variable to the stress $\boldsymbol{\sigma}$ is *not* the symmetric gradient of the displacement $\mathbf{u}$. To emphasize this unusual point, $\mathbf{e}$ will be called in the remainder of this section the *total strain*.

One last striking (and somewhat disturbing) feature of the above model is the fact that the *full* stress tensor $\boldsymbol{\sigma}$ must be continuous anywhere in the stress-gradient body Ω. It is emphasized that this is a constitutive law effect. Indeed, from the point of vie of equilibrium, stress-gradient materials are Cauchy materials: their equilibrium only requires the classical continuity of the traction vector. The higher-order constitutive law induced by the representation (3.92) of the complementary energy requires the continuity of the other components of the stress tensor, as was proved mathematically by Sab, Legoll, and Forest [SLF16].

For centrosymmetric, linearly elastic stress-gradient materials, the complementary strain energy density reads

$$w^*(\boldsymbol{\sigma}, \mathbf{R}) = \tfrac{1}{2}\boldsymbol{\sigma} : \mathbf{S} : \boldsymbol{\sigma} + \tfrac{1}{2}\mathbf{R} \therefore \mathbf{M} \therefore \mathbf{R}, \tag{3.94}$$

where $\mathbf{S}$ and $\mathbf{M}$ are the classical and generalized compliances. Both are tensors with minor and major symmetries. Besides, owing to the fact that $\mathbf{M}$ operates on the space of trace-free, third-rank tensors, we must have: $\mathbf{K}_6 \therefore \mathbf{M} \therefore \mathbf{K}_6 = \mathbf{M}$.

In reference [Tra16], we showed that for isotropic, linearly elastic stress-gradient materials, the complementary strain energy is fully defined by two elastic coefficients and three material internal lengths. Drawing inspiration from the simplified model of Altan and Aifantis [AA92] and Altan and Aifantis [AA97] for strain-gradient materials (see also references [FA10]; [GP07]), we then introduced a simplified model for stress-gradient materials, with only one material internal length. In the simplified model of Altan and Aifantis [AA92] and Altan and Aifantis [AA97], the strain energy density w reads

$$\begin{aligned} w(\boldsymbol{\varepsilon}, \mathbf{grad}\,\boldsymbol{\varepsilon}) = \mu\Big[\boldsymbol{\varepsilon} : \boldsymbol{\varepsilon} + \frac{\nu}{1-2\nu}(\mathbf{I}_2 : \boldsymbol{\varepsilon})^2\Big] \\ + \mu\ell^2\Big[\mathbf{grad}\,\boldsymbol{\varepsilon} \therefore \mathbf{grad}\,\boldsymbol{\varepsilon} + \frac{\nu}{1-2\nu}(\mathbf{I}_2 : \mathbf{grad}\,\boldsymbol{\varepsilon}) \cdot (\mathbf{I}_2 : \mathbf{grad}\,\boldsymbol{\varepsilon})\Big], \end{aligned} \tag{3.95}$$

where ℓ denotes the material internal length. Likewise, in the proposed simplified model for isotropic, linearly elastic stress-gradient materials, the complementary strain energy density reads

$$w^*(\boldsymbol{\sigma}, \mathbf{R}) = \frac{1}{4\mu}\Big[\boldsymbol{\sigma} : \boldsymbol{\sigma} - \frac{\nu}{1+\nu}(\mathbf{I}_2 : \boldsymbol{\sigma})^2\Big] + \frac{\ell^2}{4\mu}\Big[\mathbf{R} \therefore \mathbf{R} - \frac{\nu}{1+\nu}(\mathbf{I}_2 : \mathbf{R}) \cdot (\mathbf{I}_2 : \mathbf{R})\Big]. \tag{3.96}$$

It should be observed that a similar model was also introduced by Polizzotto [Pol14]. For $\ell \to 0$, the classical Hooke's model is retrieved. Conversely, for $\ell \to +\infty$, the trace-free

part $\mathbf{R}$ of $\mathbf{grad}\,\boldsymbol{\sigma}$ is penalized and must vanish. In the absence of body-forces ($\mathbf{b} = \mathbf{0}$), $\boldsymbol{\sigma}$ is divergence-free, so that $\mathbf{grad}\,\boldsymbol{\sigma} - \mathbf{R} = \mathbf{0}$. In other words, the full stress-gradient vanishes: the stress field is phase-wise constant for large values of the material internal length.

Remark 3.2. *The boundary-value problem* (3.93) *can be extended to more general boundary conditions. For example, for a stress-gradient body* Ω*, clamped on* $\partial\Omega_u \subset \partial\Omega$ *and subjected to prescribed tractions* $\overline{\mathbf{T}}$ *on* $\partial\Omega_T \subset \partial\Omega$ *(*$\partial\Omega_u \cap \partial\Omega_T = \emptyset$*,* $\partial\Omega_u \cup \partial\Omega_T = \partial\Omega$*), the boundary conditions read*

$$\mathbf{sym}(\mathbf{u} \otimes \mathbf{n}) + \boldsymbol{\phi} \cdot \mathbf{n} = \mathbf{0} \qquad (\partial\Omega_u) \tag{3.97a}$$

$$(\mathbf{I}_2 - \mathbf{n} \otimes \mathbf{n}) \cdot \boldsymbol{\phi} \cdot \mathbf{n} = \mathbf{0} \qquad (\partial\Omega_T) \tag{3.97b}$$

$$\boldsymbol{\sigma} \cdot \mathbf{n} = \overline{\mathbf{T}} \qquad (\partial\Omega_T) \tag{3.97c}$$

they replace (3.93d).

More strikingly, it is perfectly valid to prescribe stress-free ($\boldsymbol{\sigma} = \mathbf{0}$*) rather than traction-free (*$\boldsymbol{\sigma} \cdot \mathbf{n} = \mathbf{0}$*) boundary conditions. More generally – provided that rigid body motions are prevented – boundary condition* (3.93d) *can be replaced with:* $\boldsymbol{\sigma}|_{\partial\Omega} = \overline{\boldsymbol{\sigma}}$*, where the prescribed stress* $\overline{\boldsymbol{\sigma}}(\mathbf{x})$ *may depend on the observation point* $\mathbf{x} \in \partial\Omega$ *belonging to the boundary. It is emphasized that in this case, the* full *stress tensor is prescribed at the boundary, which is at odds with classical elasticity. Remembering that the higher-order constitutive law induces the continuity of the full stress tensor (see remarks below equation* (3.93)*), the fact that this type of boundary conditions leads to a well-posed boundary-value problem [SLF16] should however not come as a surprise.*

3.5.2 Homogenization of stress-gradient materials

In this section, we consider a heterogeneous (macroscopic) structure composed of stress-gradient materials. We introduce three different length-scales: *i.* the typical size d of the heterogeneities, *ii.* the size L_{meso} of the RVE and *iii.* the typical size L_{macro} of the structure and the length scale of its loading.

We assume that the heterogeneous structure is *homogenizable* and seek its effective behavior. This requires that separation of scales prevails, that is $d \ll L_{\text{meso}} \ll L_{\text{macro}}$. Besides this standard condition, it is further required that one of the following conditions is fullfilled: $\ell \sim d$ or $\ell \ll d$, where ℓ denotes the material internal length defined in section 3.5.1.

What is the expected macroscopic behavior of such heterogeneous materials? The very same question was explored by Forest, Pradel, and Sab [FPS01] in the case of Cosserat media. By means of asymptotic expansions, these authors proved that under the above assumptions, the heterogeneous material behaves macroscopically as a classical, linearly elastic material. The same argument would apply here, leading to the same conclusion. The macroscopic behavior of the heterogeneous, stress-gradient material is then characterized by the effective compliance $\mathbf{S}^{\text{eff}}$, which relates the average (macroscopic) total strain $\langle\mathbf{e}\rangle$ to the average (macroscopic) stress $\langle\boldsymbol{\sigma}\rangle$ through the standard constitutive equation $\langle\mathbf{e}\rangle = \mathbf{S}^{\text{eff}} : \langle\boldsymbol{\sigma}\rangle$.

The effective compliance $\mathbf{S}^{\text{eff}}$ is then computed as the limit for large SVEs Ω of the *apparent* compliance $\mathbf{S}^{\text{app}}(\Omega)$: $\mathbf{S}^{\text{eff}} = \lim_{|\Omega|\to+\infty} \mathbf{S}^{\text{app}}(\Omega)$. In turn, similarly to classical materials (see

section 2.1.2), the apparent compliance of the SVE Ω is defined as the linear operator that maps the average stress $\langle\boldsymbol{\sigma}\rangle$ to the average total strain $\langle\mathbf{e}\rangle$: $\langle\boldsymbol{\sigma}\rangle = \mathbf{C}^{\text{app}}(\Omega) : \langle\mathbf{e}\rangle$, where $\mathbf{e}$ and $\boldsymbol{\sigma}$ are the local total strains and stresses that solve the corrector problem defined by the field equations (3.93a) to (3.93c) (with vanishing body-forces, $\mathbf{b} = \mathbf{0}$) and appropriate boundary conditions, that ensure the following generalization of Hill–Mandel's lemma to be satisfied [Tra16]

$$\langle\boldsymbol{\sigma} : \mathbf{e} + \mathbf{grad}\,\boldsymbol{\sigma} \therefore \boldsymbol{\phi}\rangle = \langle\boldsymbol{\sigma}\rangle : \langle\mathbf{e}\rangle. \tag{3.98}$$

In reference [Tra16], we extended the classical essential, natural and periodic boundary conditions to stress-gradient materials. For example, the generalized natural boundary condition reads $\boldsymbol{\sigma}|_{\partial\Omega} = \overline{\boldsymbol{\sigma}}$, where the constant, second-rank, symmetric tensor $\overline{\boldsymbol{\sigma}}$ denotes the macroscopic (prescribed) stress. Note that the *full* stress tensor must be prescribed at the boundary (see remark 3.2). For these boundary conditions, it can then be shown that

$$\frac{1}{2}\overline{\boldsymbol{\sigma}} : \mathbf{S}^{\text{app}} : \overline{\boldsymbol{\sigma}} = \inf_{\boldsymbol{\sigma}} W^*(\boldsymbol{\sigma}), \tag{3.99}$$

where the infimum is taken over the space of divergence-free stress tensors $\boldsymbol{\sigma}$ that are such that $\boldsymbol{\sigma}|_{\partial\Omega} = \overline{\boldsymbol{\sigma}}$. This in turn allowed us to prove that for a given microstructure with given (local) elastic coefficients μ and ν, increasing the material internal length tends to decrease the effective stiffness. Conversely, decreasing the size of the heterogeneities (the material internal length being unchanged) tends to decrease the effective stiffness.

Strain-gradient models are often invoked to account for size-effects in nanocomposites. This is relevant for most nanocomposites, where so-called "positive" (or stiffening) size-effects are usually observed. However, numerical evidence from atomistic simulations suggest that some nanoparticles/polymer composites [Dav+14]; [OCG05] might exhibit "negative" (softening) size-effects. For such materials, strain-gradient models are inadequate, while stress-gradient have the required qualitative behavior. It should be noted that the softening size-effect exhibited by stress-gradient materials has already been observed by Polizzotto [Pol14] and Challamel, Wang, and Elishakoff [CWE16] (albeit with slightly different material models).

With the above homogenization framework at hand, we then went on to derive classical Eshelby-based estimates of the effective compliance of composites with monosized spherical inhomogeneities (a: common radius of all inhomogeneities), both matrix and inhomogeneities being stress-gradient materials.

This first required the solution to Eshelby's problem of the spherical inhomogeneity, which was derived analytically in reference [Tra16]. The closed-form expressions are too complex to be reported here. As an illustration, we consider in figure 3.4 the case of a stiff inhomogeneity ($\mu_{\text{i}} = 10\mu_{\text{m}}$ and $\nu_{\text{i}} = \nu_{\text{m}} = 0.25$) subjected to a uniaxial stress at infinity ($\boldsymbol{\sigma}^{\infty} = \sigma^{\infty}\mathbf{e}_z \otimes \mathbf{e}_z$) and we study the influence of the material internal lengths ℓ_{i} and ℓ_{m} on the solution. Figure 3.4 (left) plots the axial stress σ_{zz} along the polar axis of the inhomogeneity for various combinations of the material internal lengths (ℓ_{i} of the inhomogeneities and ℓ_{m}) of the matrix. The classical case ($\ell_{\text{i}} = \ell_{\text{m}} = 0$) is also represented. From these plots, it is readily deduced that Eshelby's theorem [Esh57] does not hold for stress-gradient elasticity. In other words, the

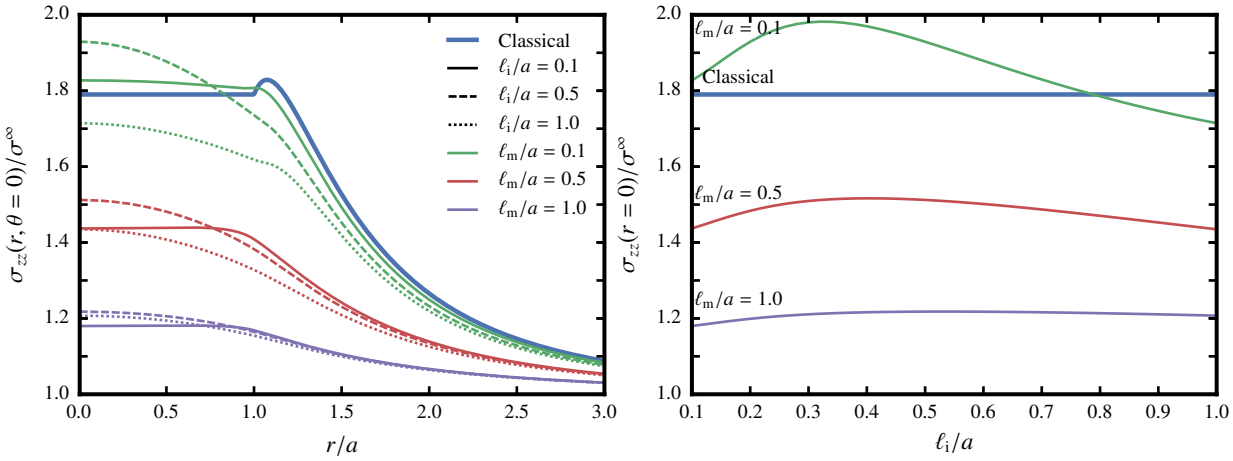

Figure 3.4: Solution to Eshelby's spherical inhomogeneity problem (uniaxial loading at infinity). *Left:* plot of the axial stress σ_{zz} along the polar axis ($\theta = 0$) as a function of the distance to the center of the inhomogeneity, r. Line types (solid, dashed, dotted) correspond to various values of the material internal length ℓ_i of the inhomogeneity. *Right:* plot of the axial stress $\sigma_{zz}(r = 0)$ at the center of the inhomogeneity as a function of the inhomogeneity's material internal length ℓ_i. For both graphs, colors correspond to various values of the material internal length ℓ_m of the matrix. The thick line corresponds to the classical solution ($\ell_i = \ell_m = 0$).

stress is not uniform within the inhomogeneity. Indeed, it is recalled that the elastic stress-gradient model requires the continuity of the *full* stress tensor at the matrix–inhomogeneity interface, which induces a boundary layer at the matrix–inhomogeneity interface. It can be verified on the closed-form expressions that the thickness of this boundary layer is about a few ℓ_i within the inhomogeneity. As a consequence, the stress field is nearly uniform at the core of the inhomogeneity for small values of the material internal length ℓ_i. Similarly, for small values of the material internal length ℓ_m of the matrix, the non-uniform stress within the inhomogeneity is close to the classical value.

Closer inspection of figure 3.4 (left) shows that at a given point within the inhomogeneity, the radial stress does not evolve monotonically with the inhomogeneity's material internal length ℓ_i. This is better illustrated on figure 3.4 (right), which shows the radial stress at the center of the inhomogeneity as a function of ℓ_i, for various values of ℓ_m. It is observed that the radial stress at the center reaches a maximum for a finite value of ℓ_i, which increases as ℓ_m increases.

From the solution to Eshelby's spherical inhomogeneity, the stress-based approach proposed by Benveniste [Ben87] can readily be extended to stress-gradient materials to derive Mori–Tanaka [MT73] estimates of the effective compliance of composites with spherical inhomogeneities. Again, closed-form expressions are intractable, but numerical evaluation of these estimates is straightforward.

As an illustration, the resulting effective bulk and shear moduli κ^{eff} and μ^{eff} are plotted in figure 3.5 as a function of the volume fraction f of inclusions. The classical moduli of both phases are such that $\mu_i = 10\mu_m$ and $\nu_i = \nu_m = 0.25$. Parametric studies not reproduced here show that the dilute stress concentration tensor is not very sensitive to ℓ_i: we therefore assumed that $\ell_i = \ell_m$.

As expected, it is observed that for small values of the material internal length, the proposed

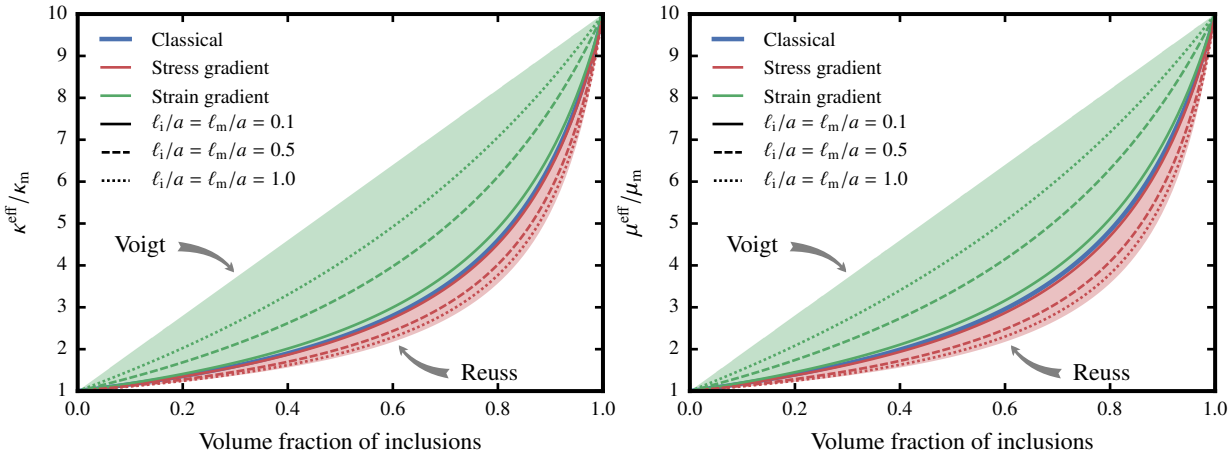

Figure 3.5: Mori–Tanaka estimates of the effective bulk (*left*) and shear (*right*) moduli of the composite κ^{eff} and μ^{eff}, as a function of the volume fraction of inclusions, f. The estimates are represented for both stress- and strain-gradient materials.

estimates are close to the classical Mori–Tanaka estimates. Conversely, for larger values of the material internal length, these estimates tend to the classical bound of Reuss. This was also expected, since large material internal lengths tend to favor phase-wise constant stress fields (as already argued above). It should however be noted that the limit as $\ell_i, \ell_m \to +\infty$ is purely formal. Indeed, the above scale bridging is carried under the assumption that $\ell \ll a$ or $\ell \sim a$. As a consequence, the largest material internal length considered in figure 3.5 is $\ell_i = \ell_m = a$.

Figure 3.5 also shows the recently published Mori–Tanaka estimates of the effective elastic properties of strain-gradient materials [MG14]. These estimates are based on the so-called simplified strain gradient elasticity [AA92]; [AA97]; [GP07]. It is recalled that our own simplified material model (described in section 3.5.1) is very close in spirit to that of Gao and Park [GP07], which makes the comparison in figure 3.5 relevant.

Figure 3.5 is a visual illustration of the essential differences between strain- and stress-gradient materials that were already pointed out in section 3.5.1. Indeed, the region comprised between the Reuss and Voigt bounds is clearly divided in two non-overlapping subregions. Strain-gradient materials systematically fall in the region comprised between the classical effective properties and the corresponding upper-bounds of Voigt (stiffening size-effect), while stress-gradient materials systematically fall in the region comprised between the classical effective properties and the corresponding lower-bounds of Reuss (softening size-effect). This again shows that, although conceptually similar (one might be tempted to say that they are "dual"), the strain- and stress-gradient models define widely different materials.

3.5.3 Hashin–Shtrikman bounds for composites with spherical inclusions

In reference [Tra16], we also extended the Hashin–Shtrikman principle to stress-gradient materials. Besides the classical stress-polarization $\boldsymbol{\tau}$, the Hashin–Shtrikman functional now also depends on a stress-gradient polarization $\boldsymbol{\kappa}$ (third-rank tensor). Using phase-wise constant polarizations then allowed us to derive bounds on the effective properties of composites with

monosized, spherical inclusions. Quite remarkably, the resulting bounds depend explicitly on the two-point probability function, even for isotropic microstructures; this is at odds with classical elasticity. The derivation of these bounds is briefly outlined in the present section.

Following the exposition of chapter 2 (sections 2.2 and 2.3), we first define Green operators for stress-gradient materials. We consider a homogeneous, elastic, stress-gradient body Ω, with classical compliance $\mathbf{S}_0$ and generalized compliance $\mathbf{M}_0$. We introduce the classical and generalized stiffnesses $\mathbf{C}_0 = \mathbf{S}_0^{-1}$ and $\mathbf{L}_0 = \mathbf{M}_0^{-1}$. The body Ω is fully clamped at its boundary $\partial\Omega$, and subjected to the eigenstress $\boldsymbol{\tau}$ as well as the eigen-stress-gradient $\boldsymbol{\kappa}$. The corresponding boundary value problem reads [compare with (3.93)]

$$\begin{aligned}
&\mathbf{div}\,\boldsymbol{\sigma} = \mathbf{0} && \mathbf{R} = \mathbf{grad}\,\boldsymbol{\sigma} && (\Omega), && (3.100a)\\
&\mathbf{e} = \mathbf{S}_0 : (\boldsymbol{\sigma} - \boldsymbol{\tau}) && \boldsymbol{\phi} = \mathbf{M}_0 \therefore (\mathbf{R} - \boldsymbol{\kappa}) && (\Omega), && (3.100b)\\
&\mathbf{e} = \boldsymbol{\epsilon}[\mathbf{u}] + \mathbf{div}\,\boldsymbol{\phi} && && (\Omega), && (3.100c)\\
&\mathbf{sym}(\mathbf{u} \otimes \mathbf{n}) + \boldsymbol{\phi} \cdot \mathbf{n} = \mathbf{0} && && (\partial\Omega), && (3.100d)
\end{aligned}$$

where equation $(3.100a)_2$ accounts for the fact that $\mathbf{grad}\,\boldsymbol{\sigma}$ is trace-free, since $\boldsymbol{\sigma}$ is divergence-free. The above problem (3.100) is linear, and we introduce the four Green operators $\boldsymbol{\Gamma}_0^{e\tau}$, $\boldsymbol{\Gamma}_0^{e\kappa}$, $\boldsymbol{\Gamma}_0^{\phi\tau}$ and $\boldsymbol{\Gamma}_0^{\phi\kappa}$ (of order 4, 5, 5 and 6, respectively) such that the solution reads

$$\mathbf{e} = -\boldsymbol{\Gamma}_0^{e\tau}[\boldsymbol{\tau}] - \boldsymbol{\Gamma}_0^{e\kappa}[\boldsymbol{\kappa}] \quad \text{and} \quad \boldsymbol{\phi} = -\boldsymbol{\Gamma}_0^{\phi\tau}[\boldsymbol{\tau}] - \boldsymbol{\Gamma}_0^{\phi\kappa}[\boldsymbol{\kappa}]. \tag{3.101}$$

For vanishing generalized compliance $\mathbf{M}_0$, the operator $\boldsymbol{\Gamma}_0^{e\tau}$ coincides with the classical fourth-rank Green operator for essental boundary conditions (see section 2.2.1). The operators $\boldsymbol{\Gamma}_0^{e\kappa}$ and $\boldsymbol{\Gamma}_0^{\phi\tau}$ are adjoint in the sense: $\langle \boldsymbol{\tau} : \boldsymbol{\Gamma}_0^{e\kappa}[\boldsymbol{\kappa}]\rangle = \langle \boldsymbol{\Gamma}_0^{\phi\tau}[\boldsymbol{\tau}] \therefore \boldsymbol{\kappa}\rangle$. Closed-form expressions are derived in Fourier space for periodic boundary conditions in reference [Tra16].

We then introduce the following Hashin–Shtrikman functional [compare with equation (2.36)]

$$\begin{aligned}
\mathrm{HS}(\boldsymbol{\tau}, \boldsymbol{\kappa}; \overline{\boldsymbol{\varepsilon}}) = {}& \tfrac{1}{2}\overline{\boldsymbol{\varepsilon}} : \mathbf{C}_0 : \overline{\boldsymbol{\varepsilon}} + \overline{\boldsymbol{\varepsilon}} : \langle \boldsymbol{\tau}\rangle - \tfrac{1}{2}\langle \boldsymbol{\tau} : (\mathbf{C} - \mathbf{C}_0)^{-1} : \boldsymbol{\tau}\rangle - \tfrac{1}{2}\langle \boldsymbol{\kappa} : (\mathbf{L} - \mathbf{L}_0)^{-1} : \boldsymbol{\tau}\rangle \\
& - \tfrac{1}{2}\langle \boldsymbol{\tau} : \boldsymbol{\Gamma}_0^{e\tau}[\boldsymbol{\tau}]\rangle - \tfrac{1}{2}\langle \boldsymbol{\tau} : \boldsymbol{\Gamma}_0^{e\kappa}[\boldsymbol{\kappa}]\rangle - \tfrac{1}{2}\langle \boldsymbol{\kappa} : \boldsymbol{\Gamma}_0^{\phi\tau}[\boldsymbol{\tau}]\rangle - \tfrac{1}{2}\langle \boldsymbol{\kappa} : \boldsymbol{\Gamma}_0^{\phi\tau}[\boldsymbol{\tau}]\rangle,
\end{aligned} \tag{3.102}$$

where $\overline{\boldsymbol{\varepsilon}}$ again denotes the macroscopic (prescribed) strain. The extremum Hashin–Shtrikman principle then reads

$$\mathbf{C}_0 \overset{\geq}{\leq} \mathbf{C} \text{ and } \mathbf{L}_0 \overset{\geq}{\leq} \mathbf{L} \quad \Rightarrow \quad \mathrm{HS}(\boldsymbol{\tau}; \boldsymbol{\kappa}; \overline{\boldsymbol{\varepsilon}}) \overset{\geq}{\leq} \tfrac{1}{2}\overline{\boldsymbol{\varepsilon}} : \mathbf{C}^{\mathrm{app}}(\Omega) : \overline{\boldsymbol{\varepsilon}} \quad \text{for all} \boldsymbol{\tau} \in \mathscr{T}_2(\Omega) \text{ and } \boldsymbol{\kappa} \in \mathscr{T}_3(\Omega), \tag{3.103}$$

where $\mathscr{T}_3(\Omega)$ denotes the space of third-rank tensor fields defined over Ω, symmetric with respect to their first two indices, with square-integrables components.

In the above inequality, $\mathbf{C}^{\mathrm{app}}(\Omega)$ denotes the apparent stiffness of the stress-gradient SVE with generalized essential boundary conditions.

Following the classical approach of Hashin and Shtrikman [HS62a] (see also section 3.1.5), we then used phase-wise constant trial stress- and stress-gradient-polarizations to derive bounds

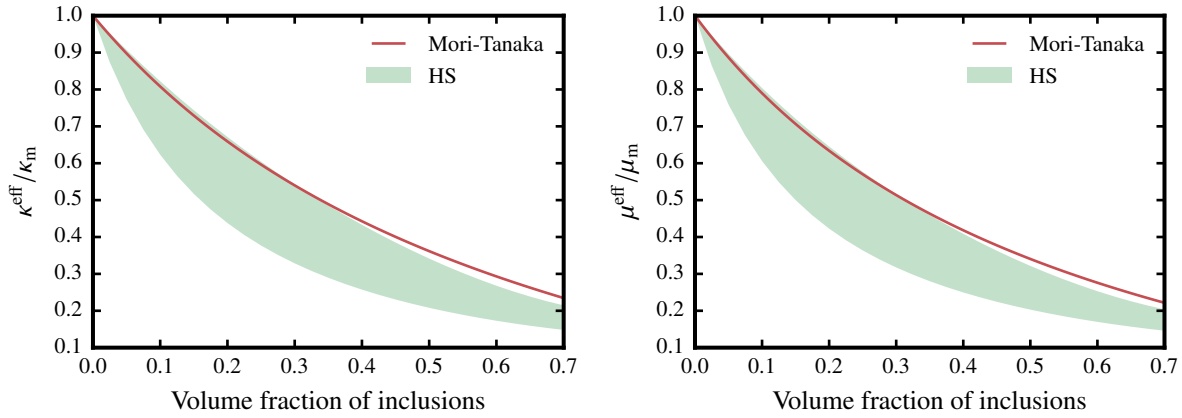

Figure 3.6: Hashin–Shtrikman bounds on, and Mori–Tanaka estimates of the effective bulk (*left*) and shear (*right*) moduli of the composite κ^{eff} and μ^{eff}, as a function of the volume fraction of inhomogeneities, f. For volume fractions above 40 %, the estimates violate the bounds.

on the effective stiffness of stress-gradient bodies. The derivation shows that the optimal trial stress-gradient polarization $\boldsymbol{\kappa}$ vanishes, while the optimal trial stress-polarization solves the linear system (3.28) obtained in the classical case, where the classical fourth-rank Green operator $\mathbf{\Gamma}_0^{\infty}$ should be replaced with its generalized counterpart $\mathbf{\Gamma}_0^{e\tau,\infty}$. It is quite remarkable that –even in the isotropic case– the two-point probability functions do not vanish in the above derivation. This means that these functions must be specified in order to evaluate Hashin–Shtrikman bounds.

The model of Verlet and Weis [VW72] is known to give an excellent approximation of the two-point probability functions of a random assembly of hard spheres in thermodynamical equilibrium. Using this model, we were able to derive closed-form expressions of the bounds.

As expected, these bounds depend on the radius a of the spherical inhomogeneities (through the ratios ℓ_{i}/a and ℓ_{m}/a). The results are too complex to be presented here, but were thoroughly investigated numerically in reference [Tra16]. Figure 3.6 (which reproduces figure 8.4 in reference [Tra16]) presents the bounds on the effective elastic moduli for increasing volume fraction of soft spherical inhomogeneities ($\mu_{\text{i}} = 0.1\mu_{\text{m}}$, $\nu_{\text{i}} = \nu_{\text{m}} = 0.125$, $\ell_{\text{i}} = \ell_{\text{m}} = 0.2a$). This case provides a striking example of Mori–Tanaka estimates that *violate* the Hashin–Shtrikman bounds!

This is a quite unusual result, since Mori–Tanaka estimates are usually found to coincide with one of the Hashin–Shtrikman bounds. However, it should be recalled here that Eshelby's theorem [Esh57] does not hold for stress-gradient materials. In other words, the equivalent inclusion method of Eshelby is not exact for this class of materials. Therefore, it is in principle possible to derive *two* families of Mori–Tanaka estimates from the solutions to Eshelby's inhomogeneity *and* inclusion problems.

We realized a posteriori that Hashin–Shtrikman bounds ought to be compared to Mori–Tanaka estimates that rely on the inclusion problem, rather than the inhomogeneity problem as done in reference [Tra16]. However, whether based on the inhomogeneity or inclusion problem, the estimates will *not* depend on the two-point probability functions. It is therefore very likely that these estimates will differ from any of the Hashin–Shtrikman bounds.

To close this section, we should again emphasize that for stress-gradient materials, the Hashin–Shtrikman bounds depend on the two-point probability functions (even in the isotropic case). This was expected, because of the existence of material internal lengths, which ought to be compared to correlation lengths. Simple tests carried out in reference [Tra16] tend to indicate that, at fixed correlation lengths [defined e.g. as the quantities $\int_0^{+\infty} S_{\alpha\beta}(r)\,\mathrm{d}r$] the bounds are not very sensitive to the exact shape of the two-point probability functions $S_{\alpha\beta}(r)$. Besides volume fractions, the correlation lengths are therefore the governing microstructural parameters for stress-gradient materials.

3.5.4 Closing remarks

In the present section, we have discussed a new material model with internal material lengths. This model was initially developed by Forest and Sab [FS12] and further analyzed mathematically by Sab, Legoll, and Forest [SLF16]. It relies on the assumption that the complementary strain energy density depends on the stress tensor and its gradient; such materials were coined *stress-gradient materials*.

While the stress-gradient model is mathematically sound, it raises many theoretical questions regarding its physical meaning. How should we understand such boundary conditions where the whole stress tensor (rather than the traction vector) is prescribed? What is the meaning of the generalized displacement $\boldsymbol{\phi}$ in terms of an underlying microstructure?

As far as I am concerned, the question that puzzles me most is the meaning of the vector field $\mathbf{u}$. Indeed, dualization of the equilibrium equations shows that $\mathbf{u}$ is work-conjugate to the body forces $\mathbf{b}$ (which would indicate that $\mathbf{u}$ is indeed the local displacement), but *not* to the prescribed boundary tractions $\overline{\mathbf{T}}$! Equally disturbing is the kinematic boundary condition (3.97a) that allows the "displacement" $\mathbf{u}$ not to vanish at the boundary of a *clamped* body!

To resolve this paradox, I think that the couple $(\mathbf{u}, \boldsymbol{\phi})$ ought to be split (through a linear transformation) in a different fashion $(\mathbf{u}', \boldsymbol{\phi}')$ so as to lead to a boundary value problem that is strictly equivalent to (3.93), while leading to more familiar kinematic boundary conditions. This is very similar in my mind to gage invariance in electromagnetism; I have so far had no success in finding this transformation.

Regarding the homogenization of stress-gradient materials, the results presented here pave the way to the modelling of materials exhibiting softening size-effects. Experimental feedback pertaining to the very existence of such materials is now needed in order to assert the relevance of the stress-gradient material.

Finally, it should be emphasized again that we focused here on heterogeneous, stress-gradient materials that behave macroscopically as classical materials. Analysis of the reverse problem, namely homogenization of classical heterogenous materials as stress-gradient materials, is an exciting perspective. It should offer new insights into the meaning of the degrees of freedom $\mathbf{u}$ and $\boldsymbol{\phi}$.

Chapter 4

Galerkin discretization of the Lippmann–Schwinger equation

The present chapter is devoted to the numerical approximation of the Lippmann–Schwinger equation. It gathers work published in references [BD10]; [BD12]; [BD14]; [BDS13]; [BDS14]; [Bri17a]; [Tra+16]. Section 4.1 sets the general framework shared by both methods presented subsequently. These methods differ only by the (finite dimensional) subspace of trial stress-polarizations that is selected for the discretization of the initial problem.

In section 4.2, we consider trial stress-polarizations that are constant over the cells of a uniform cartesian grid. This results in a variational form of the so-called *FFT-based methods* initially introduced by Moulinec and Suquet [MS94]; [MS98]. Our variational approach sheds a new light on these legacy schemes, that ease their mathematical analysis while allowing for some minor improvements (such as: faster convergence and filtering of the Gibbs-like oscillations). It is observed that these methods are meant to be virtually exact (up to vanishing discretization errors), and we were indeed able to prove that the solution to the discretized Lippmann–Schwinger equation converges to that of the continuous Lippmann–Schwinger equation.

Conversely, the method presented in section 4.3 is *not* meant to be exact. Our intention was rather to derive "good enough" estimates of the macroscopic properties at a moderate cost. The method is restricted to matrix–inhomogeneities microstructures, where the inhomogeneities assume simple geometries (spherical, spheroidal). We consider trial stress-polarizations that are polynomial over each inhomogeneity. The resulting method can be seen as a variational form of the equivalent inclusion method (EIM) initiated by Moschovidis and Mura [MM75]. Unlike FFT-based methods, the variational form of the EIM is clearly superior to the legacy method. It is shown to perform extremely well in two dimensions. To our disappointment, this does not extend to the three dimensional case, where it turns out to be barely more accurate than standard Hashin–Shtrikman bounds.

4.1 General setting

In the present section, we lay out the variational framework on which both numerical methods that will be presented in this chapter rely. We first reformulate in section 4.1.1 the Lippmann–Schwinger equation introduced in sections 2.3.1 and 3.1.1 as a standard variational problem.

Then, we briefly discuss some general issues related to the Galerkin discretization of this variational problem.

4.1.1 The Lippmann–Schwinger equation as a variational problem

It is recalled that the Lippmann–Schwinger equations (2.30), (2.33) and (3.3) are equivalent to the corrector problems (2.11), (2.16) and (3.11) with essential, periodic and mixed boundary conditions, respectively. The strong form of the generic Lippmann–Schwinger reads

$$(\mathbf{C} - \mathbf{C}_0)^{-1} \,:\, \boldsymbol{\tau} + \boldsymbol{\Gamma}_0[\boldsymbol{\tau}] = \overline{\boldsymbol{\varepsilon}}, \tag{4.1}$$

where $\boldsymbol{\tau} \in \mathcal{T}_2(\Omega)$ is the unknown stress-polarization, $\overline{\boldsymbol{\varepsilon}}$ is the macroscopic (prescribed) stress. Depending on the boundary conditions, $\boldsymbol{\Gamma}_0$ denotes one of the following fourth-rank Green operators

1. essential BCs, problem (2.11): $\boldsymbol{\Gamma}_0 \equiv \boldsymbol{\Gamma}_0^{\text{ess}}$ (see section 2.2.1),
2. periodic BCs, problem (2.16): $\boldsymbol{\Gamma}_0 \equiv \boldsymbol{\Gamma}_0^{\text{per}}$ (see section 2.2.2),
3. mixed BCs, problem (3.11): $\boldsymbol{\Gamma}_0 \equiv \left(\boldsymbol{\tau} \mapsto \boldsymbol{\Gamma}_0^{\infty}[\boldsymbol{\tau} - \chi\langle\boldsymbol{\tau}\rangle]\right)$ (see section 3.1).

Contracting with a test stress-polarization $\boldsymbol{\varpi} \in \mathcal{T}_2(\Omega)$ and taking the volume average over the whole domain Ω, the above equation is readily turned into the following variational problem

$$\text{Find } \boldsymbol{\tau} \in \mathcal{T}_2(\Omega) \text{ such that } a(\boldsymbol{\tau}, \boldsymbol{\varpi}) = \overline{\boldsymbol{\varepsilon}} \,:\, \langle\boldsymbol{\varpi}\rangle \text{ for all } \boldsymbol{\varpi} \in \mathcal{T}_2(\Omega), \tag{4.2}$$

where

$$a(\boldsymbol{\tau}, \boldsymbol{\varpi}) = \langle \boldsymbol{\varpi} \,:\, (\mathbf{C} - \mathbf{C}_0)^{-1} \,:\, \boldsymbol{\tau} \rangle + \langle \boldsymbol{\varpi} \,:\, \boldsymbol{\Gamma}_0[\boldsymbol{\tau}] \rangle. \tag{4.3}$$

In the above problem, the bilinear form a is symmetric owing to the symmetry of the fourth-rank Green operator with respect to the scalar product $\langle \boldsymbol{\tau}, \boldsymbol{\eta} \rangle = \langle \boldsymbol{\tau} \,:\, \boldsymbol{\eta} \rangle$ (see section 2.2.4).

4.1.2 Galerkin discretization of the Lippmann–Schwinger equation

Solving equation (4.2) exactly requires a full exploration of the infinite-dimensional space $\mathcal{T}_2(\Omega)$, which is in general not possible. Galerkin approximations of the solution to this equation are defined by restricting this exploration to a finite-dimensional subspace $\mathcal{T}_2^h(\Omega) \subset \mathcal{T}_2(\Omega)$ as follows

$$\text{Find } \boldsymbol{\tau}^h \in \mathcal{T}_2^h(\Omega) \text{ such that } a(\boldsymbol{\tau}^h, \boldsymbol{\varpi}^h) = \overline{\boldsymbol{\varepsilon}} \,:\, \langle\boldsymbol{\varpi}^h\rangle \text{ for all } \boldsymbol{\varpi}^h \in \mathcal{T}_2^h(\Omega), \tag{4.4}$$

where the "h" superscript refers to a discretization parameter (as yet unspecified). The solution $\boldsymbol{\tau}^h$ to the discrete problem (4.4) (assuming that it exists and is unique) is deemed to approximate the solution to the continuous problem (4.1) or (4.2).

At this point, several remarks ought to be made. First, the present discussion is restricted to proper Galerkin discretizations, where trial and test functions belong to the same finite dimensional subspace; we have not explored Petrov–Galerkin discretizations. Second, problem (4.4) is a *consistent* discretization of problem (4.2): the bilinear form a is evaluated *exactly* over $\mathcal{T}_2^h(\Omega) \times \mathcal{T}_2^h(\Omega)$; whether this is necessary will be further discussed in section 4.2.4. Finally, the discrete problem (4.4) classically reduces to a symmetric linear system. Indeed, the solution $\boldsymbol{\tau}^h$ can be expanded in the basis $\boldsymbol{\Phi}_1^h, \dots, \boldsymbol{\Phi}_N^h$ of the finite dimensional discretization space $\mathcal{T}_2^h(\Omega)$

$$\boldsymbol{\tau}^h = \sum_{\alpha=1}^{N} q_\alpha \boldsymbol{\Phi}_\alpha^h, \tag{4.5}$$

where the unknown scalars $q_1, \dots, q_N$ solve the linear system $A \cdot q = b$, with

$$A_{\alpha\beta} = a(\boldsymbol{\Phi}_\alpha^h, \boldsymbol{\Phi}_\beta^h) \quad \text{and} \quad b_\alpha = \overline{\boldsymbol{\varepsilon}} : \langle \boldsymbol{\Phi}_\alpha^h \rangle. \tag{4.6}$$

The above discretization raises a number of questions that are to be discussed in the remainder of this chapter.

Selection of the discretization space The actual definition of the finite dimensional subspace $\mathcal{T}_2^h(\Omega)$ is of course a critical step. This space must fullfill the mathematical requirements that ensure convergence to the exact solution $\|\boldsymbol{\tau}^h - \boldsymbol{\tau}\| \to 0$ when $h \to 0$ for a well chosen norm [EG04]. We will discuss below two very different choices

1. the space of cell-wise constant trial and test stress-polarizations, for microstructures that are discretized over a uniform grid (see section 4.2),
2. the space of trial and test stress-polarizations that are polynomial over each inclusion, for matrix-inclusion microstructures with simple geometries (see section 4.3).

The first choice is akin to the h-version of the finite element method, where accuracy improvements result from refinements of the mesh (here, the grid). The second choice might be compared to the p-version of the finite element method [BSK81], where the polynomial degree of the shape functions is increased in order to improve the quality of the approximation.

It should be noted at this point that the boundary conditions are not identical in both cases. On the one hand, cell-wise constant stress-polarizations are best suited to periodic boundary conditions, thus leading to a variational form of the so-called "FFT-based numerical homogenization method" of Moulinec and Suquet [MS94] and Moulinec and Suquet [MS98]. On the other hand, inclusion-wise polynomial stress-polarizations combine well with the mixed boundary conditions introduced in section 3.1.2, thus leading to a variational form of the so-called "equivalent inclusion method" of Moschovidis and Mura [MM75].

Assembly of the matrix A It is well-known that even in a standard, displacement based finite element setting, this step is performance critical for large systems. This is all the more so in the present case because: *i.* the matrix A defined by equation $(4.6)_1$ is generally *full* rather than

sparse and *ii.* evaluation of the non-local term $\boldsymbol{\Phi}_\alpha : \boldsymbol{\Gamma}_0[\boldsymbol{\Phi}_\beta]$, which is required to form $A_{\alpha\beta}$, is complex, if possible at all.

To address the first point, we will make use of the structure of the full matrix A: in a periodic setting, this matrix is block-circulant, and a *matrix-free* strategy [Bar+94] is adopted to compute matrix-vector products $x \mapsto A \cdot x$. As for the second point, it is observed that a *consistent* discretization of the Lippmann–Schwinger equation (4.1) is by no means required to achieve good numerical performance. We will therefore introduce the following non-consistent discretization

$$\text{Find } \boldsymbol{\tau}^h \in \mathcal{T}_2^h(\Omega) \text{ such that } a^h(\boldsymbol{\tau}^h, \boldsymbol{\varpi}^h) = \overline{\boldsymbol{\varepsilon}} : \langle \boldsymbol{\varpi}^h \rangle \text{ for all } \boldsymbol{\varpi}^h \in \mathcal{T}_2^h(\Omega), \tag{4.7}$$

where a^h denotes a suitable approximation of the bilinear form a over $\mathcal{T}_2^h(\Omega) \times \mathcal{T}_2^h(\Omega)$. This approximation must be *asymptotically consistent* in the sense of Ern and Guermond [EG04] (see section 4.2.4).

Selection of the linear solver – Preconditioning This point is closely related to the previous one. Implementation of A as a matrix-free operator has a number of consequences: it precludes the use of direct linear solvers (Krylov-based iterative linear solvers will generally be used in the present work) and requires appropriate preconditioners. The latter point has not yet been fully investigated.

4.1.3 Galerkin approximation and the Hashin–Shtrikman principle

It is readily observed that problem (4.2) is equivalent to finding the critical point of the Hashin–Shtrikman functional HS defined by equations (2.36) or (3.16) over the space $\mathcal{T}_2(\Omega)$. Indeed,

$$\mathrm{HS}(\boldsymbol{\tau}; \overline{\boldsymbol{\varepsilon}}) = \tfrac{1}{2}\overline{\boldsymbol{\varepsilon}} : \mathbf{C}_0 : \overline{\boldsymbol{\varepsilon}} + \overline{\boldsymbol{\varepsilon}} : \langle \boldsymbol{\tau} \rangle - \tfrac{1}{2} a(\boldsymbol{\tau}, \boldsymbol{\tau}), \tag{4.8}$$

so that the gradient of HS with respect to the stress-polarization $\boldsymbol{\tau}$ reads

$$\frac{\partial \mathrm{HS}}{\partial \boldsymbol{\tau}}(\boldsymbol{\tau}; \overline{\boldsymbol{\varepsilon}}) : \boldsymbol{\varpi} = \overline{\boldsymbol{\varepsilon}} : \langle \boldsymbol{\varpi} \rangle - a(\boldsymbol{\tau}, \boldsymbol{\varpi}), \tag{4.9}$$

which indeed vanishes at the solution to the variational problem (4.2). Similarly, solving the discrete problem (4.4) is equivalent to finding the critical point of the Hashin–Shtrikman functional over the discretization space $\mathcal{T}_2^h(\Omega)$.

Furthermore, from the Hashin–Shtrikman principle (see section 2.3.2), if the reference material is stiffer (resp. softer) than all phases, solving the discrete problem (4.4) is equivalent to minimizing (resp. maximizing) the Hashin–Shtrikman functional over the discretization space $\mathcal{T}_2^h(\Omega)$. In that case, the resulting estimate $\boldsymbol{\tau}^h$ delivers a rigorous bound on the apparent elastic energy. Indeed, substituting $\boldsymbol{\varpi}^h$ with $\boldsymbol{\tau}^h$ in equation (4.4) leads to

$$\mathrm{HS}(\boldsymbol{\tau}^h; \overline{\boldsymbol{\varepsilon}}) = \tfrac{1}{2}\overline{\boldsymbol{\varepsilon}} : \mathbf{C}_0 : \overline{\boldsymbol{\varepsilon}} + \tfrac{1}{2}\overline{\boldsymbol{\varepsilon}} : \langle \boldsymbol{\tau}^h \rangle, \tag{4.10}$$

and plugging in inequality (2.38) finally gives

$$\mathbf{C}_0 \overset{\geq}{\leq} \mathbf{C} \quad \Rightarrow \quad \tfrac{1}{2}\overline{\boldsymbol{\varepsilon}} : \mathbf{C}_0 : \overline{\boldsymbol{\varepsilon}} + \tfrac{1}{2}\overline{\boldsymbol{\varepsilon}} : \langle \boldsymbol{\tau}^h \rangle \overset{\geq}{\leq} \tfrac{1}{2}\overline{\boldsymbol{\varepsilon}} : \mathbf{C}^{\mathrm{app}}(\Omega) : \overline{\boldsymbol{\varepsilon}}. \tag{4.11}$$

It should be noted however that for the above result to hold, a *consistent* discretization must be adopted. In other words, the bilinear form a must be evaluated exactly over $\mathcal{T}_2^h(\Omega)\times\mathcal{T}_2^h(\Omega)$, which might be too costly (if possible at all).

In any cases, the estimate $\boldsymbol{\tau}^h$ of the true stress-polarization $\boldsymbol{\tau}$ delivers an estimate of the apparent stiffness of the SVE Ω. Indeed, regardless of the (essential, periodic or mixed) boundary conditions, we have for the true stress-polarization [see equations (2.32), (2.34) and (3.10)]

$$\mathbf{C}^{\mathrm{app}}(\Omega) : \overline{\boldsymbol{\varepsilon}} = \mathbf{C}_0 : \overline{\boldsymbol{\varepsilon}} + \langle \boldsymbol{\tau} \rangle, \tag{4.12}$$

and the estimate $\mathbf{C}^{\mathrm{app},h}(\Omega)$ of the apparent stiffness can be defined similarly

$$\mathbf{C}^{\mathrm{app},h}(\Omega) : \overline{\boldsymbol{\varepsilon}} = \mathbf{C}_0 : \overline{\boldsymbol{\varepsilon}} + \langle \boldsymbol{\tau}^h \rangle. \tag{4.13}$$

It is observed that the evaluation of $\mathbf{C}^{\mathrm{app},h}(\Omega)$ thus defined from the approximate solution $\boldsymbol{\tau}^h$ is fairly straightforward (provided that the basis functions $\boldsymbol{\Phi}_1, \ldots, \boldsymbol{\Phi}_N$ are simple enough).

***

In the previous section, it was shown that the Lippmann–Schwinger equation could be reformulated as a variational problem that lends itself to standard Galerkin discretization. Various choices of subspaces of trial and test functions can lead to widely different numerical schemes. The remainder of this chapter is devoted to two such numerical schemes.

Uniform grid, periodic Lippmann–Schwinger solvers are first addressed in the following section. In a periodic setting, these solvers result from the discretization over a cartesian grid of the stress-polarization as a cell-wise constant field.

4.2 Uniform grid, periodic Lippmann–Schwinger solvers

UGPLS solvers are more widely known as "FFT-based methods" which is a very unfortunate name. In reference [Bri17a], I therefore introduced the more accurate terminology "Uniform grid, periodic Lippmann–Schwinger solver" to describe the various methods that will be discussed below. Although a bit verbose (and not widely adopted!), this terminology will be used in the present chapter.

UGPLS solvers are designed for microstructures that are discretized over a cartesian grid. Because periodic boundary conditions are assumed, the convolution product arising from the $\boldsymbol{\Gamma}_0[\boldsymbol{\tau}]$ term in the Lippmann–Schwinger equation (4.1) can be computed efficiently in Fourier space, by means of the fast Fourier transform (FFT). They belong to the family of full-field homogenization techniques: refining the grid leads to a more accurate local description of the mechanical fields that solve the corrector problem (2.16). However, it should be observed that, contrary to alternative techniques such as the finite element method (FEM), this refinement must be *uniform* (which comes with a cost).

UGPLS solvers were introduced by Moulinec and Suquet in their seminal papers [MS94]; [MS98]. Their so-called "basic scheme" (see section 4.2.2 below) is both conceptually elegant and simple to implement. Although UGPLS solvers have been around for about 25 years now, it is fair to say that this topic remained confined to a handful of scientists until the early 2010s. At that time new developments were proposed by a larger number of groups around the world, including Moulinec, Suquet and coworkers [Mon+]; [MS14]; [Vin+14], Willot and coworkers [WAP14]; [Wil15]; [WP08], Zeman, Vondřejc and coworkers [Geu+17]; [MVZ16]; [VZM14]; [VZM15]; [Zem+10], Kabel, Schneider and coworkers [KBS14]; [KFS15]; [KMS15]; [Sch15]; [Sch17]; [SMK17]; [SOK15], Eisenlohr, Lebensohn and coworkers [ALR14]; [Che+15]; [Eis+13]; [LKE12], Gélébart and coworkers [GM13]; [GO15a], to cite but a few teams.

Regarding the development of the method itself, significant progress has now been made on the selection of iterative linear solvers [BD10]; [EM99]; [MMS01]; [MS14]; [Zem+10], discretization of the mechanical fields [BD10]; [BD12]; [Bri17a]; [SMK17]; [VZM14]; [VZM15]; [WAP14]; [Wil15]; [WP08]; [Yvo12], convergence with respect to the grid size [BD12]; [Sch15]. UGPLS solvers were designed to handle material non-linearities from the very beginning [MMS01]; [MS94]; [MS98], although alternative approaches (akin to the standard nested global–local loops used in FEM approaches) have also been proposed [GM13]. Geometric non-linearities were discussed in references [Eis+13]; [KBS14]; [KFS15].

Regarding application to "real-life materials", it is often advocated that UGPLS solvers can easily be coupled with 3D imaging techniques. Indeed, the images of the microstructure readily provide the regular grid that is required by these full-field methods. While perfectly true, this statement should be qualified by the fact that periodic boundary conditions are implicitly assumed in the simulation. Depending on the application, this assumption may not be relevant. Despite this minor shortcoming, a wide range of materials have been investigated by means of UGPLS solvers: crystal plasticity of ice [Mon+], creep of cementitious materials [ŠB10] and glass reinforced plastic composites [Lav+15], fiber reinforced plastics at large strains [KBS14], etc. This diversity shows the versatility of these methods.

My contributions to this field were published in references [BD10]; [BD12]; [Bri17a]. They are mostly methodological, and confined to linear elasticity. They cover the derivation of rigorous bounds on the effective properties, the use of Krylov-space iterative linear solvers, alternative discretizations, proof of convergence with respect to the grid-size, a posteriori errors. These topics are covered in the remainder of section 4.2.

Section 4.2.1 introduces notations for the discrete and periodic Fourier transforms. Section 4.2.2 introduces the "basic scheme" of Moulinec and Suquet, and serves as a motivation for the subsequent developments. Sections 4.2.3 and 4.2.4 discuss the selection of the approximation subspace $\mathcal{T}_2^h(\Omega)$ and convergence with respect to the grid-size. Section 4.2.5 discusses both *a priori* and *a posteriori* error estimates. Finally, section 4.2.6 lists a few perspectives for future work.

4.2.1 Fourier series and discrete Fourier transforms

One essential common feature of all UGPLS solvers is the fact that discretization is carried out over a cartesian grid $\mathcal{G}^h$ of size $N_1 \times \cdots \times N_d$ defined over the unit-cell $\Omega = (0, L_1) \times \cdots \times (0, L_d)$.

Although it is by no means required, it will be assumed in the remainder of section 4.2, for the sake of simplicity, that the cells are cubic; h denotes the side of the cubic grid cells: $h = L_1/N_1 = \cdots = L_d/N_d$. Cells of the grid $\mathcal{G}^h$ are indexed by $\mathbf{n} \in \{0, \ldots, N_1 - 1\} \times \cdots \times \{0, \ldots, N_d - 1\}$.

In the periodic setting adopted here, most mechanical fields are periodic and can (will) therefore be expanded in Fourier series. As an example, we recall here the expression of the Fourier coefficients $\tilde{\boldsymbol{\tau}}_{\mathbf{k}}$ ($\mathbf{k} \in \mathbb{Z}^d$) of the stress-polarization $\boldsymbol{\tau}(\mathbf{x})$ ($\mathbf{x} \in \Omega$)

$$\tilde{\boldsymbol{\tau}}_{\mathbf{k}} = \frac{1}{L_1 \ldots L_d} \int_{\mathbf{x}\in\Omega} \boldsymbol{\tau}(\mathbf{x}) \exp\left[-2\mathrm{i}\pi\left(k_1 x_1/L_1 + \cdots + k_d x_d/L_d\right)\right] \mathrm{d}V_{\mathbf{x}}, \tag{4.14}$$

as well as the resulting expansion of $\boldsymbol{\tau}$ as a Fourier series

$$\boldsymbol{\tau}(\mathbf{x}) = \sum_{\mathbf{k}\in\mathbb{Z}^d} \hat{\boldsymbol{\tau}}_{\mathbf{k}} \exp\left[2\mathrm{i}\pi\left(k_1 x_1/L_1 + \cdots + k_d x_d/L_d\right)\right]. \tag{4.15}$$

The discrete trial stress-polarization $\boldsymbol{\tau}^h$ introduced in section 4.1.2 is also periodic. As such, we will introduce its Fourier coefficients $\tilde{\boldsymbol{\tau}}^h_{\mathbf{k}}$. The discretization itself [as introduced in equation (4.5)] will of course be defined with respect to the cartesian grid $\mathcal{G}^h$

$$\boldsymbol{\tau}^h(\mathbf{x}) = \sum_{n_1=0}^{N_1-1} \cdots \sum_{n_d=0}^{N_d-1} \boldsymbol{\tau}^h_{\mathbf{n}}\, \Phi^h_{\mathbf{n}}(\mathbf{x}), \tag{4.16}$$

where the parameters $\boldsymbol{\tau}^h_{\mathbf{n}}$ are attached to the cells of the grid $\mathcal{G}^h$. For suitable choices of the (scalar) shape functions $\Phi^h_{\mathbf{n}}$, the Fourier coefficients $\tilde{\boldsymbol{\tau}}^h_{\mathbf{k}}$ can be related to the discrete Fourier transform of the parameters $\boldsymbol{\tau}^h_{\mathbf{n}}$, defined as follows, for $\mathbf{k} \in \mathbb{Z}^d$

$$\hat{\boldsymbol{\tau}}^h_{\mathbf{k}} = \sum_{n_1=0}^{N_1-1} \cdots \sum_{n_d=0}^{N_d-1} \boldsymbol{\tau}^h_{\mathbf{n}} \exp\left[-2\mathrm{i}\pi\left(k_1 n_1/N_1 + \cdots + k_d n_d/N_d\right)\right], \tag{4.17}$$

which is readily inverted

$$\boldsymbol{\tau}^h_{\mathbf{n}} = \frac{1}{N_1 \cdots N_d} \sum_{k_1=0}^{N_1-1} \cdots \sum_{k_d=0}^{N_d-1} \hat{\boldsymbol{\tau}}^h_{\mathbf{k}} \exp\left[2\mathrm{i}\pi\left(k_1 n_1/N_1 + \cdots + k_d n_d/N_d\right)\right]. \tag{4.18}$$

It is emphasized that $\tilde{\boldsymbol{\tau}}^h_{\mathbf{k}}$ (Fourier coefficients of $\boldsymbol{\tau}^h$) and $\hat{\boldsymbol{\tau}}^h_{\mathbf{k}}$ (discrete Fourier transform of $\boldsymbol{\tau}^h_{\mathbf{n}}$) should not be confused. Although $\tilde{\boldsymbol{\tau}}^h_{\mathbf{k}}$ can be related to $\hat{\boldsymbol{\tau}}^h_{\mathbf{k}}$ for appropriate choices of the $\Phi^h_{\mathbf{n}}$, these quantities are widely different. For one thing, the $\tilde{\boldsymbol{\tau}}^h_{\mathbf{k}}$ generally define an infinite set of discrete values, while the $\hat{\boldsymbol{\tau}}^h_{\mathbf{k}}$ define a $(N_1, \ldots, N_d)$-periodic (therefore, finite) set of discrete values.

To close this section, it is recalled that the fast Fourier transform (FFT) provides an efficient algorithm for the numerical computation of discrete Fourier transforms [CT65].

4.2.2 Overview of the "basic scheme"

It has already been mentioned that the first UGPLS solver was introduced by Moulinec and Suquet, who proposed in references [MS94]; [MS98] what is now known as the "basic scheme". The starting point is the strong form of the Lippmann–Schwinger equation (4.1), where the stress-polarization $\boldsymbol{\tau}$ is replaced with the strain $\boldsymbol{\varepsilon} = (\mathbf{C} - \mathbf{C}_0)^{-1} : \boldsymbol{\tau}$

$$\boldsymbol{\varepsilon} = \overline{\boldsymbol{\varepsilon}} - \boldsymbol{\Gamma}_0[(\mathbf{C} - \mathbf{C}_0) : \boldsymbol{\varepsilon}]. \tag{4.19}$$

Moulinec and Suquet suggest to solve this equation iteratively, using simple fixed-point iterations

$$\boldsymbol{\varepsilon}^{t+1} = \overline{\boldsymbol{\varepsilon}} - \boldsymbol{\Gamma}_0[(\mathbf{C} - \mathbf{C}_0) : \boldsymbol{\varepsilon}^t] = \boldsymbol{\varepsilon}^t - \boldsymbol{\Gamma}_0[\mathbf{C} : \boldsymbol{\varepsilon}^t], \tag{4.20}$$

with $\boldsymbol{\varepsilon}^0 = \overline{\boldsymbol{\varepsilon}}$. In equation (4.20), the last equality results from property $(2.26)_2$ of the fourth-rank Green operator. Convergence of iterations (4.20) is addressed in reference [MMS01]. The t-th iterate of the basic scheme may be written

$$\boldsymbol{\varepsilon}^t = \left(\mathbf{I} - \mathbf{H} + \mathbf{H}^2 + \cdots + (-1)^t \mathbf{H}^t\right)[\overline{\boldsymbol{\varepsilon}}], \tag{4.21}$$

where $\mathbf{H}$ denotes the operator $\boldsymbol{\varepsilon} \mapsto \boldsymbol{\Gamma}_0[(\mathbf{C} - \mathbf{C}_0) : \boldsymbol{\varepsilon}]$. Convergence is therefore ensured if the norm of $\mathbf{H}$ is strictly lower than 1. For isotropic elasticity, Michel, Moulinec, and Suquet [MMS01] derive the following sufficient convergence condition

$$2\kappa_0 > \kappa(\mathbf{x}) \quad \text{and} \quad 2\mu_0 > \mu(\mathbf{x}) \quad (\mathbf{x} \in \Omega), \tag{4.22}$$

where κ_0 and μ_0 (resp. κ, μ) denote the bulk and shear moduli of the reference material (resp. local bulk and shear moduli of the composite). Furthermore, the optimum values of κ_0 and μ_0 are found to be

$$2\kappa_0 = \min_{\mathbf{x}\in\Omega} \kappa(\mathbf{x}) + \max_{\mathbf{x}\in\Omega} \kappa(\mathbf{x}) \quad \text{and} \quad 2\mu_0 = \min_{\mathbf{x}\in\Omega} \mu(\mathbf{x}) + \max_{\mathbf{x}\in\Omega} \mu(\mathbf{x}). \tag{4.23}$$

Implementation of iterations (4.20) requires the steps listed in algorithm 4.1 below.

Algorithm 4.1 (The basic scheme of Moulinec and Suquet [MS94]; [MS98])**.** *The t-th iterate $\boldsymbol{\varepsilon}^t$ is given.*

1. *Compute the local stress* $\boldsymbol{\sigma}^t = \mathbf{C} : \boldsymbol{\varepsilon}^t$
2. *Compute the Fourier coefficients* $\tilde{\boldsymbol{\sigma}}^t_{\mathbf{k}}$ *for all* $\mathbf{k} \in \mathbb{Z}^d$*, using equation* (4.14)
3. *Sum the Fourier series* (2.21) *to compute* $\delta\boldsymbol{\varepsilon}^t = -\boldsymbol{\Gamma}_0[\boldsymbol{\sigma}^t]$
4. *Update the local strain* $\boldsymbol{\varepsilon}^{t+1} = \boldsymbol{\varepsilon}^t + \delta\boldsymbol{\varepsilon}^t$

It is clear that the above algorithm is conceptual, since it would require the computation of an infinite set of Fourier coefficients, as well as the summation of an (infinite) Fourier series. For practical implementation, some discretization is required. This is arguably the step that is missing justification in the seminal papers [MS94]; [MS98] of Moulinec and Suquet. It is outlined in the remainder of this section.

Introducing the cartesian grid $\mathcal{G}^h$ (see section 4.2.1), it will be assumed that the strain field $\boldsymbol{\varepsilon}^t$ can be approximated in some sense by the cell values $\boldsymbol{\varepsilon}^{h,t}_{\mathbf{n}}$, where the cell index $\mathbf{n}$ belongs to $\{0,\dots,N_1-1\}\times\cdots\{0,\dots,N_d-1\}$. Assuming that the local stiffness $\mathbf{C}$ is also discretized as $\mathbf{C}^h_{\mathbf{n}}$ over the grid $\mathcal{G}^h$, the cell values of the stress $\boldsymbol{\sigma}^t$ read $\boldsymbol{\sigma}^{h,t}_{\mathbf{n}} = \mathbf{C}^h_{\mathbf{n}} : \boldsymbol{\varepsilon}^{h,t}_{\mathbf{n}}$.

It remains to explain how the strain increment $\delta\boldsymbol{\varepsilon}^t = \boldsymbol{\varepsilon}^{t+1} - \boldsymbol{\varepsilon}^t = -\boldsymbol{\Gamma}_0[\boldsymbol{\sigma}^t]$ is to be approximated. Assuming that $N_1 = 2M_1+1,\dots,N_d = 2M_d+1$ are all odd numbers, the cell-values $\delta\boldsymbol{\varepsilon}^{h,t}_{\mathbf{n}}$ of $\delta\boldsymbol{\varepsilon}^{h,t}$ are defined as the inverse discrete Fourier transform of the following quantity

$$\delta\hat{\boldsymbol{\varepsilon}}^{h,t}_{\mathbf{k}} = -\tilde{\boldsymbol{\Gamma}}_0(\mathbf{k}') : \hat{\boldsymbol{\sigma}}^{h,t}_{\mathbf{k}} \quad \text{where} \quad k'_i = \begin{cases} k_i & \text{for } k_i = 0,\dots,M_i \\ k_i - N_i & \text{for } k_i = M_i+1,\dots,N_i-1 \end{cases} \quad (i=1,\dots,d). \tag{4.24}$$

It is recalled that in equation (4.24), $\tilde{\boldsymbol{\Gamma}}_0$ denotes the Fourier transform of the continuous fourth-rank Green operator [see equation (A.1)]. Summing up the approximations introduced above, the discrete version of the basic scheme is listed in algorithm 4.2 below.

Algorithm 4.2 (Discrete version of the basic scheme of Moulinec and Suquet [MS94]; [MS98])**.** *The t-th iterate $\boldsymbol{\varepsilon}^{h,t}_{\mathbf{n}}$ is given.*

1. *Compute the cell-values of the stress $\boldsymbol{\sigma}^{h,t}_{\mathbf{n}} = \mathbf{C}^h_{\mathbf{n}} : \boldsymbol{\varepsilon}^{h,t}_{\mathbf{n}}$*
2. *Compute the discrete Fourier transform $\hat{\boldsymbol{\sigma}}^{h,t}_{\mathbf{k}}$ of the $\boldsymbol{\sigma}^{h,t}_{\mathbf{n}}$*
3. *Compute $\delta\hat{\boldsymbol{\varepsilon}}^{h,t}_{\mathbf{k}}$ from equation (4.24)*
4. *Compute the inverse discrete Fourier transform $\delta\boldsymbol{\varepsilon}^{h,t}_{\mathbf{n}}$ of the $\delta\hat{\boldsymbol{\varepsilon}}^{h,t}_{\mathbf{k}}$*
5. *Compute $\boldsymbol{\varepsilon}^{h,t+1}_{\mathbf{n}} = \boldsymbol{\varepsilon}^{h,t}_{\mathbf{n}} + \delta\boldsymbol{\varepsilon}^{h,t}_{\mathbf{n}}$*

Remark 4.1. *It should be emphasized that equation (4.24) mixes discrete and continuous (periodic) Fourier transforms. Also, since $N_1,\dots,N_d$ are all odd numbers, it is readily shown that the inverse Fourier transform of $\delta\hat{\boldsymbol{\varepsilon}}^{h,t}_{\mathbf{k}}$ defined by equation (4.24) is indeed real. The case where one at least of the N_i is even is more complex. It is addressed somewhat heuristically in reference [MS98] (end of section 2.4). Recently, Vondřejc [Von16] proposed a rigorous analysis of this case.*

Implementation of the above algorithm is very simple and would only require a FFT library as external dependency. This makes the basic scheme a very attractive (and indeed, successful) scheme for the numerical homogenization of heterogeneous materials. It nevertheless has two major shortcomings: *i.* convergence of the fixed-point iterations may be very slow for high elastic contrasts and *ii.* the resulting approximate fields may exhibit strong Gibbs oscillations. Point *i.* was explored as early as 2001 by Michel, Moulinec, and Suquet [MMS01], who proposed an alternative iterative based on augmented Lagrangians (see also the so-called "accelerated scheme" of Eyre and Milton [EM99]). Point *ii.* was discussed much more recently, first by Willot and Pellegrini [WP08], then Brisard and Dormieux [BD10] and Brisard and Dormieux [BD12]. Other contributions to this point include references [Bri17a]; [SMK17];

[WAP14]; [Wil15]; [Yvo12], among which the work by Willot [Wil15] is worth being singled out.

To close this section, it should be observed that the derivation of the basic scheme is somewhat unusual. Indeed, Moulinec and Suquet first selected the iterative linear solver (namely, fixed-point iterations), then discretized the resulting (linear) iterations. This approach is very restrictive, as the linear solver that is selected must be able to handle both continuous and discrete problems (which is extremely restrictive, and, in the end, not necessary). In the general approach outlined in section 4.1.2, the reverse approach is adopted: the continuous problem is first discretized. Only then is the most appropriate linear solver chosen. This is presented in section 4.2.3 below, which gives an overview of the principles introduced by Brisard and Dormieux in references [BD10] and [BD12].

4.2.3 Consistent discretization of the periodic Lippmann–Schwinger equation

In this section, the general framework introduced in section 4.1.2 is applied to the periodic Lippmann–Schwinger equation, discretized over a cartesian grid $\mathcal{G}^h$ of size $N_1 \times \cdots \times N_d$. We first need to define the approximation space $\mathcal{T}_2^h(\Omega)$, where $\Omega = (0, L_1) \times \cdots \times (0, L_d)$ denotes the periodic unit-cell. Since the only requirement is for the trial stress-polarization to be square-integrable, it is natural to consider cell-wise constant approximations. Then, $\boldsymbol{\tau}_{\mathbf{n}}^h$ denotes the constant value of $\tau^h \in \mathcal{T}_2^h(\Omega)$ over cell $\mathbf{n}$ of the grid $\mathcal{G}^h$

$$\boldsymbol{\tau}^h(\mathbf{x}) = \sum_{n_1=0}^{N_1-1} \cdots \sum_{n_d=0}^{N_d-1} \chi^h(\mathbf{x} - \mathbf{x}_{\mathbf{n}}^h)\, \boldsymbol{\tau}_{\mathbf{n}}^h, \tag{4.25}$$

where χ^h denotes the indicator function of the cell centered at the origin [$\chi^h(\mathbf{x}) \in \{0, 1\}$, $\chi^h(\mathbf{x}) = 1 \iff 2|x_i| \leq h$ for all $i = 1, \dots, d$], and $\mathbf{x}_{\mathbf{n}}^h$ denotes the center of cell $\mathbf{n}$

$$\mathbf{x}_{\mathbf{n}}^h = h\big[(n_1 + \tfrac{1}{2})\,\mathbf{e}_1 + \cdots + (n_d + \tfrac{1}{2})\,\mathbf{e}_d\big]. \tag{4.26}$$

In reference [BD10], I introduced a consistent discretization of the periodic Lippmann–Schwinger equation (4.1) over the discretization space $\mathcal{T}_2^h(\Omega)$ thus defined. This requires *exact* evaluation of the bilinear form a defined by equation (4.3) over $\mathcal{T}_2^h(\Omega) \times \mathcal{T}_2^h(\Omega)$. It is readily found that the first term of a, which is local in space, evaluates to

$$\langle \boldsymbol{\varpi}^h : (\mathbf{C} - \mathbf{C}_0)^{-1} : \boldsymbol{\tau}^h \rangle = \frac{1}{N_1 \cdots N_d} \sum_{n_1=0}^{N_1-1} \cdots \sum_{n_d=0}^{N_d-1} \boldsymbol{\varpi}_{\mathbf{n}}^h : (\mathbf{C}_{\mathbf{n}}^h - \mathbf{C}_0)^{-1} : \boldsymbol{\tau}_{\mathbf{n}}^h, \tag{4.27}$$

where the equivalent stiffness $\mathbf{C}_{\mathbf{n}}^h$ of cell $\mathbf{n}$ is defined so as to ensure that $(\mathbf{C}_{\mathbf{n}}^h - \mathbf{C}_0)^{-1}$ is the volume average of $(\mathbf{C} - \mathbf{C}_0)^{-1}$ over cell $\mathbf{n}$

$$\big(\mathbf{C}_{\mathbf{n}}^h - \mathbf{C}_0\big)^{-1} = \frac{1}{h^d} \int_{\mathbf{x} \in \Omega} \chi^h(\mathbf{x} - \mathbf{x}_{\mathbf{n}}^h) \big[\mathbf{C}(\mathbf{x}) - \mathbf{C}_0\big]^{-1} \mathrm{d}V_{\mathbf{x}}. \tag{4.28}$$

Although simple, equation (4.28) is an important result, as it provides a consistent rule to define the equivalent stiffness of heterogeneous grid cells. Alternatives to this strategy are: the majority rule, Reuss/Voigt estimates or the laminate mixing rule recently introduced by Kabel, Merkert, and Schneider [KMS15] where extensive comparisons between these strategies are provided. It should be mentioned that these authors deliberately excluded equation (4.28) from this comparison. The reason for this is the observation that

> "the Brisard–Dormieux mixing rule is necessary to ensure that the computed effective properties constitute a bound on the effective stiffness, and thus tend to increase the error."

I believe this is a fair argument, the implications of which I would like to explore further. Still, at the time of publication, equation (4.28) was an original take on the issue of heterogeneous cells within the framework of UGPLS solvers.

Evaluation of the non-local term of $a(\boldsymbol{\tau}^h, \boldsymbol{\varpi}^h)$ in equation (4.3) is more complex. The following identity holds [BD10]

$$\langle \boldsymbol{\varpi}^h \,:\, \boldsymbol{\Gamma}_0[\boldsymbol{\tau}^h] \rangle = \frac{1}{N_1^2 \cdots N_d^2} \sum_{k_1=0}^{N_1-1} \cdots \sum_{k_d=0}^{N_d-1} \operatorname{conj}(\hat{\boldsymbol{\varpi}}^h_{\mathbf{k}}) \,:\, \hat{\boldsymbol{\Gamma}}^{h,\mathrm{c}}_{0,\mathbf{k}} \,:\, \hat{\boldsymbol{\tau}}^h_{\mathbf{k}}, \tag{4.29}$$

where conj denotes the complex conjugate, and the so-called *consistent, discrete Green operator* reads

$$\hat{\boldsymbol{\Gamma}}^{h,\mathrm{c}}_{0,\mathbf{k}} = \frac{1}{\pi^{2d}} \sum_{p_1 \in \mathbb{Z}} \cdots \sum_{p_d \in \mathbb{Z}} \left[\frac{\sin \pi z_1 \cdots \sin \pi z_d}{(z_1 + p_1) \cdots (z_d + p_d)} \right]^2 \tilde{\boldsymbol{\Gamma}}_0((z_1 + p_1)\,\mathbf{e}_1 + \cdots + (z_d + p_d)\,\mathbf{e}_d), \tag{4.30}$$

with $z_1 = k_1/N_1$, …, $z_d = k_d/N_d$. One should not be deterred by the seemingly complex above expressions, as they have very profound implications.

First, equation (4.29) shows that the non-local term $\langle \boldsymbol{\varpi}^h \,:\, \boldsymbol{\Gamma}_0[\boldsymbol{\tau}^h] \rangle$ can be evaluated from the discrete Fourier transform of the cell values of $\boldsymbol{\tau}^h$ and $\boldsymbol{\varpi}^h$. It is emphasized that this equality is *exact* and the sum is *finite*, as opposed to the general expression (2.21) of the periodic Green operator, where the sum is infinite.

Second, it is observed that equation (4.30) mixes periodic Fourier transforms (tilde notation, $\tilde{\bullet}$) and discrete Fourier transforms (hat notation, $\hat{\bullet}$). This is neither a mistake, nor an approximation. It comes from the fact that the Fourier coefficients of a periodic, cell-wise function can be related to the discrete Fourier transform of its cell values [BD12, equation (50)]. Now, introducing $\hat{\boldsymbol{\eta}}^h_{\mathbf{k}} = \hat{\boldsymbol{\Gamma}}^h_{0,\mathbf{k}} \,:\, \hat{\boldsymbol{\tau}}^h_{\mathbf{k}}$ and its inverse discrete Fourier transform $\boldsymbol{\eta}^h_{\mathbf{n}}$

$$\boldsymbol{\eta}^h_{\mathbf{n}} = \frac{1}{N_1 \cdots N_d} \sum_{k_1=0}^{N_1-1} \cdots \sum_{k_d=0}^{N_d-1} \exp\left[2\mathrm{i}\pi(k_1 n_1/N_1 + \cdots + k_d n_d/N_d)\right] \hat{\boldsymbol{\Gamma}}^h_{0,\mathbf{k}} \,:\, \hat{\boldsymbol{\tau}}^h_{\mathbf{k}}, \tag{4.31}$$

then applying Plancherel's theorem to equation (4.29) leads to the alternative expression

$$\langle \boldsymbol{\varpi}^h \,:\, \boldsymbol{\Gamma}_0[\boldsymbol{\tau}^h] \rangle = \frac{1}{N_1 \cdots N_d} \sum_{n_1=0}^{N_1-1} \cdots \sum_{n_d=0}^{N_d-1} \boldsymbol{\varpi}^h_{\mathbf{n}} \,:\, \boldsymbol{\eta}^h_{\mathbf{n}}. \tag{4.32}$$

Finally, gathering equations (4.27) and (4.32), the discrete variational problem (4.4) is reduced to the following linear system

$$(\mathbf{C}^h_{\mathbf{n}} - \mathbf{C}_0)^{-1} \,:\, \boldsymbol{\tau}^h_{\mathbf{n}} + \boldsymbol{\eta}^h_{\mathbf{n}} = \overline{\boldsymbol{\varepsilon}}, \tag{4.33}$$

where the unknowns are the cell values $\boldsymbol{\tau}^h_{\mathbf{n}}$. Owing to the symmetry of the bilinear form a, the above linear system is symmetric. In reference [BD10], we further selected the stiffness $\mathbf{C}_0$ of the reference material so as to be strictly stiffer or softer than all phases in the composite. As already argued in section 4.1.3, this ensures that the resulting numerical estimate of the apparent stiffness is in fact a bound. More importantly, the linear operator of the system is then positive (or negative) definite, which allows for the use of the conjugate gradient solver instead of the fixed-point iterations initially proposed by Moulinec and Suquet [MS94]; [MS98].

This resulted in a dramatic performance improvement over the basic scheme in terms of number of iterations, even for very high elastic contrasts (see figure 4.1). At this point, it is worth recalling that (as already argued in section 4.1.2) implementation of the above scheme follows a matrix-free pattern, where the conjugate gradient solver is provided with a `function` (in the programming sense) that maps $\boldsymbol{\tau}^h_{\mathbf{n}}$ to $(\mathbf{C}^h_{\mathbf{n}} - \mathbf{C}_0)^{-1} \,:\, \boldsymbol{\tau}^h_{\mathbf{n}} + \boldsymbol{\eta}^h_{\mathbf{n}}$ according to the following steps (see algorithm 4.3).

Algorithm 4.3 (Application of the discrete Green operator)**.** *The cell values $\boldsymbol{\tau}^h_{\mathbf{n}}$ of the trial stress-polarization are given.*

1. *Compute the discrete Fourier transform $\hat{\boldsymbol{\tau}}^h_{\mathbf{k}}$ of $\boldsymbol{\tau}^h_{\mathbf{n}}$.*
2. *Compute $\hat{\boldsymbol{\eta}}^h_{\mathbf{k}} = \hat{\boldsymbol{\Gamma}}^h_{0,\mathbf{k}} \,:\, \hat{\boldsymbol{\tau}}^h_{\mathbf{k}}$.*
3. *Compute the inverse discrete Fourier transform $\boldsymbol{\eta}^h_{\mathbf{n}}$ of $\hat{\boldsymbol{\eta}}^h_{\mathbf{k}}$.*
4. *Return $(\mathbf{C}^h_{\mathbf{n}} - \mathbf{C}_0)^{-1} \,:\, \boldsymbol{\tau}^h_{\mathbf{n}} + \boldsymbol{\eta}^h_{\mathbf{n}}$.*

Comparing with the basic scheme (see algorithm 4.1), it is seen that the number of discrete Fourier transforms required to compute one matrix-vector product is identical to that of one iteration of the basic scheme. Therefore, it is fair to compare the performance of the basic scheme and the present consistent scheme in terms of number of iterations, since one iteration of the conjugate gradient method requires one matrix-vector product.

When reference [BD10] was published, I attributed the observed acceleration to the replacement of the linear solver solely. I have now come to understand that the high-frequency content of the consistent discrete Green operator also plays a significant role. This was discussed in section 4.4 of reference [BD12]. However, evaluation of the consistent discrete Green operator is costly. Indeed, the series defined by equation (4.30) is only slowly converging. An interesting summation strategy that further allows to bound the truncation error from above was proposed in appendix C of reference [BD10]. Unfortunately, this acceleration technique is not sufficient in 3D, where evaluation of equation (4.30) becomes unpractical. In such cases, non-consistent discretizations are advisable.

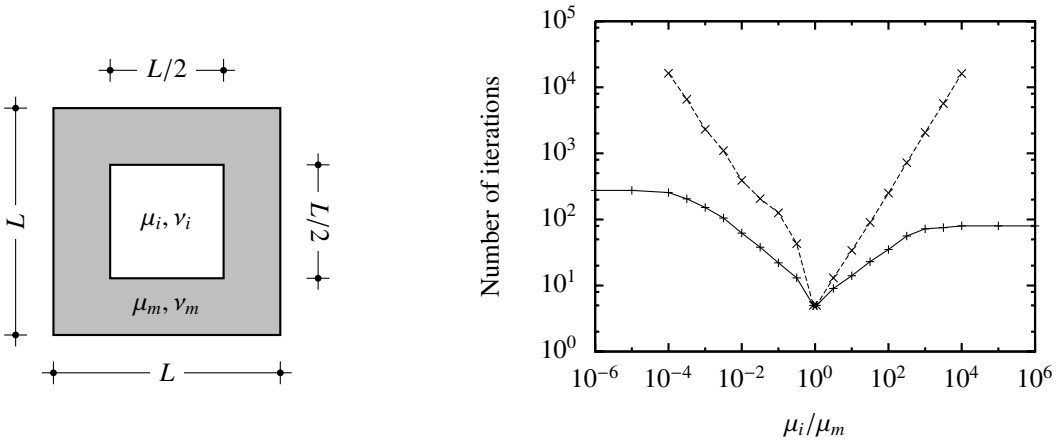

Figure 4.1: Comparison of the basic scheme of Moulinec and Suquet [MS94]; [MS98] and the consistent discretization of Brisard and Dormieux [BD10], combined with a conjugate gradient solver. Within a plane strain elasticity setting, a square inclusion of side $L/2$ is embedded in a square unit-cell of side $L/2$. The elastic properties of the matrix are $\mu_\mathrm{m} = 1$ and $\nu_\mathrm{m} = 0.3$, while the Poisson ratio of the inhomogeneity is $\nu_\mathrm{i} = 0.2$ (the shear modulus μ_i varies). All simulations were performed on a 128×128 grid. Similar stopping criteria were adopted for both numerical schemes. The plot on the right shows that the combination of a CG solver with the consistent discretization always converges in a bounded number of iterations, while the basic scheme requires an increasing number of iterations when the elastic contrast increases. (Reproduced from reference [BD10])

4.2.4 Asymptotically consistent discretization of the periodic Lippmann–Schwinger equation

Non-consistent discretizations of the periodic Lippmann–Schwinger equation in fact date back to the very first paper by Moulinec and Suquet [MS94]. Indeed, in the basic scheme they introduced, the bilinear form $a(\boldsymbol{\tau}^h, \boldsymbol{\varpi}^h)$ is not computed exactly, as will be discussed below. However, this numerical scheme was not recognized as *asymptotically consistent* (in the sense of Ern and Guermond [EG04]) before our paper [BD12].

The initial motivation for reference [BD12] came from one question raised during my PhD defense. Indeed, in reference [BD10], the reference material was required to be stiffer or softer than all phases (in order to comply with the Hashin–Shtrikman principle). One referee naturally asked what would happen if the reference material did *not* comply with this requirement?

Of course, the numerical scheme then no longer delivers a rigorous bound on the apparent stiffness. Is it legitimate to treat the result as an estimate? In other words, does refining the grid spacing h result in an improved estimate of the apparent stiffness?

When the Hashin–Shtrikman principle applies, the question is somewhat trivial. Indeed, the Hashin–Shtrikman functional is then optimized over a subspace that gets larger[1]: the bound *must* improve (note that this does not insure convergence to the exact value). For an arbitrary reference material, the Hashin–Shtrikman functional exhibits a saddle-point, and the above no longer applies. Indeed, even uniqueness of the saddle-point was not asserted. I therefore set out to study the convergence of UGPLS schemes.

[1] Strictly speaking, this is true only for *refinements* (by subdivision) of the initial grid, since it must be ensured that the various optimization subspaces form a hierarchy of subsets.

At this point, it must be emphasized that prior to reference [BD12], "convergence" generally referred to the iterative solver (at fixed grid-spacing h), rather than the discretization: much effort has thus been devoted to the derivation of efficient iterative solvers that reach convergence in as few iterations as possible. In section 4.2.3, it was shown that discretizing the periodic Lippmann–Schwinger equation and solving the resulting linear system are two problems that can be largely addressed separately. In this section, we therefore disregard the iterative linear solver and focus on the following question: "does $\|\boldsymbol{\tau}^h - \boldsymbol{\tau}\| \to 0$ as $h \to 0$?", in which the functional norm is as yet unspecified. This question had not been investigated at the time of publication of reference [BD12]; it required a proper mathematical setting, and I soon found out that the framework initially set up for the analysis of finite element schemes [EG04] was perfectly suited to the task.

Selecting the appropriate functional space for the periodic Lippmann–Schwinger equation (4.1) (which turned out to be the space $\mathcal{T}_2(\Omega)$ of second-rank, symmetric tensors with Ω-periodic, square integrable components), I was first able to prove that (under minor restrictions), the solution was indeed unique, regardless of the choice of the reference material. Furthermore, I was able to prove the convergence of the numerical scheme introduced in reference [BD10]. I called this scheme *consistent*, since within this framework, the bilinear form $a(\boldsymbol{\tau}^h, \boldsymbol{\varpi}^h)$ was computed exactly over the discretization space $\mathcal{T}_2^h(\Omega)$ of cell-wise constant trial stress-polarizations.

It was then natural to consider the same convergence question for the basic scheme of Moulinec and Suquet [MS94] and Moulinec and Suquet [MS98]. It should be recalled that this scheme was initially obtained through collocation, rather than Galerkin discretization: how to reconstruct a tensor field $\boldsymbol{\varepsilon}^h(\mathbf{x})$ from the cell estimates $\boldsymbol{\varepsilon}^h_{\mathbf{n}}$ was not really discussed.

I therefore *chose*[2] a reconstruction as a cell-wise constant field. Referring to algorithm 4.1, this meant that the first term of $a(\boldsymbol{\tau}^h, \boldsymbol{\varpi}^h)$ [involving the local constitutive law, see equation (4.3)] was computed exactly, while the second term [involving the non-local Green operator, see equation (4.3)] was approximated. This scheme could thus be regarded as a non-consistent discretization of the periodic Lippmann–Schwinger equation of type (4.7). I was again able to prove that the basic scheme was *asymptotically consistent*, which warranted a positive answer to the convergence question for the basic scheme.

This analysis further allowed me to set up a unique framework into which most UGPLS scheme could be cast. Indeed, I realized that most of these schemes can be seen as non-consistent discretizations of the periodic Lippmann–Schwinger solver, where the bilinear form $a(\boldsymbol{\tau}^h, \boldsymbol{\varpi}^h)$ is approximated as follows [compare with equations (4.27) and (4.29) in the consistent case]

$$\begin{aligned} a(\boldsymbol{\tau}^h, \boldsymbol{\varpi}^h) \approx a^h(\boldsymbol{\tau}^h, \boldsymbol{\varpi}^h) = \frac{1}{N_1 \cdots N_d} \sum_{n_1=0}^{N_1-1} \cdots \sum_{n_d=0}^{N_d-1} \boldsymbol{\varpi}^h_{\mathbf{n}} : (\mathbf{C}^h_{\mathbf{n}} - \mathbf{C}_0)^{-1} : \boldsymbol{\tau}^h_{\mathbf{n}} \\ + \frac{1}{N_1^2 \cdots N_d^2} \sum_{k_1=0}^{N_1-1} \cdots \sum_{k_d=0}^{N_d-1} \operatorname{conj}(\hat{\boldsymbol{\varpi}}^h_{\mathbf{k}}) : \hat{\boldsymbol{\Gamma}}^h_{0,\mathbf{k}} : \hat{\boldsymbol{\tau}}^h_{\mathbf{k}}, \end{aligned} \tag{4.34}$$

[2] An alternative choice is considered in section 4.2.6.

where $\mathbf{C}^h_{\mathbf{n}}$ denotes an equivalent stiffness of cell $\mathbf{n}$ [computed for example through the consistency rule (4.28)], while $\hat{\mathbf{\Gamma}}^h_{0,\mathbf{k}}$ is a so-called *discrete Green operator*.

Many UGPLS schemes can be cast in this form, as was shown for example in reference [BD12] for the basic scheme of Moulinec and Suquet [MS94]; [MS98] (*truncated* discrete Green operator) and our variational scheme introduced in reference [BD10] (*consistent* discrete Green operator). I showed more recently [Bri17a] that the approach of Willot and collaborators [WAP14]; [Wil15] was also amenable to the above abstraction (*finite-difference* discrete Green operator).

This unified presentation has two beneficial side effects. First, it means that the same mathematical framework can be employed to prove the convergence of this variety of numerical schemes: it suffices to prove that the discrete Green operator under consideration is asymptotically consistent (in the sense of Ern and Guermond [EG04]).

Second, it means that a unified numerical code can be designed, that offers a uniform interface for all these variants. In this spirit, I wrote `Janus`[3]. Freely available under a BSD-3 license, this library offers a fairly general framework in which a UGPLS scheme is seen as the combination of

1. a discretization of the continuous Green operator: through e.g truncation, filtering of high-frequencies, finite differences, …
2. an iterative linear solver, which might be fixed-point iterations [MS94]; [MS98], iterations based on an augmented Lagrangian approach [MMS01], conjugate gradient iterations [BD10]; [Zem+10] or even more general Krylov-based iterative linear solvers such as SYMMLQ [BD12].

The code is implemented in such a way that it is independent on the dimensionality as well as the exact nature of the problem: thermal conduction and linear elasticity are of course readily available, but extensions to permeability analysis [BD14] or heterogeneous plates [NSB09] are even possible with very little effort. In all cases, the code only requires the implementation of the *continuous* discrete Green operator, while taking care automatically of its discretization. It is parallelized, thus allowing the analysis of fairly large microstructures. Figure 4.2 shows a simple application of this code.

4.2.5 Asserting the quality of the solution

Asserting the quality of a numerical solution to a boundary value problem is almost as important as, if not more important than, computing the numerical solution itself. This has become common practice among the finite element community, which has developed a rather wide range of general purpose tools to bound the error on the solution.

Within the framework of UGPLS methods, such matters have not yet drawn much attention, although it is widely accepted that the quality of the numerical solution can be significantly affected by the choice of the discrete Green operator (the grid-size h being fixed) [BD12]; [SOK15]; [WAP14]; [Wil15]; [WP08]. In the case of the filtered, discrete Green operator, the solution even depends on the stiffness $\mathbf{C}_0$ of the reference material, which can be selected so as to minimize the discretization error. Clearly, there is a need to be able to quantify this error.

[3] `https://github.com/sbrisard/janus`, last retrieved 2017-03-08

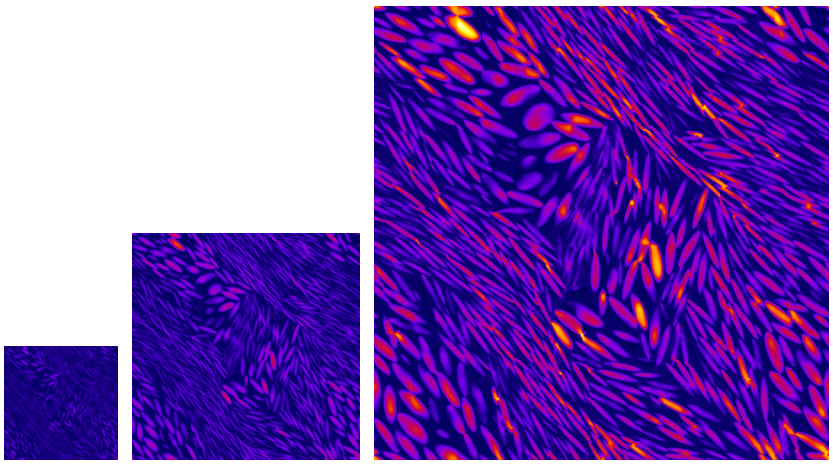

Figure 4.2: A simle application of the `Janus` library. The above figure shows a map of the stress-polarization τ_{xy} for the microstructure displayed in figure 1.3, subjected to a unit macroscopic shear strain $E_{xy} = 1$. Three simulations are presented, for increasing grid sizes: 256^3, 512^3 and 1024^3. For the latter, the total number of unknowns is about 10^9.

My intent when I set out to produce error estimators for UGPLS methods was to rely as much as possible on tools already available for finite element analysis. In particular, the elegance and versatility of estimators derived from the *constitutive relation error* [LL83]; [LP05] drew my attention very early on. The work described in this section is still in progress; it is carried out in collaboration with L. Chamoin[4].

In its most basic form, the constitutive relation error relies on the Prager–Synge theorem, which states that for any well-posed problem of linear, elastic equilibrium

$$U^*(\hat{\boldsymbol{\sigma}} - \boldsymbol{\sigma}) + U(\check{\boldsymbol{\varepsilon}} - \boldsymbol{\varepsilon}) = U^*(\hat{\boldsymbol{\sigma}} - \mathbf{C} : \check{\boldsymbol{\varepsilon}}), \tag{4.35}$$

where $\boldsymbol{\sigma}$ and $\boldsymbol{\varepsilon}$ denote the stress and strain at equilibrium ($\boldsymbol{\sigma} = \mathbf{C} : \boldsymbol{\varepsilon}$), while $\hat{\boldsymbol{\sigma}}$ and $\check{\boldsymbol{\varepsilon}}$ denote an arbitrary statically admissible stress field and an arbitrary kinematically admissible strain field ($\hat{\boldsymbol{\sigma}} \neq \mathbf{C} : \check{\boldsymbol{\varepsilon}}$). Finally, U is the strain energy and U^* is the complementary stress energy. Identity (4.35) is extremely useful to bound modelling or discretization errors. Indeed, it results from this identity that

$$U^*(\hat{\boldsymbol{\sigma}} - \boldsymbol{\sigma}) \leq U^*(\hat{\boldsymbol{\sigma}} - \mathbf{C} : \check{\boldsymbol{\varepsilon}}) \quad \text{and} \quad U(\check{\boldsymbol{\varepsilon}} - \boldsymbol{\varepsilon}) \leq U^*(\hat{\boldsymbol{\sigma}} - \mathbf{C} : \check{\boldsymbol{\varepsilon}}). \tag{4.36}$$

In the above inequalities, the left-hand side measures the distance (in energy norm) between the exact (unknown) stress ($\boldsymbol{\sigma}$) and strain ($\boldsymbol{\varepsilon}$) fields and what can be regarded as approximate stress ($\hat{\boldsymbol{\sigma}}$) and strain ($\check{\boldsymbol{\varepsilon}}$) fields. The right-hand side provides a rigorous, computable bound on this error. The only requirement for $\hat{\boldsymbol{\sigma}}$ and $\check{\boldsymbol{\varepsilon}}$ is to be admissible (in the static and kinematic sense, respectively). The right-hand side of both inequalities is called error in constitutive relation, since it measures the degree of violation of the local constitutive law by the (non-associated) stress and strain fields $\hat{\boldsymbol{\sigma}}$ and $\check{\boldsymbol{\varepsilon}}$.

In a displacement-based finite element setting, application of the above results proceeds as follows. A kinematically admissible strain field $\boldsymbol{\varepsilon}^h = \boldsymbol{\epsilon}[\mathbf{u}^h]$ is readily derived from the

[4]LMT Cachan (ENS Cachan/CNRS/Paris 6 University), Cachan Cedex, France

finite element displacement field $\mathbf{u}^h$. Reconstructing a statically admissible stress field $\hat{\boldsymbol{\sigma}}^h$ is a more involved task, which can however be carried out in a fairly systematic way [LP05]. In particular, it should be noted that this reconstruction is rather inexpensive, as it involves a series of local linear problems (formulated on patches of elements, rather than the whole finite element model). Then, the constitutive relation error is computed, thus delivering a bound on the discretization error.

Application of the above framework to UGPL solvers is more involved, since these solvers generally do not produce kinematically admissible displacement fields (the principal unknown being the stress-polarization, or equivalently the strain). Quoting from the introduction of reference [Bri17a], we "first observe that many authors have already proposed strategies to reconstruct kinematically admissible displacement fields. To name but a few: Moulinec and Suquet [MS98] produce strain fields which are by construction compatible; Willot and Pellegrini [WP08] and Monchiet and Bonnet [MB12] use projections onto the space of compatible strain fields; Zeman, Vondřejc, Novák, and Marek [Zem+10] and Vondřejc et al. (see [VZM14]; [VZM15] and references therein) use the displacement as their primary unknown in a Galerkin setting. Finally, within the framework of large strains, Kabel, Böhlke, and Schneider [KBS14] produce compatible deformation gradients. In most cases, a statically admissible stress field can be recovered with little effort. However, both displacement and stress fields are approximated with trigonometric polynomials; as such, they are susceptible to the Gibbs phenomenon [BD12]; [VZM15]; [Wil15]; [WP08]. By contrast, approximations of the displacement field that are local *in space* are less likely to result in spurious oscillations. This has recently been confirmed by Willot [Wil15] and Schneider, Ospald, and Kabel [SOK15]. Relying on a finite difference discretization of the corrector problem, both derive new UGPLS solvers which deliver a local approximation of the displacement field. Whether or not local approximations are preferable to trigonometric polynomials is really application dependent."

More importantly, the displacement field that we reconstruct lends itself to further reconstruction of a statically admissible stress field based on the so-called *strong extension condition* (see §8.3.1 in reference [LP05]). This means that from the displacement field that we reconstruct, it is fairly straightforward to produce a statically admissible stress field, using the exact same automated tools as for finite element models. None of the techniques quoted above would allow for such a short-cut in the production of a-posteriori error bounds.

Partly quoting again the introduction of reference [Bri17a], we now present the principles of the proposed reconstruction. Before we proceed, two observations should be made. Firstly, the reconstruction applies to *any* UGPLS solver, whether or not based on a Galerkin approach. For solvers that deliver approximations of the strain $\boldsymbol{\varepsilon}^h_{\mathbf{n}}$, estimates of the stress-polarization $\boldsymbol{\tau}^h_{\mathbf{n}}$ can readily be retrieved by means of the identity $\boldsymbol{\tau}^h_{\mathbf{n}} = (\mathbf{C}^h_{\mathbf{n}} - \mathbf{C}_0) : \boldsymbol{\varepsilon}^h_{\mathbf{n}}$. These discrete values will be regarded here as cell-values of a cell-wise constant stress-polarization field $\boldsymbol{\tau}^h$. Secondly, we focus here on approximating the *periodic fluctuations* $\mathbf{u}^h$ of the displacement field. In other words, the approximation of the *total* displacement field that solves problem (2.16) reads: $\overline{\boldsymbol{\varepsilon}} \cdot \mathbf{x} + \mathbf{u}^h(\mathbf{x})$.

If the true solution $\boldsymbol{\tau}$ to equation (4.1) were known exactly, then the (periodic fluctuation of the) displacement $\mathbf{u}^{\text{per}}$ would be the periodic solution to the following equation

$$\mathbf{div}\big(\mathbf{C}_0 : \epsilon[\mathbf{u}] + \boldsymbol{\tau}\big) = \mathbf{0}, \tag{4.37}$$

with $\langle \mathbf{u} \rangle = \mathbf{0}$. We therefore seek the approximate displacement field $\mathbf{u}^h$ as the periodic solution to equation (4.37), where the true stress-polarization $\boldsymbol{\tau}$ is replaced with the approximate, cell-wise constant, $\boldsymbol{\tau}^h$

$$\mathbf{div}\big(\mathbf{C}_0 : \boldsymbol{\epsilon}[\mathbf{u}^h] + \boldsymbol{\tau}^h\big) = \mathbf{0}. \tag{4.38}$$

The displacement is discretized over the same d-dimensional cartesian grid that was used for the UGPLS solver; interpolation is achieved through Q_1 shape functions. Periodicity of the discretized displacement is enforced by construction (using periodic shape functions).

Due to the periodic boundary conditions and the homogeneity of the material, the finite element approximation of equation (4.38) results in a *block-circulant* stiffness matrix. This suggests to formulate this approximation in the Fourier space, where all frequencies are uncoupled. More precisely, while the *nodal* displacements are the solution to a $(Nd) \times (Nd)$ system (where $N = N_1 \times \cdots \times N_d$ is the total number of nodes), the *modal* displacements (that is, the discrete Fourier transform of the nodal displacements) are the solution to N systems of size $d \times d$, which can be solved at virtually no cost. Of course, this approach requires the computation of direct and inverse discrete Fourier transforms: using the fast Fourier transform guarantees the overall efficiency of the proposed method.

Skipping the lengthy technical details, the proposed method reduces to the following steps

Algorithm 4.4 (Reconstruction of the displacement field according to reference [Bri17a])**.** *The cell-values $\boldsymbol{\tau}^h_{\mathbf{n}}$ of the stress-polarization are given.*

1. *Compute the discrete Fourier transform $\hat{\boldsymbol{\tau}}^h_{\mathbf{k}}$ of $\boldsymbol{\tau}^h_{\mathbf{n}}$.*
2. *For each of the $N = N_1 \times \cdots \times N_d$ discrete frequency*
   a) *Compute the modal strain-displacement vector $\hat{\mathbf{B}}^h_{\mathbf{k}}$ from equation (40) in reference [Bri17a].*
   b) *Compute the modal stiffness matrix $\hat{\mathbf{K}}^h_{\mathbf{k}}$ from equations (46) and (47) in reference [Bri17a].*
   c) *Solve the following $d \times d$ linear system to find the modal displacement $\hat{\mathbf{u}}^h_{\mathbf{k}}$*

$$\hat{\mathbf{K}}^h_{\mathbf{k}} \cdot \hat{\mathbf{u}}^h_{\mathbf{k}} = -\hat{\boldsymbol{\tau}}^h_{\mathbf{k}} \cdot \operatorname{conj} \hat{\mathbf{B}}^h_{\mathbf{k}}. \tag{4.39}$$

3. *Compute the inverse discrete Fourier transform of $\hat{\mathbf{u}}^h_{\mathbf{k}}$ to find the nodal values $\mathbf{u}^h_{\mathbf{n}}$ of the displacement.*
4. *If necessary, evaluate the reconstructed displacement field $\mathbf{u}^h$ at any point through standard (Q_1) interpolation between the nodal values $\mathbf{u}^h_{\mathbf{n}}$.*

Algorithm 4.4 should be understood as a post-processing of the output produced by *any* UGPLS solver. It is observed that the cost of this post-processing is less than one iteration of the solver (compare with algorithm 4.3).

This procedure was successfully implemented in reference [Bri17a], where it was first used to produce rigorous upper bounds on the effective elastic stiffness of a periodic microstructure.

It was then compared to various alternative displacement reconstruction techniques (including techniques based on trigonometric polynomials). To do so, the error in energy norm was measured against Hashin's coated spheres reference solution [Has62] as first proposed by Schneider, Ospald, and Kabel [SOK15]. It was observed that the performances of all procedures were comparable[5].

Our procedure offers the additional benefit that it conforms with the strong extension condition of Ladevèze and Pelle [LP05], which means that reconstructing statically admissible stress fields becomes a trivial task. In turn, this paves the way to using the whole constitutive relation error machinery initially developed within the framework of displacement-based finite elements. As mentioned earlier, this extension is currently under investigation with Ludovic Chamoin.

To close this section, it should be noted that the work published in reference [Bri17a] and presented here could be understood as the derivation of a new FE-based discrete Green operator. Indeed, algorithm 4.4 maps a cell-wise constant prestress to a Q_1 displacement, from which a cell-wise constant strain can readily be obtained. However, implementation of this discrete Green operator within an iterative UGPLS solvers remains costly, because of the numerous (small) linear systems that ought to be solved at each iterations. This cost can be reduced by means of reduced integration, as recently proved by Schneider, Merkert, and Kabel [SMK17].

4.2.6 Closing remarks

This section closes the discussion of uniform grid, periodic Lippmann–Schwinger solvers with a few conclusions and perspectives. First of all, I would like to recall that my two main contributions to this field were

1. the introduction of the variational form of the Lippmann–Schwinger equation and its Galerkin discretization.
2. the observation that *any* matrix-free iterative linear solver could be substituted to the fixed-point iterations and augmented Lagrangian iterations initially proposed by Moulinec et Suquet [MS94]; [MS98] and Michel, Moulinec and Suquet [MMS01].

Regarding the first item, the variational formulation offers a common setting for *all* variants of UGPLS solvers. Indeed, most of these differ by the choice of (asymptotically consistent) discrete Green operators for strains: truncated [MS94]; [MS98], consistent or filtered [BD12], based on finite differences [WAP14]; [Wil15] or finite elements [SMK17]; [Yvo12]. As a consequence, proof of convergence can in all instances be established by means of mathematical tools that are standard within the finite element community [EG04], as illustrated in reference [BD12] for the truncated and consistent discrete Green operators.

Galerkin discretizations rely heavily on the selection of the discretization space (see section 4.1.2). In the present case, $\mathcal{T}_2^h(\Omega)$ was defined as the space of cell-wise constant stress-polarizations. Similarly to displacement-based finite elements, this raises the question of higher-

[5] Which probably indicates that the energy norm was not the best suited to compare the various displacement fields

order approximations of the trial stress-polarization by e.g. cell-wise linear or quadratic functions. I decided very early on not to pursue this route, for both theoretical and technical reasons. On the theoretical side of things, such higher-order approximations are not consistent with the relatively low regularity of the true stress-polarization. At the present time, $\boldsymbol{\tau}$ is indeed known to be with square integrable components only[6]. On the technical side of things, the discrete Fourier transform are at the heart of the techniques discussed here. This kind of transforms treat all unknowns on an equal footing, since they are assigned the same (frequency-dependent) weighting. This is at odds with higher-order approximations, where all unknowns do not play equal roles. In a nodal approach (where unknowns are attached to vertices of the grid[7]), corner-nodes and mid-side nodes are unknowns that play different roles. Similarly, in an elemental approach (where unknowns are attached to cells of the grid), the coefficients of the polynomial expansion of the trial-stress again play very different roles. This complicates significantly the implementation, which was therefore not attempted.

Approximations that are local in space seem fairly natural. However, alternate discretizations by means of trigonometric polynomials can also shed a different light on existing schemes (and help develop new ones). Although the discretization of the unknown fields was not fully specified at this time, it is fair to assume that Moulinec and Suquet [MS94]; [MS98] had such approximations in mind when they first proposed the basic scheme. More recently, discretizations based on trigonometric polynomials have been thoroughly explored in a variational setting by Vondřejc and coauthors [Von16]; [VZM14]; [VZM15]. It is interesting to observe that in this case, contrary to our spatial approach, evaluation of the second term of the bilinear form a [see equation (4.3)] becomes trivial, while the first term requires more attention. This led the authors to proposed two schemes: the Fourier-Galerkin method with exact (Ga) or numerical (GaNi) integration [Von16]. Should spatial discretization be preferred over spectral discretization? There is no definite answer to this question, which really depends on the use-case. Both approaches are valuable and should be developed in parallel, even more so because they can both be implemented seamlessly in the *same* numerical code.

Turning now to the second item (iterative linear solvers). It is true that the variational setting adopted here led to a clear separation between discretization and solution of the resulting linear system, while both steps were intertwined in the original papers of Moulinec and Suquet [MS94]; [MS98]. The natural consequence was that it allowed for the use of any matrix-free iterative linear solver. Very early on, it was then observed that conjugate gradient solvers could outperform fixed-point iterations [BD10]; [Zem+10], which do not even converge for infinite contrasts [MMS01]. However, it must be admitted that even Krylov-based iterative linear solvers sometimes perform very poorly. In particular, microstructures that embed very stiff *and* very soft inclusions (pores) simultaneously lead to highly ill-conditioned linear systems. This obviously calls for the use of a preconditioner. My experience is that main-stream, matrix-free preconditioners (this is a requirement!) do not help in these situations: a specific preconditioner must therefore be designed. To the best of my knowledge, this issue has not yet been addressed. I do believe that this constitutes the main challenge that needs to be overcome

[6] Although it is reasonable to expect $\boldsymbol{\tau}$ to be more regular in homogeneous regions.

[7] This would probably not be the best approach, since the low regularity of $\boldsymbol{\tau}$ –which might be discontinuous at the interface between two cells– would then require to duplicate nodes.

by UGPLS solvers. From this perspective, the recent work of Ying [Yin15] (although in a widely different context) might offer a good starting point.

Finally, I should like to add that there are many discussions centered around the "best" UGPLS scheme. This debate is somewhat endless (if not pointless). In practice, one needs a robust scheme that is reasonably fast (if not the fastest). If I had to make a recommendation, I would probably suggest to use the discrete Green operator based on finite differences, recently proposed by Willot [Wil15], combined with conjugate gradient iterations (provided that the matrix of the system is positive definite or negative definite). In my view, the operator of Willot is superior to the filtered discrete Green operator that I proposed in reference [BD12]. Like the filtered operator, it is fairly insensitive to the Gibbs phenomenon. Unlike the filtered operator, it produces a numerical solution that does not depend on the reference material $\mathbf{C}_0$ (which can then be optimized for the total number of iterations). Furthermore, its evaluation is cheaper, which reduces the overall cost of one iteration of the UGPLS scheme.

***

The class of UGPLS solvers introduced in the previous section is virtually exact in the sense that the discretization error vanishes as the grid-spacing tends to zero. We now turn to the equivalent inclusion method (EIM), that is *not* intended to be exact. It is rather hoped to deliver cheap but accurate estimates of the macroscopic properties.

4.3 A variational form of the equivalent inclusion method

In the present section, a Galerkin discretization of the modified Lippmann–Schwinger equation (3.3) introduced in section 3.1.1 of chapter 3 is proposed for "simple" microstructures (assemblies of spherical or spheroidal inclusions). The resulting numerical homogenization method can be seen as the variational form of the equivalent inclusion method of Moschovidis and Mura [MM75] (EIM); our method will therefore be called the EIM-G (for Galerkin).

The EIM-G was first introduced in my PhD thesis [Bri11], where it was then called PIM (polarized inclusion method); at that time, I failed to relate the PIM and the EIM. Besides, the PIM was restricted to trial stress-polarizations that were constant over each inclusion.

I then strived to extend the method to higher-order, polynomial trial stress-polarizations. This eventually led to two papers: in reference [BSD13], I introduced the modified Lippmann–Schwinger equation, which clarified some boundary condition issues that I had encountered during the course of my PhD work. Then, in reference [BDS14], I introduced the general framework for the EIM-G.

While the principles underlying the EIM-G are fairly simple, its implementation can be involved, because of the influence tensors that are required to assemble the matrix of the linear system (see section 4.3.1 below). A significant amount of work was devoted to the analytical evaluation of these tensors for disks (plane elasticity) and spheres (3D elasticity), involving intensive use of a computer algebra system[8]. The results of these symbolic calculations should be useful to anyone who attempts to implement the EIM-G. However, they amount to more than

[8] In the present case, I found `maxima` (`http://maxima.sourceforge.net/`, last retrieved 2017-03-29) extremely well-suited to the task. It is distributed under the GNU General Public License.

50 pages of appendices, which was unacceptable for a publication in the *International Journal of Solids and Structures*. They were therefore deposited on the HAL hosting platform [BDS13] as a Technical Report.

The present section is organized as follows. Section 4.3.1 provides a general description of the method, skipping most of the technical details, which can be found in references [BDS14] and [BDS13]. Two applications are then discussed in section 4.3.2: it is observed that the EIM-G performs extremely well in 2D, less so in 3D. Finally, rather than produce *estimates* of the apparent stiffness of SVEs, this method is used in section 4.3.3 to capture its *fluctuations* , within the framework of variance reduction.

Before we proceed to introduce the EIM-G, it is noted that the present section conforms with Eshelby's terminology. According to Eshelby, who first introduced the equivalent inclusion method in his seminal paper [Esh57], an inclusion denotes a bounded region with same elastic properties as the surrounding matrix, subjected to an eigenstress (or eigenstrain). Conversely, an inhomogeneity denotes a bounded region with elastic properties that differ from the surrounding matrix.

4.3.1 Overview of the method

The EIM-G is devoted to simple microstructures made of assemblies of inhomogeneities with well-defined geometries. The SVE is again denoted Ω; it is populated with N inhomogeneities $\Omega_1, \dots, \Omega_N$ centered at $\mathbf{x}_1, \dots, \mathbf{x}_N$. Furthermore, χ_α denotes the indicator function of inhomogeneity Ω_α, centered at the origin: $\chi_\alpha(\mathbf{x}) \in \{0, 1\}$, $\mathbf{x} \in \Omega_\alpha \iff \chi_\alpha(\mathbf{x} - \mathbf{x}_\alpha) = 1$ ($\chi_\alpha = \chi_\beta$ if inhomogeneities Ω_α and Ω_β are identical up to a translation). The matrix is denoted $\Omega_0 = \Omega \setminus (\Omega_1 \cup \dots \cup \Omega_N)$. All phases have a linear elastic behavior: $\mathbf{C}_0$ (resp. $\mathbf{C}_\alpha$) denotes the stiffness of the matrix (resp. inhomogeneity $\alpha = 1, \dots, N$).

The EIM-G can be defined as a Galerkin discretization of the Lippmann–Schwinger equation with piece-wise polynomial trial stress-polarizations. Unlike the cell-based methods introduced in section 4.2, all calculations are performed in the real space: periodic boundary conditions are replaced with the mixed boundary conditions introduced in section 3.1 of chapter 3 (which requires the SVE Ω to be ellipsoidal). In other words, we seek an approximate solution to the Lippmann–Schwinger equation (4.1) where the modified Green operator $\boldsymbol{\Gamma}_0$ is defined as follows $\boldsymbol{\Gamma}_0[\boldsymbol{\tau}] = \boldsymbol{\Gamma}_0^\infty[\boldsymbol{\tau} - \chi\langle\boldsymbol{\tau}\rangle]$.

Taking advantage of the fact that inhomogeneities occupy a "small" bounded region of the whole SVE Ω, it is hoped that the stress-polarization within each inhomogeneity can be reasonably described by a low-order polynomial. This is certainly not true of the matrix, which occupies a "larger" domain. This heuristics motivates the choice of the matrix as reference material for the Lippmann–Schwinger equation. From equation (2.28), the stress-polarization within the matrix is then rigorously null, and there is no need for higher-order polynomials to describe this field.

Following the general approach described in section 4.1.2, we need to define the approximation space $\mathcal{T}_2^h(\Omega)$. In the EIM-G, the trial stress-polarization is a polynomial of degree p

in each inhomogeneity

$$\boldsymbol{\tau}^p(\mathbf{x}) = \sum_{\alpha=1}^{N} \sum_{\substack{(k_1,\dots,k_d)\in\mathbb{N}^d \\ k_1+\cdots+k_d\le p}} \chi_\alpha(\mathbf{x}-\mathbf{x}_\alpha)\big[(\mathbf{x}-\mathbf{x}_\alpha)\cdot\mathbf{e}_1\big]^{k_1}\cdots\big[(\mathbf{x}-\mathbf{x}_\alpha)\cdot\mathbf{e}_d\big]^{k_d}\,\boldsymbol{\tau}_\alpha^{k_1,\dots,k_d}. \quad (4.40)$$

In the above definition, the superscript p refers to the discretization parameter (it replaces the superscript h previously used in sections 4.1 and 4.2). The notation introduced above is somewhat cumbersome, and it was abbreviated in reference [BDS14] as follows

$$\boldsymbol{\tau}^p(\mathbf{x}) = \sum_{\alpha=1}^{N} \sum_{\substack{k_\bullet\in\mathbb{N}^d \\ k_1+\cdots+k_d\le p}} \chi_\alpha(\mathbf{x}-\mathbf{x}_\alpha)\,(x_\bullet - \mathbf{x}_{\alpha,\bullet})^{k_\bullet}\,\boldsymbol{\tau}_\alpha^{k_\bullet}. \quad (4.41)$$

where the convenient tuple notation $k_\bullet = (k_1,\dots,k_d)$, as well as some generalized product and exponentiation rules, were introduced. Considering the fact that only a few, essential, equations will be presented here, we will however stick for the sake of clarity with the explicit notation (4.40).

It should be observed that expression (4.40) is not intrinsic, in the sense that the components of the unknown coefficients $\boldsymbol{\tau}_\alpha^{k_1,\dots,k_d}$ do not behave as true tensors in a change of basis. If only one basis is considered (as will generally be the case), all other tensor operations (addition, contraction, …) remain meaningful: the $\boldsymbol{\tau}_\alpha^{k_1,\dots,k_d}$ will therefore be called *pseudotensors*, and will essentially be considered as true tensors in the remainder of this section.

Adopting the same form (4.40) for the test stress-polarization $\boldsymbol{\varpi}^p$ as for the trial stress-polarization $\boldsymbol{\tau}^p$, and plugging these expressions into the variational problem (4.4), the following linear system with $\boldsymbol{\tau}_\alpha^{k_1,\dots,k_d}$ as unknowns was finally obtained in reference [BDS14]

$$\sum_{\beta=1}^{N} \sum_{\substack{(l_1,\dots,l_d)\in\mathbb{N}^d \\ l_1+\cdots+l_d\le p}} \mathbf{A}_{\alpha\beta}^{k_1,\dots,k_d;l_1,\dots,l_d} : \boldsymbol{\tau}_\beta^{l_1,\dots,l_d} = \mathscr{M}_\alpha^{k_1,\dots,k_d}\overline{\boldsymbol{\varepsilon}}, \quad (4.42)$$

where the blocks of the matrix $\mathbf{A}_{\alpha\beta}^{k_1,\dots,k_d;l_1,\dots,l_d}$ are given by

$$\mathbf{A}_{\alpha\alpha}^{k_1,\dots,k_d;l_1,\dots,l_d} = \mathscr{M}_\alpha^{k_1+l_1,\dots,k_d+l_d}(\mathbf{C}_\alpha-\mathbf{C}_0)^{-1}+\mathbf{S}_\alpha^{k_1,\dots,k_d;l_1,\dots,l_d}-\frac{\mathscr{M}_\alpha^{k_1,\dots,k_d}\,\mathscr{M}_\alpha^{l_1,\dots,l_d}}{V}\mathbf{P}_\Omega, \quad (4.43)$$

for $\alpha=\beta$, and

$$\mathbf{A}_{\alpha\beta}^{k_1,\dots,k_d;l_1,\dots,l_d} = \mathbf{T}_{\alpha\beta}^{k_1,\dots,k_d;l_1,\dots,l_d}(\mathbf{r}_{\alpha\beta}) - \frac{\mathscr{M}_\alpha^{k_1,\dots,k_d}\,\mathscr{M}_\beta^{l_1,\dots,l_d}}{V}\mathbf{P}_\Omega, \quad (4.44)$$

for $\alpha\neq\beta$. In the above expressions, $\mathbf{r}_{\alpha\beta}=\mathbf{x}_\beta-\mathbf{x}_\alpha$, $\mathscr{M}_\alpha^{k_1,\dots,k_d}$ denotes the moment of order $(k_1,\dots,k_d)$ of inclusion α

$$\mathscr{M}_\alpha^{k_1,\dots,k_d} = \int_{\mathbf{x}\in\mathbb{R}^d} \chi_\alpha^{k_1,\dots,k_d}(\mathbf{x})\,\mathrm{d}V_\mathbf{x}, \quad \text{with} \quad \chi_\alpha^{k_1,\dots,k_d}(\mathbf{x}) = \chi_\alpha(\mathbf{x})x_1^{k_1}\cdots x_d^{k_d}, \quad (4.45)$$

	$d=2$	$d=3$
$p=0$	$3N$	$6N$
$p=1$	$9N$	$24N$
$p=2$	$18N$	$60N$
$p=3$	$30N$	$108N$

Table 4.1: Number of (scalar) unknowns of the EIM-G as a function of the degree p of the polynomials, and the dimension d of the physical space; N denotes the number of inhomogeneities.

while $\mathbf{T}_{\alpha\beta}^{k_1,\ldots,k_d;l_1,\ldots,l_d}$ and $\mathbf{S}_{\alpha}^{k_1,\ldots,k_d;l_1,\ldots,l_d}$ are the so-called influence and self-influence pseudotensors

$$\mathbf{T}_{\alpha\beta}^{k_1,\ldots,k_d;l_1,\ldots,l_d}(\mathbf{r}) = \int_{\mathbf{x},\mathbf{y}\in\mathbb{R}^d} \chi_{\alpha}^{k_1,\ldots,k_d}(\mathbf{x})\chi_{\beta}^{l_1,\ldots,l_d}(\mathbf{y})\,\boldsymbol{\Gamma}_0^{\infty}(\mathbf{r}+\mathbf{y}-\mathbf{x})\,\mathrm{d}V_{\mathbf{x}}\,\mathrm{d}V_{\mathbf{y}}, \tag{4.46}$$

$$\mathbf{S}_{\alpha}^{k_1,\ldots,k_d;l_1,\ldots,l_d} = \mathbf{T}_{\alpha\beta}^{k_1,\ldots,k_d;l_1,\ldots,l_d}(\mathbf{0}). \tag{4.47}$$

Provided that $\mathscr{M}_{\alpha}^{k_1,\ldots,k_d}$, $\mathbf{T}_{\alpha\beta}^{k_1,\ldots,k_d;l_1,\ldots,l_d}$ and $\mathbf{S}_{\alpha}^{k_1,\ldots,k_d;l_1,\ldots,l_d}$ can be computed, the matrix $A_{\alpha\beta}^{k_1,\ldots,k_d;l_1,\ldots,l_d}$ can be assembled, and the linear system (4.42) can be solved for the unknown coefficients $\boldsymbol{\tau}_{\alpha}^{k_1,\ldots,k_d}$. It should be observed that this matrix is dense, but relatively small (although it grows exponentially with p, see table 4.1). It is symmetric (since the bilinear form a is symmetric), and positive or negative if the matrix is softer or stiffer than all inhomogeneities.

Inversion of the linear system (4.42) is therefore fairly straightforward. The difficult part is, of course, the computation of the influence and self-influence pseudotensors. In sections 4.1 and 4.2 of reference [BDS14], multipole expansions were used to compute closed-form expressions of these pseudotensors for d-dimensional spheres. This was implemented in a computer algebra system, the results being gathered in reference [BDS13]. To be fair, it should be noted that the proposed method (relying on multipole expansions) is not fully justified. Indeed, it relies on the observation that the multipole expansions seem to be finite (higher-order terms being rigorously null). We were however not able to prove what must therefore be considered as a conjecture.

During the course of the PhD of El Assami [El 15], we attempted to extend the EIM-G to assemblies of ellipsoids. This required the evaluation of the corresponding influence pseudotensors. In this case, multipole expansions delivered expressions that turned out to be untractable[9]. We therefore had to resort to numerical integration.

Following Berveiller, Fassifehri, and Hihi [BFH87], we first expressed the convolution product in expression (4.46) of the influence pseudotensors as a simple product in the Fourier space, thus reducing the integral over $\mathbb{R}^d \times \mathbb{R}^d$ to an integral over $\mathbb{R}^d$ only. This integral is further reduced to an integral over the unit sphere (see section 2.3 and appendix A in reference [El 15]).

[9] We were however able to produce a general expression of the influence pseudotensors $\mathbf{T}_{\alpha\beta}^{k_1,\ldots,k_d;l_1,\ldots,l_d}(\mathbf{r})$ up to r^{-2} terms. This expression is not restricted to ellipsoids: it applies to *any* inhomogeneities.

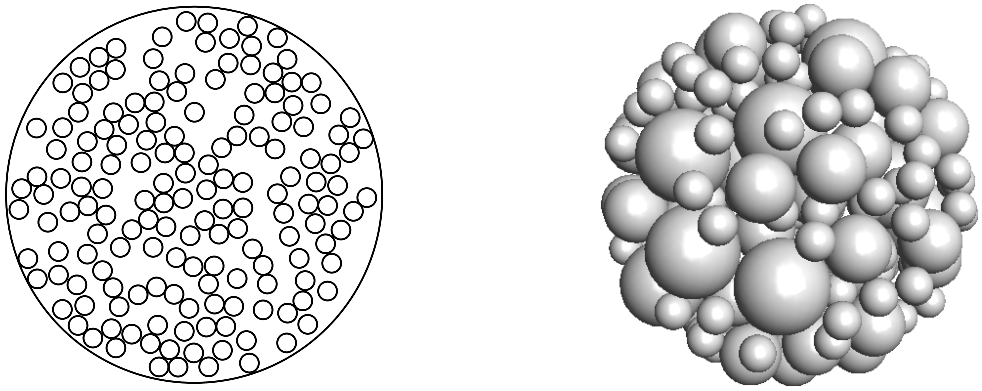

Figure 4.3: Left: graphical representation of one out of the 1 000 SVEs considered in section "Monodisperse assemblies of circular pores in plane strain elasticity". Circular, monodisperse pores are embedded in a homogeneous matrix; the porosity is $\varphi = 0.4$. Right: graphical representation of one out of the 100 SVEs considered in section "Polydisperse assembly of spherical pores in 3D elasticity". Spherical, polydisperse pores are embedded in a homogeneous matrix (only the pores are shown in this image); the porosity is $\varphi = 0.45$.

The computational gain is considerable; however, numerical evaluation of this integral remains challenging, as the integrand is highly localized. Typical Gauss integration is therefore ill-suited to the task, as most integration points do not contribute to the integral. For lack of time, we were however not able to propose a more efficient integration strategy (which would probably first require to localize the support of the integrand).

4.3.2 Application to assemblies of disks and spheres

The present section reproduces section 5 ("Applications") in reference [BDS14]. It illustrates the performances and limitations of the EIM-G.

In the present section, two applications of the variational form of the equivalent inclusion method (EIM-G) derived above are proposed. The first application (see section "Monodisperse assemblies of circular pores in plane strain elasticity") is a plane strain elasticity application, while the second application (see section "Polydisperse assembly of spherical pores in 3D elasticity") is a 3D elasticity application. It is recalled that the EIM-G requires the SVE to be of ellipsoidal shape [BSD13]. Therefore, circular and spherical SVEs are considered here.

Monodisperse assemblies of circular pores in plane strain elasticity

The present example deals with porous media in plane strain elasticity. The circular SVE Ω contains N circular pores of radius a. The porosity is $\varphi = 0.4$; with $N = 160$ pores, the radius R of the SVE Ω is $R = 20a$ (see figure 4.3, left). The shear modulus and Poisson ratio of the matrix are μ_0 (arbitrary value) and $\nu_0 = 0.3$.

To account for statistical fluctuations of the apparent mechanical properties of each individual SVE, 1 000 configurations were considered. The (mean) apparent shear modulus of these microstructures is then estimated through the EIM-G, and the results are reported in table 4.2 for various values of p (it is recalled that p is the maximum degree of the polynomial expansions used to approximate the stress-polarization $\boldsymbol{\tau}$). Due to the large number of independent

Order p	Bound on μ^{app}	DOFs
0	$0.310\,\mu_0$	480
1	$0.278\,\mu_0$	1 440
2	$0.257\,\mu_0$	2 880
3	$0.247\,\mu_0$	4 800

Table 4.2: Upper bounds on the apparent shear modulus of a monodisperse assembly of circular pores in plane strain elasticity, for increasing orders p of the EIM-G. For each value of p, the corresponding number of degrees of freedom (DOFs) is also reported.

configurations considered here, the amplitude of the 99 % confidence interval is smaller than one unit in the last place of each value reported in table 4.2.

Since the reference medium (the matrix) is stiffer than the inclusions, results presented in section 4.1.3 apply, and the estimates of μ^{app} are in fact upper bounds on this quantity. This is consistent with the fact that this bound decreases as p increases, as expected (the functional HS is minimized on sub-spaces of increasing dimension).

Observation of the results presented in table 4.2 shows that increasing p significantly improves the upper bound on μ^{app}. Indeed, from $p = 0$ to $p = 3$, the upper-bound is reduced by approximately 20 %, while the total number of degrees of freedom is multiplied by a factor 10.

In order to quantify the error on the apparent shear modulus, the above results were compared to finite element (FEM) estimates computed on the same 1 000 configurations. Strictly speaking, EIM-G and FEM computations are not equivalent. Indeed, essential boundary conditions were adopted for convenience for the FEM models, while EIM-G models require mixed boundary conditions. Since the SVEs under consideration are very large ($R/a = 20$), finite-size effects should be negligible, and the apparent shear moduli resulting from these two sets of boundary conditions are expected to coincide [Hil63].

The FEM estimate of the apparent shear modulus was found to be $0.244\,\mu_0$; again, the 99 % confidence interval is narrow enough to ensure that this value is correct up to one unit in the last place. Using this value as a reference, figure 4.4 shows in semi-log scale the relative error on μ^{app} as a function of the number of degrees of freedom. Observing figure 4.4, it seems that the EIM-G converges exponentially with respect to the number of degrees of freedom. This empirical result was expected, as similar asymptotic behaviors are also observed with the p-version of the FEM, which is very similar in spirit to EIM-G [SDR04].

Comparison of the respective sizes of the EIM-G and FEM models emphasizes the efficiency of the EIM-G. Indeed, each of the 1 000 FEM models contained about 320 000 degrees of freedom (this figure was variable from one configuration to another), while with only 4 800 degrees of freedom, the EIM-G achieves a relative error of approximately 1.2 %. In other words, the EIM-G can provide at a relatively low cost estimates of some quantities of interest with a small (but finite) error. Of course, if high accuracy is required, then the FEM should be preferred to the EIM-G.

To close this section, it should also be noted that the Hashin–Shtrikman upper-bound on μ^{app} reads in this case [HS62a]: $\mu^{\text{HS+}} = 0.349\,\mu_0$. Clearly, this bound is a poor estimate in plane strain elasticity of the effective shear modulus of a composite with circular inclusions. Even the 0-th order EIM-G bound leads to an improvement of 11 %.

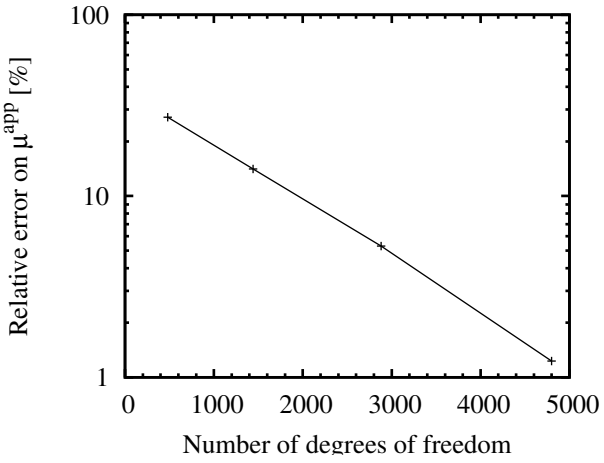

Figure 4.4: Relative error on μ^{app} as a function of the number of degrees of freedom of the EIM-G, in semi-log scale. Convergence seems to be exponential.

Order p	Bound on μ^{app}	DOFs
0	0.381	1 200
1	0.371	4 800
2	0.363	12 200

Table 4.3: Upper bounds on the apparent shear modulus of a polydisperse assembly of spherical pores in 3D elasticity, for increasing orders p of the EIM-G. For each value of p, the corresponding number of degrees of freedom (DOFs) is also reported.

Polydisperse assembly of spherical pores in 3D elasticity

The present example deals with porous media in 3D elasticity. The spherical SVE Ω contains $N_1 = 20$ (resp. $N_2 = 40$, $N_3 = 140$) spherical pores of radius a_1 (resp. $a_2 = 0.7\,a_1$, $a_3 = 0.4\,a_1$). The total porosity is $\varphi = 0.45$, so that the radius R of the SVE Ω is $R = 4.56\,a_1$ (see figure 4.3, right). The shear modulus and Poisson ratio of the matrix are μ_0 (arbitrary value) and $\nu_0 = 0.3$.

To account for statistical fluctuations, 100 such SVEs were generated. It should be noted that fluctuations were smaller in the present, 3D case than in the previous, plane strain one. In both cases, the amplitude of the statistical error (99 % confidence interval) was identical, even if the number of generated configurations was ten times smaller in the 3D application.

The (mean) apparent shear modulus μ^{app} of these microstructures is then estimated through the EIM-G, and the results are reported in table 4.3 for various values of p. Again, the results are accurate (with probability 99 %) within one unit in the last place. For the same reasons as previously, they can be considered as upper bounds on μ^{app} (which is again consistent with the fact that this bound decreases as p increases).

However, observing table 4.3, it seems that the relative improvement of the bounds is much lower in the present case than in the previous, plane strain case, for the same increase of the number of degrees of freedom. It is necessary to thoroughly investigate this apparent loss of efficiency; this investigation ought to be carried out in future work.

4.3.3 Application to variance reduction

This section is devoted to the post-doctoral work of Michaël Bertin, whom I supervised in collaboration with Dr. F. Legoll[10,11]. This work has benefited from a French government grant managed by ANR within the frame of the national program Investments for the Future ANR-11-LABX-022-01. The goal of this project was to use low order EIM-G estimates of the apparent stiffness of a SVE as a surrogate model for variance reduction by means of a control variate approach. After a brief overview of the problem and of control variate techniques, some results of this study will be presented.

Numerical evaluation of the effective properties of random heterogeneous materials must face three sources of errors: *i.* discretization errors, *ii.* statistical errors and *iii.* finite-size bias. Item *i.* affects any numerical simulation. It is controlled by e.g. the size of the mesh and will not be considered here. Items *ii.* and *iii.* are specific to random homogenization. This is best understood by recalling equation (2.4) that defines the effective stiffness of a random heterogeneous material

$$\mathbf{C}^{\text{eff}} = \lim_{|\Omega|\to+\infty} \mathbb{E}[\mathbf{C}^{\text{app}}(\Omega)], \tag{4.48}$$

which shows that the effective stiffness is the limit for large SVEs of the apparent stiffness. In practice, the largest affordable SVE Ω is selected and the limit is approximated as follows

$$\mathbf{C}^{\text{eff}} \approx \mathbb{E}[\mathbf{C}^{\text{app}}(\Omega)], \tag{4.49}$$

the truncation errors induced by the above approximation being referred to as finite-size bias (item *iii.*). Then, the ensemble average of equation (4.49) is estimated empirically from a large number of independent realizations $\omega_1, \omega_2, \ldots, \omega_M$. For each realization ω_i, the corrector problem is solved, which delivers (up to discretization errors) the apparent stiffness $\mathbf{C}^{\text{app}}(\Omega, \omega_i)$; the ensemble average is estimated as follows

$$\mathbb{E}[\mathbf{C}^{\text{app}}(\Omega)] \approx \frac{1}{M} \sum_{i=1}^{M} \mathbf{C}^{\text{app}}(\Omega, \omega_i). \tag{4.50}$$

Statistical errors (item *ii.*) stem from the fact that M is large, but finite. These errors are of course governed by the central limit theorem. More precisely, the error on C^{app}_{ijkl} scales as

$$\text{const.} \times \frac{\sqrt{\text{var}[C^{\text{app}}_{ijkl}(\Omega)]}}{\sqrt{M}}, \tag{4.51}$$

where the constant is related to the probability that the true error is effectively smaller than the above value (const. = 2.6 for the 99 % confidence interval).

The asymptotic behavior (for large SVEs) of both statistical error and bias have recently been studied mathematically for periodic boundary conditions [GNO15]; [GO15b]; [Nol14].

[10] Laboratoire Navier, UMR 8205, CNRS, ENPC, IFSTTAR, Université Paris-Est (Marne-la-Vallée, France)
[11] F. Legoll was PI for this project.

To the best of our knowledge, essential and natural boundary conditions have only been studied empirically [Kan+03].

The present section is devoted to the statistical error (item *ii.*): discretization errors and finite-size bias will not be considered. In other words, the size of the SVE Ω is fixed, we assume that discretization errors are controlled and we focus on the approximation induced by the finiteness of the sum in equation (4.50). The SVE Ω to which the apparent stiffness $\mathbf{C}^{\text{app}}(\Omega)$ refers will therefore be omitted in what follows.

Equation (4.51) shows that controlling the statistical error by means of the number M of realizations (the denominator of this equation) is rather costly. It is however observed that another way of reducing the statistical error is to control the numerator of this equation.

To do so, the random variable to be ensemble averaged [namely, $\mathbf{C}^{\text{app}}(\omega)$] is replaced with another random variable, the variance of which is hopefully smaller. This is the essence of the control variate approach [BLL16]; [LM15], which is briefly described below.

Introducing the so-called surrogate model $\mathbf{D}(\omega)$ (to be specified later), we have trivially

$$\mathbb{E}[\mathbf{C}^{\text{app}}] = \mathbb{E}[\mathbf{C}^{\text{app}} - \mathbf{D}] + \mathbb{E}[\mathbf{D}]. \tag{4.52}$$

If the ensemble average of the surrogate model $\mathbf{D}(\omega)$ is known exactly, then the ensemble average of $\mathbf{C}^{\text{app}}$ can be estimated from the following empirical formula

$$\mathbb{E}[\mathbf{C}^{\text{app}}] \approx \mathbb{E}[\mathbf{D}] + \frac{1}{M}\sum_{i=1}^{M}[\mathbf{C}^{\text{app}}(\omega_i) - \mathbf{D}(\omega_i)], \tag{4.53}$$

and the statistical error is effectively reduced (for a fixed number M of realizations) if the variance of $\mathbf{C}^{\text{app}} - \mathbf{D}$ is smaller than the variance of $\mathbf{C}^{\text{app}}$. A "good" surrogate model should therefore be *i.* simple enough for its ensemble average to be determined analytically and *ii.* highly correlated to the initial random variable $\mathbf{C}^{\text{app}}$. It should be emphasized that the surrogate model does not need to approximate the random variable, provided that both exhibit similar fluctuations.

Remark 4.2. *When a closed-form expression of the ensemble average $\mathbb{E}[\mathbf{D}]$ of the surrogate model is not available, this quantity can be estimated empirically. Then, equation (4.53) is replaced with*

$$\mathbb{E}[\mathbf{C}^{\text{app}}] \approx \frac{1}{M'}\sum_{i=1}^{M'}\mathbf{D}(\omega_i) + \frac{1}{M}\sum_{i=1}^{M}[\mathbf{C}^{\text{app}}(\omega_i) - \mathbf{D}(\omega_i)], \tag{4.54}$$

where M' is presumably much larger than M. Provided that the surrogate model $\mathbf{D}$ is simple enough, evaluation of the first term in equation (4.54) is not too costly.

Error on $\mathbb{E}[\mathbf{C}^{\text{app}}]$ is then the sum of two terms, each of which can be evaluated by means of the central limit theorem as follows

$$\text{const.} \times \left(\frac{\sqrt{\text{var}[D_{ijkl}]}}{\sqrt{M'}} + \frac{\sqrt{\text{var}[C^{\text{app}}_{ijkl} - D_{ijkl}]}}{\sqrt{M}} \right). \tag{4.55}$$

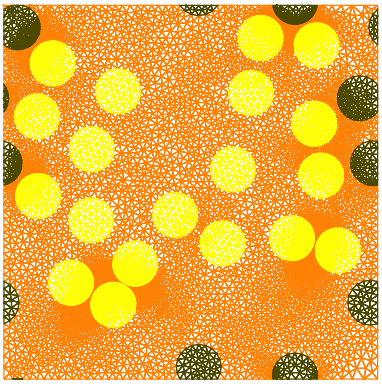

Figure 4.5: A realization of the microstructure considered in section 4.3.3, and the mesh used to estimate the apparent conductivity by means of the finite element method.

Remark 4.3. *In practical applications, the surrogate model* $\mathbf{D}$ *is replaced with* $\rho\,\mathbf{D}$*, where* ρ *is a free, scalar parameter, which is selected* a posteriori *so as to minimize the variance of the components of* $\mathbf{C}^{\mathrm{app}} - \rho\,\mathbf{D}$*. This optimization is carried out component-wise, so that* ρ *effectively depends on the component* C^{app}_{ijkl} *under consideration.*

In the work of M. Bertin, we developed a variance reduction strategy for the evaluation of the apparent properties of matrix–inhomogeneities microstructures. This strategy was tested extensively in 2D, for random, periodic assemblies of circular, monosized inhomogeneities embedded in a homogeneous matrix. These tests were really performed within the framework of scalar problems (thermal conduction). The tensors $\mathbf{C}^{\mathrm{app}}(\omega)$ should therefore be understood as second-rank, positive definite tensors (thermal conductivity). We assume that matrix and inhomogeneities are both isotropic, with conductivities $\mathbf{C}_{\mathrm{m}} = \kappa_{\mathrm{m}}\,\mathbf{I}$ and $\mathbf{C}_{\mathrm{i}} = \kappa_{\mathrm{i}}\,\mathbf{I}$, respectively. The material contrast c is defined as the ratio $c = \kappa_{\mathrm{i}}/\kappa_{\mathrm{m}}$.

Although the ensemble average $\mathbb{E}[\mathbf{C}^{\mathrm{app}}]$ is not expected to be isotropic for SVEs of finite size, we will concentrate in what follows on the trace of the apparent conductivity $\kappa^{\mathrm{app}}(\omega) = \frac{1}{2}\operatorname{tr}\mathbf{C}^{\mathrm{app}}(\omega)$.

We used the $p = 0$ EIM-G estimate of the apparent conductivity as a surrogate model. In other words, we optimized the Hashin–Shtrikman functional with trial heat flux polarizations that are constant in each circular inclusion for two independent macroscopic temperature gradients. The resulting bound $\mathbf{D}(\omega)$ on the conductivity tensor is used as a surrogate model. It should be noted that, rather than controlling $\kappa^{\mathrm{app}}(\omega)$ by one scalar random variable $\operatorname{tr}\mathbf{D}(\omega)$ only, we chose to consider the three components of $\mathbf{D}(\omega)$ simultaneously. The surrogate model therefore reads $\rho_{11}D_{11}(\omega) + \rho_{22}D_{22}(\omega) + \rho_{12}D_{12}(\omega)$, where ρ_{11}, ρ_{22} and ρ_{12} are optimized a posteriori.

The apparent conductivity $\mathbf{C}^{\mathrm{app}}(\omega)$ is estimated by means of the finite element method with periodic boundary conditions. We used `GMSH`[12] to generate the mesh and `FreeFem++`[13] as a solver. A preliminary study was devoted to the optimization of the mesh-size (see figure 4.5) so as to control discretization errors, which will not be further discussed.

[12] http://gmsh.info/, last retrieved 2017-04-26
[13] http://www.freefem.org/, last retrieved 2017-04-26

Likewise, finite-size errors are not considered in this work, the purpose of which is to show that the cost of estimating the apparent stiffness of SVEs of a given size can be reduced, while ensuring the same accuracy. We therefore picked SVEs which were deemed "large enough", and generated assemblies of 25 disks of radius $a = 0.3$ in a periodic simulation box of size $L \times L$, with $L = 5.0$; the volume fraction of inhomogeneities is $f \approx 28\,\%$. The microstructures were generated by means of a standard Monte-Carlo simulation of hard disks, using a in-house code, which allows for the specification of a minimum distance between inhomogeneities.

It should be emphasized that, in the present application, the volume fraction of inhomogeneities is fixed. This decision relies on the previous knowledge that, when allowed to fluctuate, the volume fraction f is an excellent surrogate model for the estimation of the apparent conductivity $\mathbb{E}[\mathbf{C}^{\text{app}}]$. In other words, how to control the fluctuations induced on the apparent conductivity $\mathbb{E}[\mathbf{C}^{\text{app}}]$ by the fluctuations of the volume fraction f is already fairly well-known. Killing the fluctuations of the latter quantity effectively allowed us to explore other sources of fluctuations.

Implementation of the EIM-G surrogate model required some minor adaptations with respect to the general framework introduced in section 4.3.1. Indeed, it should be recalled that the method was initially derived for the modified Green operator and the corresponding mixed boundary conditions introduced in section 3.1. In the present study, periodic boundary conditions were used. As a consequence, the closed-form expressions of the influence tensors[14] presented in reference [BDS13] cannot be used. For periodic boundary conditions, these tensors are expressed as Fourier series [Suq90] that unfortunately converge very slowly (this point is further discussed in section 4.3.4).

We therefore chose to evaluate the influence tensors numerically by means of two-inhomogeneity finite element models. The first inhomogeneity, at the center of the periodic cell, was subjected to an "eigen- heat flux". The location of the second (free of eigen- heat flux) inhomogeneity was varied; its average temperature gradient was recorded for each location. A table of influence tensors was then precomputed and a suitable interpolation scheme further devised by M. Bertin to estimate these tensors for any separation $\mathbf{r}_{\alpha\beta} = \mathbf{x}_\beta - \mathbf{x}_\alpha$ between inhomogeneities α and β. The linear system defining the optimal trial heat flux polarization is then assembled in the usual way.

Of course, the ensemble average of the proposed surrogate model is not known in closed-form. Following remark 4.2, it was therefore estimated numerically. This was not too penalizing, as generating one microstructure and applying the EIM-G is extremely fast. Indeed, it should be recalled that for thermal conduction problems, the size of the EIM-G matrix is only $2N \times 2N$, and the corresponding linear system must be solved for only 2 independent right-hand sides for each realization.

M. Bertin performed an exhaustive parametric study of the proposed strategy, where the material contrast c, the size of the SVE L and the minimal distance between inclusions were varied. The full study will be published in an article currently in preparation. In the present document, we concentrate on the effect of the material contrast. Figure 4.6 shows, as a function

[14] For the 0-th order EIM-G, it can readily be verified that all influence pseudotensors are indeed tensors.

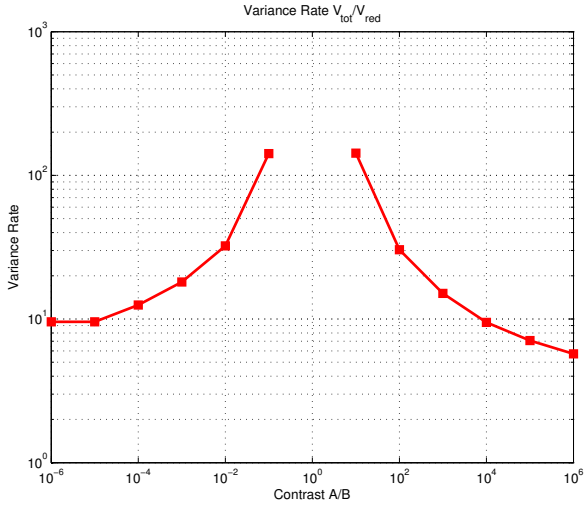

Figure 4.6: Efficiency of the variance reduction method as a function of the material contrast.

of the material contrast c, the effectivity index e of the method, defined as follows

$$e = \frac{\mathrm{var}[\kappa^{\mathrm{app}}]}{\mathrm{var}[\kappa^{\mathrm{app}} - \rho_{11} D_{11} + \rho_{22} D_{22} + \rho_{12} D_{12}]}. \tag{4.56}$$

Large values of e indicate a significant reduction of the statistical error, by a factor $\sqrt{e}$ at equal computational cost.

Observation of figure 4.6 shows that for moderate contrasts, the method is highly effective, with $10 \lesssim e \lesssim 100$ ($3 \lesssim \sqrt{e} \lesssim 10$). For larger contrasts, the effectivity index decreases as expected, and levels off. The asymptotic value is greater than 1, indicating that we still profit from this approach.

The above result is quite remarkable. Indeed, table 4.2 and figure 4.4 show that the 0-th order EIM-G generally delivers poor estimates of the apparent stiffness: in other words, the proposed surrogate model $\mathbf{D}(\omega)$ does not capture the *values* of $\mathbf{C}^{\mathrm{app}}(\omega)$ accurately. However, figure 4.6 shows that it does capture its *fluctuations* accurately.

These promising preliminary results open a number of exciting perspectives. We first intend to extend this work to three dimensions and linear elasticity. Of particular interest would then be the cases where neither $\mathbf{C}_{\mathrm{i}} \leq \mathbf{C}_{\mathrm{m}}$, nor $\mathbf{C}_{\mathrm{i}} \geq \mathbf{C}_{\mathrm{m}}$ hold. In such cases, our surrogate model is no longer a bound on the apparent stiffness. Whether this affects the efficiency of our method ought to be asserted. Also, non-linear behaviors should be considered. To this end, a similar reduced model, based on the Hashin–Shtrikman could in principle be used, using the techniques introduced by Ponte Castañeda [Pon16] and Ponte Castañeda [Pon91], Willis [Wil91], or Peigney and Peigney [PP17]. Finally, we would like to be able to handle more complex microstructures. A possible approach would then be to adopt UGPLS solvers for both "true" and surrogate models: for the surrogate model, the number of iterations would be set to a low value. This is motivated by the observation that a few iterations of a UGPLS solver generally suffice to deliver a trial stress-polarization $\boldsymbol{\tau}$ that reveals the microstructure (and should therefore somehow capture the fluctuations of the apparent stiffness).

4.3.4 Closing remarks

It has already been mentioned that the numerical method proposed in the present section 4.3 can be seen as the variational form of the classical equivalent inclusion method (EIM) previously introduced by Eshelby [Esh57] and Moschovidis and Mura [MM75]. In the EIM-G, the stress-polarization is polynomial over each inhomogeneity. A Galerkin-type approach is then used to find the coefficients of the polynomials that define this stress-polarization. In the EIM-T proposed by Moschovidis and Mura [MM75], the determination of these polynomials is based on Taylor expansions within each inhomogeneity. Quoting liberally from [BDS14], this results in a number of shortcomings.

1. There is no guarantee that the resulting discrete problem is well-posed. In other words, the EIM-T might fail to deliver an estimate of the solution in some circumstances.
2. Increasing the degree p of the polynomial expansions does not necessarily improve the quality of the approximate solution. This has already been reported by many authors [BLR06]; [Fon+01]; [RH91].
3. Since the EIM-T is based on the standard Lippmann–Schwinger equation in an unbounded domain ($\boldsymbol{\tau} + \boldsymbol{\Gamma}_0^{\infty}[\boldsymbol{\tau}] = \bar{\boldsymbol{\varepsilon}}$), there is no guarantee that the resulting estimate of the apparent stiffness is symmetric, positive definite.
4. Computing this estimate requires the computation of the average stress $\langle\boldsymbol{\sigma}\rangle$ and strain $\langle\boldsymbol{\varepsilon}\rangle$ through complex surface integrals at the boundary $\partial\Omega$ of the SVE[15] [FGS02]; [Fon+01]. Such operations are costly and potentially inaccurate.

Regarding items 1 and 2, the Hashin–Shtrikman principle guarantees well-posedness of the EIM-G. Besides, when the matrix is stiffer or softer than the inhomogeneities, the estimates of the apparent stiffness are ordered with respect to p: in other words, the quality of these estimates is non-decreasing (it might not increase with p, though).

Regarding items 3 and 4, the EIM-G is based on the modified Lippmann–Schwinger equation (3.3). The corresponding estimate of the apparent stiffness is fully determined from the volume average $\langle\boldsymbol{\tau}^p\rangle$ of the trial stress-polarization [see the comments surrounding equation (4.13)], which is trivially computed from its polynomial expansions.

Clearly, the proposed EIM-G is superior to its classical alternative EIM-T. However, it has been shown in section 4.3.2 that it performs very satisfactorily in two dimensions, less so in three dimensions. This is probably due to the fact that, in the latter case, the degree p is not large enough. Unfortunately, going beyond $p = 2$ or $p = 3$ is not an option (owing to the exponential increase of the number of unknowns). Another option would be to change the representation (4.41) of the trial stress-polarization. The natural alternative would be to consider linear combinations of spherical harmonics (rather than polynomials). This however would lead to highly technical developments, with the risk that no improvement of the method be observed in the end. For this reason, I am reluctant to go down this route. Still, it is remarkable that even low-order instances of the EIM-G seem to be able to capture the *fluctuations* of the apparent stiffness (see section 4.3.3). Maybe the real value of this method lies in this niche.

[15] Incidentally, it is observed that the average strain $\langle\boldsymbol{\varepsilon}\rangle$ over the SVE Ω does *not* coincide with the prescribed strain at infinity $\bar{\boldsymbol{\varepsilon}}$ and must therefore be computed in this approach.

Finally, it should be observed that the present method was formulated within the framework of the mixed boundary conditions introduced in section 3.1.2. In view of the known superiority of periodic bounday conditions [Kan+03], such choice might seem questionable. It is indeed possible to formulate the EIM-G within the framework of periodic boundary conditions (and in fact, we did so in section 4.3.3). Practical implementation is however complex. Indeed, the influence and self-influence pseudotensors are then expressed as d-dimensional Fourier series (lattice sums) that are ill-suited to numerical evaluation, owing to their slow convergence. At the time this work was performed, I therefore settled for the mixed boundary conditions, which lead to explicit expressions of the influence and self-influence pseudotensors [BDS13]. To, Bonnet, and Hoang [TBH16] have since proposed summation techniques that might probably be ported to the present problem. Nevertheless, it is observed that, like the periodic boundary conditions, the mixed boundary conditions are "intermediate", in that they are more compliant than essential boundary conditions and less compliant than natural boundary conditions. Mixed boundary conditions might well turn out to be just as favorable as periodic boundary conditions from the point of view of size effects. This point has not been investigated.

Chapter 5

Perspectives

Intentionally left blank

***

In the present chapter, I have sketched out a few research topics that I intend to explore in the coming years. These topics constitute both a continuation of and a departure from my earlier work. Continuation, as most of these topics are closely related to the intricate relationships between microstructure and macroscopic properties and require numerical (full-field) simulations. Continuation, since the Hashin–Shtrikman principle will remain an essential tool. My future work will also depart from my previous work, as I would like to put more emphasis on the *application* of numerical methods to real (or realistic) situations, rather than their *development*.

The work presented in this report opens a large number of exciting perspectives, which cannot be explored simultaneously. It will therefore be necessary to prioritize these topics. Top priority will of course be given to research projects that are nearly complete (in the sense that I cannot – or do not want to – further contribute to these topics). This category includes: error estimators for UGPLS solvers (see section **??**), Ms-FEM techniques for plates (see section **??**) and improved Hashin–Shtrikman bounds (see section **??**). As for new research topics, I will first focus on: atomistic-to-continuum upscaling (see section **??**) and unsaturated media (see section **??**). Having the opportunity to supervise PhD students will undoubtedly give a significant boost to these projects.

As a closure, I would like to add that teaching is deeply rooted in my research project. I have already mentioned in section 1.4 how passionate I am about all aspects of teaching, from preparing lessons and handouts to actually facing the students. Depending on opportunities, I intend to further increase my involvement in teaching, as illustrated by my recent appointment to the responsibility of the *Plates and Shells* course at École des Ponts ParisTech.

Appendix A

On the fourth-rank Green operator The case of isotropic reference materials

In the present appendix, closed-form expressions of the fourth-rank Green operator are gathered for various types of boundary conditions. The reference material is supposed to be isotropic: μ_0 (resp. ν_0) denotes its shear modulus (resp. Poisson ratio).

A.1 Expression for periodic boundary conditions

The fourth-rank Green operator for periodic boundary conditions is defined in section 2.2.2 [see in particular equation (2.21)]. The Fourier coefficients of the Green operator read, for $\mathbf{k} \neq \mathbf{0}$ [Suq90]

$$\tilde{\Gamma}^{\text{per}}_{0,ijhl}(\mathbf{k}) = \frac{1}{4\mu_0}(\delta_{ih}n_jn_l + \delta_{il}n_jn_h + \delta_{jh}n_in_l + \delta_{jl}n_in_h) - \frac{n_in_jn_hn_l}{2\mu_0(1-\nu_0)}, \tag{A.1}$$

where $\mathbf{n} = \mathbf{k}/\|\mathbf{k}\|$. For $\mathbf{k} = \mathbf{0}$, $\tilde{\boldsymbol{\Gamma}}^{\text{per}}_0(\mathbf{0}) = \mathbf{0}$ since problem (2.20) defining the Green operator implies $\langle\boldsymbol{\varepsilon}\rangle = \mathbf{0}$.

A.2 Expression for boundary conditions at infinity

The fourth-rank Green operator of the whole space is defined in section 2.2.3 [see in particular equation (2.24)]. In the equations below, $r = \|\mathbf{r}\|$ and $\mathbf{n} = \mathbf{r}/r$.

For $d = 2$ (plane strain elasticity)

$$\mathbf{P}_0 = \frac{1-2\nu_0}{4\mu_0(1-\nu_0)}\mathbf{J} + \frac{3-4\nu_0}{8\mu_0(1-\nu_0)}\mathbf{K}, \tag{A.2a}$$

$$\begin{aligned}\Gamma^{\infty}_{0,ijkl}(\mathbf{r}) = \frac{1}{8\pi\mu_0(1-\nu_0)r^2}\big[&-\delta_{ij}\delta_{kl} + (1-2\nu_0)(\delta_{ik}\delta_{jl} + \delta_{il}\delta_{jk}) + 2(\delta_{ij}n_kn_l + \delta_{kl}n_in_j)\\ &+ 2\nu_0(\delta_{ik}n_jn_l + \delta_{il}n_jn_k + \delta_{jk}n_in_l + \delta_{jl}n_in_k) - 8n_in_jn_kn_l\big].\end{aligned} \tag{A.2b}$$

For $d = 3$ (3D elasticity)

$$\mathbf{P}_0 = \frac{1-2\nu_0}{6\mu_0(1-\nu_0)}\mathbf{J} + \frac{4-5\nu_0}{15\mu_0(1-\nu_0)}\mathbf{K}, \tag{A.3a}$$

$$\begin{aligned}\Gamma^{\infty}_{0,ijkl}(\mathbf{r}) = \frac{1}{16\pi\mu_0(1-\nu_0)r^3}\big[&-\delta_{ij}\delta_{kl} + (1-2\nu_0)(\delta_{ik}\delta_{jl}+\delta_{il}\delta_{jk}) + 3(\delta_{ij}n_kn_l + \delta_{kl}n_in_j)\\ &+ 3\nu_0(\delta_{ik}n_jn_l + \delta_{il}n_jn_k + \delta_{jk}n_in_l + \delta_{jl}n_in_k) - 15n_in_jn_kn_l\big].\end{aligned} \tag{A.3b}$$

Appendix B

On the evaluation of the Hashin–Shtrikman functional

In chapter 3, bounds on the effective stiffness are derived by means of the modified Hashin–Shtrikman principle introduced in section 3.1.3. Provided that the reference material is stiffer than all phases constituting the composite, these bounds read (see section 3.1.5)

$$\lim_{|\Omega|\to+\infty} \mathbb{E}\big[\mathrm{HS}(\chi\boldsymbol{\tau};\overline{\boldsymbol{\varepsilon}})\big] \geq \tfrac{1}{2}\overline{\boldsymbol{\varepsilon}} : \mathbf{C}^{\mathrm{eff}} : \overline{\boldsymbol{\varepsilon}}, \tag{B.1}$$

where the modified Hashin–Shtrikman functional HS is defined as follows [see equation (3.16)]

$$\mathrm{HS}(\chi\boldsymbol{\tau};\overline{\boldsymbol{\varepsilon}}) = \tfrac{1}{2}\overline{\boldsymbol{\varepsilon}} : \mathbf{C}_0 : \overline{\boldsymbol{\varepsilon}} + \overline{\boldsymbol{\varepsilon}} : \langle\boldsymbol{\tau}\rangle - \tfrac{1}{2}\langle\boldsymbol{\tau} : (\mathbf{C}-\mathbf{C}_0)^{-1} : \boldsymbol{\tau}\rangle - \tfrac{1}{2}\langle\boldsymbol{\tau} : \boldsymbol{\Gamma}_0^{\infty}[\chi(\boldsymbol{\tau}-\langle\boldsymbol{\tau}\rangle)]\rangle, \tag{B.2}$$

The trial stress-polarization $\boldsymbol{\tau}$ is a random field suitably defined over the whole space $\mathbb{R}^d$; in equation (B.1), it is truncated to the RVE Ω by means of its indicator function χ. The present appendix is devoted to the evaluation of the left-hand side of inequality (B.1), under the following assumptions on the trial stress-polarization $\boldsymbol{\tau}$.

Assumption B.1 (Weak statistical homogeneity of $\boldsymbol{\tau}$)**.** *The ensemble averages* $\mathbb{E}\big[\chi_\alpha(\mathbf{x})\,\boldsymbol{\tau}(\mathbf{x})\big]$ *and* $\mathbb{E}\big[\chi_\alpha(\mathbf{x})\chi_\beta(\mathbf{x}+\mathbf{r})\boldsymbol{\tau}(\mathbf{x})\otimes\boldsymbol{\tau}(\mathbf{x}+\mathbf{r})\big]$ *are translation-invariant (with respect to* $\mathbf{x}$*) for all* $\alpha,\beta = 1,\dots,N$.

Summing over α and β, this means in particular that $\mathbb{E}\big[\boldsymbol{\tau}(\mathbf{x})\big]$ and $\mathbb{E}\big[\boldsymbol{\tau}(\mathbf{x})\otimes\boldsymbol{\tau}(\mathbf{x}+\mathbf{r})\big]$ are translation-invariant.

Assumption B.2 (Weak ergodicity of $\boldsymbol{\tau}$)**.** *The volume and ensemble averages of* $\boldsymbol{\tau}$ *coincide for large RVEs* Ω*:* $\lim_{|\Omega|\to+\infty}\langle\boldsymbol{\tau}\rangle \to \mathbb{E}\boldsymbol{\tau}$.

Assumption B.3. *The autocovariance of* $\boldsymbol{\tau}$*, defined as*

$$\mathbf{R}_{\tau\tau}(\mathbf{r}) = \mathbb{E}\big[\boldsymbol{\tau}(\mathbf{0})\otimes\boldsymbol{\tau}(\mathbf{r})\big] - \mathbb{E}\boldsymbol{\tau}\otimes\mathbb{E}\boldsymbol{\tau}, \tag{B.3}$$

is square integrable and differentiable at the origin.

In what follows, each term of $\mathbb{E}\big[\mathrm{HS}(\chi\boldsymbol{\tau};\overline{\boldsymbol{\varepsilon}})\big]$ is evaluated in turn. From the weak homogeneity of $\boldsymbol{\tau}$, it is readily found that $\mathbb{E}\big[\overline{\boldsymbol{\varepsilon}} : \langle\boldsymbol{\tau}\rangle\big] = \overline{\boldsymbol{\varepsilon}} : \mathbb{E}\boldsymbol{\tau}$. Then

$$\begin{aligned}\mathbb{E}\big[\langle\boldsymbol{\tau} : (\mathbf{C}-\mathbf{C}_0)^{-1} : \boldsymbol{\tau}\rangle\big] &= \mathbb{E}\big[\langle(\mathbf{C}-\mathbf{C}_0)^{-1} :: (\boldsymbol{\tau}\otimes\boldsymbol{\tau})\rangle\big]\\ &= \sum_{\alpha=1}^{N}\frac{1}{V}\int_{\mathbf{x}\in\Omega}(\mathbf{C}_\alpha-\mathbf{C}_0)^{-1} :: \mathbb{E}\big[\chi_\alpha(\mathbf{x})\,\boldsymbol{\tau}(\mathbf{x})\otimes\boldsymbol{\tau}(\mathbf{x})\big]\,\mathrm{d}V_{\mathbf{x}}\\ &= \sum_{\alpha=1}^{N}(\mathbf{C}_\alpha-\mathbf{C}_0)^{-1} :: \mathbb{E}\big[\chi_\alpha(\mathbf{0})\,\boldsymbol{\tau}(\mathbf{0})\otimes\boldsymbol{\tau}(\mathbf{0})\big],\end{aligned} \tag{B.4}$$

where the weak homogeneity of $\boldsymbol{\tau}$ has again been used. We now turn to the evaluation of the last term in equation (B.2). More precisely, we seek the limit: $\lim_{|\Omega|\to+\infty}\mathbb{E}\big[\boldsymbol{\tau} : \boldsymbol{\Gamma}_0^\infty[\chi(\boldsymbol{\tau}-\langle\boldsymbol{\tau}\rangle)]\big]$. We start with two preliminary results.

Theorem B.1. *Let $\boldsymbol{\tau}_1$ and $\boldsymbol{\tau}_2$ be two random stress-polarization fields such that the ensemble averages $\mathbb{E}\big[\boldsymbol{\tau}_1(\mathbf{x})\big]$ and $\mathbb{E}\big[\boldsymbol{\tau}_2(\mathbf{x})\big]$ are translation-invariant (with respect to $\mathbf{x}$). It is further assumed that $\lim_{|\Omega|\to+\infty}\langle\boldsymbol{\tau}_2\rangle = \mathbb{E}\boldsymbol{\tau}_2$. Then, for all $\mathbf{x}\in\mathbb{R}^d$*

$$\lim_{|\Omega|\to+\infty}\mathbb{E}\big[\boldsymbol{\tau}_1(\mathbf{x}) : \boldsymbol{\Gamma}_0^\infty[\chi(\boldsymbol{\tau}_2-\langle\boldsymbol{\tau}_2\rangle)](\mathbf{x})\big] = \lim_{|\Omega|\to+\infty}\mathbb{E}\big[\boldsymbol{\tau}_1(\mathbf{x}) : \boldsymbol{\Gamma}_0^\infty[\chi(\boldsymbol{\tau}_2-\mathbb{E}\boldsymbol{\tau}_2)](\mathbf{x})\big], \tag{B.5}$$

provided that these limits exist.

Theorem B.2. *Let $\boldsymbol{\tau}_1$ and $\boldsymbol{\tau}_2$ be two random stress-polarization fields such that the ensemble averages $\mathbb{E}\big[\boldsymbol{\tau}_1(\mathbf{x})\big]$, $\mathbb{E}\big[\boldsymbol{\tau}_2(\mathbf{x})\big]$ and $\mathbb{E}\big[\boldsymbol{\tau}_1(\mathbf{x})\otimes\boldsymbol{\tau}_2(\mathbf{x}+\mathbf{r})\big]$ are translation-invariant (with respect to $\mathbf{x}$). The cross-correlation $\mathbf{R}_{12}(\mathbf{r}) = \mathbb{E}\big[\boldsymbol{\tau}_1(\mathbf{0})\otimes\boldsymbol{\tau}_2(\mathbf{r})\big]$ is assumed to be square integrable over the whole space $\mathbb{R}^d$ and differentiable at the origin. Then,*

$$\lim_{|\Omega|\to+\infty}\mathbb{E}\big[\boldsymbol{\tau}_1(\mathbf{x}) : \boldsymbol{\Gamma}_0^\infty[\chi\boldsymbol{\tau}_2](\mathbf{x})\big] = \mathbf{P}_0 :: \mathbf{R}_{12}(\mathbf{0}) + \lim_{\delta\to0}\int_{\substack{\mathbf{r}\in\mathbb{R}^d\\ \|\mathbf{r}\|\geq\delta}}\boldsymbol{\Gamma}_0^\infty(\mathbf{r}) :: \mathbf{R}_{12}(\mathbf{r})\,\mathrm{d}V_{\mathbf{r}}, \tag{B.6}$$

for all $\mathbf{x}\in\mathbb{R}^d$ fixed. In the above, χ denotes the indicator function of Ω.

The proofs of these theorems can be found in sections B.1 and B.2. From theorem B.1, we first find that

$$\lim_{|\Omega|\to+\infty}\mathbb{E}\big[\boldsymbol{\tau} : \boldsymbol{\Gamma}_0^\infty[\chi(\boldsymbol{\tau}-\langle\boldsymbol{\tau}\rangle)]\big] = \lim_{|\Omega|\to+\infty}\mathbb{E}\big[\boldsymbol{\tau} : \boldsymbol{\Gamma}_0^\infty[\chi(\boldsymbol{\tau}-\mathbb{E}\boldsymbol{\tau})]\big], \tag{B.7}$$

then, from theorem B.2

$$\lim_{|\Omega|\to+\infty}\mathbb{E}\big[\boldsymbol{\tau}(\mathbf{x}) : \boldsymbol{\Gamma}_0^\infty[\chi(\boldsymbol{\tau}(\mathbf{x})-\mathbb{E}\boldsymbol{\tau})]\big] = \mathbf{P}_0 :: \mathbf{R}_{\tau\tau}(\mathbf{0}) + \lim_{\delta\to0}\int_{\substack{\mathbf{r}\in\mathbb{R}^d\\ \|\mathbf{r}\|\geq\delta}}\boldsymbol{\Gamma}_0^\infty(\mathbf{r}) :: \mathbf{R}_{\tau\tau}(\mathbf{r})\,\mathrm{d}V_{\mathbf{r}}, \tag{B.8}$$

for all $\mathbf{x}\in\mathbb{R}^d$. The above point-wise equality also holds on (volume) average

$$\lim_{|\Omega|\to+\infty}\mathbb{E}\big[\langle\boldsymbol{\tau} : \boldsymbol{\Gamma}_0^\infty[\chi(\boldsymbol{\tau}-\mathbb{E}\boldsymbol{\tau})]\rangle\big] = \mathbf{P}_0 :: \mathbf{R}_{\tau\tau}(\mathbf{0}) + \lim_{\delta\to0}\int_{\substack{\mathbf{r}\in\mathbb{R}^d\\ \|\mathbf{r}\|\geq\delta}}\boldsymbol{\Gamma}_0^\infty(\mathbf{r}) :: \mathbf{R}_{\tau\tau}(\mathbf{r})\,\mathrm{d}V_{\mathbf{r}}. \tag{B.9}$$

Gathering equations (B.4) and (B.9) finally delivers equation (3.23).

B.1 Proof of Theorem B.1

For the sake of simplicity, the proof is restricted to ellipsoidal domains Ω. For $\mathbf{x} \in \mathbb{R}^d$ fixed

$$\mathbb{E}\big[\boldsymbol{\tau}_1(\mathbf{x}) : \boldsymbol{\Gamma}_0^\infty[\chi(\boldsymbol{\tau}_2 - \langle\boldsymbol{\tau}_2\rangle)](\mathbf{x})\big] = \mathbb{E}\big[\boldsymbol{\tau}_1(\mathbf{x}) : \boldsymbol{\Gamma}_0^\infty[\chi(\boldsymbol{\tau}_2 - \mathbb{E}\boldsymbol{\tau}_2)](\mathbf{x})\big] - \mathbb{E}\big[\boldsymbol{\tau}_1(\mathbf{x}) : \delta\boldsymbol{\varepsilon}_2(\mathbf{x})\big], \quad \text{(B.10)}$$

where $\delta\boldsymbol{\varepsilon}_2 = -\boldsymbol{\Gamma}_0^\infty[\chi(\mathbb{E}\boldsymbol{\tau}_2 - \langle\boldsymbol{\tau}_2\rangle)]$. Therefore, we must prove that the last term tends to 0. Observing that $\chi(\mathbb{E}\boldsymbol{\tau}_2 - \langle\boldsymbol{\tau}_2\rangle)$ is constant within the ellipsoidal domain Ω, and null outside Ω, we find from Eshelby's theorem [Esh57] that

$$\mathbb{E}\big[\boldsymbol{\tau}_1(\mathbf{x}) : \delta\boldsymbol{\varepsilon}_2(\mathbf{x})\big] = \mathbb{E}\big[\boldsymbol{\tau}_1(\mathbf{x}) : \mathbf{P}_\Omega : (\mathbb{E}\boldsymbol{\tau}_2 - \langle\boldsymbol{\tau}_2\rangle)\big] = \mathbb{E}\boldsymbol{\tau}_1 : \mathbf{P}_\Omega : (\mathbb{E}\boldsymbol{\tau}_2 - \langle\boldsymbol{\tau}_2\rangle), \quad \text{(B.11)}$$

which tends to zero.

B.2 Proof of theorem B.2

Before we proceed to prove this result, we first clarify how the limit "as $|\Omega| \to +\infty$" must be understood. We consider a sequence of domains $(\Omega)_{n\in\mathbb{N}}$, such that $\Omega_0 \subset \Omega_1 \subset \Omega_2 \subset \ldots$ and $\bigcup_{n\in\mathbb{N}} \Omega_n = \mathbb{R}^d$. We must then prove for $\mathbf{x} \in \mathbb{R}^d$ fixed

$$\lim_{n\to+\infty} \mathbb{E}\big[\boldsymbol{\tau}_1(\mathbf{x}) : \boldsymbol{\Gamma}_0^\infty[\chi_n\boldsymbol{\tau}_2](\mathbf{x})\big] = \mathbf{P}_0 :: \mathbf{R}_{12}(\mathbf{0}) + \lim_{\delta\to0} \int_{\substack{\mathbf{r}\in\mathbb{R}^d \\ \|\mathbf{r}\|\geq\delta}} \boldsymbol{\Gamma}_0^\infty(\mathbf{r}) :: \mathbf{R}_{12}(\mathbf{r})\, \mathrm{d}V_{\mathbf{r}}, \quad \text{(B.12)}$$

where χ_n denotes the indicator function of Ω_n.

It can readily be verified that $\chi_n(\mathbf{x}) \to 1$ as $n \to +\infty$ for all $\mathbf{x} \in \mathbb{R}^d$. Fixing $\mathbf{x} \in \mathbb{R}^d$ and observing that the Ω_n form a growing sequence, it is possible to find $n_0 \in \mathbb{N}$ and $R_1 > 0$ such that the ball centered at $\mathbf{x}$, with radius R_1 is fully included in Ω_n for all $n \geq n_0$. From the general expression (2.24) of the Green operator

$$\begin{aligned}
\boldsymbol{\tau}_1(\mathbf{x}) : \boldsymbol{\Gamma}_0^\infty[\chi_n\boldsymbol{\tau}_2](\mathbf{x}) &= \boldsymbol{\tau}_1(\mathbf{x}) : \mathbf{P}_0 : \boldsymbol{\tau}_2(\mathbf{x}) \\
&\quad + \lim_{\delta\to0}\Big[\boldsymbol{\tau}_1(\mathbf{x}) : \int_{\|\mathbf{y}-\mathbf{x}\|\geq\delta} \chi_n(\mathbf{y})\, \boldsymbol{\Gamma}_0^\infty(\mathbf{y}-\mathbf{x}) : \boldsymbol{\tau}_2(\mathbf{y})\, \mathrm{d}V_{\mathbf{y}}\Big] \\
&= \mathbf{P}_0 :: \big[\boldsymbol{\tau}_1(\mathbf{x}) \otimes \boldsymbol{\tau}_2(\mathbf{x})\big] \\
&\quad + \lim_{\delta\to0}\Big[\int_{\|\mathbf{y}-\mathbf{x}\|\geq\delta} \chi_n(\mathbf{y})\, \boldsymbol{\Gamma}_0^\infty(\mathbf{y}-\mathbf{x}) :: \big[\boldsymbol{\tau}_1(\mathbf{x}) \otimes \boldsymbol{\tau}_2(\mathbf{y})\big]\, \mathrm{d}V_{\mathbf{y}}\Big],
\end{aligned} \quad \text{(B.13)}$$

for $n \geq n_0$. Taking the ensemble average

$$\mathbb{E}\big[\boldsymbol{\tau}_1(\mathbf{x}) : \boldsymbol{\Gamma}_0^\infty[\chi_n\boldsymbol{\tau}_2](\mathbf{x})\big] = \mathbf{P}_0 :: \mathbf{R}_{12}(\mathbf{0}) + \lim_{\delta\to0}\Big[\int_{\|\mathbf{y}-\mathbf{x}\|\geq\delta} \chi_n(\mathbf{y})\, \boldsymbol{\Gamma}_0^\infty(\mathbf{y}-\mathbf{x}) :: \mathbf{R}_{12}(\mathbf{y}-\mathbf{x})\, \mathrm{d}V_{\mathbf{y}}\Big], \quad \text{(B.14)}$$

and, introducing the new variable $\mathbf{r} = \mathbf{y} - \mathbf{x} = r\mathbf{n}$ ($\|\mathbf{n}\| = 1$)

$$\mathbb{E}\big[\boldsymbol{\tau}_1(\mathbf{x}) : \boldsymbol{\Gamma}_0^\infty[\chi_n\boldsymbol{\tau}_2](\mathbf{x})\big] = \mathbf{P}_0 :: \mathbf{R}_{12}(\mathbf{0}) + \lim_{\delta\to 0}\int_{\delta\le\|\mathbf{r}\|} \chi_n(\mathbf{x}+\mathbf{r})\,\boldsymbol{\Gamma}_0^\infty(\mathbf{r}) :: \mathbf{R}_{12}(\mathbf{r})\,\mathrm{d}V_{\mathbf{r}} \tag{B.15}$$

$$\begin{aligned} &= \mathbf{P}_0 :: \mathbf{R}_{12}(\mathbf{0}) + \lim_{\delta\to 0}\int_{\substack{\|\mathbf{n}\|=1\\ \delta\le r\le R_1}} \boldsymbol{\Gamma}_0^\infty(\mathbf{n}) :: \mathbf{R}_{12}(\mathbf{0})\,\frac{\mathrm{d}r}{r}\,\mathrm{d}S_{\mathbf{n}} \\ &\quad + \lim_{\delta\to 0}\int_{\substack{\|\mathbf{n}\|=1\\ \delta\le r\le R_1}} \boldsymbol{\Gamma}_0^\infty(\mathbf{n}) :: \big[\mathbf{R}_{12}(r\mathbf{n}) - \mathbf{R}_{12}(\mathbf{0})\big]\,\frac{\mathrm{d}r}{r}\,\mathrm{d}S_{\mathbf{n}} \\ &\quad + \int_{\|\mathbf{r}\|\ge R_1} \chi_n(\mathbf{x}+\mathbf{r})\,\boldsymbol{\Gamma}_0^\infty(\mathbf{r}) :: \mathbf{R}_{12}(\mathbf{r})\,\mathrm{d}V_{\mathbf{r}}. \end{aligned} \tag{B.16}$$

where the fact that $\boldsymbol{\Gamma}_0^\infty$ is homogeneous of degree $-d$ has been used. The second term in the above expression vanishes, since the isotropic average of the Green operator is null. In the third term, the integrand is regular owing to the differentiability of $\mathbf{R}_{12}$ at the origin. Therefore

$$\begin{aligned} \mathbb{E}\big[\boldsymbol{\tau}_1(\mathbf{x}) : \boldsymbol{\Gamma}_0^\infty[\chi_n\boldsymbol{\tau}_2](\mathbf{x})\big] &= \mathbf{P}_0 :: \mathbf{R}_{12}(\mathbf{0}) + \int_{\substack{\|\mathbf{n}\|=1\\ 0\le r\le R_1}} \boldsymbol{\Gamma}_0^\infty(\mathbf{n}) :: \big[\mathbf{R}_{12}(r\mathbf{n}) - \mathbf{R}_{12}(\mathbf{0})\big]\,\frac{\mathrm{d}r}{r}\,\mathrm{d}S_{\mathbf{n}} \\ &\quad + \int_{\|\mathbf{r}\|\ge R_1} \chi_n(\mathbf{x}+\mathbf{r})\,\boldsymbol{\Gamma}_0^\infty(\mathbf{r}) :: \mathbf{R}_{12}(\mathbf{r})\,\mathrm{d}V_{\mathbf{r}}. \end{aligned} \tag{B.17}$$

From the dominated convergence theorem, observing that $|\chi_n(\mathbf{x}+\mathbf{r})| \le 1$ and $\chi_n(\mathbf{x}+\mathbf{r}) \to 1$ as $n \to +\infty$ for all $\mathbf{r} \in \mathbb{R}^d$, the limit of the above expression as $n \to +\infty$ is readily evaluated

$$\begin{aligned} \lim_{n\to+\infty} \mathbb{E}\big[\boldsymbol{\tau}_1(\mathbf{x}) : \boldsymbol{\Gamma}_0^\infty[\chi_n\boldsymbol{\tau}_2](\mathbf{x})\big] &= \mathbf{P}_0 :: \mathbf{R}_{12}(\mathbf{0}) + \int_{\substack{\|\mathbf{n}\|=1\\ 0\le r\le R_1}} \boldsymbol{\Gamma}_0^\infty(\mathbf{n}) :: \big[\mathbf{R}_{12}(r\mathbf{n}) - \mathbf{R}_{12}(\mathbf{0})\big]\,\frac{\mathrm{d}r}{r}\,\mathrm{d}S_{\mathbf{n}} \\ &\quad + \int_{\|\mathbf{r}\|\ge R_1} \boldsymbol{\Gamma}_0^\infty(\mathbf{r}) :: \mathbf{R}_{12}(\mathbf{r})\,\mathrm{d}V_{\mathbf{r}}, \end{aligned} \tag{B.18}$$

provided that the last integral exists. The above expression shows that the seeked limit does not depend on the observation point $\mathbf{x}$. We can now retrace our steps through equations (B.16) and (B.15), successively, replacing $\chi_n(\mathbf{x}+\mathbf{r})$ with 1: equation (B.12) is then retrieved, and the proof is complete.

Bibliography

[AA92] B. Altan and E. Aifantis. “On the structure of the mode III crack-tip in gradient elasticity”. In: *Scripta Metallurgica et Materialia* 26.2 (1992), pp. 319–324.

[AA97] B. Altan and E. Aifantis. “On some aspects in the special theory of gradient elasticity”. In: *Journal of the Mechanical Behavior of Materials* 8.3 (1997), pp. 231–282.

[All+87] A. J. Allen, R. C. Oberthur, D. Pearson, P. Schofield, and C. R. Wilding. “Development of the fine porosity and gel structure of hydrating cement systems”. In: *Philosophical Magazine Part B* 56.3 (1987), pp. 263–288.

[ALR14] B. S. Anglin, R. A. Lebensohn, and A. D. Rollett. “Validation of a numerical method based on Fast Fourier Transforms for heterogeneous thermoelastic materials by comparison with analytical solutions”. In: *Computational Materials Science* 87.0 (2014), pp. 209–217.

[Arm15] G. Armstrong. “An introduction to polymer nanocomposites”. In: *European Journal of Physics* 36.6 (2015), p. 063001.

[ASI16] R. Atif, I. Shyha, and F. Inam. “Mechanical, thermal, and electrical properties of graphene-epoxy nanocomposites – A Review”. In: *Polymers* 8.8 (2016), p. 281.

[AT87] M. P. Allen and D. J. Tildesley. *Computer simulation of liquids*. Oxford Science Publications, 1987.

[Aze+13] A. A. Azeez, K. Y. Rhee, S. J. Park, and D. Hui. “Epoxy clay nanocomposites – processing, properties and applications: A review”. In: *Composites Part B: Engineering* 45.1 (2013), pp. 308–320.

[Bar+94] R. Barrett, M. Berry, T. Chan, J. Demmel, J. Donato, J. Dongarra, V. Eijkhout, R. Pozo, C. Romine, and H. van der Vorst. *Templates for the Solution of Linear Systems: Building Blocks for Iterative Methods*. Society for Industrial and Applied Mathematics, 1994.

[BD10] S. Brisard and L. Dormieux. “FFT-based methods for the mechanics of composites: A general variational framework”. In: *Computational Materials Science* 49.3 (2010), pp. 663–671.

[BD12] S. Brisard and L. Dormieux. “Combining Galerkin approximation techniques with the principle of Hashin and Shtrikman to derive a new FFT-based numerical method for the homogenization of composites”. In: *Computer Methods in Applied Mechanics and Engineering* 217-220.0 (2012), pp. 197–212.

[BD14] F. Bignonnet and L. Dormieux. “FFT-based bounds on the permeability of complex microstructures”. In: *International Journal for Numerical and Analytical Methods in Geomechanics* 38.16 (2014), pp. 1707–1723.

[BDC91] Y. Benveniste, G. Dvorak, and T. Chen. “On diagonal and elastic symmetry of the approximate effective stiffness tensor of heterogeneous media”. In: *Journal of the Mechanics and Physics of Solids* 39.7 (1991), pp. 927–946.

[BDK10a] S. Brisard, L. Dormieux, and D. Kondo. “Hashin–Shtrikman bounds on the bulk modulus of a nanocomposite with spherical inclusions and interface effects”. In: *Computational Materials Science* 48.3 (2010), pp. 589–596.

[BDK10b] S. Brisard, L. Dormieux, and D. Kondo. “Hashin–Shtrikman bounds on the shear modulus of a nanocomposite with spherical inclusions and interface effects”. In: *Computational Materials Science* 50.2 (2010), pp. 403–410.

[BDS13] S. Brisard, L. Dormieux, and K. Sab. *Self-influence and influence pseudotensors of d-dimensional spheres*. Tech. rep. Oct. 2013, p. 53.

[BDS14] S. Brisard, L. Dormieux, and K. Sab. “A variational form of the equivalent inclusion method for numerical homogenization”. In: *International Journal of Solids and Structures* 51.3-4 (2014), pp. 716–728.

[Ben87] Y. Benveniste. “A new approach to the application of Mori–Tanaka’s theory in composite materials”. In: *Mechanics of Materials* 6.2 (1987), pp. 147–157.

[BFH87] M. Berveiller, O. Fassifehri, and A. Hihi. “The problem of two plastic and heterogeneous inclusions in an anisotropic medium”. In: *International Journal of Engineering Science* 25.6 (1987), pp. 691–709.

[BG17] S. Brisard and S. Ghabezloo. “Variational estimates of the poroelastic coefficients”. In: *Proceedings of the 6th Biot Conference on Poromechanics*. Ed. by ASCE. 2017.

[BG18] S. Brisard and S. Ghabezloo. “Variational estimates of the eigenstrain influence tensors”. In: — (2018). In preparation.

[Bha16] M. Bhattacharya. “Polymer Nanocomposites – A Comparison between Carbon Nanotubes, Graphene, and Clay as Nanofillers”. In: *Materials* 9.4 (2016), p. 262.

[Big+14] F. Bignonnet, K. Sab, L. Dormieux, S. Brisard, and A. Bisson. “Macroscopically consistent non-local modeling of heterogeneous media”. In: *Computer Methods in Applied Mechanics and Engineering* 278.0 (2014), pp. 218–238.

[BL13] S. Brisard and P. Levitz. “Small-angle scattering of dense, polydisperse granular porous media: Computation free of size effects”. In: *Physical Review E* 87.1 (2013), p. 013305.

[BLL16] X. Blanc, C. Le Bris, and F. Legoll. “Some variance reduction methods for numerical stochastic homogenization”. In: *Philosophical Transactions of the Royal Society of London A: Mathematical, Physical and Engineering Sciences* 374.2066 (2016).

[BLR06] B. Benedikt, M. Lewis, and P. Rangaswamy. "On elastic interactions between spherical inclusions by the equivalent inclusion method". In: *Computational Materials Science* 37.3 (2006), pp. 380–392.

[BM66] M. J. Beran and J. Molyneux. "Use of classical variational principles to determine bounds for the effective bulk modulus in heterogeneous media". In: *Quarterly of Applied Mathematics* 24.2 (1966), pp. 107–118.

[Bor+01] M. Bornert, R. Masson, P. Ponte Castañeda, and A. Zaoui. "Second-order estimates for the effective behaviour of viscoplastic polycrystalline materials". In: *Journal of the Mechanics and Physics of Solids* 49.11 (2001), pp. 2737–2764.

[Bri+12] S. Brisard, R. S. Chae, I. Bihannic, L. Michot, P. Guttmann, J. Thieme, G. Schneider, P. J. M. Monteiro, and P. Levitz. "Morphological quantification of hierarchical geomaterials by X-ray nano-CT bridges the gap from nano to micro length scales". In: *American Mineralogist* 97.2 (2012), pp. 480–483.

[Bri11] S. Brisard. "Morphological analysis and numerical homogenization: application to cement paste". Theses. Université Paris-Est, Jan. 2011.

[Bri17a] S. Brisard. "Reconstructing displacements from the solution to the periodic Lippmann–Schwinger equation discretized on a uniform grid". In: *International Journal for Numerical Methods in Engineering* 109.4 (2017), pp. 459–486.

[Bri17b] S. Brisard. "Towards improved Hashin–Shtrikman bounds on the effective moduli of random composites". In: *Mechanics & Industry* 18.2 (2017), p. 214.

[Bro55] W. F. J. Brown. "Solid Mixture Permittivities". In: *The Journal of Chemical Physics* 23.8 (1955), pp. 1514–1517.

[BSD13] S. Brisard, K. Sab, and L. Dormieux. "New boundary conditions for the computation of the apparent stiffness of statistical volume elements". In: *Journal of the Mechanics and Physics of Solids* 61.12 (2013), pp. 2638–2658.

[BSK81] I. Babuška, B. A. Szabo, and I. N. Katz. "The *p*-version of the finite element method". In: *SIAM Journal on Numerical Analysis* 18.3 (1981), pp. 515–545.

[BSZ96] M. Bornert, C. Stolz, and A. Zaoui. "Morphologically representative pattern-based bounding in elasticity". In: *Journal of the Mechanics and Physics of Solids* 44.3 (1996), pp. 307–331.

[Bur07] V. A. Buryachenko. *Micromechanics of Heterogeneous Materials*. Springer, 2007.

[Can+15] É. Cancès, V. Ehrlacher, F. Legoll, and B. Stamm. "An embedded corrector problem to approximate the homogenized coefficients of an elliptic equation". In: *Comptes Rendus Mathematique* 353.9 (2015), pp. 801–806.

[Can+18] É. Cancés, V. Ehrlacher, F. Legoll, and B. Stamm. "An embedded corrector problem for homogenization — Part II: Numerical method". In: (2018). In preparation.

[CB09] O. Coussy and S. Brisard. "Prediction of drying shrinkage beyond the pore isodeformation". In: *Journal of Mechanics of Materials and Structures* 4.2 (2009), pp. 263–279.

[CD02] X. Chateau and L. Dormieux. “Micromechanics of saturated and unsaturated porous media”. In: *International Journal for Numerical and Analytical Methods in Geomechanics* 26.8 (2002), pp. 831–844.

[Che+15] L. Chen, J. Chen, R. Lebensohn, Y. Ji, T. Heo, S. Bhattacharyya, K. Chang, S. Mathaudhu, Z. Liu, and L.-Q. Chen. “An integrated fast Fourier transform-based phase-field and crystal plasticity approach to model recrystallization of three dimensional polycrystals”. In: *Computer Methods in Applied Mechanics and Engineering* 285 (2015), pp. 829–848.

[Chi+05] N. Chisholm, H. Mahfuz, V. K. Rangari, A. Ashfaq, and S. Jeelani. “Fabrication and mechanical characterization of carbon/SiC-epoxy nanocomposites”. In: *Composite Structures* 67.1 (2005), pp. 115–124.

[CJS06] J. Cho, M. Joshi, and C. Sun. “Effect of inclusion size on mechanical properties of polymeric composites with micro and nano particles”. In: *Composites Science and Technology* 66.13 (2006), pp. 1941–1952.

[Cou10] O. Coussy. *Mechanics and Physics of Porous Solids*. The Atrium, Southern Gate, Chichester, West Sussex, PO19 8SQ, United Kingdom: John Wiley & Sons, Ltd, 2010.

[CT65] J. W. Cooley and J. W. Tukey. “An algorithm for the machine calculation of complex Fourier series”. In: *Mathematics of Computation* 19.90 (1965), pp. 297–301.

[CWE16] N. Challamel, C. M. Wang, and I. Elishakoff. “Nonlocal or gradient elasticity macroscopic models: A question of concentrated or distributed microstructure”. In: *Mechanics Research Communications* 71 (2016), pp. 25–31.

[DAB57] P. Debye, H. R. Anderson Jr., and H. Brumberger. “Scattering by an Inhomogeneous Solid. II. The Correlation Function and Its Application”. In: *Journal of Applied Physics* 28.6 (1957), pp. 679–683.

[Dav+14] D. Davydov, E. Voyiatzis, G. Chatzigeorgiou, S. Liu, P. Steinmann, M. C. Böhm, and F. Müller-Plathe. “Size Effects in a Silica-Polystyrene Nanocomposite: Molecular Dynamics and Surface-enhanced Continuum Approaches”. In: *Soft Materials* 12.sup1 (2014), S142–S151.

[DB92] G. J. Dvorak and Y. Benveniste. “On Transformation Strains and Uniform Fields in Multiphase Elastic Media”. In: *Proceedings of the Royal Society of London A: Mathematical, Physical and Engineering Sciences* 437.1900 (1992), pp. 291–310.

[DKU06] L. Dormieux, D. Kondo, and F.-J. Ulm. “A micromechanical analysis of damage propagation in fluid-saturated cracked media”. In: *Comptes Rendus Mécanique* 334.7 (2006), pp. 440–446.

[Dua+05] H. L. Duan, J. Wang, Z. P. Huang, and B. L. Karihaloo. “Size-dependent effective elastic constants of solids containing nano-inhomogeneities with interface stress”. In: *Journal of the Mechanics and Physics of Solids* 53.7 (2005), pp. 1574–1596.

[EG04] A. Ern and J.-L. Guermond. *Theory and Practice of Finite Elements*. 1st ed. Vol. 159. Applied Mathematical Sciences. New York: Springer-Verlag, 2004.

[Eis+13] P. Eisenlohr, M. Diehl, R. Lebensohn, and F. Roters. "A spectral method solution to crystal elasto-viscoplasticity at finite strains". In: *International Journal of Plasticity* 46 (2013), pp. 37–53.

[El 15] Y. El Assami. "Homogénéisation en viscoélasticité linéaire non-vieillissante par la méthode de l'inclusion équivalente : application aux matériaux cimentaires". Thèse de doctorat. Université Paris-Est, May 2015.

[EM99] D. J. Eyre and G. W. Milton. "A fast numerical scheme for computing the response of composites using grid refinement". In: *European Physical Journal-Applied Physics* 6.1 (1999). Progress in Electromagnetics Research Symposium (PIERS 98), NANTES, FRANCE, JUL 13-17, 1998, pp. 41–47.

[Esh57] J. D. Eshelby. "The Determination of the Elastic Field of an Ellipsoidal Inclusion, and Related Problems". In: *Proceedings of the Royal Society of London. Series A, Mathematical and Physical Sciences* 241.1226 (1957), pp. 376–396.

[FA10] S. Forest and E. C. Aifantis. "Some links between recent gradient thermo-elasto-plasticity theories and the thermomechanics of generalized continua". In: *International Journal of Solids and Structures* 47.25–26 (2010), pp. 3367–3376.

[Fer91] M. Ferrari. "Asymmetry and the high concentration limit of the Mori-Tanaka effective medium theory". In: *Mechanics of Materials* 11.3 (1991), pp. 251–256.

[FGS02] C. Fond, S. Géhant, and R. Schirrer. "Effects of mechanical interactions on the hydrostatic stress in randomly distributed rubber particles in an amorphous polymer matrix". In: *Polymer* 43.3 (2002), pp. 909–919.

[Fon+01] C. Fond, A. Riccardi, R. Schirrer, and F. Montheillet. "Mechanical interaction between spherical inhomogeneities: an assessment of a method based on the equivalent inclusion". In: *European Journal of Mechanics - A/Solids* 20.1 (2001), pp. 59–75.

[FP03] T. Fornes and D. Paul. "Modeling properties of nylon 6/clay nanocomposites using composite theories". In: *Polymer* 44.17 (2003), pp. 4993–5013.

[FPS01] S. Forest, F. Pradel, and K. Sab. "Asymptotic analysis of heterogeneous Cosserat media". In: *International Journal of Solids and Structures* 38.26–27 (2001), pp. 4585–4608.

[FS12] S. Forest and K. Sab. "Stress gradient continuum theory". In: *Mechanics Research Communications* 40.0 (2012), pp. 16–25.

[GBN06] S. Garrault, T. Behr, and A. Nonat. "Formation of the C-S-H Layer during Early Hydration of Tricalcium Silicate Grains with Different Sizes". In: *The Journal of Physical Chemistry B* 110.1 (2006), pp. 270–275.

[Geu+17] T. de Geus, J. Vondřejc, J. Zeman, R. Peerlings, and M. Geers. "Finite strain FFT-based non-linear solvers made simple". In: *Computer Methods in Applied Mechanics and Engineering* 318 (2017), pp. 412–430.

[GM13] L. Gélébart and R. Mondon-Cancel. “Non-linear extension of FFT-based methods accelerated by conjugate gradients to evaluate the mechanical behavior of composite materials”. In: *Computational Materials Science* 77.0 (2013), pp. 430–439.

[GM75] M. E. Gurtin and A. I. Murdoch. “A continuum theory of elastic material surfaces”. In: *Archive for Rational Mechanics and Analysis* 57.4 (1975), pp. 291–323.

[GM78] M. E. Gurtin and A. I. Murdoch. “Surface stress in solids”. In: *International Journal of Solids and Structures* 14.6 (1978), pp. 431–440.

[GNO15] A. Gloria, S. Neukamm, and F. Otto. “Quantification of ergodicity in stochastic homogenization: optimal bounds via spectral gap on Glauber dynamics”. In: *Inventiones mathematicae* 199.2 (2015), pp. 455–515.

[GO15a] L. Gélébart and F. Ouaki. “Filtering material properties to improve FFT-based methods for numerical homogenization”. In: *Journal of Computational Physics* 294 (2015), pp. 90–95.

[GO15b] A. Gloria and F. Otto. “Quantitative estimates on the periodic approximation of the corrector in stochastic homogenization”. In: *ESAIM: Proc.* 48 (2015), pp. 80–97.

[GP07] X.-L. Gao and S. Park. “Variational formulation of a simplified strain gradient elasticity theory and its application to a pressurized thick-walled cylinder problem”. In: *International Journal of Solids and Structures* 44.22–23 (2007), pp. 7486–7499.

[Has02] Z. Hashin. “Thin interphase/imperfect interface in elasticity with application to coated fiber composites”. In: *Journal of the Mechanics and Physics of Solids* 50.12 (2002), pp. 2509–2537.

[Has62] Z. Hashin. “The Elastic Moduli of Heterogeneous Materials”. In: *Journal of Applied Mechanics* 29.1 (1962), pp. 143–150.

[Hil63] R. Hill. “Elastic properties of reinforced solids: Some theoretical principles”. In: *Journal of the Mechanics and Physics of Solids* 11.5 (1963), pp. 357–372.

[HJ13] C.-Y. Hui and A. Jagota. “Surface Tension, Surface Energy, and Chemical Potential Due to Their Difference”. In: *Langmuir* 29.36 (2013), pp. 11310–11316.

[HS62a] Z. Hashin and S. Shtrikman. “A variational approach to the theory of the elastic behaviour of polycrystals”. In: *Journal of the Mechanics and Physics of Solids* 10.4 (1962), pp. 343–352.

[HS62b] Z. Hashin and S. Shtrikman. “On some variational principles in anisotropic and nonhomogeneous elasticity”. In: *Journal of the Mechanics and Physics of Solids* 10.4 (1962), pp. 335–342.

[Hue90] C. Huet. “Application of variational concepts to size effects in elastic heterogeneous bodies”. In: *Journal of the Mechanics and Physics of Solids* 38.6 (1990), pp. 813–841.

[Jen00] H. M. Jennings. “A model for the microstructure of calcium silicate hydrate in cement paste”. In: *Cement and Concrete Research* 30.1 (2000), pp. 101–116.

[Jen08] H. M. Jennings. “Refinements to colloid model of C–S–H in cement: CM–II”. In: *Cement and Concrete Research* 38.3 (2008), pp. 275–289.

[Kan+03] T. Kanit, S. Forest, I. Galliet, V. Mounoury, and D. Jeulin. “Determination of the size of the representative volume element for random composites: statistical and numerical approach”. In: *International Journal of Solids and Structures* 40.13-14 (2003), pp. 3647–3679.

[KBS14] M. Kabel, T. Böhlke, and M. Schneider. “Efficient fixed point and Newton–Krylov solvers for FFT-based homogenization of elasticity at large deformations”. In: *Computational Mechanics* 54.6 (2014), pp. 1497–1514.

[KFS15] M. Kabel, S. Fliegener, and M. Schneider. “Mixed boundary conditions for FFT-based homogenization at finite strains”. In: *Computational Mechanics* 57.2 (2015), pp. 193–210.

[Kha+17a] M. H. Khalili, S. Brisard, M. Bornert, P. Aimedieu, J.-M. Pereira, and J.-N. Roux. “Discrete Digital Projections Correlation: A Reconstruction-Free Method to Quantify Local Kinematics in Granular Media by X-ray Tomography”. In: *Experimental Mechanics* (2017), pp. 1–12.

[Kha+17b] M. H. Khalili, J.-N. Roux, J.-M. Pereira, S. Brisard, and M. Bornert. “Numerical study of one-dimensional compression of granular materials. I. Stress-strain behavior, microstructure, and irreversibility”. In: *Physical Review E* 95 (3 2017), p. 032907.

[Kha+17c] M. H. Khalili, J.-N. Roux, J.-M. Pereira, S. Brisard, and M. Bornert. “Numerical study of one-dimensional compression of granular materials. II. Elastic moduli, stresses, and microstructure”. In: *Physical Review E* 95 (3 2017), p. 032908.

[KL08] S. K. Kanaun and V. M. Levin. *Self-Consistent Methods for Composites Vol.1: Static Problems*. Vol. 148. Solid Mechanics and its Applications. Springer, 2008.

[KMS15] M. Kabel, D. Merkert, and M. Schneider. “Use of composite voxels in FFT-based homogenization”. In: *Computer Methods in Applied Mechanics and Engineering* 294 (2015), pp. 168–188.

[Kor73] J. Korringa. “Theory of elastic constants of heterogeneous media”. In: *Journal of Mathematical Physics* 14.4 (1973), pp. 509–513.

[Krö74] E. Kröner. “On the Physics and Mathematics of Self-Stresses”. In: *Topics in Applied Continuum Mechanics*. Ed. by J. L. Zeman and F. Ziegler. Springer Verlag Wien, 1974, pp. 22–38.

[Lav+15] K. Lavergne F. and. Sab, J. Sanahuja, M. Bornert, and C. Toulemonde. “Estimation of creep strain and creep failure of a glass reinforced plastic by semi-analytical methods and 3D numerical simulations”. In: *Mechanics of Materials* 89 (2015), pp. 130–150.

[Lev98] P. Levitz. "Off-lattice reconstruction of porous media: critical evaluation, geometrical confinement and molecular transport". In: *Advances in Colloid and Interface Science* 76–77 (1998), pp. 71–106.

[LH07] H. Le Quang and Q.-C. He. "Size-dependent effective thermoelastic properties of nanocomposites with spherically anisotropic phases". In: *Journal of the Mechanics and Physics of Solids* 55.9 (2007), pp. 1889–1921.

[LH08] H. Le Quang and Q.-C. He. "Variational principles and bounds for elastic inhomogeneous materials with coherent imperfect interfaces". In: *Mechanics of Materials* 40.10 (2008), pp. 865–884.

[LKE12] R. A. Lebensohn, A. K. Kanjarla, and P. Eisenlohr. "An elasto-viscoplastic formulation based on fast Fourier transforms for the prediction of micromechanical fields in polycrystalline materials". In: *International Journal of Plasticity* 32-33 (2012), pp. 59–69.

[LL83] P. Ladevèze and D. Leguillon. "Error Estimate Procedure in the Finite Element Method and Applications". In: *SIAM Journal on Numerical Analysis* 20.3 (1983), pp. 485–509.

[LM15] F. Legoll and W. Minvielle. "A Control Variate Approach Based on a Defect-Type Theory for Variance Reduction in Stochastic Homogenization". In: *Multiscale Modeling & Simulation* 13.2 (2015), pp. 519–550.

[LP05] P. Ladevèze and J.-P. Pelle. *Mastering Calculations in Linear and Nonlinear Mechanics*. Mechanical Engineering Series. New York: Springer-Verlag, 2005.

[MA04] P. Müller and S. Andrés. "Elastic effects on surface physics". In: *Surface Science Reports* 54.5-8 (2004), pp. 157–258.

[Mak14] L. Makkonen. "Misconceptions of the Relation between Surface Energy and Surface Tension on a Solid". In: *Langmuir* 30.9 (2014), pp. 2580–2581.

[May+16] N. Mayercsik, S. Brisard, M. Vandamme, and K. Kurtis. "Using Fractal Geometry to Recover the 3D Air Void, Scale-Independent, Microstructure Information From 2D Sections of Mortars". In: *Advances in Civil Engineering Materials* 5.2 (2016), pp. 1–21.

[MB12] V. Monchiet and G. Bonnet. "A polarization-based FFT iterative scheme for computing the effective properties of elastic composites with arbitrary contrast". In: *International Journal for Numerical Methods in Engineering* 89.11 (2012), pp. 1419–1436.

[McC70] J. McCoy. *On the displacement field in an elastic medium with random variation of material properties*. Vol. 5. Recent Advances in Engineering Sciences. New York: Gordon and Breach, 1970.

[MG14] H. Ma and X.-L. Gao. "A new homogenization method based on a simplified strain gradient elasticity theory". In: *Acta Mechanica* 225.4-5 (2014), pp. 1075–1091.

[Mil02] G. W. Milton. *The Theory of Composites*. Cambridge Monographs on Applied and Computational Mathematics. Cambridge University Press, 2002.

[Mil81] G. Milton. "Bounds on the Electromagnetic, Elastic, and Other Properties of Two-Component Composites". In: *Physical Review Letters* 46.8 (1981), pp. 542–545.

[Mil82] G. Milton. "Bounds on the elastic and transport properties of two-component composites". In: *Journal of the Mechanics and Physics of Solids* 30.3 (1982), pp. 177–191.

[Min64] R. D. Mindlin. "Micro-structure in linear elasticity". In: *Archive for Rational Mechanics and Analysis* 16.1 (1964), pp. 51–78.

[Mit+15] G. Mittal, V. Dhand, K. Y. Rhee, S.-J. Park, and W. R. Lee. "A review on carbon nanotubes and graphene as fillers in reinforced polymer nanocomposites". In: *Journal of Industrial and Engineering Chemistry* 21 (2015), pp. 11–25.

[MK88] G. W. Milton and R. V. Kohn. "Variational bounds on the effective moduli of anisotropic composites". In: *Journal of the Mechanics and Physics of Solids* 36.6 (1988), pp. 597–629.

[MM75] Z. A. Moschovidis and T. Mura. "Two-ellipsoidal inhomogeneities by the equivalent inclusion method". In: *Journal of Applied Mechanics* 42.4 (1975), pp. 847–852.

[MMS01] J. C. Michel, H. Moulinec, and P. Suquet. "A computational scheme for linear and non-linear composites with arbitrary phase contrast". In: *International Journal for Numerical Methods in Engineering* 52.1–2 (2001), pp. 139–160.

[Mon+] M. Montagnat, O. Castelnau, P. Bons, S. Faria, O. Gagliardini, et al. "Multiscale modeling of ice deformation behavior". In: *Journal of Structural Geology* 61 (). Microdynamics of Ice, pp. 78–108.

[MP82] G. W. Milton and N. Phan-Thien. "New Bounds on Effective Elastic Moduli of Two-Component Materials". In: *Proceedings of the Royal Society of London A: Mathematical, Physical and Engineering Sciences* 380.1779 (1982), pp. 305–331.

[MS14] H. Moulinec and F. Silva. "Comparison of three accelerated FFT-based schemes for computing the mechanical response of composite materials". In: *International Journal for Numerical Methods in Engineering* 97.13 (2014), pp. 960–985.

[MS94] H. Moulinec and P. Suquet. "A fast numerical method for computing the linear and nonlinear properties of composites". In: *Comptes-rendus de l'Académie des sciences série II* 318.11 (1994), pp. 1417–1423.

[MS98] H. Moulinec and P. Suquet. "A numerical method for computing the overall response of nonlinear composites with complex microstructure". In: *Computer Methods in Applied Mechanics and Engineering* 157.1-2 (1998), pp. 69–94.

[MT73] T. Mori and K. Tanaka. “Average stress in matrix and average elastic energy of materials with misfitting inclusions”. In: *Acta Metallurgica* 21.5 (1973), pp. 571–574.

[MVH17] C. Morin, V. Vass, and C. Hellmich. “Micromechanics of elastoplastic porous polycrystals: Theory, algorithm, and application to osteonal bone”. In: *International Journal of Plasticity* 91 (2017), pp. 238–267.

[MVZ16] N. Mishra, J. Vondřejc, and J. Zeman. “A comparative study on low-memory iterative solvers for FFT-based homogenization of periodic media”. In: *Journal of Computational Physics* 321 (2016), pp. 151–168.

[MW91] A. M. Memari and H. H. West. “Computation of bridge design forces from influence surfaces”. In: *Computers & Structures* 38.5-6 (1991), pp. 547–556.

[Nol14] J. Nolen. “Normal approximation for a random elliptic equation”. In: *Probability Theory and Related Fields* 159.3 (2014), pp. 661–700.

[NSB09] T.-K. Nguyen, K. Sab, and G. Bonnet. “Bounds for the effective properties of heterogeneous plates”. In: *European Journal of Mechanics - A/Solids* 28.6 (2009), pp. 1051–1063.

[OCG05] G. Odegard, T. Clancy, and T. Gates. “Modeling of the mechanical properties of nanoparticle/polymer composites”. In: *Polymer* 46.2 (2005), pp. 553–562.

[Ost06] M. Ostoja-Starzewski. “Material spatial randomness: From statistical to representative volume element”. In: *Probabilistic Engineering Mechanics* 21.2 (2006), pp. 112–132.

[Pal15] P. Palmero. “Structural Ceramic Nanocomposites: A Review of Properties and Powders’ Synthesis Methods”. In: *Nanomaterials* 5.2 (2015), pp. 656–696.

[PH10] B. Pichler and C. Hellmich. “Estimation of Influence Tensors for Eigenstressed Multiphase Elastic Media with Nonaligned Inclusion Phases of Arbitrary Ellipsoidal Shape”. In: *Journal of Engineering Mechanics* 136.8 (2010), pp. 1043–1053.

[Pol14] C. Polizzotto. “Stress gradient versus strain gradient constitutive models within elasticity”. In: *International Journal of Solids and Structures* 51.9 (2014), pp. 1809–1818.

[Pon16] P. Ponte Castañeda. “Stationary variational estimates for the effective response and field fluctuations in nonlinear composites”. In: *Journal of the Mechanics and Physics of Solids* 96 (2016), pp. 660–682.

[Pon91] P. Ponte Castañeda. “The effective mechanical properties of nonlinear isotropic composites”. In: *Journal of the Mechanics and Physics of Solids* 39.1 (1991), pp. 45–71.

[Por82] G. Porod. “General Theory”. In: *Small angle X-ray scattering*. Ed. by O. Glatter and O. Kratky. Academic Press, 1982. Chap. 2, pp. 17–51.

[PP17] B. Peigney and M. Peigney. “Bounds for nonlinear composite conductors via the translation method”. In: *Journal of the Mechanics and Physics of Solids* 101 (2017), pp. 93–117.

[PW95] P. Ponte Castañeda and J. R. Willis. “The effect of spatial distribution on the effective behavior of composite materials and cracked media”. In: *Journal of the Mechanics and Physics of Solids* 43.12 (1995), pp. 1919–1951.

[Rey+01] E. Reynaud, T. Jouen, C. Gauthier, G. Vigier, and J. Varlet. “Nanofillers in polymeric matrix: a study on silica reinforced PA6”. In: *Polymer* 42.21 (2001), pp. 8759–8768.

[RH91] G. J. Rodin and Y.-L. Hwang. “On the problem of linear elasticity for an infinite region containing a finite number of non-intersecting spherical inhomogeneities”. In: *International Journal of Solids and Structures* 27.2 (1991), pp. 145–159.

[Ric04] I. G. Richardson. “Tobermorite/jennite- and tobermorite/calcium hydroxide-based models for the structure of C–S–H: applicability to hardened pastes of tricalcium silicate, beta-dicalcium silicate, Portland cement, and blends of Portland cement with blast-furnace slag, metakaolin, or silica fume”. In: *Cement and Concrete Research* 34.9 (2004), pp. 1733–1777.

[RT95] A. P. Roberts and M. Teubner. “Transport properties of heterogeneous materials derived from Gaussian random fields: Bounds and simulation”. In: *Physical Review E* 51.5 (1995), pp. 4141–4154.

[Sab92] K. Sab. “On the homogenization and the simulation of random materials”. In: *European Journal of Mechanics - A/Solids* 11.5 (1992), pp. 585–607.

[ŠB10] V. Šmilauer and Z. P. Bažant. “Identification of viscoelastic C–S–H behavior in mature cement paste by FFT-based homogenization method”. In: *Cement and Concrete Research* 40.2 (2010), pp. 197–207.

[Sch15] M. Schneider. “Convergence of FFT-based homogenization for strongly heterogeneous media”. In: *Mathematical Methods in the Applied Sciences* 38.13 (2015), pp. 2761–2778.

[Sch17] M. Schneider. “An FFT-based fast gradient method for elastic and inelastic unit cell homogenization problems”. In: *Computer Methods in Applied Mechanics and Engineering* 315 (2017), pp. 846–866.

[SDR04] B. Szabó, A. Düster, and E. Rank. “The *p*-Version of the Finite Element Method”. In: *Encyclopedia of Computational Mechanics*. Ed. by E. Stein, R. De Borst, and T. J. R. Hugues. John Wiley & Sons, Ltd, 2004. Chap. 5, pp. 119–139.

[SDS09] E. A. Stefanescu, C. Daranga, and C. Stefanescu. “Insight into the Broad Field of Polymer Nanocomposites: From Carbon Nanotubes to Clay Nanoplatelets, via Metal Nanoparticles”. In: *Materials* 2.4 (2009), pp. 2095–2153.

[She05] V. B. Shenoy. “Atomistic calculations of elastic properties of metallic fcc crystal surfaces”. In: *Physical Review B* 71 (9 2005), p. 094104.

[Shu50] R. Shuttleworth. "The Surface Tension of Solids". In: *Proceedings of the Physical Society. Section A* 63.5 (1950), p. 444.

[SLF16] K. Sab, F. Legoll, and S. Forest. "Stress Gradient Elasticity Theory: Existence and Uniqueness of Solution". In: *Journal of Elasticity* 123.2 (2016), pp. 179–201.

[SMK17] M. Schneider, D. Merkert, and M. Kabel. "FFT-based homogenization for microstructures discretized by linear hexahedral elements". In: *International Journal for Numerical Methods in Engineering* 109.10 (2017), pp. 1461–1489.

[SOK15] M. Schneider, F. Ospald, and M. Kabel. "Computational homogenization of elasticity on a staggered grid". In: *International Journal for Numerical Methods in Engineering* (2015).

[SP01] J. Schjødt-Thomsen and R. Pyrz. "The Mori–Tanaka stiffness tensor: diagonal symmetry, complex fibre orientations and non-dilute volume fractions". In: *Mechanics of Materials* 33.10 (2001), pp. 531–544.

[Suq90] P. Suquet. "A simplified method for the prediction of homogenized elastic properties of composites with a periodic structure". In: *Comptes-rendus de l'Académie des sciences série II* 311.7 (1990), pp. 769–774.

[TBH16] Q.-D. To, G. Bonnet, and D.-H. Hoang. "Explicit effective elasticity tensors of two-phase periodic composites with spherical or ellipsoidal inclusions". In: *International Journal of Solids and Structures* 94-95 (2016), pp. 100–111.

[Tor02] S. Torquato. *Random Heterogeneous Materials*. Vol. 16. Interdisciplinary Applied Mathematics. New York: Springer, 2002.

[Tor97] S. Torquato. "Effective stiffness tensor of composite media–I. Exact series expansions". In: *Journal of the Mechanics and Physics of Solids* 45.9 (1997), pp. 1421–1448.

[Tra+11] A. B. Tran, J. Yvonnet, Q.-C. He, C. Toulemonde, and J. Sanahuja. "A multiple level set approach to prevent numerical artefacts in complex microstructures with nearby inclusions within XFEM". In: *International Journal for Numerical Methods in Engineering* 85.11 (2011), pp. 1436–1459.

[Tra+16] V.-P. Tran, J. Guilleminot, S. Brisard, and K. Sab. "Stochastic modeling of mesoscopic elasticity random field". In: *Mechanics of Materials* 93 (2016), pp. 1–12.

[Tra+18a] V. P. Tran, S. Brisard, J. Guilleminot, and K. Sab. "Homogenization of stress-gradient materials — Part I: a simplified material model". In: — (2018). In preparation.

[Tra+18b] V. P. Tran, S. Brisard, J. Guilleminot, and K. Sab. "Homogenization of stress-gradient materials — Part II: Mori–Tanaka estimates". In: — (2018). In preparation.

[Tra16] V. P. Tran. "Modélisation à plusieurs échelles d'un milieu continu hétérogène aléatoire". PhD thesis. Université Paris-Est, École doctorale SIE, Oct. 2016.

[UCH04] F. Ulm, G. Constantinides, and F. Heukamp. “Is concrete a poromechanics materials?–A multiscale investigation of poroelastic properties”. In: *Materials and Structures* 37 (1 2004), pp. 43–58.

[Vin+14] P.-G. Vincent, P. Suquet, Y. Monerie, and H. Moulinec. “Effective flow surface of porous materials with two populations of voids under internal pressure: II. Full-field simulations”. In: *International Journal of Plasticity* 56 (2014), pp. 74–98.

[Von16] J. Vondřejc. “Improved guaranteed computable bounds on homogenized properties of periodic media by the Fourier–Galerkin method with exact integration”. In: *International Journal for Numerical Methods in Engineering* 107.13 (2016), pp. 1106–1135.

[VW72] L. Verlet and J.-J. Weis. “Equilibrium Theory of Simple Liquids”. In: *Physical Review A* 5.2 (1972), pp. 939–952.

[VZM14] J. Vondřejc, J. Zeman, and I. Marek. “An FFT-based Galerkin method for homogenization of periodic media”. In: *Computers & Mathematics with Applications* 68.3 (2014), pp. 156–173.

[VZM15] J. Vondřejc, J. Zeman, and I. Marek. “Guaranteed upper–lower bounds on homogenized properties by FFT-based Galerkin method”. In: *Computer Methods in Applied Mechanics and Engineering* 297 (2015), pp. 258–291.

[WAP14] F. Willot, B. Abdallah, and Y.-P. Pellegrini. “Fourier-based schemes with modified Green operator for computing the electrical response of heterogeneous media with accurate local fields”. In: *International Journal for Numerical Methods in Engineering* 98.7 (2014), pp. 518–533.

[WBH99] J. Widjajakusuma, B. Biswal, and R. Hilfer. “Quantitative prediction of effective material properties of heterogeneous media”. In: *Computational Materials Science* 16.1–4 (1999), pp. 70–75.

[Wil01] J. R. Willis. “Lectures on mechanics of random media”. In: *Mechanics of random and multiscale microstructures*. Ed. by D. Jeulin and M. Ostoja–Starzewski. CISM courses and lectures 430. Springer, 2001, pp. 221–267.

[Wil15] F. Willot. “Fourier-based schemes for computing the mechanical response of composites with accurate local fields”. In: *Comptes Rendus Mécanique* 343.3 (2015), pp. 232–245.

[Wil77] J. R. Willis. “Bounds and self-consistent estimates for the overall properties of anisotropic composites”. In: *Journal of the Mechanics and Physics of Solids* 25.3 (1977), pp. 185–202.

[Wil91] J. R. Willis. “On methods for bounding the overall properties of nonlinear composites”. In: *Journal of the Mechanics and Physics of Solids* 39.1 (1991), pp. 73–86.

[WP08] F. Willot and Y.-P. Pellegrini. “Fast Fourier transform computations and build-up of plastic deformation in 2D, elastic-perfectly plastic, pixelwise disordered porous media”. In: *Continuum models and discrete systems CMDS 11*. Ed. by D. Jeulin and S. Forest. Presses Mines ParisTech, 2008, pp. 443–450.

[Yin15] L. Ying. “Sparsifying Preconditioner for the Lippmann–Schwinger Equation”. In: *Multiscale Modeling & Simulation* 13.2 (2015), pp. 644–660.

[Yvo12] J. Yvonnet. “A fast method for solving microstructural problems defined by digital images: a space Lippmann–Schwinger scheme”. In: *International Journal for Numerical Methods in Engineering* 92.2 (2012), pp. 178–205.

[ZD73] R. Zeller and P. H. Dederichs. “Elastic Constants of Polycrystals”. In: *Physica Status Solidi (B)* 55.2 (1973), pp. 831–842.

[Zem+10] J. Zeman, J. Vondřejc, J. Novák, and I. Marek. “Accelerating a FFT-based solver for numerical homogenization of periodic media by conjugate gradients”. In: *Journal of Computational Physics* 229.21 (2010), pp. 8065–8071.